REPORT DOCUMENTATION PAGE

Form Approved
OMB No. 0704-0188

1. REPORT DATE *(DD-MM-YYYY)*
10/31/2014

2. REPORT TYPE
Final Report

3. DATES COVERED *(From - To)*
08/01/2008 - 07/31/2014

4. TITLE AND SUBTITLE
(MURI 08) - ROTORCRAFT BROWNOUT ADVANCED UNDERSTANDING, CONTROL, AND MITIGATION

5a. CONTRACT NUMBER

5b. GRANT NUMBER
FA9550-08-1-0406

5c. PROGRAM ELEMENT NUMBER

6. AUTHOR(S)
J. Gordon Leishman

5d. PROJECT NUMBER

5e. TASK NUMBER

5f. WORK UNIT NUMBER

7. PERFORMING ORGANIZATION NAME(S) AND ADDRESS(ES)
University of Maryland
College Park, MD 20742

8. PERFORMING ORGANIZATION REPORT NUMBER

9. SPONSORING / MONITORING AGENCY NAME(S) AND ADDRESS(ES)
Air Force Office of Scientific Research
875 North Randolf Street
Suite 325, Rm 3112
Arlington, VA 22203

10. SPONSOR/MONITOR'S ACRONYM(S)
AFMC AFOSR/RSA

11. SPONSOR/MONITOR'S REPORT NUMBER(S)

12. DISTRIBUTION / AVAILABILITY STATEMENT

Distribution A

13. SUPPLEMENTARY NOTES

14. ABSTRACT

This MURI research concerns the problem of rotorcraft brownout, which is one of the military's most significant operational problems. Brownout occurs when loose, dusty material sitting on the ground is uplifted by the intense rotor wake as it interacts with the ground. The consequences of brownout is a degraded visual environment (DVE) for the pilot(s) as well as various motion cue anomalies, which poses a serious safety of flight issue. An interdisciplinary research program is being undertaken to advance the understanding of the fluid dynamic mechanisms responsible for brownout and DVE conditions, which is also leading toward a comprehensive predictive methodology for the problem. While classic mechanisms of sediment mobility under the action of near-wall flows have been documented in this research, several other unique mechanisms of sediment uplift arise because the unsteady, three-dimensional, and strongly vortical features of the rotor wake. The rotor blade tip vortices, in particular, are responsible for mobilizing and uplifting sediment particles from the ground. Several types of modeling approaches are being developed, ranging from those based on inviscid assumptions with semi-empirical models representing sediment mobility, to sophisticated two-phase computational flu

15. SUBJECT TERMS

Rotorcraft brownout, fluid mechanics, two-phase flow, dust flows

16. SECURITY CLASSIFICATION OF:

a. REPORT	b. ABSTRACT	c. THIS PAGE	17. LIMITATION OF ABSTRACT	18. NUMBER OF PAGES
U	U	U	U	157

19a. NAME OF RESPONSIBLE PERSON
J. Gordon Leishman

19b. TELEPHONE NUMBER *(include area code)*
301-405-2376

MURI 08
“Rotorcraft Brownout Advanced Understanding, Control, and Mitigation”

Final Report
Period Ending July 31, 2014

Grant/Contract Title: (MURI 08) ROTORCRAFT BROWNOUT ADVANCED UNDERSTANDING, CONTROL, AND MITIGATION
Grant/Contract Number: FA9550-08-1-0406

Principal Investigator: J. Gordon Leishman*
Department of Aerospace Engineering
University of Maryland
College Park MD 20742

Program Manager: Douglas Smith
USAF AFMC AFOSR/RSA Flow Interactions & Control

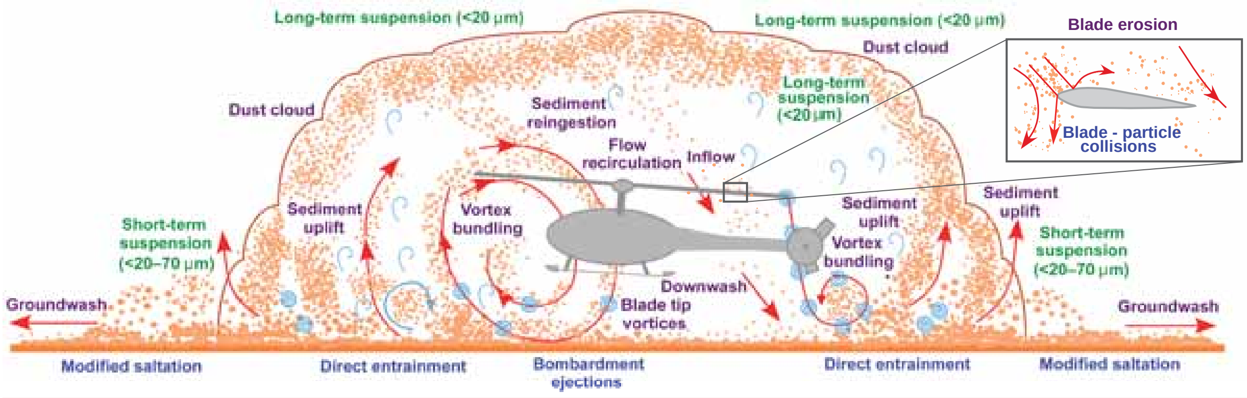

---

[*] Minta Martin Professor of Engineering. E-mail: leishman@umd.edu. Phone: (301)405-1126.

Summary

This MURI research has investigated the problem of rotorcraft brownout, which is one of the military's most significant problems encountered by helicopters and tiltrotors when they are operated in a desert-like environment. Brownout occurs when loose sediment material sitting on the ground is uplifted by the intense rotor wake generated by the rotor system. The consequences of brownout is a degraded visual environment (DVE) for the pilot as well as the possibility of motion cue anomalies, which poses a serious safety of flight issue. An interdisciplinary research program has been undertaken to advance the understanding of the fluid dynamic mechanisms responsible for brownout and DVE conditions, which has also led to various types of predictive methodologies. While classic mechanisms of sediment mobility under the action of a flow over a surface covered with a sediment bed have been shown contribute to the problem of brownout, several other unique mechanisms of sediment uplift also arise because of the unsteady, three-dimensional and strongly vortical nature of the rotor wake. The rotor blade tip vortices, in particular, have been shown by means of laboratory experiments and modeling simulations to be responsible for mobilizing and uplifting most of the sediment particles from the ground. Several types of modeling approaches have been developed in this MURI research, ranging from those based on inviscid assumptions with semi-empirical models representing sediment mobility and uplift, to sophisticated two-phase computational fluid dynamic methods based more on first principles. Such computational approaches have also provided a rigorous basis to better understand the possibilities of developing brownout mitigation strategies from the perspective of both rotor design and flight path management. This final report summarizes the work done under this MURI research program, which has run from August 2008 to July 2014.

Introduction

This comprehensive, Multidisciplinary University Research Initiative (MURI) program has advanced the understanding the rotorcraft brownout problem. Brownout is a phenomenon that occurs during rotorcraft operations near the ground in desert environments, and is characterized by a heavy dust suspension that forms around the rotorcraft. The intensity of this dust cloud is often to the degree that it can obscure the pilots vision. Furthermore, the rapid motion of the dust cloud that is usually produced in brownout conditions can lead to the pilot experiencing motion anomalies such as vection illusions. In severe cases of brownout, the pilot's can experience vertigo, which can lead to a loss of control of the rotorcraft. Brownout is the Air Force Special Operations Command's most significant operational problem, with more than half of all human-factor related rotorcraft mishaps during landings and takeoffs being attributed to encounters with brownout conditions.

This MURI research program has been structured to provide advances in the physical understanding of rotorcraft brownout, and has also been focused toward the development of a comprehensive methodology to predict and understand how it might be possible to mitigate the effects of brownout. While the problem of brownout has been better understood by performing research into the underlying fluid dynamics of how the action of the rotor wake near the ground mobilizes and uplifts sediment particles, brownout is also a broader problem that comes under the classification of flight in a Degraded Visual Environment (DVE). The research goals of the MURI have been achieved by better understanding rotor and airframe aerodynamics when operating in ground effect, with particular emphasis on understanding the detailed dual-phase nature of the rotor-induced

Figure 1: Photograph of a landing helicopter beginning to encounter brownout conditions.

particle flow near the ground. In particular, details of the fluid dynamic interactions of the rotor wake with the mobile sediment bed have been researched to expose the mechanisms responsible for sediment particle uplift as well as the resulting transport of particles around the rotor and the rotorcraft as a whole.

The formation of the brownout dust cloud is a fundamentally complex, two-phase fluid dynamics phenomenon with its origin in the effects of the energetic rotor wake on the loose sediment particles lying on the ground. Factors that influence the mobilization and transport of the resulting two-phase flow include the processes of particle mobilization, entrainment, suspension, bombardment and deposition. If the dust clouds become sufficiently dense, then a fluid dynamic coupling can be produced to the degree that the particles can modify the rotor wake flow. However, the understanding of the brownout problem is extremely difficult, in part because the dust cloud formation is affected by many parameters including (but not limited to): rotor disk loading, blade loading, number and placement of rotors, number of blades, blade twist, blade tip shape, fuselage shape, as well as sediment type and surface condition. Some types of rotorcraft seem to be particularly susceptible to brownout problems as a consequence of the reingestion of suspended dust through the rotor disk followed by bombardment of this dust back onto the sediment bed and the ejection of yet more dust.

In this MURI research program, detailed measurements of the fluid dynamics of the rotor wake as it interacts with the ground and with a mobile sediment bed have been conducted at various geometric scales, and in both air and water, to provide fundamental insight into the boundary layer flow on the ground and the mechanisms of particle mobilization. While most of the experiments have been performed with the rotor hovering over a ground plane and a mobile sediment bed, some more recent dual-phase flow experiments have been conducted with a rotor translating over the bed and so representing an actual flight maneuver. In this latter case, the bundling of rotor wake vortices on the ground plane ahead of the translating rotor has been shown to be a primary

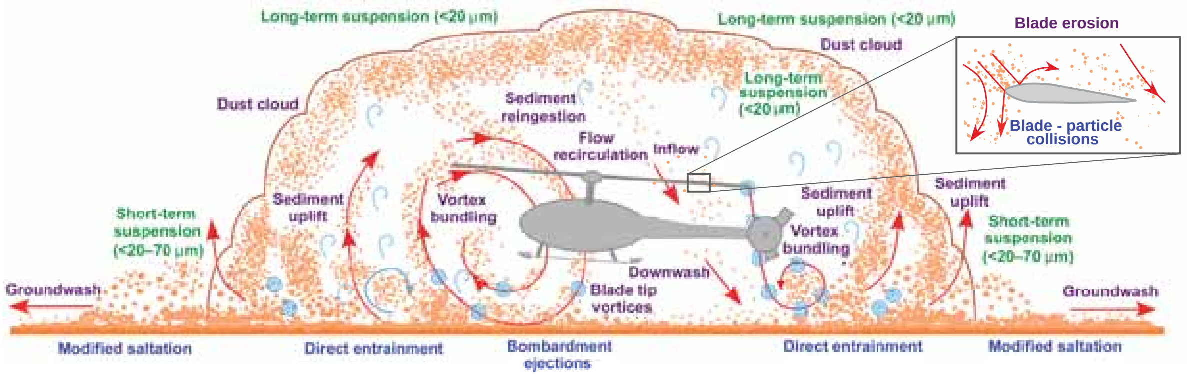

Figure 2: Schematic showing the mechanisms of particle mobilization and uplift as a helicopter encounters brownout conditions.

mechanism that affects the mobilization and uplift of sediment particles and hence the formation of brownout dust clouds.

The computational tasks in the MURI effort have been focused on more accurately capturing the vortical wake system generated by the rotor and preserving this vorticity as it is convected towards the ground. The modeling work has included of rotor induced particle flows as well as vortex-fuselage-tail rotor interacting flows. The computational work in this MURI has also been concerned with using advanced techniques and architectures for the computational simulation of brownout. For example, methods have been developed to improve the computational speed of the techniques used to predict particle motion, such as by using clustering methods and fast-multipole methods, and also with the use of heterogeneous computing architectures. In particular, particle clustering methods have been explored to significantly reduce the computational time in the simulation of a large numbers of convecting particles. However, it has been shown that clustering methods must be applied judiciously so as to preserve the accuracy of the resulting dust cloud simulations.

The validation of the various modeling approaches has been an important goal of this MURI research program. While much validation work has been done based on outcomes from laboratory measurements, including validation of the mechanisms of vortex-induced particle motion, the ultimate challenge is to predict the behavior of a brownout dust cloud generated by an actual helicopter during a landing in a desert environment. Because of the challenges in learning about the problem and developing modeling tools, progress toward this latter end has taken much longer than was initially anticipated, mainly because it needs to synthesize understanding and modeling advancements made in the other tasks, including pilot-in-the-loop simulations that can be executed in real-time. The recent focus has been on developing a hybrid approaches that take advantage of the best features of the work that had already been performed under other tasks. However, a lack of measurements of the brownout phenomenon at full-scale (i.e., with actual helicopters flown by pilots in actual brownout conditions) continues to impede the validation of modeling activities.

Meantime, the the MURI work has progressed toward better understanding the actual brownout problem by using various simulations. The MURI team has used a state of the art a flight simulator with advanced visuals, which has been used to render and display brownout dust cloud simulations in real time. A physics-based and GPU-accelerated brownout simulation methodology has been successfully developed to represent the dynamic motion of dust particles and the optical attenuation caused by dust particles. Two new methodologies were developed, namely a dust cloud illumination methodology to calculate the optical attenuation caused by dust clouds that affects the visualization of dust clouds from the pilot's perspective, and a methodology to render individual dust particles on computer graphics. The calculations of velocities induced on dust particles, their positions, and the optical attenuation have been implemented on GPUs. In the future, this system may help to verify the fidelity of the dust cloud simulations through pilot assessments, and also begin to explore other strategies for the mitigation of brownout through flight path management.

The research outcomes in this MURI have shown that brownout can be successfully mitigated by means of modifications to aspects of the rotor design, but this may not be a practical approach, i.e., in practice the rotor design is driven and constrained by many other factors besides brownout concerns. The research work has also shown that brownout can be mitigated by appropriate flight path management by the pilot, i.e., where pilots fly prescribed airspeed and altitude profiles to minimize the severity of brownout. However, the number of variables involved in the flight path management problem mean that the ideal or optimum flight paths will be dependent on the type of rotorcraft (e.g., single main rotor, tandem, tiltrotor, etc.), the weight and center of gravity of the aircraft, the physical nature of the sediment and the sediment bed, as well as potentially the different flying skills of each pilot.

Mitigation may also help to reduce another problem plaguing rotorcraft operating in desert environments, which is the rapid abrasion seen on the rotor blades. Abrasion leads to rotor performance degradation as well as high maintenance costs and significant downtime because of the frequent replacement of rotor blades. With the ability to predict with growing confidence the position of particles with respect to the rotor blades and airframe, future work may lead to models that can improve the design of more abrasion resistant rotor blades.

This final report summarizes the progress made in the MURI effort, primarily over the last two years, and also indicates profitable avenues for future research into the brownout problem. Further information on the research efforts can be obtained directly from the Principal Investigator or from each of the respective task leaders. This MURI research has also had a strong educational and training component, and the students participating in the program have been identified under each task. Eleven students have successfully completed their Ph.D. degrees under the support of the MURI and a further twenty have completed their M.S. degrees; several students have completed both their M.S. and Ph.D. degrees under this MURI. Most of these students are now pursuing further research in government labs or in industry. In particular, one Ph.D. student from the program (Joe Milluzzo) has established a successful career as a professor at the U.S. Naval Academy. Another student (Monica Syal) works in the rotorcraft industry and was recently publicized by NVIDIA (a manufacturer of GPUs) as being one of their major success stories in use of GPUs for scientific simulation. Several other students from the MURI program are now working at U.S. Government laboratories.

Faculty Participating in this MURI

University of Maryland

- J. Gordon Leishman, D.Sc., Ph.D., Professor, Department of Aerospace Engineering (PI)
- James Baeder, Ph.D., Associate Professor, Department of Aerospace Engineering
- Roberto Celi, Ph.D., Professor, Department of Aerospace Engineering
- Anya Jones, Ph.D., Assistant Professor, Department of Aerospace Engineering
- Kenneth Kiger, Ph.D., Professor, Department of Mechanical Engineering
- Ugo Piomeli, Ph.D., Professor, Department of Mechanical Engineering
- Ramani Duraiswami, Ph.D., Associate Professor, Department of Computer Science & Institute for Advanced Computer Studies
- Nail Gumerov, Ph.D., Senior Research Scientist, Department of Computer Science & Institute for Advanced Computer Studies

Dartmouth College/Earth Sciences

- W. Brian Dade, Ph.D., Associate Professor of Earth Sciences
- Benoit Cushman Roisin, Ph.D., Professor of Engineering

Iowa State University

- Ganish Rajagopolan, Ph.D., Professor, Department of Aerospace Engineering

Arizona State University

- Kyle Squires, Ph.D., Professor, Department of Aerospace Engineering

University of Texas at Arlington

- Stefan Dancila, Ph.D., Associate Professor, Department of Mechanical and Aerospace Engineering

MURI Graduate Students

University of Maryland

- Phillip Knowles, GRA – Graduated Ph.D. 2009
- Bradley Johnson, GRA – Graduated M.S. 2009
- Timothy Lee, GRA – Graduated M.S. 2010
- Bharath Govindarajan, GRA – Graduated M.S. 2011, Graduated Ph.D. 2014
- Joseph Milluzzo, GRA – Graduated M.S. 2011, Graduated Ph.D. 2014
- Anish Sydney, GRA – Graduated M.S. 2011, Graduated Ph.D. 2014
- Ajay Baharani, GRA – Graduated M.S. 2011
- Jayson Geisler, GRA – Graduated M.S. 2011
- Benjamin Hance, GRA – Graduated M.S. 2012
- Monica Syal, GRA – Graduated M.S. 2009, Graduated Ph.D. 2013
- John Tritschler, GRA – Graduated Ph.D. 2012
- Jillian Alfred, GRA – Graduated M.S. 2013
- Qi Hu, GRA – Graduated Ph.D. 2013
- Jürgen Rauleder, GRA – Graduated Ph.D. 2014
- Tarandeep Singh Kalra, GRA – Graduated Ph.D. 2014
- Sebastian Thomas, GRA – Graduated Ph.D. 2014
- Rahul Mulinti, GRA – Ph.D. expected 2014
- Mark Glucksman-Glaser, GRA – Graduated M.S. 2013
- Nathan Doane, GRA – M.S. expected 2015
- Jaime Reel, GRA – Graduated M.S. 2014
- Kyle Corfman, GRA – M.S. expected 2014
- Gino Perrotta, GRA – Graduated M.S. 2014

Arizona State University

- Fernando Morales, GRA – Graduated M.S. 2012
- Dennis Dunn – Ph.D. expected 2014

Iowa State University

- Sayan Gosh, GRA – Graduated M.S. 2010
- William Polzin, GRA – Graduated M.S. 2012

Dartmouth College

- Chris Martin, GRA – Graduated B.A. 2012
- Nathan Hamm, GRA – Graduated Ph.D. 2012

Conference and Journal Publications

1. Leishman, J. G., “Challenges in Understanding the Fluid Dynamics of Brownout,” American Helicopter Society Specialist’s Conference, 2nd International Forum on Rotorcraft Multidisciplinary Technology, Seoul, Korea, October 2009.

2. Celi, R., “The AFOSR MURI on Rotorcraft Brownout: Advanced Understanding, Control, and Mitigation,” Naval Aviation Center for Rotorcraft Advancement (NACRA) Semiannual InterService DVE Workshop, NAS Patuxent River, MD, June 2009.

3. Knowles, P., and Kiger, K., “Quantification of Particle Concentration in Sheet Illumination Imaging Technique,” 62nd Annual Meeting of the APS Division of Fluid Dynamics, November 2009.

4. Morales, F., Naqvi, I., Squires, K. D., and Piomelli, U., “Euler-Lagrange Simulations of Particle Interactions with Coherent Vortices in Turbulent Boundary Layers,” Presented at the 62nd Annual Meeting of the Division of Fluid Dynamics, Minneapolis, MN, November 2009.

5. Morales, F., Naqvi, I., Squires, K. D., and Piomelli, U., “Euler-Lagrange Simulations of Particle Interactions with Coherent Vortices in Turbulent Boundary Layers,” *Bulletin of the American Physical Society*, Vol. 54, No. 19, 2009.

6. Dade, B., “Near-Bed Aeolian Sediment Transport Under Non-Uniform Flows,” American Geophysical Union, Fall Meeting 2010, Abstract EP31A-0731, December 2009.

7. Milluzzo, J., and Leishman, J. G., “Assessment of Rotorcraft Brownout Severity in Terms of Rotor Design Parameters,” *Journal of the American Helicopter Society*, 55, 032009, 2010; DOI:10.4050/JAmerican Helicopter Society.55.032009.

8. Tritschler, J. K., and Celi, R. “The Use of the Modulation Transfer Function for Brownout Cloud Characterization,” *Journal of the American Helicopter Society*, 55, 045001, 2010; DOI:10.4050/JAmerican Helicopter Society.55.045001.

9. Johnson, B., Leishman, J. G., and Sydney, A., “Investigation of Sediment Entrainment in Brownout using High-Speed Particle Image Velocimetry,” *Journal of the American Helicopter Society*, 55, 042003, 2010; DOI:10.4050/JAmerican Helicopter Society.55.042003.

10. Knowles, P., and Kiger, K. T., "Quantification of Dispersed Phase Concentration using Light Sheet-Based Imaging Methods," *Experiments in Fluids*, DOI: 10.1007/s00348-011-1100-8.

11. Kalra, T., Lakshminarayan, V., and Baeder, J., "CFD Validation of Micro Hovering Rotor in Ground Effect," American Helicopter Society International Specialists' Conference on Aeromechanics, San Francisco, CA, January 2010.

12. Tritschler, J. K., and Celi, R., "Brownout Cloud Characterization using the Modulation Transfer Function," U.S. Navy TTCP TP-2 Workshop, Annapolis, MD, April 2010.

13. Tritschler, J. K., and Celi, R. "The Modulation Transfer Function as the Basis for a Brownout Metric," American Helicopter Society 66th Annual Forum Proceedings, Phoenix, AZ, May 10–13, 2010.

14. Tritschler, J. K., Syal, M., Celi, R., and Leishman, J. G., "A Methodology for Rotorcraft Brownout Mitigation using Rotor Design Optimization," American Helicopter Society 66th Annual Forum Proceedings, Phoenix, AZ, May 10–13, 2010.

15. Thomas, S., Ananthan, S., and Baeder, J. D., "Wake-Coupling CFD-CSD Analysis of Helicopter Rotors in Steady and Maneuvering Flight Conditions," American Helicopter Society 66th Annual Forum Proceedings, Phoenix, AZ, May 10–13, 2010.

16. Syal, M., Govindarajan, B., and Leishman, J. G., "Mesoscale Sediment Tracking Methodology to Analyze Brownout Cloud Developments," American Helicopter Society 66th Annual Forum Proceedings, Phoenix, AZ, May 10–13, 2010.

17. Kalra, T., Laksminarayan, V., and Baeder, J. D., "CFD Validation of a Micro Hovering Rotor in Ground Effect," American Helicopter Society 66th Annual Forum Proceedings, Phoenix, AZ, May 10–13, 2010.

18. Milluzzo, J., Sydney, A., Rauleder, J., and Leishman, J. G., "In Ground Effect Aerodynamics of Rotors with Different Blade Tips," American Helicopter Society 66th Annual Forum Proceedings, Phoenix, AZ, May 10–13, 2010.

19. Ghosh, S., Lohry, M., and Rajagopalan, G., "Rotor Configurational Effect on Brownout," Presented at the 28th AIAA Applied Aerodynamics Conference, Chicago, IL, June 2010.

20. Kiger, K. T., and Knowles, P., “Quantification of Dispersed Phase Concentration using Light Sheet-Based Imaging Methods,” 15th International Symposium on Applications of Laser Techniques to Fluid Mechanics, Lisbon, Portugal, July 2010.

21. Leishman, J. G., “Challenges in Understanding the Fluid Dynamics of Brownout: Review and Update,” Presented at the American Helicopter Society International Meeting on Advanced Rotorcraft Technology and Safety Operations, Omiya, Japan, November 1–3, 2010.

22. Geiser, J., and Kiger, K. T., “Vortex Ring Breakdown Induced by Topographic Forcing,” 13th European Turbulence Conference, Warsaw, Poland, 12–15 September. *Journal of Physics: Conference Series, Advances in Turbulence*, 2011.

23. Knowles, P. L., and Kiger, K. T., “Quantification of Dispersed Phase Concentration using Light Sheet Imaging Methods,” *Experiments in Fluids*, DOI 10.1007/s00348-011-1100-8, 2011.

24. Tritschler, J. K., and Celi, R., “The Use of the Modulation Transfer Function for Brownout Cloud Characterization,” *Journal of the American Helicopter Society*, Vol. 55, 045001, doi: 10.4050/JAHS.55.045001, October 2011, pp 1–4.

25. Hu, Q., Syal, M., Gumerov, N., Duraiswami, R., and Leishman, J. G., “Toward Improved Aeromechanics Simulations using Recent Advancements in Scientic Computing,” American Helicopter Society 67th Annual Forum Proceedings, Virginia Beach, VA, May 3–5, 2011.

26. Syal, M., and Leishman, J. G., “Comparisons of Predicted Brownout Dust Clouds with Photogrammetry Measurements,” American Helicopter Society 67th Annual Forum Proceedings, Virginia Beach, VA, May 3–5, 2011.

27. Thomas, S., Laksminarayan, V., Kalra, T., and Baeder, J. D., “Eulerian-Lagrangian Analysis of Cloud Evolution using CFD Coupled with a Sediment Tracking Algorithm,” American Helicopter Society 67th Annual Forum, Virginia Beach, VA, May 3–5, 2011.

28. Sydney, A., Baharani, A., and Leishman, J. G., “Understanding Brownout using Near-Wall High-Speed Dual-Phase Flow Measurements,” American Helicopter Society 67th Annual Forum Proceedings, Virginia Beach, VA, May 3–5, 2011.

29. Govindarajan, B., and Leishman, J. G., “ Evaluation of Particle Clustering Algorithms in the Prediction of Brownout Dust Clouds,” American Helicopter Society 67th Annual Forum Proceedings, Virginia Beach, VA, May 3–5, 2011.

30. Kalra, T., Laksminarayan, V., Baeder, J. D., and Thomas, S., “Methodological Improvements for Computational Study of a Hovering Micro-Rotor in Ground Effect,” AIAA Computational Fluid Dynamics Conference, Honolulu, HI, June 2011.

31. Syal, M., Rauleder, J., Tritschler, J., and Leishman, J. G., “On the Possibilities of Brownout Mitigation using a Slotted-Tip Rotor Blade,” 29th AIAA Applied Aerodynamics Conference, Honolulu, HI, June 2011.

32. Polzin, W. J., Guntupalli, K., and Rajagopalan, R. G., “Discrete Blade Model for Rotorcraft Brownout,” 29th AIAA Applied Aerodynamics Conference, Honolulu, HI, June 2011.

33. Morales, F., and Squires, K. D.,“Simulation of Rotor Vortex Interactions With a Particle-Laden Turbulent Boundary Layer,” AIAA Paper 2011-4041, AIAA Computational Fluid Dynamics Conference, Honolulu, HI, 2011.

34. Tritschler, J. K., Celi, R., and Leishman, J. G., “A Methodology for the Numerical Optimization of Approach Profiles for Rotorcraft Brownout Mitigation,” American Helicopter Society 3rd International Technical Specialists’ Meeting on Vertical Lift Research, Development, Test, and Evaluation, Patuxent NAS, MD, August 2011.

35. Rauleder, J., and Leishman, J. G., “Measurements of the Turbulent Flow Environment on the Ground Below a Hovering Rotor,” 37th European Rotorcraft Forum Proceedings, Gallarate, Italy, September 13–15, 2011.

36. Tritschler, J. K., and Celi, R., “Ground Level Measurements of the Modulation Transfer Function of a Brownout Cloud,” 37th European Rotorcraft Forum Proceedings, Gallarate, Italy, September 13–15, 2011.

37. Kiger, K. T., and Geiser, J., “Vortex Ring Breakdown Induced by Topographic Forcing,” 13th European Turbulence Conference, Warsaw, Poland, September 12–15, 2011 *J. Phys.: Conf. Ser.* 318 062013. DOI:10.1088/1742-6596/318/6/062013.

38. Hu, Q., Gumerov, N. A., and Duraiswami, R., “Scalable Fast Multipole Methods on Distributed Heterogeneous Architectures,” Supercomputing Conference 2011.

39. Geiser, J., and Kiger, K. T., “Effects of Ground Plane Topology on Vortex-Ground Interactions in a Forced Impinging Jet,” 64th Annual Meeting of the American Physical Society Division of Fluid Dynamics, Baltimore, MD, November 20–22, 2011.

40. Mulinti, R. and Kiger, K. T., “PTV Implementation on Two-Phase Flow in a Forced Impinging Jet,” 64th Annual Meeting of the American Physical Society Division of Fluid Dynamics, Baltimore, Maryland, November 20–22, 2011.

41. Knowles, P. L., and Kiger, K. T., “Quantification of Dispersed Phase Concentration using Light Sheet Imaging Methods,” *Experiments in Fluids*, 52(3), pp. 697–708, 2012, DOI: 10.1007/s00348-011-1100-8.

42. N. A. Gumerov, and R. Duraiswami, “Efficient FMM Accelerated Vortex Element Methods in Three Dimensions via the Lamb-Helmholtz Decomposition,” ArXiv: 1201.5430, January 2012, http://arxiv.org/.

43. Tritschler, J. K., and Celi, R., “Brownout Cloud Characterization using the Modulation Transfer Function,” *Journal of the American Helicopter Society*, April 2012.

44. Syal, M., and Leishman, J. G., “Comparisons of Predicted Brownout Dust Clouds with Photogrammetric Measurements,” *Journal of the American Helicopter Society*, July 2012.

45. Syal, M., and Leishman, J. G., “Modeling of Bombardment Ejection in the Rotorcraft Brownout Problem,” *AIAA Journal*, July 2012.

46. Hu, Q., Gumerov, N. A., and Duraiswami, R., “GPU Accelerated Fast Multipole Methods for Dynamic N-Body Simulation,” Parallel CFD 2012, Atlanta, GA, May, 2012.

47. Gumerov, N. A., and Duraiswami, R., “Efficient FMM Accelerated Vortex Element Methods in Three Dimensions via the Lamb-Helmholtz Decomposition,” *Journal of Computational Physics*, 2012.

48. Hu, Q., Gumerov, N. A., Yokota, R., Barba, L., and R. Duraiswami, “Scalable Vortex Methods using Fast Multipole Methods,” International Conference for High Performance Computing, Networking, Storage, and Analysis, SC’12.

49. Hu, Q., Gumerov, N. A., and Duraiswami, R., “Parallel Data Structures for Fast Multipole Methods, *Journal of Parallel and Distributed Computing*.

50. Hu, Q., Gumerov, N. A., and Duraiswami, R., “A Scalable Fast Multipole Method for Heterogeneous Architectures,” *Journal of Computational Physics*.

51. Tritschler, J. K., Celi, R., and Leishman, J. G., “A Methodology for Rotorcraft Brownout Mitigation Through Flight Path Optimization,” American Helicopter Society Future Vertical Lift Aircraft Design Conference, San Francisco, CA, January 2012.

52. Tritschler, J. K., Celi, R., and Leishman, J. G., “The Effect of Number of Blades on Optimum Rotor Design for Brownout Mitigation,” American Helicopter Society Future Vertical Lift Aircraft Design Conference, San Francisco, CA, January 2012.

53. Rauleder, J., and Leishman, J. G., “Flow Environment and Organized Turbulence Structures at the Ground Below a Rotor,” American Helicopter Society 68th Annual Forum Proceedings, Fort Worth, TX, May 1–3, 2012.

54. Tritschler, J. K., and Celi, R., “Modeling Issues in the Prediction of the Modulation Transfer Function of a Brownout Cloud,” American Helicopter Society International 68th Annual Forum Proceedings, Fort Worth, TX, May 1–3, 2012.

55. Tritschler, J. K., Celi, R., and Leishman, J. G., “A Methodology for Rotorcraft Brownout Mitigation Through Flight Path Optimization,” American Helicopter Society International 68th Annual Forum Proceedings, Fort Worth, TX, May 1–3, 2012.

56. Tritschler, J. K., and Celi, R., “Modeling Issues in the Prediction of the Modulation Transfer Function of a Brownout Cloud,” American Helicopter Society International 68th Annual Forum Proceedings, Fort Worth, TX, May 1–3, 2012.

57. Thomas, S., Kalra, T., and Baeder, J. D., “A Hybrid CFD Methodology to Model the Two-phase Flowfield beneath a Hovering Laboratory Scale Rotor,” AIAA Computational Fluid Dynamics Conference, New Orleans, LA, June 2012.

58. Glucksman-Glaser, M., and Jones, A., “Effects of Model Scaling on Sediment Transport in Brownout,” AIAA Paper 2012-2915, 30th AIAA Applied Aerodynamics Conference, New Orleans, LA, June 2012.

59. Lakshminarayan, V. K., Kalra, T. S., and Baeder, J. D., “Detailed Computational Investigation of a Hovering Micro-Scale Rotor in Ground Effect,” *AIAA Journal*, June 2012.

60. Mulinti, R., and Kiger, K. T., “Particle Suspension by a Forced Jet Impinging on a Mobile Sediment Bed,” 16th International Symposium on Applications of Laser Techniques to Fluid Mechanics, Lisbon, Portugal, July 9–12, 2012.

61. Tritschler, J. K., Celi, R., and Leishman, J. G., “The Effect of Number of Blades on Optimum Rotor Design for Brownout Mitigation,” Future Vertical Lift Aircraft Design Conference Proceedings, San Francisco, CA, January 18–20, 2012.

62. Thomas, S., Kalra, T., and Baeder, J. D., “A Hybrid CFD Methodology to Model the Two-phase Flowfield beneath a Hovering Laboratory Scale Rotor,” 30th AIAA Applied Aerodynamics Conference, New Orleans, LA, June 25–28, 2012.

63. Hu, Q., Gumerov, N. A., and Duraiswami, R., “Scalable Fast Multipole Methods on Distributed Heterogeneous Architectures, Proceedings of International Conference for High Performance Computing, Networking, Storage, and Analysis, Ser. SC’11, New York, NY, 2011, pp. 36:1–36:12.

64. Hu, Q., Gumerov, N. A., and Duraiswami, R., “Scalable Distributed Fast Multipole Methods,” Proceedings of the 14th International Conference on High Performance Computing and Communications, Ser. HPCC’12. New York, NY, 2012.

65. Q. Hu, N. A. Gumerov, R. Yokota, L. Barba, and R. Duraiswami, “Scalable Fast Multipole Methods for Vortex Element Methods,” International Conference for SC’12 Proceedings of the 2012 SC Companion: High Performance Computing, Networking, Storage, and Analysis, 1408–1409, IEEE Computer Society, Washington, DC, 2012.

66. Mulinti, R., Corfman, K., and Kiger, K. T., “In Situ Calibration of Volume Concentration Measurements using PTV Correlation for Particle-Laden Flows,” 65th Annual Meeting of the American Physical Society Division of Fluid Dynamics, San Diego, California, November 18–20, 2012.

67. Kalra, T., Laksminarayan, V., and Baeder, J. D., “Effect of Tip Geometry on a Hovering Rotor in Ground Effect: A Computational Study,” 31st AIAA Applied Aerodynamics Conference, San Diego, CA, June 24–27, 2013.

68. Lakshminarayan, V. K., Kalra, T. S., and Baeder, J. D., “Detailed Computational Investigation of a Hovering Micro-Scale Rotor in Ground Effect,” *AIAA Journal*, Vol. 51, (4), April

2013, pp. 893–909.

69. Milluzzo, J., and Leishman, J. G., “Development of the Turbulent Vortex Sheet in the Wake of a Hovering Rotor” 69th Annual Forum Proceedings of the American Helicopter Society, Phoenix, AZ, May 21–23, 2013.

70. Sydney, A. and Leishman, J. G., “Measurements of Rotor/Airframe Interactions in Ground Effect Over a Sediment Bed,” American Helicopter Society 69th Annual Forum Proceedings, Phoenix, AZ, May 21–23, 2013.

71. Mulinti, R., Corfman, K., and Kiger, K. T., “Particle-Turbulence Interaction of Suspended Load by Forced Jet Impinging on a Mobile Sediment Bed,” 66th Annual Meeting of the American Physical Society Division of Fluid Dynamics, Pittsburgh, PA, November 24–26, 2013.

72. Corfman, K., Mulinti, R., and Kiger, K. T., “Erosion and Transport of Particulates by Forced Jet impinging on a Mobile Sediment Bed,” 66th Annual Meeting of the American Physical Society Division of Fluid Dynamics, Pittsburgh, PA, November 24–26, 2013.

73. Rauleder, J., and Leishman, J. G., “Turbulence Modifications and Phase Couplings in Ground Effect under Simulated Brownout Conditions,” American Helicopter Society 69th Annual Forum Proceedings, Phoenix, AZ, May 21–23, 2013.

74. Alfred, J., Celi, R., and Leishman, J.G., “Rotorcraft Brownout Mitigation through Flight Path Optimization using a High-Fidelity Rotorcraft Simulation Model,” American Helicopter Society International 69th Annual Forum, Phoenix, AZ, May 21–23, 2013.

75. Thomas, S., Amiraux, M., and Baeder, J. D., “GPU-accelerated FVM-RANS Hybrid Solver for Simulating Two-phase Flow beneath a Hovering Rotor,” American Helicopter Society 69th Annual Forum Proceedings, Phoenix, AZ, May 21–23, 2013.

76. Thomas, S., Amiraux, M., and Baeder, J. D., “Modeling the Two-Phase Flowfield Beneath a Hovering Rotor on Graphics Processing Units using a FVM-RANS Hybrid Methodology,” 21st AIAA Computational Fluid Dynamics Conference, San Diego, CA June 24–27, 2013.

77. Qi Hu, Nail A. Gumerov, and Ramani Duraiswami, “GPU Accelerated Fast Multipole Methods for Dynamic N-body Simulation,” Accepted for *Computers and Fluids*, 2013.

78. B. Govindarajan, J. G. Leishman and N. A. Gumerov. “Particle-Clustering Algorithms for the Prediction of Brownout Dust Clouds,” *AIAA Journal*, 10.2514/1.J051907, 1–15, 2013.

79. Q. Hu, N. A. Gumerov, and R. Duraiswami, “Parallel Data Structures for Fast Multipole Methods,” Accepted for *Journal of Parallel Computing*. Also published on arXiv `http://arxiv.org/abs/1301.1704`.

80. Milluzzo, J., and Leishman, J. G.,. “Quantification of the Evolution of the Vortical Sheets in the Wake of a Hovering Rotor” Proceedings of 32nd AIAA Applied Aerodynamics Conference, Atlanta, GA, June 16–20, 2014.

81. Govindarajan, B. M., and Leishman, J. G., “Predictions of Rotor and Rotor/Airframe Configurational Effects on Brownout Dust Clouds,” 70th Annual Forum Proceedings of the American Helicopter Society, Montreal, Quebec, May 20–22, 2014. (Awarded best paper in the operations session.)

82. Sydney, A. and Leishman, J. G., “Measurements of The Plume-Like Three-Dimensionality of Rotor-Induced Dust Fields,” American Helicopter Society 70th Annual Forum Proceedings, Montréal, Canada, May 21–23, 2014.

83. Sydney, A., “Contributions Towards the Understanding of Rotor-Induced Dust Particle Mobilization,” Ph.D. Dissertation, Dept. of Aerospace Engineering, University of Maryland, College Park, August 2014.

84. Reel, J., and Leishman, J. G., “Mechanisms of Vortex-Induced Particle Transport as it may Affect Rotorcraft Brownout,” Presented at the American Helicopter Society 4th International Technical Specialists’ Meeting on Vertical Lift Aircraft RDT&E, Patuxent River, Maryland, August 27–28, 2014.

85. Kiger K. T., Corfman K. & Mulinti R., “Effect of Bed Form Evolution on Sediment Erosion and Suspended Load Transport in an Impinging Jet,” 17th International Symposium on Applications of Laser Techniques to Fluid Mechanics, Lisbon, Portugal, July 7–10, 2014.

86. Perrotta, G., and Jones, A., “Characterization of Rotor Wake in Ground Effect,” AIAA Region I-MA Student Paper Conference, Ithaca, NY, April 2014. (Awarded 1st place in the Graduate category.)

87. Rauleder, J., and Leishman, J. G., “Particle–Fluid Interactions in Rotor-Generated Vortex Flows,” *Experiments in Fluids*, Vol. 55, (3), 2014, pp. 1–15.

88. Rauleder, J., and Leishman, J. G., “Fluid–Particle Interaction in Vortex-Induced Dual-Phase Flows Above a Sediment Bed,” Proceedings of the 44th AIAA Fluid Dynamics Conference, Atlanta, GA, June 16–20, 2014.

89. Rauleder, J., and Leishman, J. G., “Flow Environment and Organized Turbulence Structures near a Plane below a Rotor,” *AIAA Journal*, Vol. 52, (1), 2014, pp. 146–161.

90. Gumerov2014:JCP N.A. Gumerov and R. Duraiswami, “A Method to Compute Periodic Sums,” *Journal of Computational Physics*, 272, 307–326, 2014.

91. Hu2014:JCP Q. Hu, N. A. Gumerov, and R. Duraiswami, “A Scalable Fast Multipole Method for Heterogeneous Architectures,” *Journal of Computational Physics* (under preparation).

Research Task	Interactions	Task Leader(s)
Part 1. Fundamentals of Rotor and Airframe Aerodynamics in Ground Effect Operations		
1.1 Measurements of Rotor and Fuselage Aerodynamics in Ground Effect	1.2, 1.3, 2.2, 2.3	Leishman
1.2 High Fidelity Vorticity Generation and Preservation in Ground Effect	1.1, 1.3, 2.3, 2.4, 2.5	Baeder, Chopra
1.3 Fuselage Configuration Effects on Rotorwash and Brownout	1.1, 1.2, 2.2	Leishman, Baeder
Part 2. Fundamentals of Particle Suspension		
2.1 Non-Uniform, Near-Bed Flow Field Associated With Impinging Rotorwash*	2.2, 2.3, 2.4, 2.5, 2.6	Dade, Cushman-Roisin
2.2 Dual-Phase PIV in Two-Phase Near-Wall Bounded Turbulent Flows	2.1, 2.3, 3.1, 2.6, 2,7	Leishman
2.3 Fundamental Two-Phase Measurements in Brownout Fluid Mechanics	2.2, 2.4, 2.5, 2.7	Kiger
2.4 Large-Eddy Simulation of the Interaction Between Wake Vortices and the Ground*	1.2, 2.1, 2.2, 2.3, 2.5	Piomelli
2.5 Two-Phase Large-Eddy Simulation Between Wake Vortices and Ground	1.2, 2.1, 2.2, 2.3, 2.4	Squires
2.6 Effects of Model Scaling on Sediment Transport	2.1, 2.2, 2.3, 2.4, 2.7	Jones, Leishman
2.7 Turbulent Near-Bed Flows Under Impinging Vorticity	2.1, 2.2, 2.3, 2.4, 2.6	Leishman
Part 3. Brownout Synthesis Mitigation and Validation		
3.1 Pilot-in-the-Loop Brownout Simulation and Mitigation Strategies	3.2, 3.3, 3.4	Syal, Leishman*, **
3.2 Development of Numerically Efficient Airborne Sediment Tracking Algorithms	3.1, 3.3, 3.4	Leishman, Baeder
3.3 Understanding Brownout and Developing Mitigation and Control Strategies	All	Celi, Leishman, Baeder
3.4 ABATE Simulation Framework and Validation	All	Baeder, Celi, Leishman
3.5 Computational Considerations in the Prediction of Brownout Dust Clouds	3.1, 3.2, 3.3, 3.4	Duraiswami, Gumerov, Leishman
3.6 Blade Tip Actuation for Vortex Core Modifications for Brownout Mitigation**	1.1, 2.2, 3.3, 3.4	Dancila, Leishman

Table 1: Rotorcraft Brownout MURI: Summary of tasks and task interactions. *Note: Original tasks have been closed out, restructured, or are funded separately. ** New task.

Task Descriptions and Summary of Results

The following pages provide summaries of the research in each of the MURI tasks. Further information can be obtained from the Principal Investigator or from each of the task leaders.

Part 1. Fundamentals of Rotor and Airframe Aerodynamics in Ground Effect Operations:

- Task 1.1 – Measurements of Rotor and Fuselage Aerodynamics in Ground Effect
- Task 1.2 – High Fidelity Vorticity Generation and Preservation in Ground Effect
- Task 1.3 – Fuselage Configuration Effects on Rotorwash and Brownout

Part 2. Fundamentals of Particle Suspension:

- Task 2.1 – Non-Uniform, Near-Bed Flow Field with Impinging Rotorwash
- Task 2.2 – Two-Phase PIV Near-Wall Bounded Turbulent Flows
- Task 2.3 – Fundamental Two-Phase Measurements in Brownout Fluid Mechanics
- Task 2.4 – Large-Eddy Simulation of the Interaction Between Vortices and the Ground
- Task 2.5 – Two-Phase Large Eddy Simulation Using the Mesoscopic Eulerian Formalism
- Task 2.6: Effects of Model Scaling on Sediment Transport
- Task 2.7: Turbulent Near-Bed Flows Under Impinging Vorticity

Part 3. Brownout Synthesis Mitigation and Validation:

- Task 3.1 – Pilot-in-the-Loop Brownout Simulation and Mitigation Strategies
- Task 3.2 – Development of Efficient Airborne Sediment Tracking Algorithms
- Task 3.3 – Understanding Brownout and Developing Mitigation and Control Strategies
- Task 3.4 – ABATE Simulation Framework and Validation
- Task 3.5 – Computational Considerations in the Prediction of Brownout Dust Clouds
- Task 3.6 – Blade Tip Actuation for Tip Vortex Modifications for Brownout Mitigation

Part 1: Fundamentals of Rotor and Airframe Aerodynamics in Ground Effect Operations

- Task 1.1 – Measurements of Rotor and Fuselage Aerodynamics in Ground Effect
- Task 1.2 – High Fidelity Vorticity Generation and Preservation in Ground Effect
- Task 1.3 – Fuselage Configuration Effects on Rotorwash and Brownout

Task 1.1

Measurements of Rotor and Fuselage Aerodynamics in Ground Effect

Investigator(s): J. Gordon Leishman

Institution/Department: University of Maryland/Dept. of Aerospace Engineering

Graduate Student(s): Joseph Milluzzo **Contact email:** leishman@umd.edu

Background and Technical Challenges

The problem of brownout is caused by the action of the rotor wake on the ground below the rotor, which creates unsteady flows and turbulence that act to mobilize, uplift and entrain sediment particles. In particular, as the blade tip vortices trailed from the rotor interact with mobile particles lying over the ground, they cause locally high shear stress on the bed and liberate many particles up into the flow. The tip vortices also generate intense regions of upwash, which uplift the particles well away from the bed and into the main flow. While the tip vortices are the dominant features of the rotor wake, the wake is also comprised of wake sheets containing vorticity and turbulence that are trailed from the inboard sections of the blades. These sheets can introduce significant amounts of turbulence into the developing flow on the ground. Ultimately, a detailed understanding of both the trailed tip vortices and wake sheets from the rotor system is critical to understanding the flow at the ground and the development brownout conditions.

The specific goals of this research task are to: 1. Measure the effects of rotor and airframe design and rotor operational conditions on the blade tip vortex structures, including the turbulence and Reynolds stresses in the flow at a ground plane below the rotor; 2. Characterize and understand the detailed structure and evolution of the wake sheet and its contributions to the developing turbulent flow at the ground; 3. Examine the effects of airframe shapes on the flow below the rotor at the ground with a view to understanding how an airframe may participate in the onset of sediment mobility. The outcomes of this research have furthered the physical understanding of rotor and rotor/airframe configurations in ground effect operation and have provided key measurements needed for the validation of computational modeling being done in the MURI effort.

Technical Approach

A schematic of the setup used for the rotor experiments conduced in this task is shown in Fig. 1.1. Both one-bladed and two-bladed rotor systems have been used, with blades of radius 0.408 m (16 inches) and a mean chord of 44.5 mm (1.752 inches). An integrated thrust and torque balance

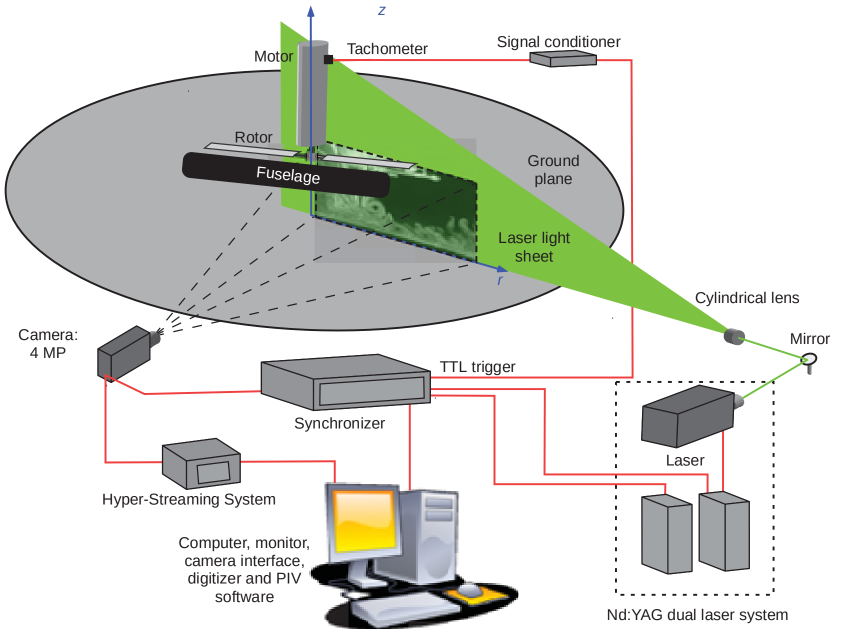

Figure 1.1: Schematic of the setup showing the rotor, body, and the ground plane.

is used to make rotor performance measurements. The rotor system has a variable collective pitch capability so that the measurements can be compared at the same (or equivalent) rotor operating conditions.

In the first phase of the work, the effects of blade tip shape on the flow was examined. In recent work, the effects of blade twist on the development of the rotor wake was studied. Two blade sets were tested: 1. A baseline untwisted blade, and 2. A twisted blade with -17° of linear twist from root to tip. Each rotor system was tested at two blade loading coefficients, C_T/σ, of 0.053 and 0.08, which were selected to represent helicopter rotor operations at low and high thrust conditions, respectively. Flow measurements have been made near the rotor and also near the ground plane.

To simulate ground effect conditions, a circular plane of diameter equal to two rotor diameters was placed parallel to the rotor plane, as also shown in Fig. 1.1. The rotor was located one radius above this ground plane. Flow diverters were placed around the periphery of the ground plane, which controlled the flow as it exited off the surface and helped to limit flow recirculation in the test cell. Honeycomb flow conditioning screens were located upstream to reduce turbulence levels into the rotor disk.

Three body shapes have also been tested in the wake below the rotor; see Fig. 1.2. These shapes are geometrically defined in terms of super-ellipsoidal functions. The bodies were mounted such that their vertical and longitudinal positions with respect to the rotor can be adjusted. A force

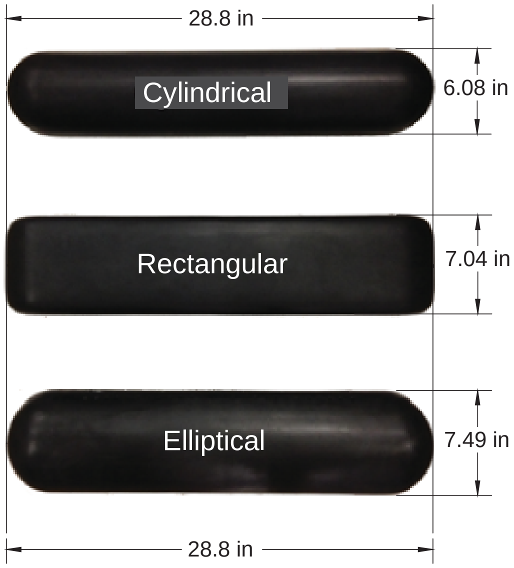

Figure 1.2: Side view of the three bodies used in the present experiments. All shapes defined in terms of super-ellipsoidal functions.

balance was used to measure the download on the bodies under the action of the rotor wake.

Various measurements have been conducted with the rotor and each body shape in turn, including flow visualization (FV) and particle image velocimetry (PIV), as well as performance (i.e., thrust, power, and body download) sweeps. The same combination of lasers and camera systems were used for the FV and PIV experiments. The laser was fired onto a high-intensity rated mirror and then into spherical and convex lenses, which produced a thin light sheet in the regions of interest (ROI). The camera was oriented so that the imaging axis was orthogonal to the laser sheet, and was focused to image the desired locations in the rotor wake and at the ground plane. The camera and laser was digitally synchronized such that the laser pulses straddled the camera images. For the FV and PIV measurements, the camera and laser were synchronized with a phase-locking encoder.

Results

Figure 1.3 shows the regions of interest (ROIs) where PIV was performed for the isolated rotor experiments with the rotor operating out of ground effect and in ground effect. Multiple interrogation regions were needed to provide the necessary spatial resolution. For the rotor operating out of ground effect (i.e., ROIs 1 and 2) and in ground effect (i.e., ROIs 1–6), the cameras were placed next to each other with a 60 mm overlap in their field of view, which allowed the temporally correlated images to be mosaiced together. Each camera had an initial ROI of 270-by-180 mm (0.66-by-0.44 *R*), yielding a total mosaiced field of view of 480-by-180 mm (1.18-by-0.44 *R*). For

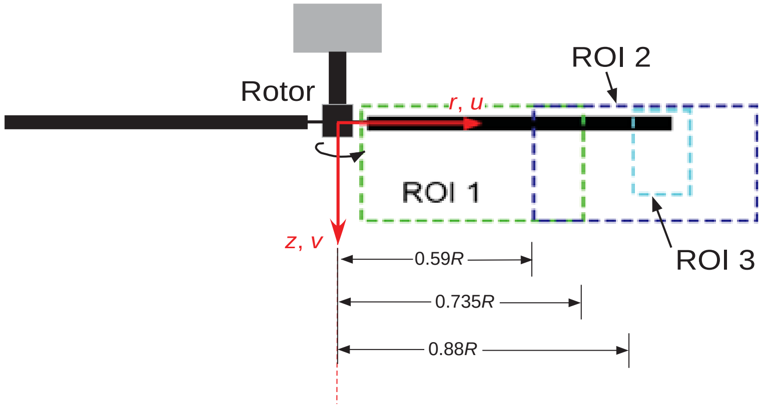

(a) Out of ground effect

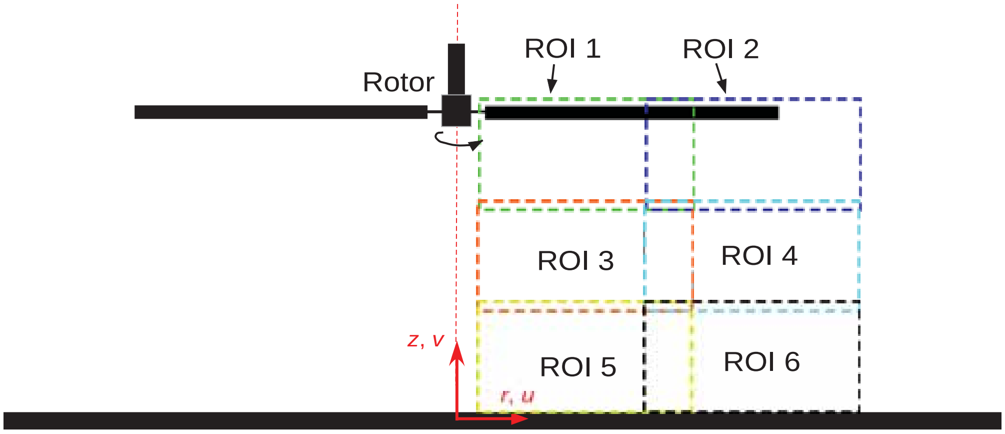

(b) In Ground Effect

Figure 1.3: Regions of interest (ROI) used for the flow measurements: (a) Out of ground effect; and (b) In ground effect.

the rotor operating out of ground effect a single camera was focused on a smaller region (i.e., ROI 3) at the blade tip (approximately 102-by-68 mm or 0.26-by-0.17 R), which provided high resolution images ($>$ 3,000 measurement points per unit radius) of the developing tip vortices and vortex sheets.

Figures 1.4 and 1.5 shows representative FV images that were taken with the reference blade at $\psi_b \approx 30^\circ$. The tip vortices produced by the untwisted blades rolled-up almost immediately behind the trailing edge of the blade tip, with the vortices effectively being fully-formed at wake ages as early as $\zeta = 3^\circ$. However, the vortices produced by the twisted blades were seen to take somewhat longer to roll-up, i.e., not until $\zeta \approx 15^\circ$–20° could they considered as fully developed.

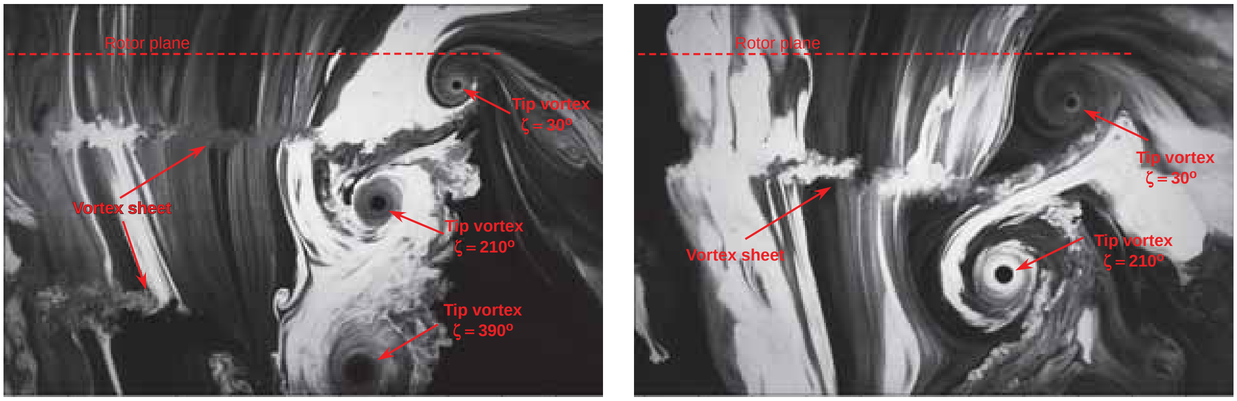

(a) Untwisted blade, $C_T/\sigma = 0.053$ (b) Untwisted blade, $C_T/\sigma = 0.080$

Figure 1.4: Flow visualization in the rotor wake near the tip of the untwisted blades for each of the operating thrusts at a blade angle of 30°: (a) $C_T/\sigma = 0.053$; (b) $C_T/\sigma = 0.080$.

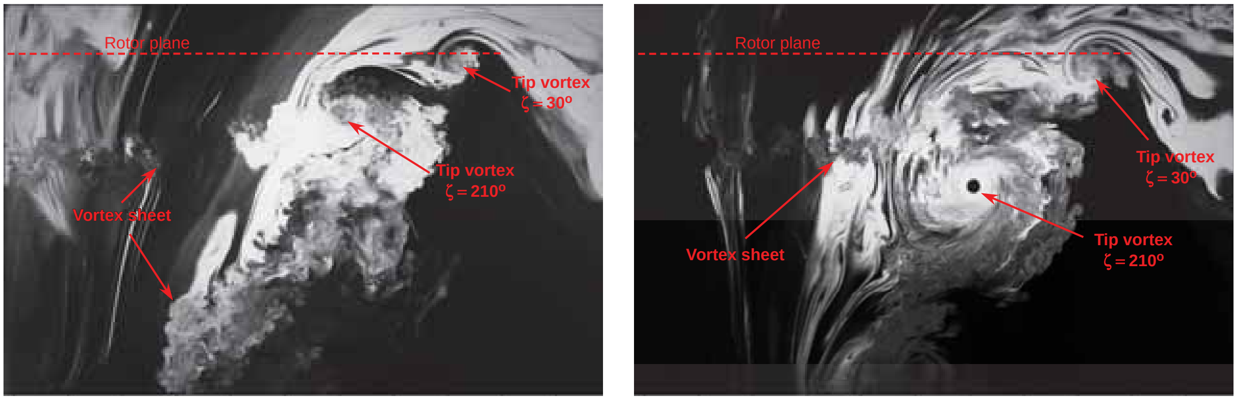

(a) Twisted blade, $C_T/\sigma = 0.053$ (b) Twisted blade, $C_T/\sigma = 0.080$

Figure 1.5: Flow visualization in the rotor wake near the tip of the twisted blades for each of the operating thrusts at a blade angle of 30°: (a) $C_T/\sigma = 0.053$; (b) $C_T/\sigma = 0.080$.

Such effects, at least partly, reflect the different loading distributions over the tip region of each blade. Furthermore, it is clear from Figs. 1.4 and 1.5 that the vortex sheets produced by the twisted blades were significantly thicker and more turbulent.

Figures 1.6 and 1.7 shows the measured locations of the tip vortices and the vortex sheets as a function of wake age for each rotor. A wave was seen to form on the sheet not long after it was initially trailed from the blade. This wave was more pronounced in the wake produced by the twisted blades, as shown in Figs. 7(a) and 7(b). Moving inboard, this wave can be seen to initially grow in magnitude. However, as the vortex sheet convected further axially in the wake it was stretched, which appeared to suppress any further growth in wave amplitude. Additionally, the sheet trailed from the rotor with untwisted blades was seen to take on two distinct slopes (i.e., negative inboard and positive outboard) as shown in Fig. 1.4; this effect occurred around $0.80R$

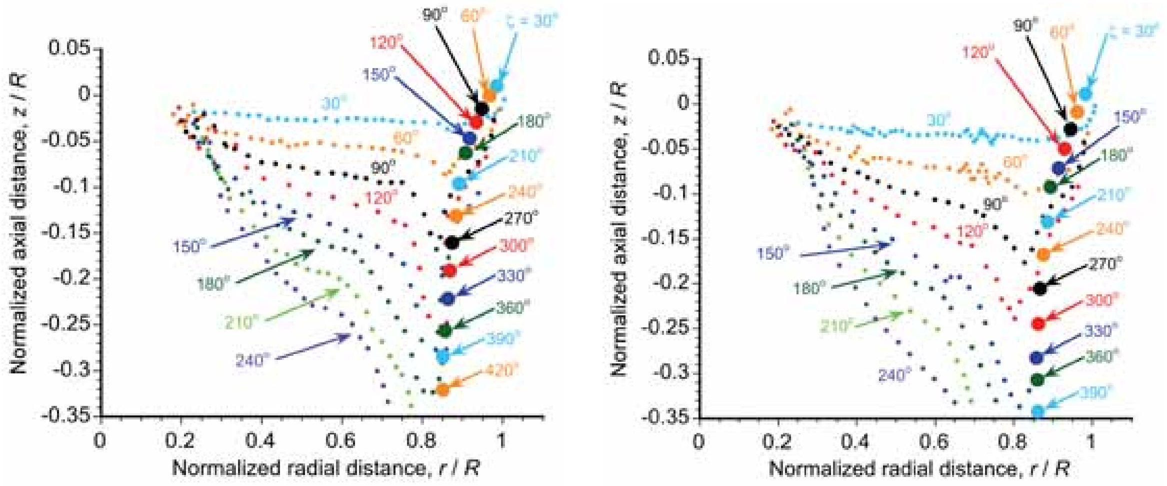

(a) Untwisted blade, $C_T/\sigma = 0.053$ (b) Untwisted blade, $C_T/\sigma = 0.080$

Figure 1.6: Axial and radial locations of the wake sheets and tip vortex locations along the wake boundary for the rotor with untwisted blades: (a) $C_T/\sigma = 0.053$**; (b)** $C_T/\sigma = 0.080$**.**

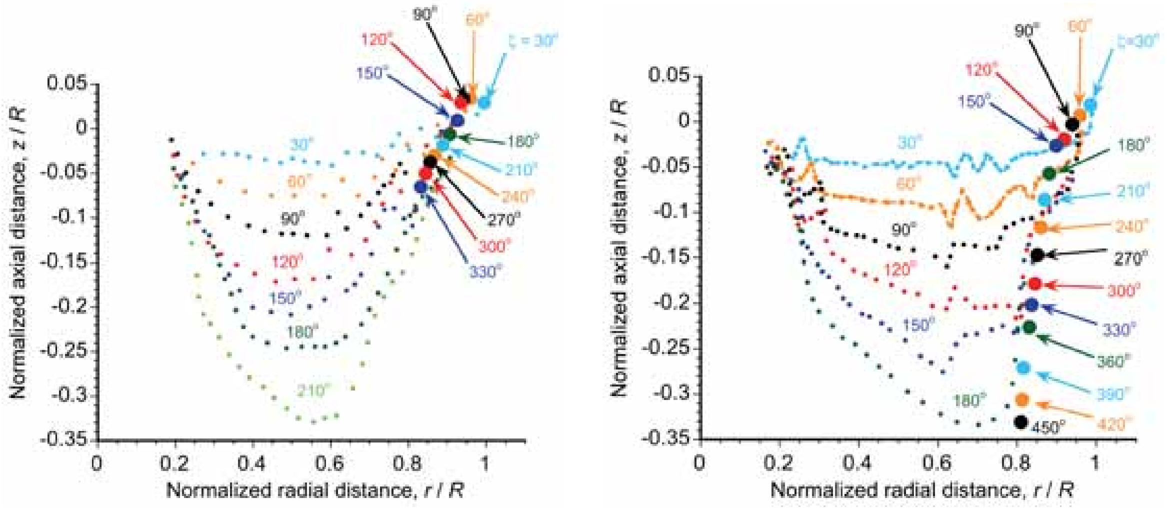

(a) Twisted blade, $C_T/\sigma = 0.053$ (b) Twisted blade, $C_T/\sigma = 0.080$

Figure 1.7: Axial and radial locations of the wake sheets and tip vortex locations along the wake boundary for the rotor with twisted blades: (a) $C_T/\sigma = 0.053$**; (b)** $C_T/\sigma = 0.080$**.**

at each of the two rotor thrust conditions; see Fig. 1.6. Notice that at low rotor thrust, the tip vortices produced by the twisted blades were convected axially more slowly than for the other cases. This slower convection caused the following blade to interact with the vortex. Such head-on interactions, which can be classified as form of perpendicular blade vortex interaction or BVI, caused the rapid diffusion of vorticity, allowing the vortex to persist in the flow for less than one rotor revolution.

The locations of the tip vortices and wake sheets as a function of wake age are shown in

Fig. 1.8 for the rotor with the untwisted blades when it was operating both out of ground effect and in ground effect. The results showed that the non-uniform convection of the wake sheets was qualitatively similar for both operating conditions, with the quickest axial convection occurring in the wake outboard of $r/R = 0.6$; see Fig. 1.8. However, the behavior of the wake sheets were significantly affected by the presence of the ground. After $\zeta = 120^\circ$, the wake sheets from the untwisted blades convected axially slower below the rotor when it was operating in ground effect. For example, Fig. 8(a) shows that at a wake age of $\zeta = 180^\circ$ only the inboard 75% of the wake sheet was above $z/R = -0.35$ for the rotor operating out of ground effect. However, when the rotor was operated in ground effect, the entire wake sheet remained above $z/R = -0.35$ until a wake age of $\zeta \geq 210^\circ$ was reached; see Fig. 8(b). In this case, the slower axial convection was because of the presence of the ground, which modified the spanwise downwash distribution in the wake below the rotor.

When the rotor was operated out of ground effect, a wave-like perturbation formed on the wake sheets shortly after they were trailed from the untwisted blade; see Fig. 1.6. However, as the sheet convected axially below the rotor it was stretched, which effectively suppressed any additional growth in the wave amplitude. From an examination of Fig. 8(b), it can be see that when the rotor was operated in ground effect, no wave-like perturbation was observed to form on the sheet. In this case, the radial stretching of the wake because of the presence of the ground appeared to be the source of the change in the behavior of the wake sheet.

Figure 1.9 shows the locations of the tip vortices and wake sheets as a function of wake age for the rotor with twisted blades when it was operating both out of ground effect and in ground effect, respectively. Similar to that of the rotor the with untwisted blades, the wake sheets trailed from the rotor with twisted blades convected axially slower than the corresponding out of ground effect case. Furthermore, the presence of the ground also resulted in the suppression of the wave-like perturbation on the wake sheets trailed from the rotor with the twisted blades, as shown in Fig. 9(b).

Imaging of the tip region allowed the developing wake sheet to be examined in detail. Specifically, the near-tip region contained over 70,000 PIV measurement points, corresponding to over 3,000 measurement points per unit radius. Figure 1.10 shows an example of three instantaneous contours of vorticity (with the corresponding velocity vectors being superimposed) at the higher thrust condition and a wake age of 6° (i.e., $\zeta = 6^\circ$). These figures show that the wake sheets were comprised of concentrated regions of counterrotating vorticity (often called Taylor–Görtler vortices) that generated significant fluctuations in the total velocity in the wake. However, the twisted

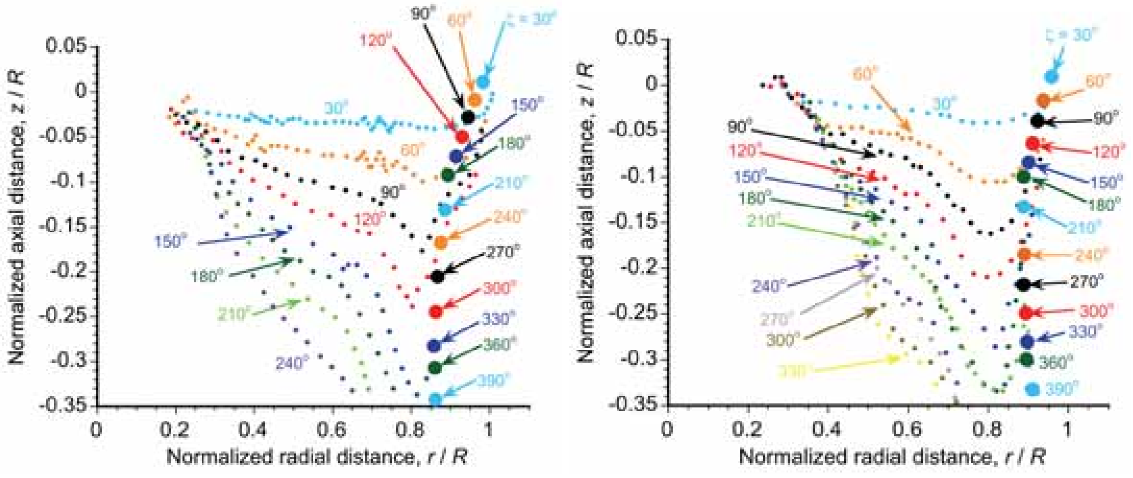

(a) Out of ground effect, $(z/R = \infty)$ (b) In ground effect, $z/R = 1.0$

Figure 1.8: Plot of the axial and radial locations (using a rotor based reference frame) of the wake sheets and tip vortices in ROIs 1 and 2 using a rotor based reference frame for the rotor with untwisted blades operated: (a) Out of ground effect ($z/R = \infty$); (b) In ground effect (z/R = 1.0).

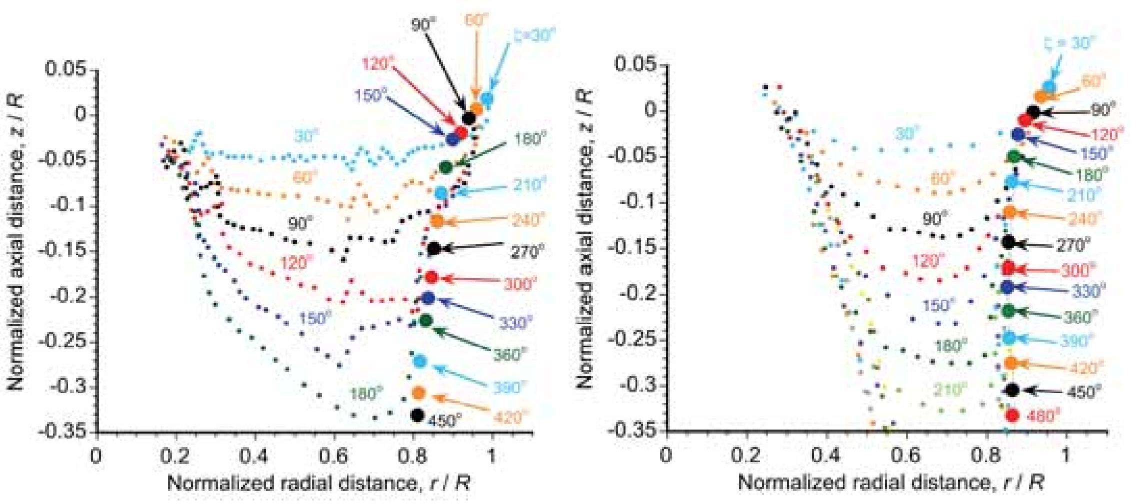

(a) Out of ground effect, $(z/R = \infty)$ (b) In ground effect, $z/R = 1.0$

Figure 1.9: Plot of the axial and radial locations (for a rotor based reference frame) of the wake sheets and tip vortices in ROIs 1 and 2 for the rotor with the twisted blades operated: (a) Out of ground effect ($z/R = \infty$); (b) In ground effect (z/R = 1.0).

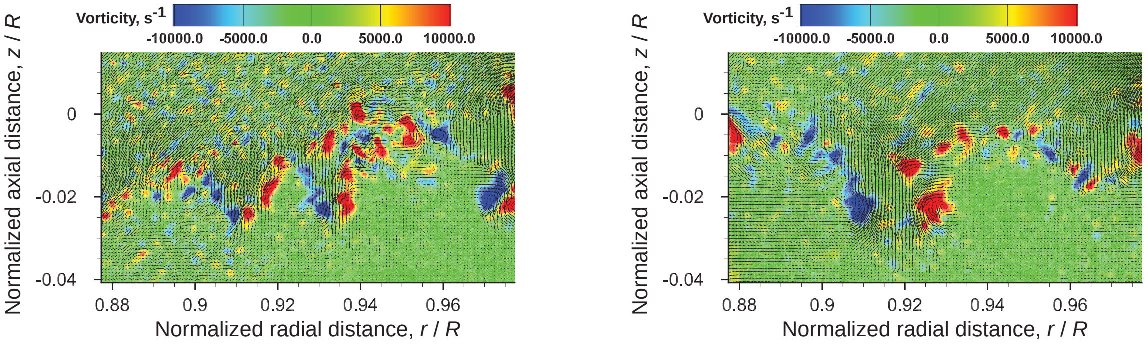

(a) Instantaneous realization one

(b) Instantaneous realization two

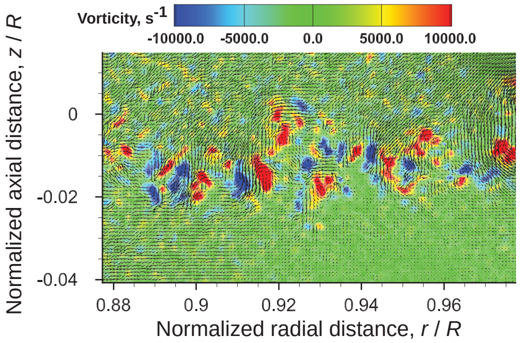

(c) Instantaneous realization three

Figure 1.10: Contours of instantaneous vorticity at $\zeta = 6^\circ$ for the rotor with twisted blades operating at the higher thrust condition.

blades produced a more intense wake sheet that contained greater vorticity, which also leads to more turbulence in the sheet. The turbulence contributions from the wake sheets are of particular interest because Task 2.7 has shown that particle mobilization and uplift can be correlated to the Reynolds stresses and discrete turbulence events at the ground. While the wake sheets appear to contribute significant turbulence into the developing rotor wake, it was very difficult to actually quantify the turbulence because of the highly aperiodic nature of the wake sheet. These instantaneous vorticity realizations show the inherently aperiodic nature of the wake sheet, with each image showing slightly different amounts and distributions of vorticity. Because the size, shape, and structure of the wake sheet varied between phase-resolved realizations at the same wake age, a turbulence analysis cannot be performed without collocating the sheet structures, otherwise the calculated turbulence values would be biased by the effects of aperiodicity.

While an examination of the flow field generated near the rotor provided significant insight into the development and initial formation of the flow features, the problem of is driven by the near-wall flow field. Specifically, the problem of brownout is linked to the structure of the near-wall vorticity.

Figures 1.11 and 1.12 show representative instantaneous realizations of the vorticity in ROIs 5 and 6 for both blade sets at a reference blade azimuth angle of $\psi_b = 30^\circ$. A considerable amount of small scale vorticity in the wakes was observed inboard near the rotor (i.e., for $r/R \leq 0.6$), and it would be expected that the small scale vorticity seen in Figs. 1.11 and 1.12 was conveyed there by the sheets. Furthermore, because the twisted blade initially trailed a more intense wake sheet, the vorticity in the near-wall flow would be expected to have higher magnitudes as compared to the corresponding untwisted blade, as shown in Figs. 1.11 and 1.12.

As discussed further in Task 2.1, the formation of a brownout cloud results from the interaction of the tip vortices with the saltation layer along the ground. Specifically, the mobilized sediment along the ground becomes "trapped" in the higher velocities induced by the vortices and is suspended around the rotor. Therefore, the question becomes, how does the vorticity in the near-wall flow affect the wall-normal velocities?

To help answer this question, contours of the wall-normal velocity in ROIs 5 and 6 are shown in Figs. 1.13 and 1.14 for the untwisted and twisted blades, respectively. The tip vortices are identified in Figs. 1.13 and 1.14 by the red (upwash) and blue (downwash) pairs. While the tip vortices induced strong upwash velocities and, therefore, would have the potential to uplift large amounts of previously mobilized sediment particles, the smaller scale vorticity (shown in Figs. 1.11 and 1.12) also induced significant upwash velocities, and closer to the rotor; see Figs. 1.13 and 1.14. It would be expected that the fluctuating velocities associated with the wake sheets could uplift sediment particles, and so will be a contributing mechanism to the problem of brownout. Without the flow fluctuations induced by the wake sheet, it is likely that the saltation layer would develop further downstream and, therefore, the initial uplift of particles would be further away from the rotor.

A body representing an airframe was introduced into the rotor wake flow to determine its effect on the developing flow over the ground plane. Scaled down bodies have also been tested in the dual-phase environment in the dust chamber; see Task 2.2. The circular and elliptical body shapes were found to produce similar flows near the ground. These bodies also showed near-wall velocity and turbulence profiles similar to those obtained with the isolated rotor, although some differences did appear at the most inboard radial locations nearer to the rotor; in particular, the rectangular body produced different Reynolds stresses at locations inboard of $1.3R$. These differences were particularly significant at about one rotor radius where the wall-jet had not yet fully developed. The results showed that at downstream distances greater than about $r/R = 1.6$ there were minimal differences in the flows at the ground as influenced by any of the bodies.

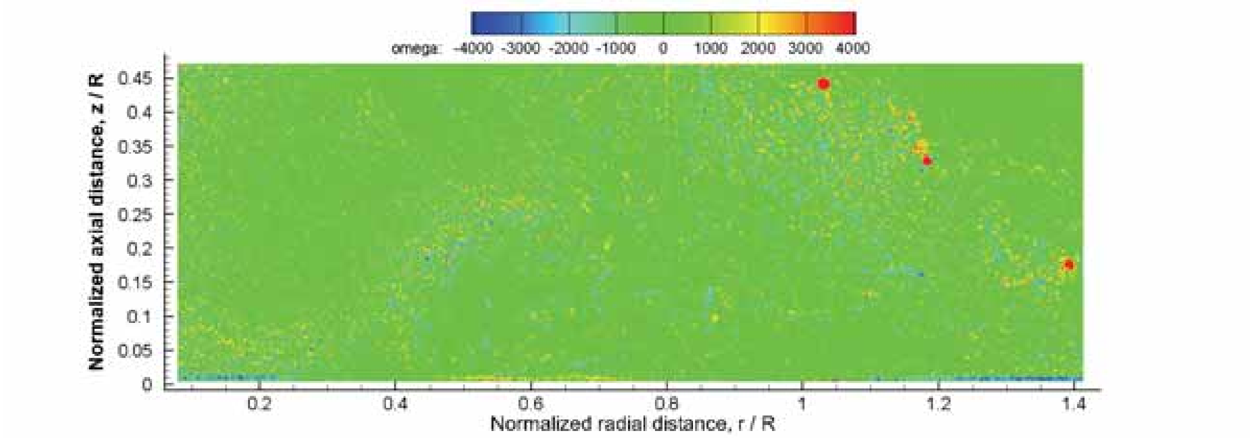

Figure 1.11: Instantaneous realization of the flow field in ROIs 5 and 6 for the rotor with the untwisted blades at a blade azimuth angle ψ_b = 30°. Background contours are of vorticity.

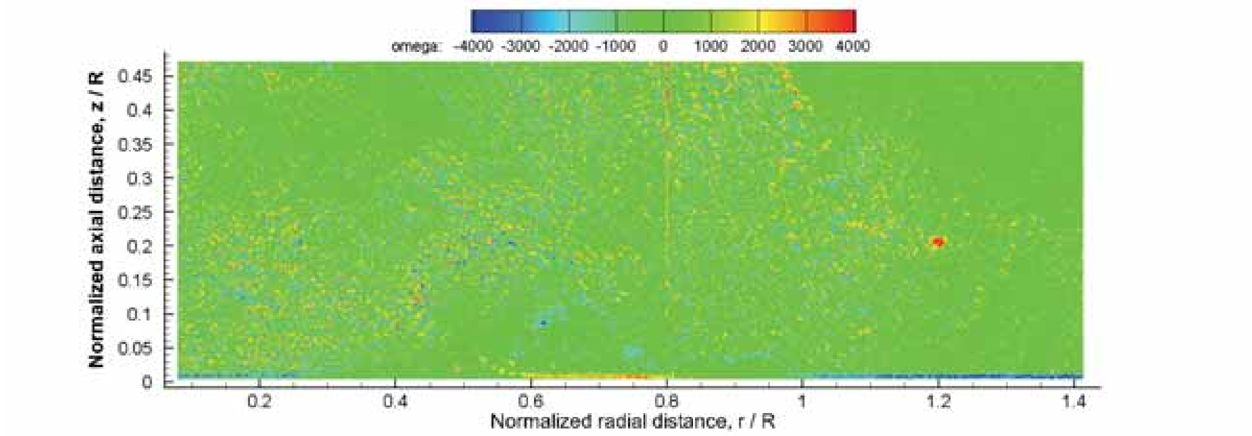

Figure 1.12: Instantaneous realization of the flow field in ROIs 5 and 6 for the rotor with the twisted blades at a blade azimuth angle ψ_b = 30°. Background contours are of vorticity.

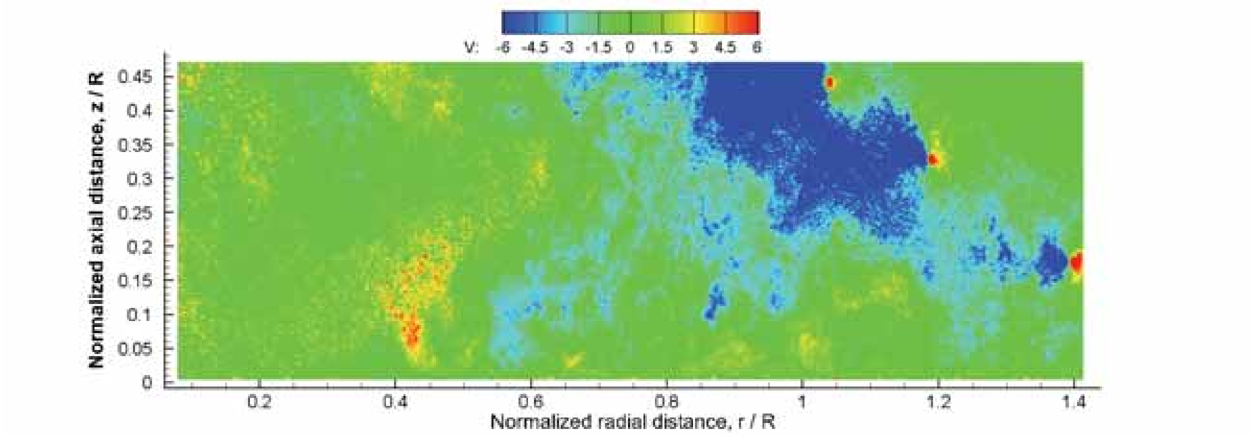

Figure 1.13: Instantaneous realization of the flow field in ROIs 5 and 6 for the rotor with the untwisted blades at a blade azimuth angle ψ_b = 30°. Background contours are of the wall-normal velocity.

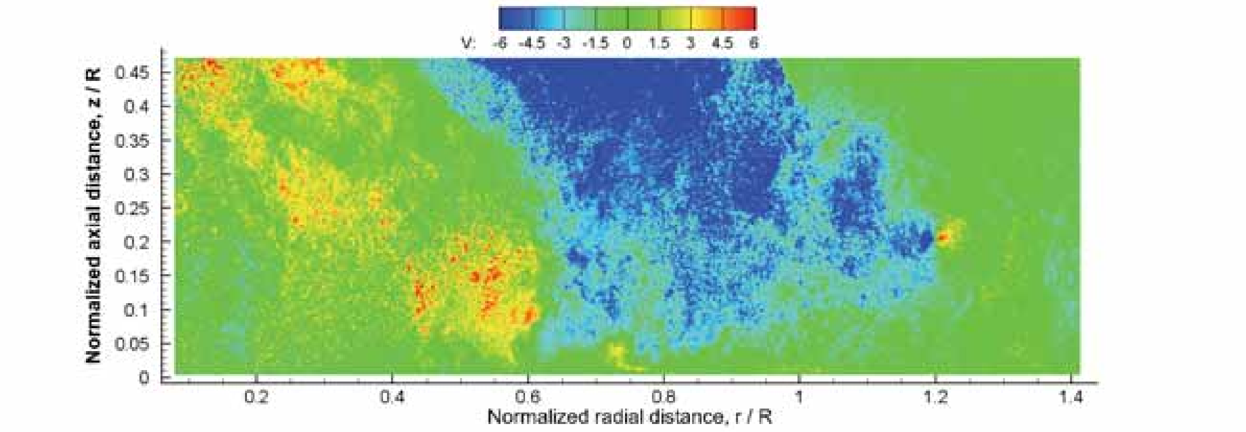

Figure 1.14: Instantaneous realization of the flow field in ROIs 5 and 6 for the rotor with the twisted blades at a blade azimuth angle ψ_b 30°. Background contours are of the wall-normal velocity.

Publications

1. Milluzzo, J., Sydney, A., Rauleder, J., and Leishman, J. G., “Ground Effect Aerodynamics of Rotors with Different Blade Tips,” 66th Annual Forum Proceedings of the American Helicopter Society, Phoenix, AZ, May 2010.

2. Milluzzo, J., and Leishman, J. G.,“Assessment of Rotorcraft Brownout Severity in Terms of Rotor Design Parameters,” *Journal of the American Helicopter Society*, July 2010.

3. Milluzzo, J., “Effects of Blade Tip Shape on Rotor In-Ground-Effect Aerodynamics,” M.S. Thesis, Aerospace Engineering Department, University of Maryland, 2011.

4. Hance, B., “The Effect of a Body on Rotor In-Ground-Effect Aerodynamics,” M.S. Thesis, Aerospace Engineering Department, University of Maryland, 2012.

5. Milluzzo, J., and Leishman, J. G., “Development of the Turbulent Vortex Sheet in the Wake of a Hovering Rotor” 69th Annual Forum Proceedings of the American Helicopter Society, Phoenix, AZ, May 2013.

6. Milluzzo, J., and Leishman, J. G.,. “Quantification of the Evolution of the Vortical Sheets in the Wake of a Hovering Rotor,” Proceedings of 32nd AIAA Applied Aerodynamics Conference, Atlanta, GA, June 16–20, 2014.

Task 1.2

High Fidelity Vorticity Generation and Preservation in Ground Effect

Investigator(s): James Baeder

Institution/Department: University of Maryland/Dept. of Aerospace Engineering

Graduate Student(s): Tarandeep Kalra

Contact email: baeder@umd.edu

Background and Technical Challenges

The action of the rotor wake on loose sediment on the ground is primarily responsible for inducing the rotorcraft brownout phenomenon. Therefore, any simulation of brownout must be capable of accurately predicting the velocity field induced by the rotor when it is operating in ground effect. This goal requires the computational methodology to be able to capture the generation of vorticity on the blade surfaces, including the tip vortex and the formation of the wake sheets, as well as the subsequent evolution and rollup into the tip vortices, and the convection and interaction of of this vorticity into the developing wall jet and boundary layer on the ground. However, the accurate prediction of the wake vorticity from the rotor plane to the ground plane with the use of high-fidelity CFD methodologies is computationally expensive, mainly because of the fine grid sizes that are needed to prevent the non-physical numerical dissipation of the vorticity at older wake ages. The increase in the physical scale of the rotor system (i.e., from laboratory or model-scale to full-scale) further increases the computational challenges because of the larger sizes of the grids that are needed to solve for the flow properties, and also the computational time needed in this case can become increasingly prohibitive.

Technical Approach

Experimental studies conducted in this MURI (see Tasks 1.1 and 2.2) have performed detailed measurements of the flow near and below sub-scale rotors operating over a ground plane. These measurements have provided valuable data to help validate the CFD models. After validation, the CFD models can then be used to provide results that can expose the relative sensitivities of various rotor (e.g., the blade tip shape) and particle parameters (e.g., the particle diameter, mass, etc.) to the severity of the brownout phenomenon. Such CFD models can also simulate combinations of rotor and particle parameters that may not easily be studied experimentally in the laboratory.

In this task, the overset version of Transonic Unsteady Rotor Navier–Stokes (UMTURNS)

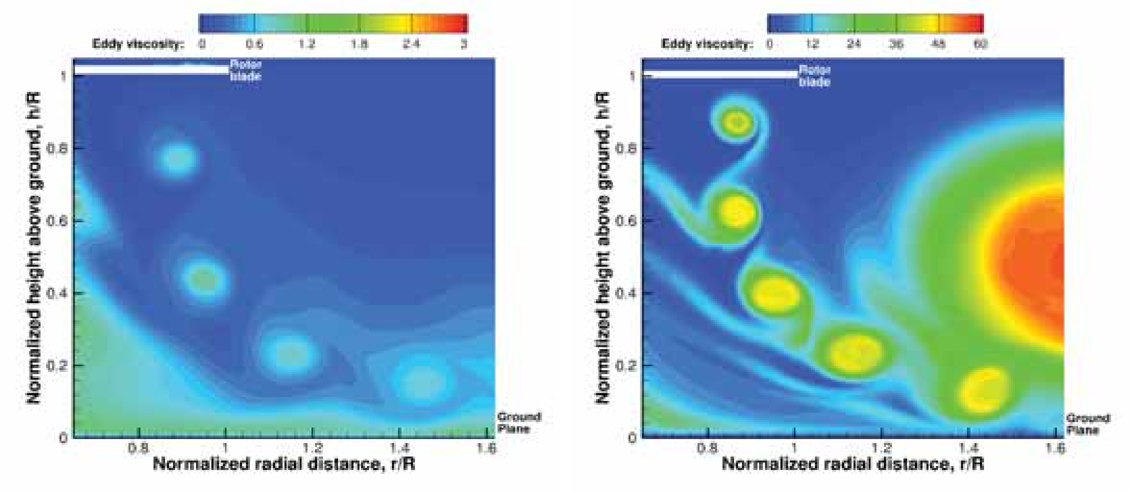

(a) Micro-rotor

(b) Sub-scale rotor

Figure 1.15: Comparison of CFD (S–A model) predicted eddy viscosity contours at an azimuthal plane of 0°. (Notice the different contour levels).

is being used to help computationally analyze the rotorcraft brownout problem. A prerequisite, however, is to predict the flow without the particles. In this solver, the inviscid terms are discretized using a third order MUSCL scheme with Roe's flux differencing. In the simulations, a fifth-order WENO scheme is used on the vortex tracking meshes to study the advantages of using a higher-order scheme to preserve the vortices to older wake ages where they would interact with the ground. The viscous terms are computed using second-order central differencing. The Spalart–Allmaras turbulence model is used in all cases for RANS closure. Time integration is performed using a second-order implicit backward-difference method scheme with dual time-stepping. The Lower-Upper Symmetric Gauss–Siedel (LUSGS) method is used for the inversion for the sub-scale rotor cases, while the micro-scale rotor cases use the diagonalized approximate factorization framework.

Results

The original methodology developed in the current task has shown good agreement with flow measurements made for a small-scale rotor (referred to as "micro-scale") hovering close to the ground. A similar application of RANS methodology using S–A turbulence model with rotational correction that was used in small-scale rotor results in excessive smearing of the flow field when applied to the sub-scale rotor. The excessive smearing for the sub-scale rotor flow field occurs because of high turbulence levels, and this observation can be made by comparing the eddy viscosity values for the small-scale and sub-scale rotor in Figs. 1.15(a) and (b) respectively. The S–A turbulence model seems to preserve the tip vortices well for the small-scale rotor because the predicted tur-

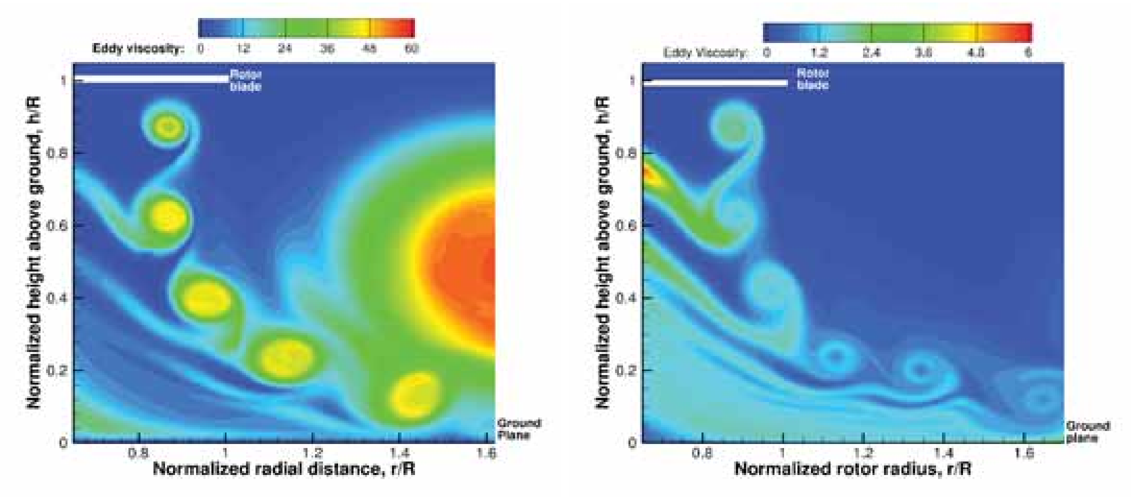

(a) S–A simulation

(b) SA-DDES simulation

Figure 1.16: Comparison of CFD predicted eddy viscosity contours at an azimuthal plane of 0° for the sub-scale rotor. (Notice the different contour levels).

bulence levels were quite low, especially in the regions of tip vortex. However, turbulence levels were observed to be an order of magnitude higher in the sub-scale rotor flow field.

An improvement over the S–A turbulence modeling is made by utilizing a hybrid RANS and LES methodology and one such approach is known as Delayed Detached Eddy Simulation (DDES). In this hybrid approach using DDES, one can model the small scale eddies in the boundary layer/near wall regions and can resolve the larger eddies in the regions of massive flow separation. DDES is implemented by modifying the distance function in S–A model that is chosen from the minimum of nearest wall distance or grid spacing for each grid point. The grid spacing is chosen from the maximum of grid spacing in all three directions and this formulation was originally designed for isotropic grids. However, the grids used in sub-scale rotor simulation involve large amount of difference in the grid spacing in the three directions and are highly anisotropic. Therefore, the grid spacing is based on a function that is dependent on the aspect ratio of grids. This hybrid methodology is referred to as SA-DDES in the following results. The resulting turbulence levels with SA-DDES are shown in Fig. 1.16(a) and are compared with the S–A model predicted levels in Fig. 1.16(b). Notice that the eddy viscosity levels have dropped by an order of magnitude in the SA-DDES simulations compared to S–A simulations.

Figure 1.17 shows a comparison of the CFD (SA-DDES) computed vorticity magnitude values in the near wake region for different tip shapes used in the sub-scale experiments. It can be seen that the tip vortices trailing from the rectangular and swept tips look similar whereas the BERP-

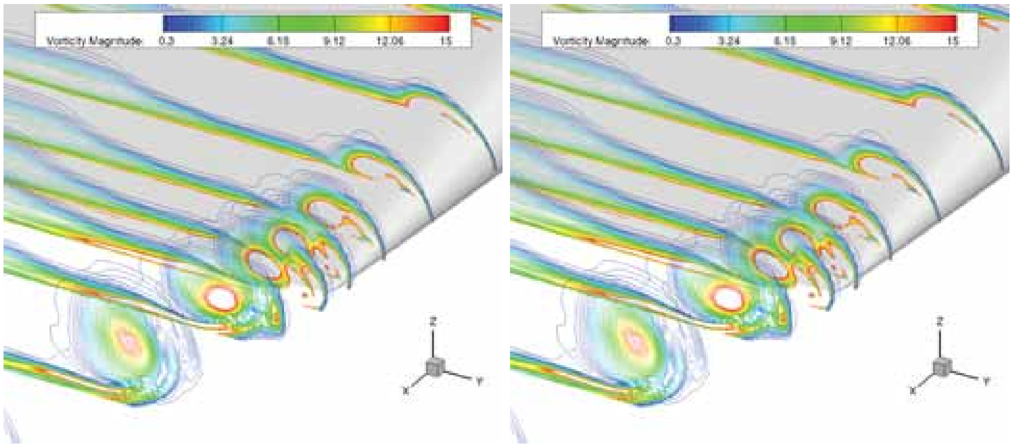

(a) Rectangular (b) Swept

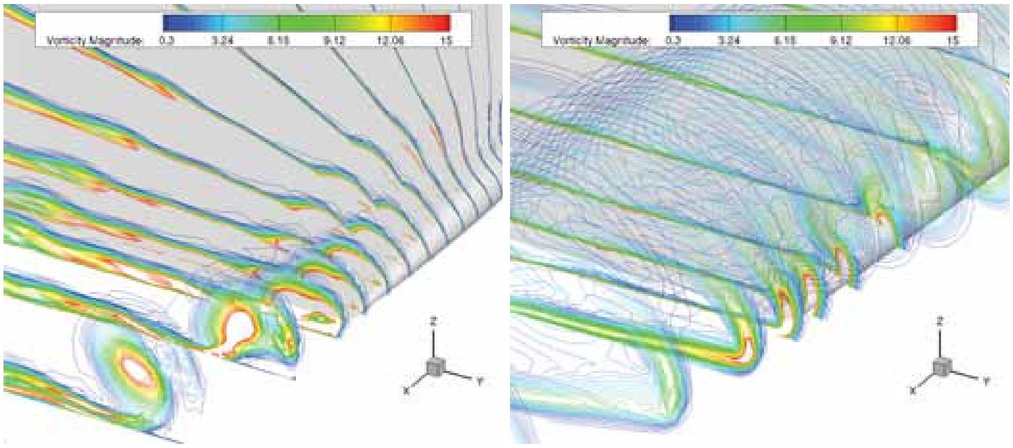

(c) BERP-like (d) Slotted

Figure 1.17: CFD (SA-DDES) predicted tip vortex formation from different blade tip shapes.

like tip has a lower vortex strength. The slotted tip produces a highly diffused vortex core, which occurs because of the turbulence produced by the internal slots at the tips of the blade and the subsequent turbulent mixing produced in the otherwise laminar tip vortex.

Figures 1.18(a) and (b) compares the core radius growth with wake age for the four tip shapes as measured in the experiments and as computed by CFD. The core radius was non-dimensionalized by the rotor blade chord. It can be seen that the core radius growth agrees well for all blade tip shapes. The initial core radius for the BERP-like tip seems to be higher in the experiments than the computations but starts to compare well with experiments beyond 750°. The growth of core radius for the slotted tip is seen to be experimentally measured only up until a wake age of 200°, however CFD can still track the core radius for the entire range of wake age and the core radius is seen to double at 800° from its value obtained at 200°.

Peak swirl velocity were compared between the experimental measurements and CFD com-

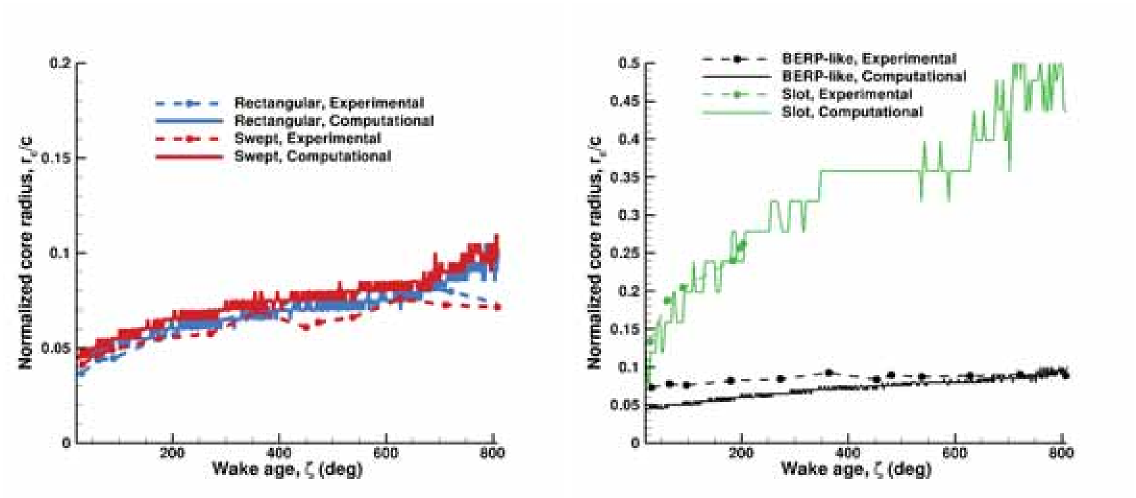

(a) Normalized core radius comparison (b) Normalized core radius comparison

Figure 1.18: Comparison of CFD (SA-DDES) predicted core radius growth as a function of wake age for different tip shapes.

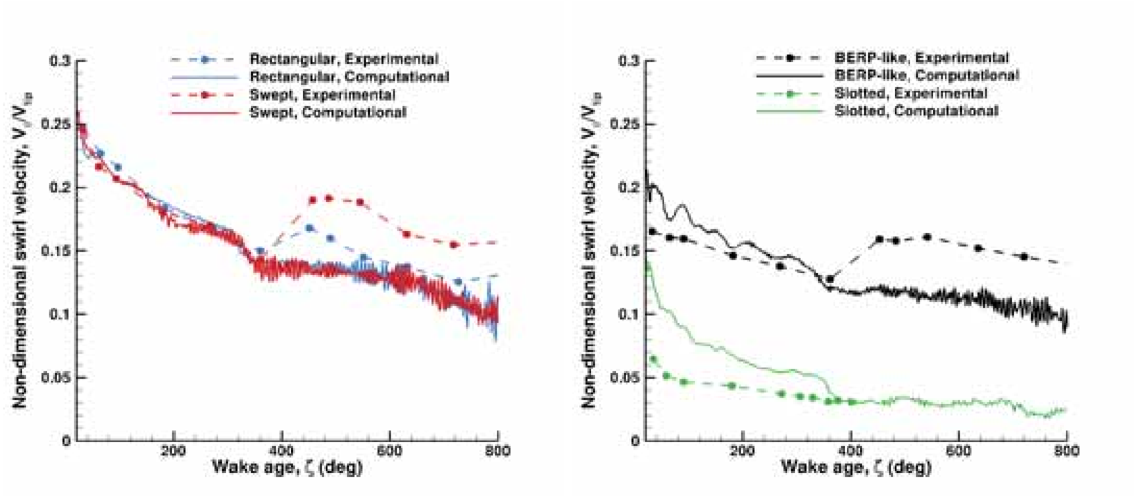

(a) Non-dimensional peak swirl velocity (b) Non-dimensional peak swirl velocity

Figure 1.19: Comparison of CFD (SA-DDES) predicted peak swirl velocity as a function of wake age for different tip shapes.

putations at various wake ages, as shown in Figs. 1.19(a) and (b). Both the experiments and computations showed a good comparison of peak swirl velocity until 360° of wake age. Beyond that, the effect of ground leads to a slight increase in peak swirl velocity in experiments whereas it continues to drop in the computations. The peak swirl velocity variation was noticed to be similar for the rectangular and swept tip shapes. The BERP-like tip shows a higher peak swirl velocity at early wake ages in computations but compares well at older wake ages with the experiments. The slotted tip case shows higher peak swirl velocity in computations but eventually decays and compares well with the experiments after 400° wake age.

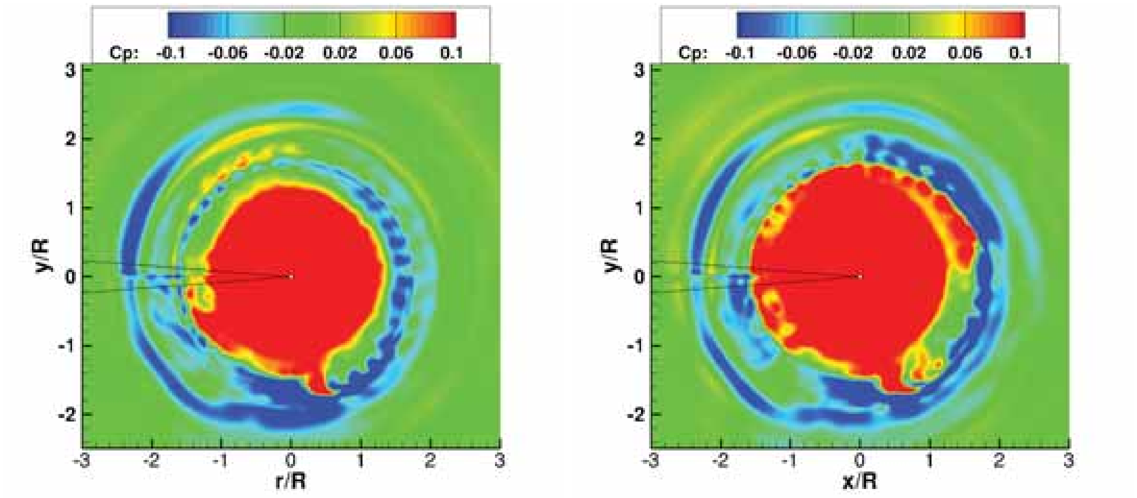

(a) Rectangular (b) Swept

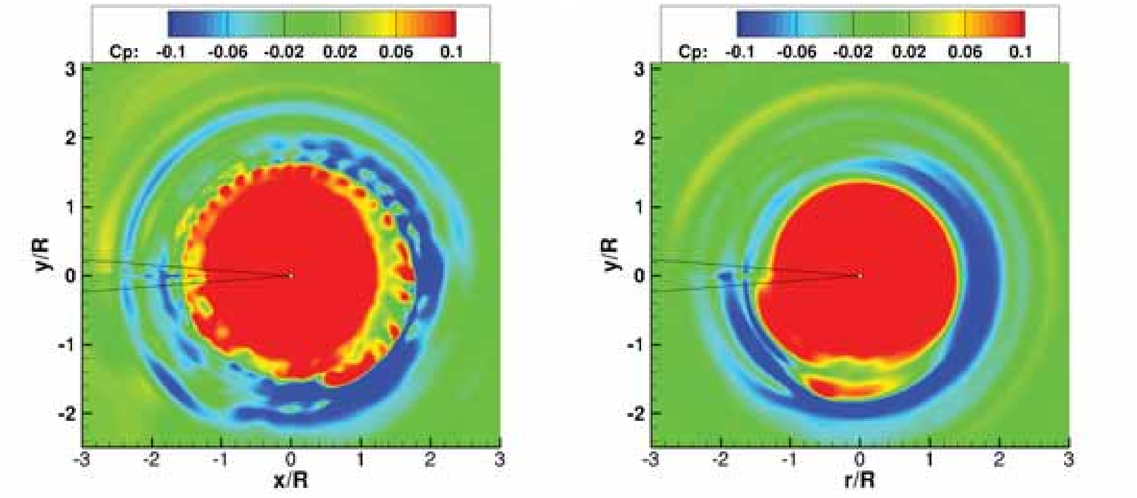

(c) BERP-like (d) Slotted

Figure 1.20: CFD (SA-DDES) predicted pressure coefficient by the 1-bladed sub-scale rotor blade for different tip shapes.

The unsteady pressure variations at the ground plane can be a contributing factor for sediment mobilization during brownout. Figures 1.20(a) and (b) show pressure coefficient at the ground plane for the all tip shapes. The flow field is extracted in computations from an instantaneous solution. The circular region extending to $x/R = 1.0$ of red contour values shows the high pressure in the inboard regions. Beyond that, one can observe lower pressure (blue contour levels) because of the presence of tip vortex that tends to induce a lower pressure region as the tip vortex passes over the ground plane. Notice the striations/fluctuations in the pressure values for the rectangular, swept and BERP-like tip shapes which are not present in the slotted tip.

Papers Published

1. Kalra, T., Laksminarayan, V., and Baeder, J. D., "Effect of Tip Geometry on a Hovering Rotor in Ground Effect: A Computational Study," 31st AIAA Applied Aerodynamics Conference, San Diego, CA, June 24–27, 2013.

2. Thomas, S., Kalra, T., and Baeder, J. D., "A Hybrid CFD Methodology to Model the Two-phase Flowfield beneath a Hovering Laboratory Scale Rotor," 30th AIAA Applied Aerodynamics Conference, New Orleans, LA June 25–28, 2012.

3. Lakshminarayan, V. K., Kalra, T. S., and Baeder, J. D., "Detailed Computational Investigation of a Hovering Micro-Scale Rotor in Ground Effect," *AIAA Journal* Vol. 51, (4), April 2013, pp. 893–909.

4. Kalra, T., Laksminarayan, V., Baeder, J. D., and Thomas, S., "Methodological Improvements for Computational Study of a Hovering Micro-Rotor in Ground Effect," 20th AIAA Computational Fluid Dynamics Conference, Honolulu, HI, June 27–30, 2011.

5. Thomas, S., Laksminarayan, V., Kalra, T., and Baeder, J. D., "Eulerian-Lagrangian Analysis of Cloud Evolution Using CFD Coupled with a Sediment Tracking Algorithm," American Helicopter Society 67th Annual Forum Proceedings, Virginia Beach, VA, May 3–5, 2011.

6. Kalra, T., Laksminarayan, V., and Baeder, "CFD Validation of a Micro Hovering Rotor in Ground Effect," American Helicopter Society 66th Annual Forum Proceedings, Phoenix, AZ, May 11–13, 2010.

Task 1.3

Fuselage Configuration Effects on Rotorwash and Brownout

Investigator(s): Ganesh Rajagopolan (until 06/30/11)

Investigator(s): J. Gordon Leishman, James Baeder (07/01/11 to date)

Institution/Department: University of Maryland, Department of Aerospace Engineering

Graduate Student(s): Bharath Govindarajan

Contact email(s): leishman@umd.edu, baeder@umd.edu

Background and Technical Challenges

Brownout is degraded visual environment (DVE) problem that is caused by clouds of dust particles being uplifted by a rotorcraft during landings and takeoffs in desert-like environments. While the motion of the dust particles is primarily caused by the effects of the rotor wake vortices and downwash field produced by the rotor, the effects of the airframe shape may further distort the development of the wake, thereby affecting the development of the flow at the ground and severity of brownout conditions. Furthermore, the presence of the tail rotor, which also produces a strong vortical wake system, can interact with both the airframe flow and with the main rotor wake, thereby potentially affecting the development of brownout conditions. Although mostly based on anecdotal evidence thus far, there has been reason to suspect that the shape of the fuselage and/or the type and positioning of the tail rotor has at least some measurable influence on the development brownout conditions, and that there could be a preferred design that could help to minimize brownout severity, e.g., to allow the pilot to better see the ground through the dust cloud.

Technical Approach

The objective of this research task was to model the role of the airframe parts besides the main rotor as they may contribute to the distortion the flow around a rotorcraft operating in ground effect, and to better understand the role of the fuselage, empennage, tail rotor, etc., in the development brownout and DVE conditions. A parallel experimental study of rotor/airframe/ground effect interactions is being conducted under Tasks 1.1 and 2.2. The specific objectives of this task are to: 1. Develop a set of computationally efficient modeling tools to study the aerodynamic interaction of the main rotor system when combined with different airframe/fuselage configurations. Consideration is being given to modeling the flow produced by tail rotor, as well as multiple rotor aircraft such as tandems and coaxials; 2. To develop modeling tools to predict and study particle transport around complete rotorcraft configurations that are operating in maneuvering flight near the ground, with a view to understanding the influence of the airframe and tail rotor on the development of brownout conditions.

An initial study into the effects of fuselage shape on the groundwash signature below a rotor was performed by Iowa State University (ISU). However, the ISU approach offered limited fidelity because it could not represent the vortical features of the rotor wake that are now known to be critically important in the mobilization and uplift of dust particles (e.g., see outcomes from Tasks 1.1 and Task 3.2). In the ISU approach, the inflow to the rotor disk was modeled using momentum source terms but this formulation does not represent the vortices produced by the rotor blades and so the flow near the ground is not representative of the real physics that drives the brownout problem. A better approach, which is based on a Lagrangian free-vortex rotor wake and surface singularity (panel) formulation of the airframe, has now been developed. This latter approach is more aligned with the physics of predicting wake rotor flows in ground effect and the onset of brownout conditions, but is also computationally more attractive than the CFD approach (Task 1.2). This approach can also be easily interfaced with other parallel research initiatives of this MURI, such as the ABATE framework described under Task 3.4, as well as the various other mitigation studies such as those being used in Task 3.3. A Lagrangian free-vortex methodology was also employed to model the tail rotor wake, and was subsequently coupled with the main rotor and surface singularity formulation for the body. This foregoing approach has provided a comprehensive model to study the particle transport physics around complete rotorcraft configurations, and has been used to make assessments of the severity of the brownout cloud as well as to investigate possible means of brownout mitigation.

A schematic of the basic methodology is shown in Fig. 1.21. The ground plane is modeled using an image system to ensure that flow tangency is satisfied at all points over the ground plane. The Lagrangian free-vortex wake methodology (also used in Task 3.2) is coupled with a surface singularity methodology made up of a series of quadrilateral and/or triangular panels; flow-tangency is enforced at the control points of these panels. The unsteady pressure on the surface of the panel (i.e., at the control point) is obtained through the use of the unsteady Bernoulli's equation (Kelvin's equation), where the unsteady terms represent the effects associated with changes in panel singularity strength, the moving vortices in the near wake, and the rolled-up tip vortices in far wake of the rotor. In some case, especially when vortices come near the panels, the unsteady terms can dominate the surface loading. The present approach provides a computationally attractive prediction of the vortical rotor wake, the wake distortions by the airframe, and the resulting unsteady

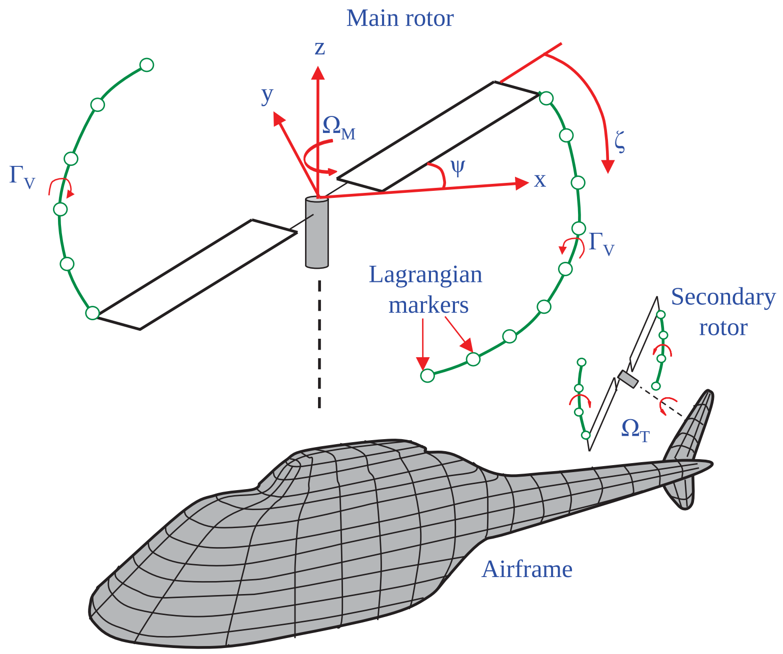

Figure 1.21: Schematic illustrating the modeling approach of the free-vortex method and coupled rotor-fuselage system in ground effect operation.

three-dimensional flow as it develops near the ground.

The modeling of the tail rotor wake has also been performed using the free-vortex method. The time-step of the procedure, Δt, is given by $\Delta t = \Delta\Psi/\Omega$, where $\Delta\Psi$ is the rotor azimuthal discretization and Ω is the rotational frequency of the rotor. Because the main and tail rotor rotate at different rotational speeds, the coupling of information (i.e., vortex positions and strengths) between the two rotors can be potentially realized in two ways: 1. The azimuthal discretization of the two rotors is set so that Δt is the same for both rotors, which is called tight coupling because information is passed between the two rotors at each and every time step; 2. The azimuthal discretizations are set to be equal, and the rotor with the lower Δt marches additional time-steps such that both rotors are now at the same physical time in the solution, which is called loose coupling because information between the rotors are passed at predetermined intervals. A schematic of this latter approach is shown in Fig. 1.22. The loose coupling methodology was adopted in the present work because it was found to be computationally faster and required less memory, but while giving equivalent accuracy compared to the tight coupling approach.

The rotor airframe model, including the tail rotor, has been used to predict flow velocities on

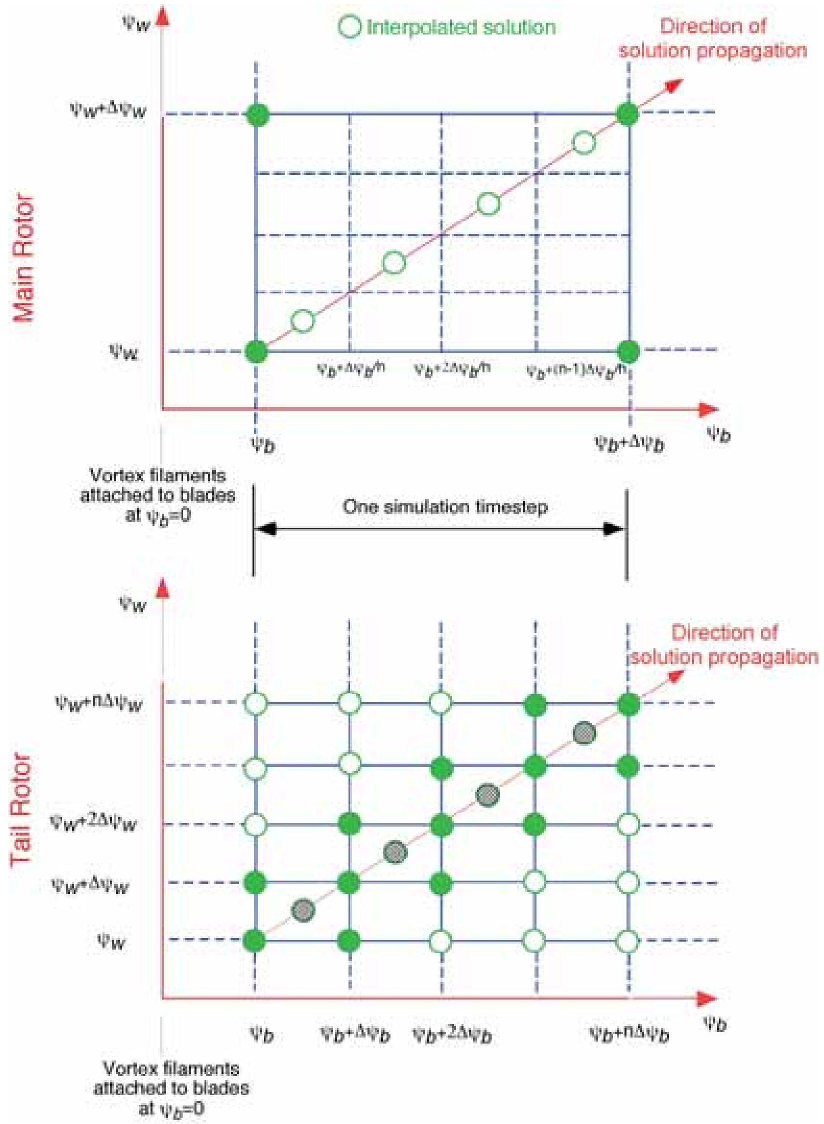

Figure 1.22: Schematic illustrating the loose coupling methodology used to compute the aerodynamic interactions between the main and tail rotors.

the ground and the resulting flow solution has been coupled with the particle uplift framework of Task 3.2 to predict the formation of the evolving dust clouds. Parallelization of the particle uplift code on GPUs (from Task 2.6) has also been undertaken so as to reduce the computational time while also preserving the accuracy of the numerical solution.

The trajectories of the dust particles in space and time are affected not only by the aerodynamic influence of the fuselage and vortex filaments, but the particles may impact the airframe and the blades, and the resulting collisions may significantly alter the trajectories of the particles. Furthermore, the presence of suspended dust particles when a rotorcraft operates in brownout conditions not only limits the visibility for the pilot but results in erosional damage of the rotor blade, which is

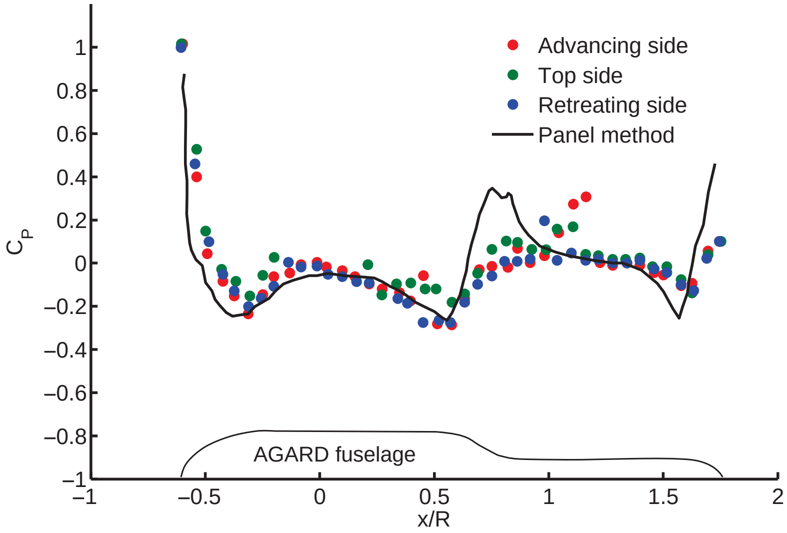

Figure 1.23: Validation of the surface singularity method with the time-averaged pressure distribution on the AGARD fuselage in a uniform free-stream flow.

often seen on the metallic leading edge and the composite blade skin aft of the leading edge. This type of damage is more common on the outboard sections of the blade, where the local flow speeds relative to the blade are highest. This erosive damage can occur rather quickly, and may render the blade aerodynamically and structurally compromised after only a few encounters brownout conditions. The particles contained in the flow through the engine can also erode the compressor blades and so can reduce engine performance. Current strategies for predicting erosion patterns, and the resulting performance degradation, stems primarily from wind-tunnel (hot erosion and cascade erosion) testing, coating life evaluations, and certain types of particle simulations. Initial work has recently been conducted in this task to develop a computational framework in which blade abrasion effects can be predicted with good accuracy and at relatively low computational cost.

Results

Validation of the Panel Method

Validation of the surface singularity method was undertaken using simple body geometries such as a sphere (exact solution) and also the slender AGARD body (i.e., a simplified helicopter fuselage) standard test case for which there are measurements. Figure 1.23 shows the variation of pressure coefficient against longitudinal distance along the AGARD body when the body is operating in a uniform free-stream flow at zero angle of attack. In this case, the rotor blades were removed but the measurements were made with the rotating hub. Each color represents the

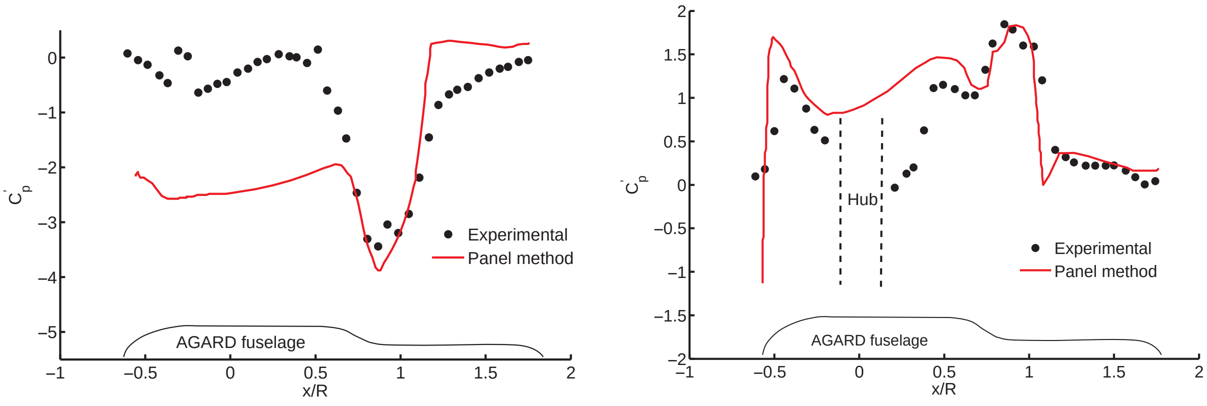

(a) Retreating side (b) Top surface

Figure 1.24: Validation of the surface singularity method for the AGARD fuselage. Steady pressure distribution on the: (a) Retreating side; (b) Top surface.

data from the pressure taps installed on the three sides of the body. The results were found to be in reasonably good agreement with the measured data, but there are discrepancies. In this case, regions of flow separation produced by the rotor hub are responsible for the differences shown.

Figure 1.24 shows the time-averaged pressures on the top and retreating side of the AGARD fuselage with the rotor in edgewise forward flight at an advance ratio, μ, of 0.05. Again, the differences in the predictions and measurements on the top surface of the body arise because of the presence of the rotor hub and its wake was not modeled. The model also over-predicts the velocity at the front end of the fuselage leading to decreased pressure values on the retreating side. Overall, however, the results are in reasonable agreement with the measurements bearing in mind the complexity of the physical problem of a rotor wake interacting with a solid body.

Interaction of Main Rotor and Tail Rotor

Figures 1.25(a) and 1.25(b) show the longitudinal and lateral views of the predicted wake geometry with and without the presence of a tail rotor, respectively, for the hovering rotor operating out of ground effect. The isolated rotor wake was noted to be periodic and axisymmetric for nearly four rotor revolutions, as shown in Fig. 1.25(a). At later wake ages, bundling of the tip vortices produced aperiodic wake developments. It was found that the presence of the tail rotor distorted the main rotor wake and also led to increased levels of aperiodicity in the wake at earlier wake ages, as shown in Fig. 1.25(b).

The tail rotor vortex filaments (highlighted in blue) were entrained through the downwash of the main rotor where it interacted with the tip vortex filaments of the main rotor at very early wake

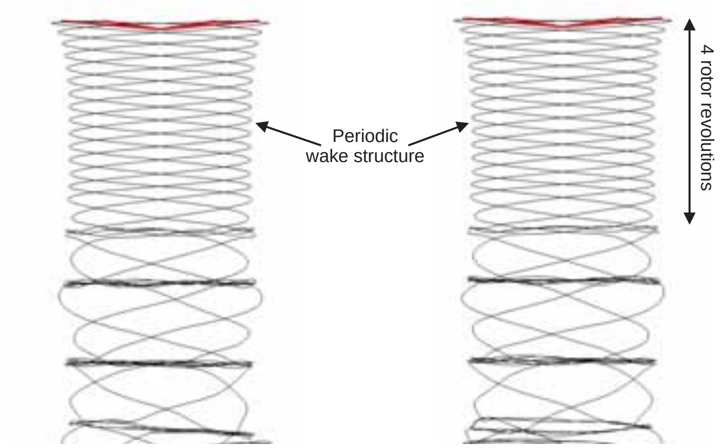

(a) Isolated SMR

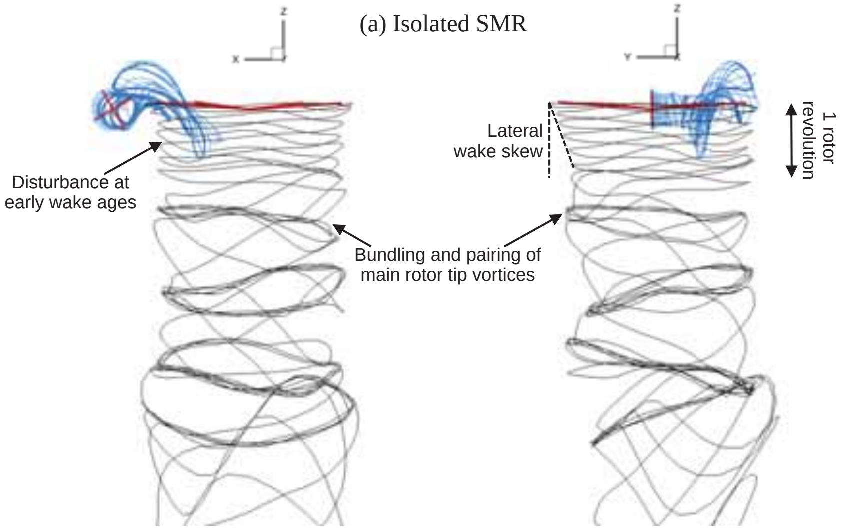

(b) SMR with TR

Figure 1.25: Longitudinal and lateral wake geometries for (a) an isolated SMR and (b) SMR with a TR operating in hover out of ground effect.

ages. As compared to the tip vortex structure of the isolated rotor, the presence of the tail rotor introduced mild disturbances in the early ages of the main rotor wake developments, which resulted in the bundling of main rotor tip vortices as early as the first rotor revolution. The induced velocity of the tail rotor on the main rotor wake also resulted in a lateral wake skew tilt exhibited by the wake of the main rotor, as shown in Fig. 1.25(b).

Interaction of Main Rotor and Fuselage

Two representative fuselage shapes were considered to approximately quantify the effect of the fuselage shape on the development of the main rotor wake and the effects produced at the ground: 1. A geometrically simplified helicopter fuselage, referred to as the UMD-AGARD fuselage, and

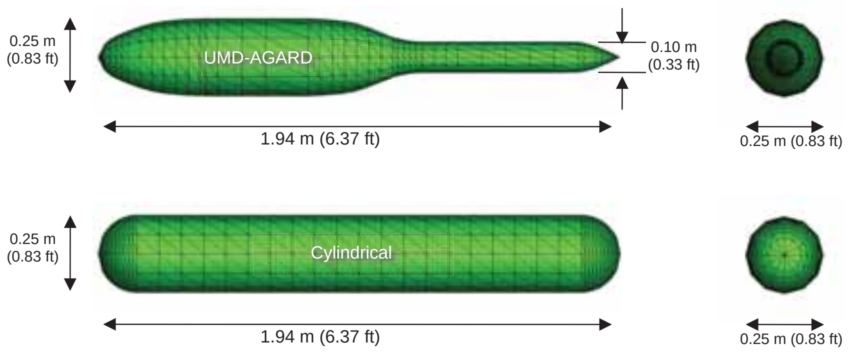

Figure 1.26: Panel representations of the two fuselage shapes.

(a) Isolated SMR

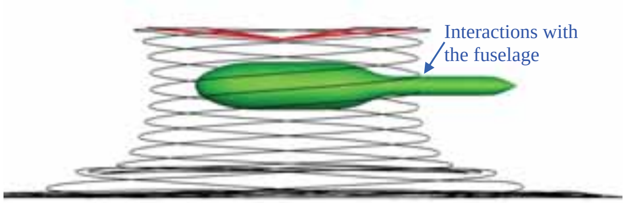

(b) UMD-AGARD fuselage

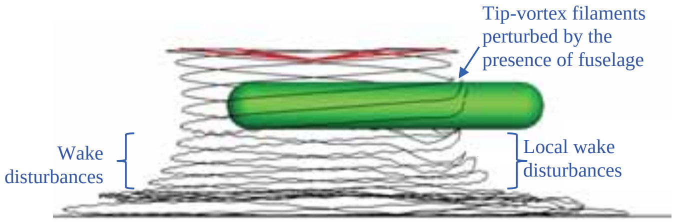

(c) Cylindrical fuselage

Figure 1.27: Comparison of the rotor wake geometries in ground effect operation for the: (a) isolated SMR, (b) SMR with the UMD-AGARD body, and (c) SMR with the cylindrical body.

2. A fuselage with a cylindrical cross-section and hemispherical caps, as shown in Fig 1.26. While the cylindrical body was of uniform cross-section, the UMD-AGARD fuselage had a cylindrical main body that tapered at the nose and a cylindrical tail boom body that tapered at the tail; see Fig. 1.26.

Figure 1.27 shows the wake geometries of the isolated SMR, as well as the SMR in the presence of the two fuselage shapes. The results are shown in terms of the filament locations as they

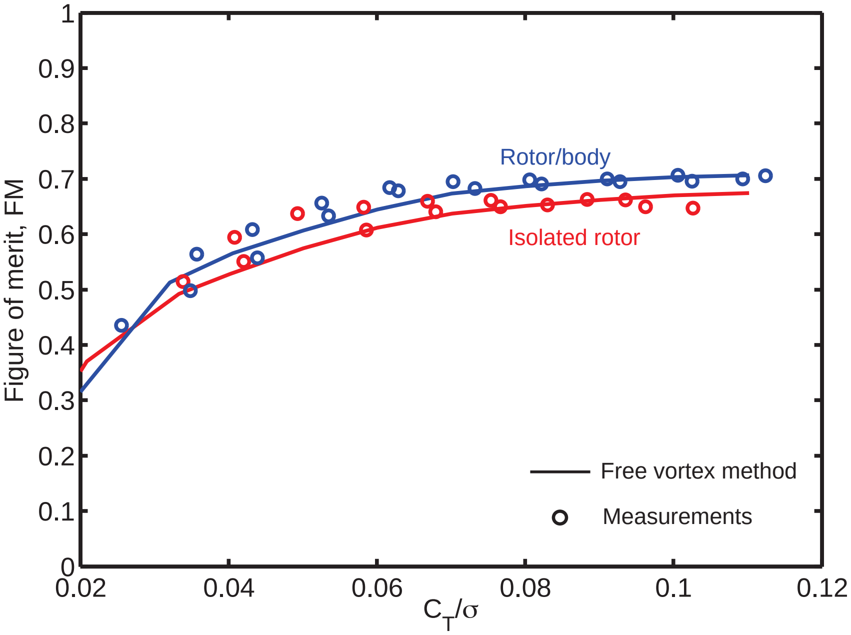

Figure 1.28: Variation of the figure of merit of the rotor with and without the presence of a fuselage.

intersect the longitudinal plane. For the UMD-AGARD fuselage, the trailed tip vortices were only minimally distorted as they slowed and stretched around the tail, but this process clearly initiates a wake disturbance and it can be seen that these disturbances are also propagated to the front of the rotor wake. This means that local wake/fuselage interactions may have some effects on the overall flow environment at the ground.

A study was also conducted to quantify the influence of the fuselage on the performance of the rotor. Figure 1.28 shows the variation of the rotor figure of merit against the blade loading coefficient, C_T/σ, with and without the AGARD fuselage (see Fig. 1.27(b)) operating in hover out of ground effect. The solid circles indicate experimental measurements, while the dashed lines represent FVM predictions. As the rotor thrust increases, the presence of the fuselage produces an increase in the rotor figure of merit; an increase of about 5% at $C_T/\sigma = 0.1$ is clearly significant.

Brownout Dust Cloud Simulations – Effects of Fuselage

The nominal landing profile for the simulations used is shown in Fig. 1.29. The maneuver begins with the rotorcraft in steady forward flight at 50 kts and at a descent rate of 100 ft min^{-1}. The helicopter then executes a flare maneuver and decelerates into a steady hover with the rotor plane stabilizing at a height of one rotor radius above the ground. The duration of the entire

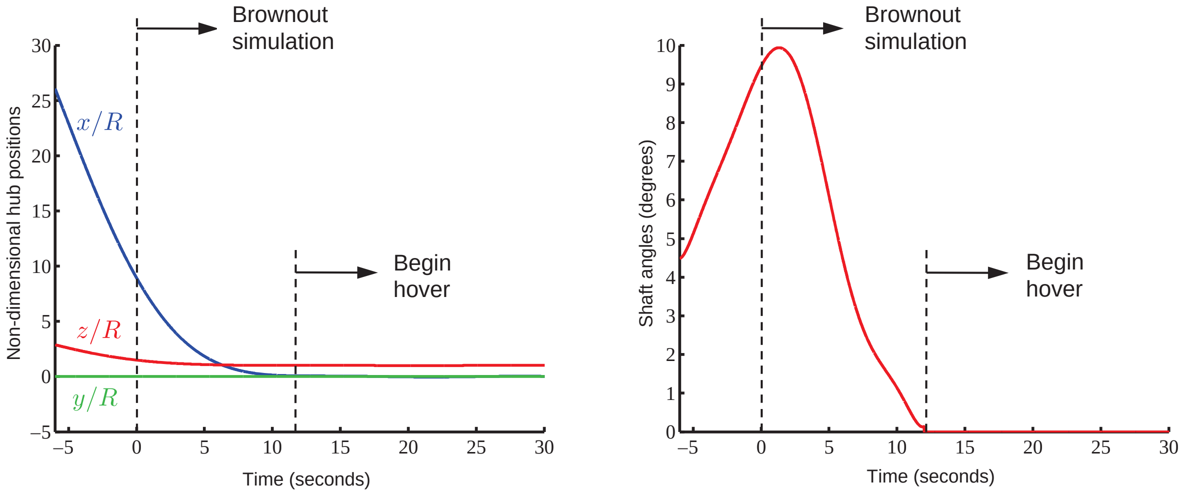

(a) Rotor hub positions

(b) Rotor shaft angle

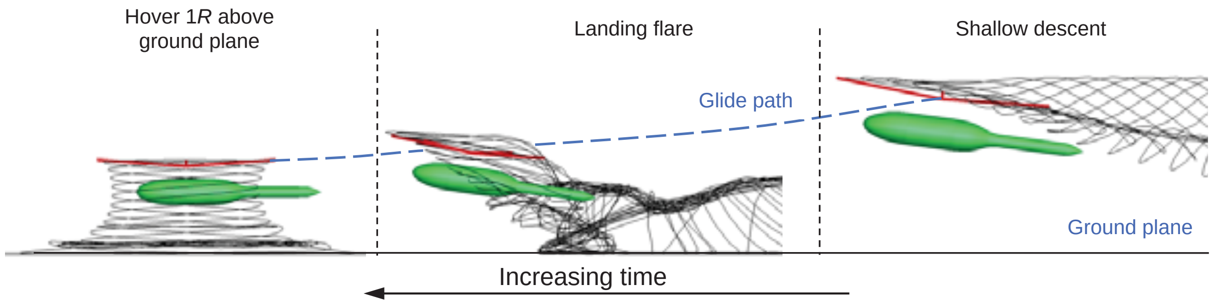

(c) Representative approach-to-touchdown maneuver

Figure 1.29: Approach profile for landing: (a) Rotor hub center positions; (b) Shaft tilt angles; (c) Overall maneuver.

approach is about 35 s, and time is referenced to the start of the brownout simulation, as shown in Fig. 1.29.

Figure 1.30 shows predictions of the dust clouds as produced by the isolated SMR at the end of the simulation, for the SMR with the UMD-AGARD fuselage, and for the SMR with the cylindrical fuselage, respectively. As shown in Fig. 1.30, the dust cloud can be decomposed into two distinct regions, an outer structure and an inner structure. The outer structure, highlighted in red, develops during the formation and propagation of the ground vortex. These structures contain particles that were uplifted through the induced velocity field produced by the propagating vortex and also by those particles that were trapped within the ground vortex and so ejecting more particles by bombardment mechanisms. The outer structure of the cloud appears to be sensitive to what happens during the transitional phase from forward flight to hover, in which wake distortions caused by the presence of the fuselage translate into more global flow distortions and further intricacies in

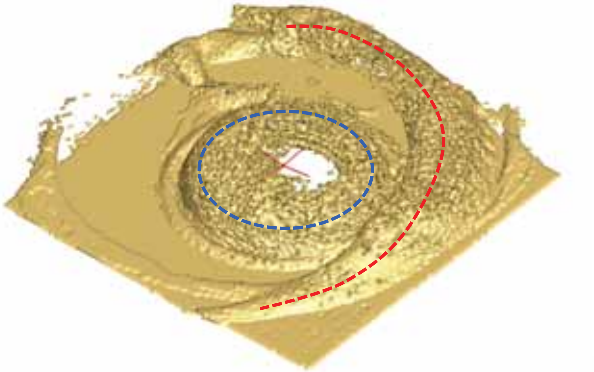

(a) Isolated SMR

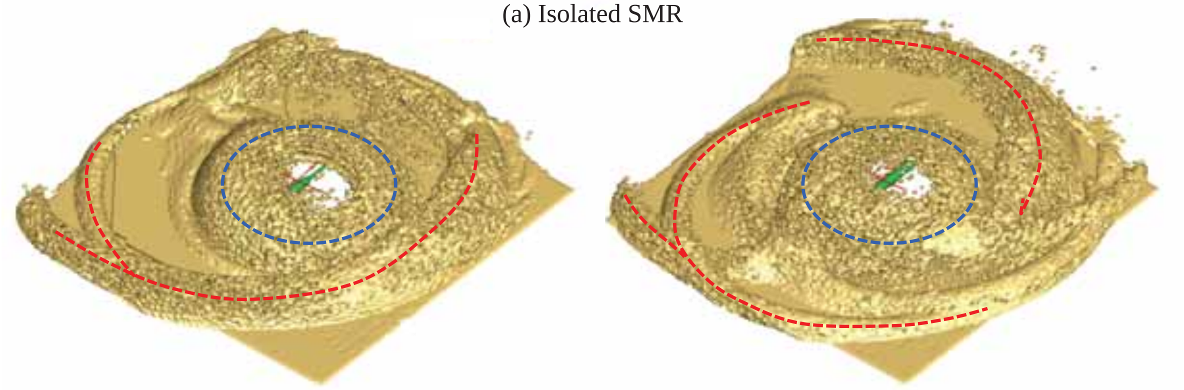

(b) UMD-AGARD fuselage (c) Cylindrical fuselage

Figure 1.30: Simulated dust cloud profiles for the (a) Isolated rotor; (b) Rotor and UMD-AGARD fuselage; and (c) Rotor and cylindrical fuselage.

the structure of the dust cloud.

The inner structure of the cloud, highlighted in blue in Fig. 1.30, is characteristic of the dome-shaped dust cloud that based on field tests in brownout conditions is often seen to engulf the rotor. Because the presence of fuselage only slightly modifies the rotor wake in hover (see Fig. 1.27), the inner structure of the cloud is seen to be fairly similar in all cases. However, it is recognized that these solutions may change when flow separation effects produced by the fuselage are included into the modeling, which cannot be predicted in this case because of the limitations of the potential flow model.

Brownout Dust Cloud Simulations – Effects of Rotor Configurations

Figure 1.31 shows the dust cloud structures formed by the SMR (with TR), coaxial, tandem, and side-by-side rotor configurations at the end of the simulated landing maneuver. The dust cloud produced by the SMR shown in Fig. 1.31(a) is similar in structure to that of the isolated SMR, but with minor differences. The aerodynamic influence of the tail rotor (shown in Fig. 1.25) causes

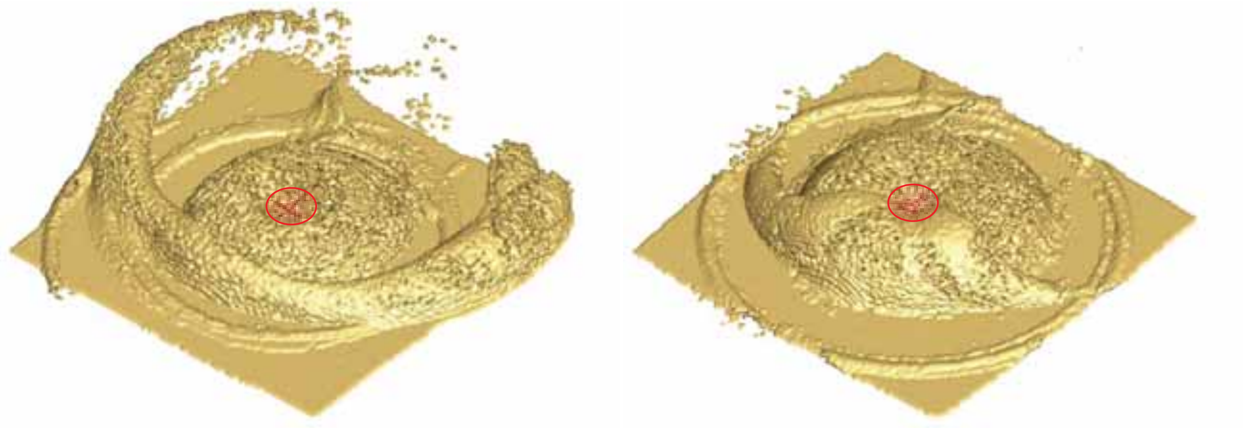

(a) SMR w/ TR (b) Coaxial

(c) Tandem (d) Side-by-side

Figure 1.31: Dust clouds formed by a SMR (with TR), coaxial, tandem, and side-by-side rotors at the end of the simulated landing maneuvers.

bundling of the tip vortices and makes the resulting dust cloud considerably less axisymmetric. The inclusion of the tail rotor also modifies the dust cloud by causing airborne particles to be entrained into its own downwash field.

Figure 1.31(b) shows the dust cloud produced by the coaxial rotor system. Unlike other rotor configurations, the lower rotor of the coaxial significantly increases the overall slipstream velocities in the wake, which causes the tip vortices to impinge on the ground earlier during the maneuver than was seen for the other rotor configurations. The vortex filaments from the upper and lower rotor bundle and convect along the ground, uplifting large quantities of dust through bombardment mechanisms. The coaxial rotor configuration produces a dome shaped dust cloud that is more axisymmetric compared to the other configurations.

The dust cloud produced by the side-by-side rotor configuration is shown in Fig. 1.31(d). It is evident that this configuration uplifts large quantities of dust that is distributed on all sides, potentially causing severe visual obscuration all around the aircraft. As was seen with the tandem rotor configuration, a strong asymmetry in the development of the dust cloud exists because of the positioning of the rotors. However, in this case, the tip vortex filaments from each rotor bundle more readily and more frequently and so forming a much stronger ground vortex, which in this case convects towards the rear of the rotorcraft, uplifting large quantities of dust in the process. The side-by-side configuration was the only configuration where large quantities of dust were continuously mobilized in hover, which is because of the relatively higher flow velocities near formed the ground and the continuous bundling of the tip vortex filaments in the outer regions of the wake.

Particle Collisions with the Blade

Blade erosion occurs because of the interaction of the rotor blades with the suspended particulates causing wear and tear of the leading edge of the blades. In a brownout environment, this erosion process is greatly accelerated. To prevent damage from dust/sand erosion, metallic abrasion strips, typically composed of stainless steel or titanium, are bonded to the blade leading edge to serve as a hard surface that absorbs the kinetic energy of the sand particle. These impacting sand particles, however, slowly erode away the metallic material. This problem is a bigger issue near the outboard blade tip, where the high blade velocity means that the dust particles impact with greater kinetic energy. Replacement of these damaged abrasion strips and caps on the rotor blades, if possible, leads to increased maintenance cost and reduced operational readiness.

For example, Figs. 1.32(a)–1.32(d) shows the trajectory of particles of sizes 10 μm, 20 μm, 50 μm, and 70 μm, respectively, as they convect around a NACA 0015 airfoil. The airfoil was operating at 10° angle of attack. The time taken by a spherical particle to respond to changes in the flow, i.e., particle time constant, is proportional to the square of particle diameter d_p^2. Therefore, larger the particle time constant, longer it takes to alter its trajectory, and consequently it has a higher probability of colliding with the airfoil. Figure 1.32(b) shows that under certain flow conditions, multiple collisions of the same particle with the airfoil surface can occur (trajectory highlighted in black).

Papers Published

1. Sayan Ghosh R., and R. Ganesh Rajagopalan, “Rotor Configurational Effect on Rotorcraft Brownout,” 28th AIAA Applied Aerodynamics Conference, 2010.

2. William J. Polzin, Kanchan Guntupalli, and R. Ganesh Rajagopalan, “Discrete Blade Model

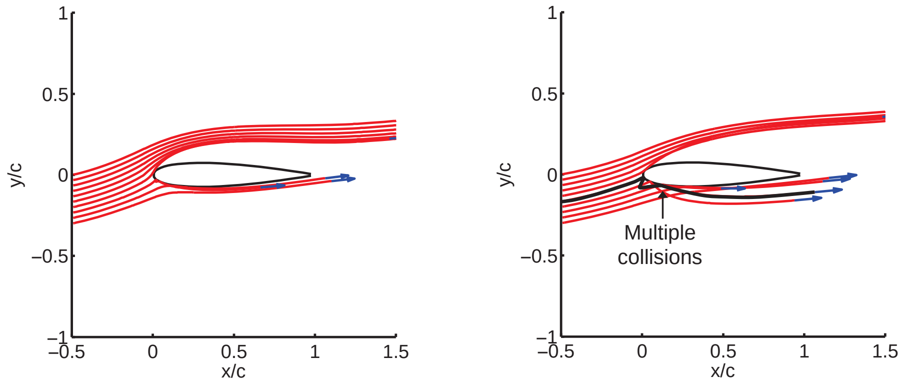

(a) $d_p = 10\ \mu m$ (b) $d_p = 20\ \mu m$

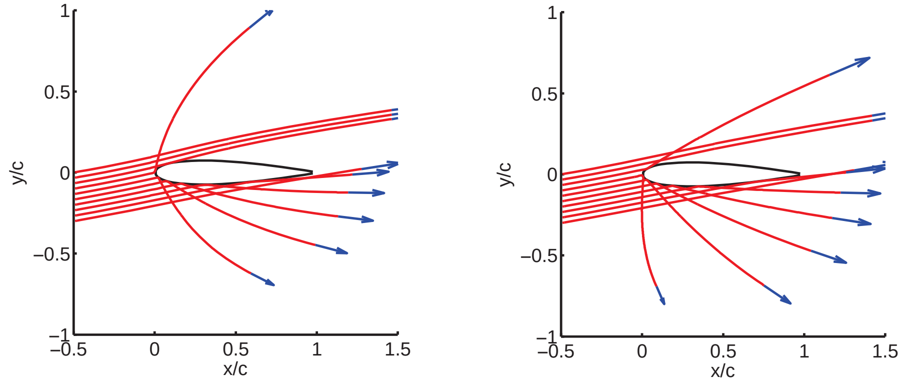

(c) $d_p = 50\ \mu m$ (d) $d_p = 70\ \mu m$

Figure 1.32: Trajectories of particles colliding with a NACA 0015 airfoil at 10° for particles sizes of (a) 10 μm, (b) 20 μm, (c) 50 μm, and (d) 70 μm.

for Rotorcraft Brownout," Presented at the 29th Applied Aerodynamics Conference, Honolulu, HI, June 2011.

3. Govindarajan, B. M., and Leishman, J. G., "Predictions of Rotor and Rotor/Airframe Configurational Effects on Brownout Dust Clouds," 70th Annual Forum Proceedings of the American Helicopter Society, Montreal, Quebec, May 20–22, 2014. (Awarded best paper in the operations session)

4. Govindarajan, B., *Contributions Toward Understanding the Effects of Rotor and Airframe Configurations on Brownout Dust Clouds*, Ph.D. Dissertation, Department of Aerospace Engineering, University of Maryland, College Park, MD, 2014.

Part 2: Fundamentals of Particle Suspension

- Task 2.1 – Non-Uniform, Near-Bed Flow Field with Impinging Rotorwash
- Task 2.2 – Two-Phase PIV Near-Wall Bounded Turbulent Flows
- Task 2.3 – Fundamental Two-Phase Measurements in Brownout Fluid Mechanics
- Task 2.4 – Large-Eddy Simulation of the Interaction Between Vortices and the Ground
- Task 2.5 – Two-Phase Large Eddy Simulation Using the Mesoscopic Eulerian Formalism
- Task 2.6: Effects of Model Scaling on Sediment Transport
- Task 2.7: Turbulent Near-Bed Flows Under Impinging Vorticity

Task 2.1

Non-Uniform, Near-Bed Flow Field Associated With Impinging Rotorwash

Investigator(s): W. Brian Dade, Benoit Cushman Roisin
Institution/Department: Dartmouth College/Earth Sciences
Contact email(s): W.B.Dade@dartmouth.edu

The work initially being performed under this task is now being continued under two other tasks, namely Task 2.6 (Effects of Model Scaling on Sediment Transport) and Task 2.7 (Turbulent Near-Bed Flows Under Impinging Vorticity). Refer to these tasks for further information.

Task 2.2

Dual-Phase PIV in Two-Phase Near-Wall Bounded Turbulent Flows

Investigator(s): J. Gordon Leishman

Institution/Department: University of Maryland/Department of Aerospace Engineering

Graduate Student(s): Anish Sydney, Jaime Reel, Nathan Doane

Contact email(s): leishman@umd.edu

Background and Technical Challenges

A helicopter rotor wake comprises a highly three-dimensional flow with locally high unsteady effects produced by the tip vortices from the rotating blades. Understanding this complicated vortically-dominated rotor wake structure becomes even more difficult as it approaches a ground plane. Complexities arise because the vortices undergo stretching and bundling as they interact with the developing wall jet like flow along the ground. The various effects produced by the tip vortices, which include locally high shear stresses and pressure forces, are then responsible for mobilizing and uplifting loose sediment particles. The mechanisms by which sediment particles are uplifted are summarized in Fig. 2.1.

The ability to properly understand the resulting two-phase flow field, as well as how it is affected by various geometric and operating parameters of the rotor, is fundamental to understanding the brownout problem. To this end, the objectives of this task are to develop and implement diagnostic techniques to measure the fundamental two-phase flow physics underlying the brownout phenomenon. The main goals are to quantify the interactions of the rotor wake with a ground plane covered with a mobile sediment bed, determine what particular characteristics of the resulting flow are responsible for sediment mobility and uplift, and then how the resulting dual-phase flow field is altered by aspects of the rotor geometry and its operating condition.

Technical Approach

Flow field measurements have been conducted in the controlled environment of a dust chamber using a prototypical flow generated by a small rotor system. A schematic of the experimental setup being used in this task is shown in Fig. 2.2. The rotor has a radius of 85 mm (3.346 in), the blades having a cambered plate section. Particle image velocimetry (PIV) experiments were conducted using both one-bladed and two-bladed rotor configurations. The teetering hub design allowed the second blade to be interchanged with an equivalent counter-mass to obtain a one-

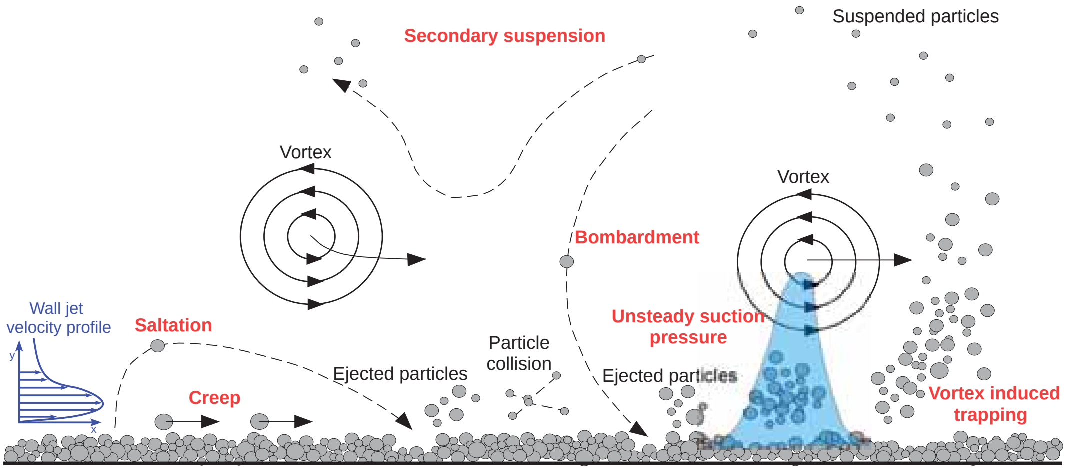

Figure 2.1: Schematic showing the different modes of sediment mobilization and uplift below a rotor.

bladed rotor. An adjustable height ground plane was arranged so that it was parallel to the rotor tip-path-plane. Several ground planes have been used in this work, including one fitted with a row of pressure transducers to allow measurements of the unsteady pressures over the ground. These transducers were spaced 1.3 cm apart except between $r/R = 1$–2 where they were spaced at 0.7 cm to obtain a higher measurement resolution. Experiments were performed with the rotor hovering at one rotor radius above the ground plane.

Measurements were initially made with the laser sheet oriented in a vertical plane, as shown in Fig. 2.2. However, to better understand the three-dimensionality of the flow, the laser light sheet was aligned to be parallel to the ground plane and the flow imaged by viewing downward onto the laser sheet. These regions were also used to study the differences in the wall-parallel velocities near the ground plane that were caused by the presence of body shapes (representing airframes) in the rotor wake. The bodies had cross-sectional shapes that were circular, elliptical, and rectangular, respectively, as shown in Fig. 2.3. These bodies are smaller versions of those used in Task 1.1. Dual-phase experiments were also performed in both the vertical and horizontal planes.

To date, most studies have consisted of experiments with the rotor operating at various fixed heights above the ground. In practice, however, rotorcraft encounter brownout conditions during takeoffs and landings, which are dynamic flight maneuvers. While certain experiments have been performed at other institutions to examine the problem of particle pickup induced by a rotor operating in a wind tunnel, the wind tunnel approach cannot properly simulate the boundary conditions at the ground plane. Therefore, a rig was developed in the present work that allows the rotor to be translated relative to the ground plane; see Fig. 2.4. This rig allows for further validation of

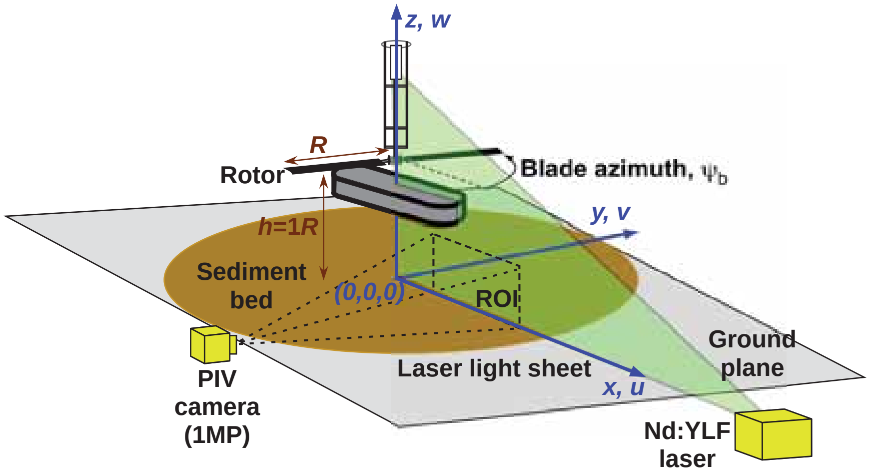

Figure 2.2: Schematic showing the experimental setup used to perform the dual-phase flow measurements.

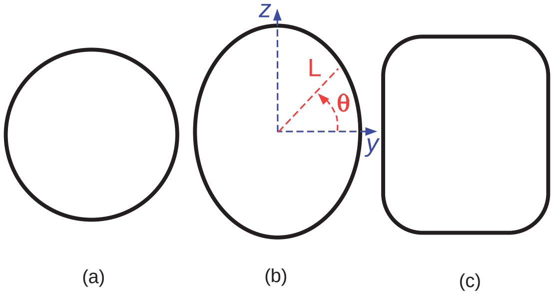

Figure 2.3: Cross-sectional views of the body shapes: (a) circular, (b) elliptical, and (c) rectangular.

the modeling outcomes (Tasks 3.2 and 3.4), providing the necessary range of motion to perform a variety of simulated flight profiles.

A range of rotor operating conditions and heights above the ground have been used to expose the details of the wake interactions with the ground, and also to isolate the different sediment uplift mechanisms that ultimately may affect the formation of the dust cloud. Dual-phase particle image velocimetry (PIV) was used to measure the resulting flows. The mobilized sediment particles were identified and tracked through the flow by using particle tracking velocimetry (PTV).

Results

The mechanisms previously identified in Fig. 2.1 cause loose particles on the bed to be mobilized and transported into the rotor flow field. The particles in the near-wall region experience several types of forces, including shear, pressure, inter-particle, and gravitational. The pronounced vertical

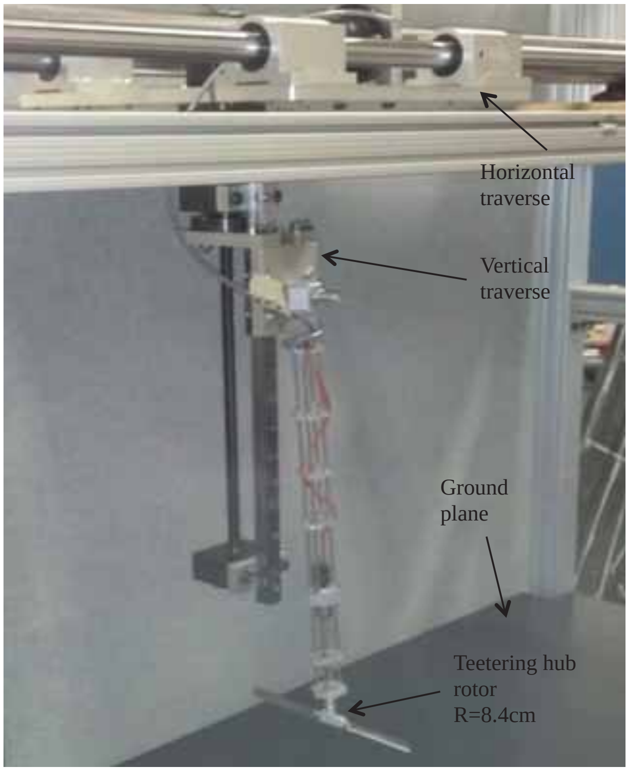

Figure 2.4: Image of the two-axis traverse system used to simulate descent and forward flight.

uplift of particles that was observed in a region strongly affected by the predominantly wall-parallel velocities and associated boundary layer shear suggests additional body forces could be acting on the particles. For example, the forces on the particles resulting from the low pressures and pressure gradients near the vortex core may be responsible for the more wall-normal particle trajectories that have been observed.

To quantify the pressure induced on the ground plane, experiments were performed with the rotor operating above the ground plane fitted with pressure transducers. A representative pressure signal from a transducer located at $r/R = 1.2$ is shown in Fig. 2.6. This radial location is near where the vortices impinge on the ground and, therefore, shows a more periodic signal, i.e., before the vortices have begun to diffuse and/or interact with each other. Notice that there is a sharp peak in pressure approximately every blade passage, which is caused by the close passage of a tip vortex over a pressure transducer.

To further examine the pressure variation along the ground, Fig. 2.7 shows pressure signals from all of the sensors as a function of wake age. Notice that the largest fluctuating pressures are seen closer to the rotor ($r/R = 0.5$), where there is more vertical downwash flow from the rotor. The pressure decreases as the blade tip vortices approach the ground plane and begin to stretch and

Figure 2.5: The dust chamber in which the flow experiments are performed.

expand radially outward. In the region of vortex impingement on the ground, the pressure become strongly negative (i.e., a suction pressure) before settling back to near ambient conditions further downstream. However, fluctuations were still seen for all radial locations. Near the rotor these fluctuations were strongest, but the effects of vortical flows and turbulence were noted to cause pressure variations as far downstream as $r/R = 4$.

The three-dimensional nature of the flow field has been examined in a horizontal plane at $z/R = 0.1$ (just above the ground plane), the results being shown in Fig. 2.8 as contours of total velocity. The tip vortices manifest as localized regions of higher flow velocities, such as the red region marked as Filament 2 in Fig. 2.8. The significant three-dimensionality of the rotor wake flow at the ground is evident. At $x/R = 0.6$–0.8, a lower velocity region under the rotor was observed, this region being just upstream of the point where the rotor wake boundary had begun to impinge on the ground. By $x/R = 0.9$, however, the rotor wake had turned radially outward. Just outboard of this radial location, two vortex filaments were observed to impinge on the ground, which are marked as Filament 1 and Filament 2, respectively. Notice that the impingement of these vortices is fairly radially asymmetric along the length of the filaments. Beyond $x/R = 1.5$, the vortex filaments

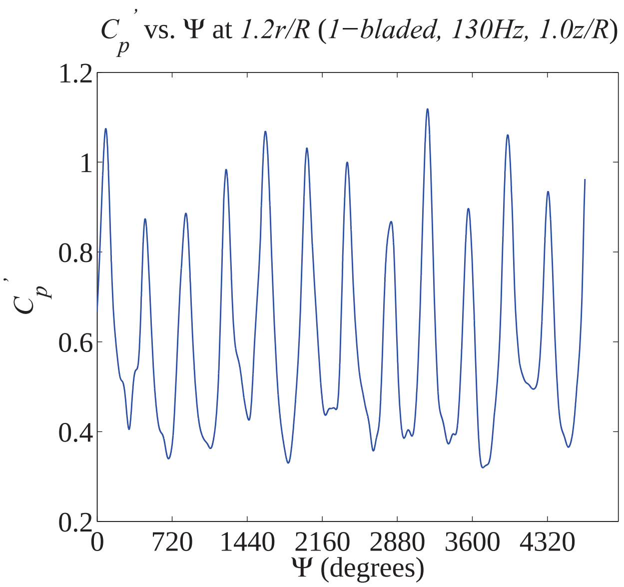

Figure 2.6: Variation of surface pressure produced at r/R = 1.2 by a one-bladed rotor hovering at z/R = 1.0.

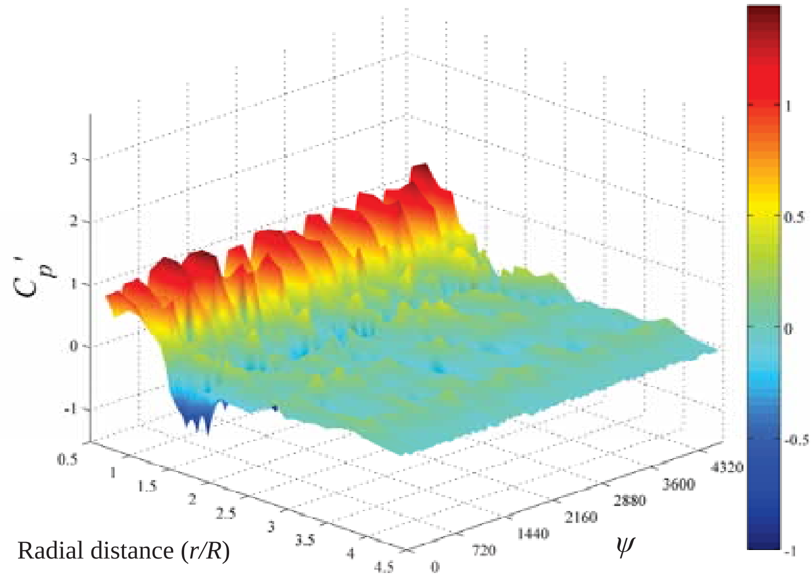

Figure 2.7: Time-histories of surface pressures produced by a one-bladed rotor hovering at z/R = 1.0.

were not distinguishable from each other because they had either merged together or had diffused, causing a highly unsteady, radially asymmetric flow environment.

The effects of placing a body (or airframe) in the rotor wake on the mobilization and uplift of sediment has been examined. Figure 2.9 shows the dual-phase flow produced by the isolated rotor compared to the flow with the rectangular body present. The background contours are of

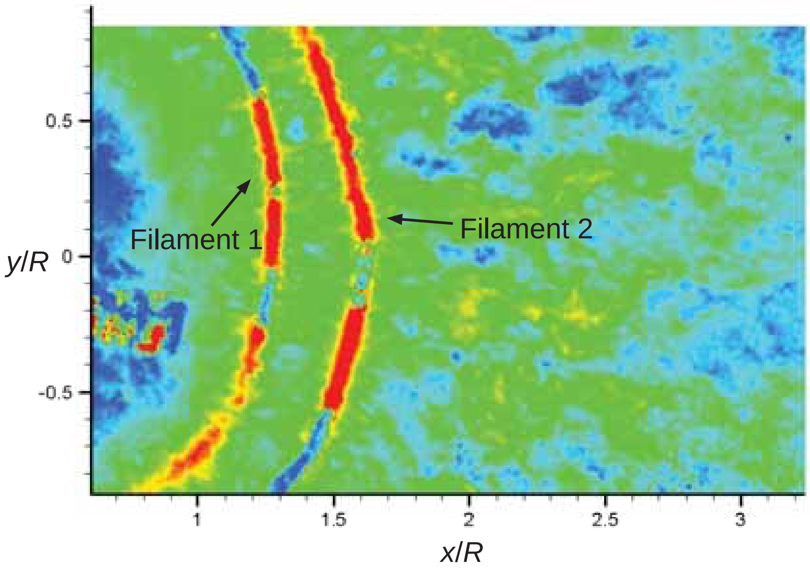

Figure 2.8: Total velocity contours for the isolated rotor hovering at $z/R = 1.0$ in a horizontal plane at $z/R = 0.1$.

total velocity and the sediment particle locations are identified as white circles; the circles have been exaggerated in size for clarity. Notice that these results are in a vertical plane coincident with the longitudinal centerline of the bodies, and show the tail region of the rectangular body. The carrier-phase measurements (i.e., the rotor wake itself) shows that the body significantly altered the flow at the tail section. The tip vortices interacted with the body at relatively young wake ages, directly impinging on the body surface and causing the vortices to rapidly diffuse in some cases. However, relatively high regions of velocity near the ground suggest that some remaining vorticity does persist to older wake ages. In general, the vortical flow at the ground with a body present was found to be significantly more diffused compared to that for the isolated rotor. Of particular interest, however, is that the flow field produced by the presence of the body appears to uplift more particles than for the isolated rotor flow.

While somewhat counterintuitive, this latter observation is a consequence of the higher peak velocity that was produced at the ground by the isolated rotor. These higher flow velocities convected the particles more radially outward away from the rotor before they could be picked up and suspended by the blade tip vortices. With the bodies present, however, the near-wall flow reached a lower peak velocity at all radial locations away from the rotor. While still above the threshold conditions required to mobilize the particles, the near-wall flow did not convect the particles radially outward as rapidly or as far as with the isolated rotor. Instead, the vortical flow near the wall (which actually contained less coherent vorticity than was produced by the isolated rotor) resulted

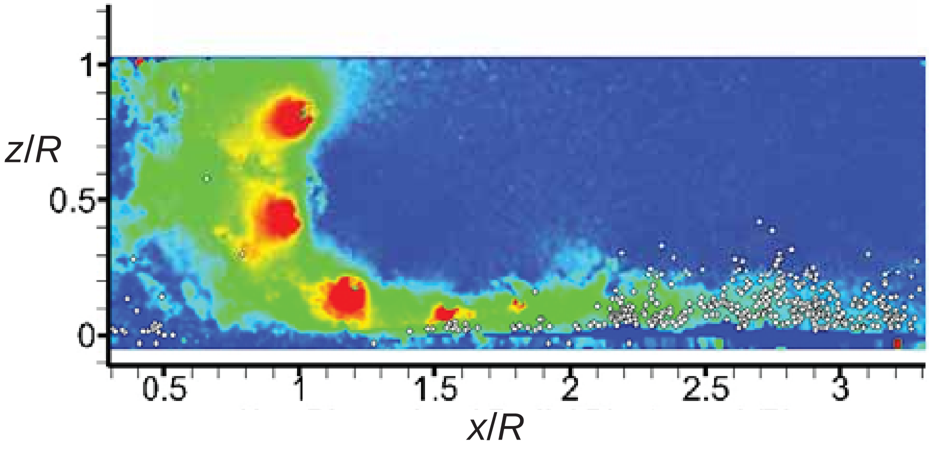

(a) Dual-phase measurements for the isolated rotor

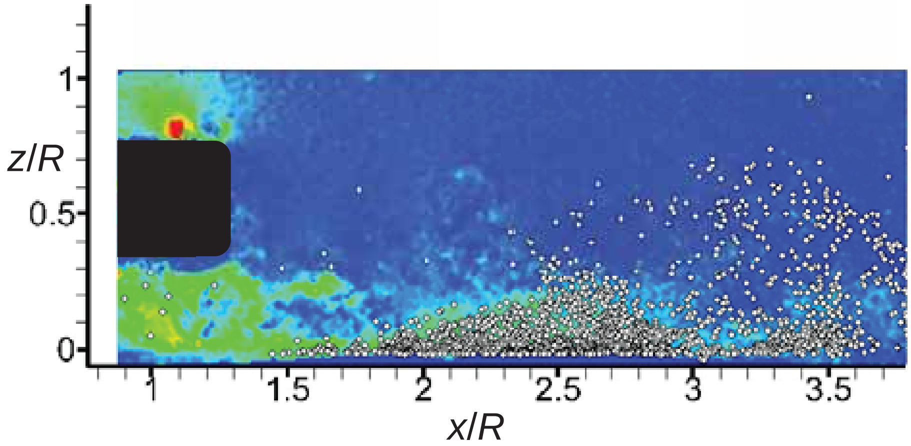

(b) Dual-phase measurements for the rectangular body

Figure 2.9: Instantaneous dual-phase measurements for the isolated rotor with the rectangular body.

in more particles being uplifted closer to the rotor.

The measurements made in the vertical imaging plane showed that the flow in the tail region of the body was significantly distorted. Therefore, the flow field was measured over several horizontal planes to better quantify such flow distortions; the single-phase results for $z/R = 0.1$ are shown in Fig. 2.10 for the isolated rotor and for the rotor with the rectangular body, respectively. The background contours are of total velocity time-averaged over 1,000 contiguous PIV realizations of the flow. The three-dimensional flow in this region was seen to be significantly altered by the presence of the bodies, causing lower average flow velocities and more radial flow asymmetries compared to those produced by the isolated rotor. Another interesting difference from the isolated rotor flow is the formation of a localized flow adjacent to the tail of the body, which is identified in

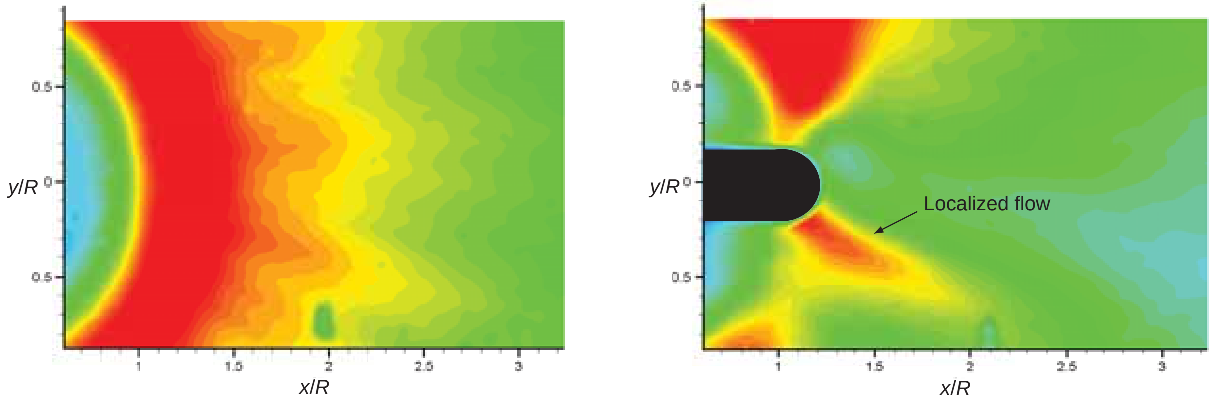

(a) Isolated rotor

(b) Rectangular body

Figure 2.10: Time-averaged total velocity contours for the isolated rotor and below the tail of each body at $z/R = 0.1$.

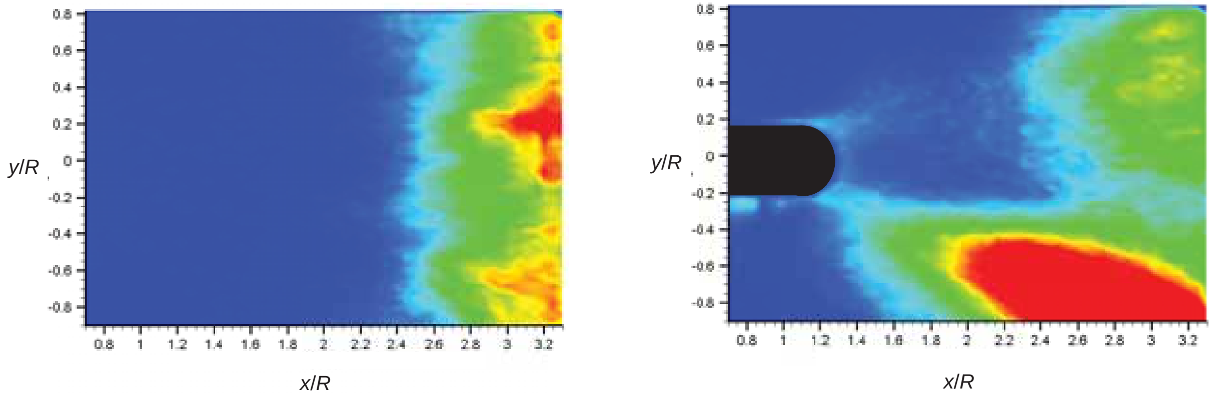

(a) Particle concentration – isolated rotor

(b) Particle concentration – rectangular body

Figure 2.11: Time-averaged particle concentration at $z/R = 0.3$ for the isolated rotor and at the tail of the rectangular body.

Fig. 2.10(b).

To examine the three-dimensional nature of the the particle field with the bodies present, dual-phase tests were conducted in a horizontal plane at $z/R = 0.3$. The particle locations were binned and time-averaged over 1,000 contiguous realizations of the flow to produce concentration maps; see Fig. 2.11. The particle concentrations produced by the isolated rotor indicated that particles were being uplifted and suspended at $x/R = 2.4$ and then continuing downstream. With the body present, however, the particles were suspended closer to the tail region at $x/R \approx 1.0$. The closer suspension of particles occured, in part, because the localized flow near the mobilized large quantities of particles relatively close to the rotor. In general, it was found that the flows produced with the bodies present caused non-uniform particle concentrations that were formed closer to the rotor.

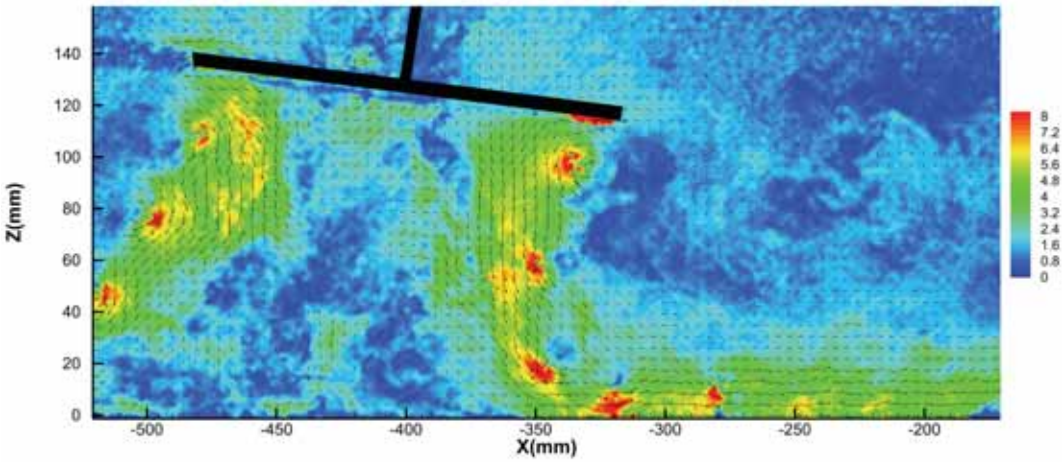

Figure 2.12: Two-bladed rotor in level forward flight at $\mu \approx 0.03$.

In practice, rotorcraft are generally performing take-off or landing maneuvers when they encounter brownout conditions. Several experiments have recently been conducted at a variety of simulated forward flight conditions using a rotor traverse rig. It was found that in low-speed forward flight in ground effect the flow produced by the rotor goes through three stages: 1. The wake was first convected out in front of the rotor; 2. The rotor then approaches a translational speed at which the flow begins to recirculate back into the rotor disk causing a ground vortex to form; 3. The rotor then attains enough forward speed to sweep the wake back behind the rotor.

A very low-speed case at $\mu \approx 0.03$ is shown in Fig. 2.12. The results show that some amount of recirculation was present in the flow, but the wake remained close to the the ground to form a wall jet, as was seen in hover. A case for $\mu \approx 0.07$ is shown in Fig. 2.13. At this slightly higher forward speed the results show that the rotor wake detached from the ground and was recirculated back into the rotor disk. Finally, for $\mu \approx 0.09$, the rotor wake and its vortices were swept well back behind the rotor; see Fig. 2.14.

A ground vortex was seen to develop in front of the rotor before the wake was swept back so a smaller region of interest was used to obtain higher resolution flow measurements. As shown in Fig. 2.15(a), contours of velocity magnitude suggest that rather than forming a typical wall-jet like flow seen in hover, the flow was reingested through the rotor disk. In the vorticity plot shown in Fig. 2.15(b), the recirculating flow has developed positive vorticity. Furthermore, the vortical structures persisted to old enough wake ages that they could be identified even as the flow had been turned upward towards the rotor disk.

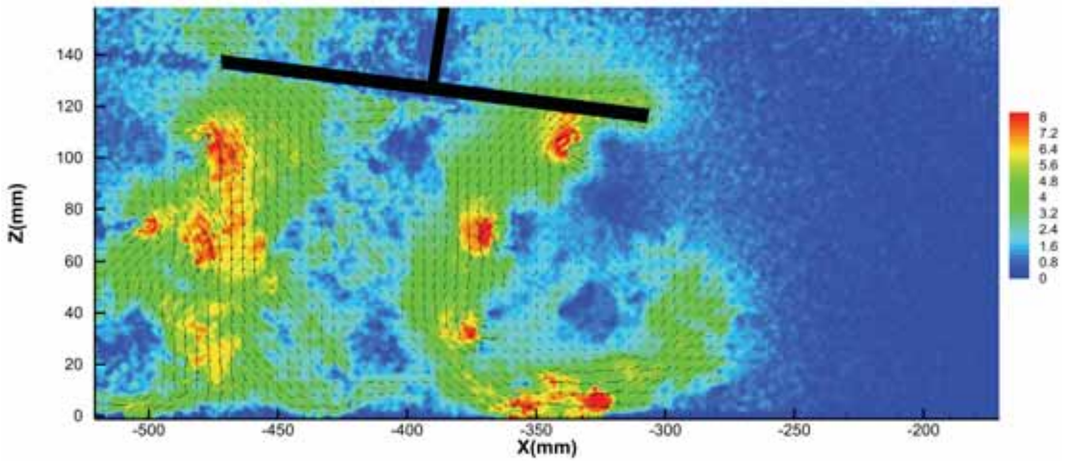

Figure 2.13: Two-bladed rotor in level forward flight at $\mu \approx 0.07$.

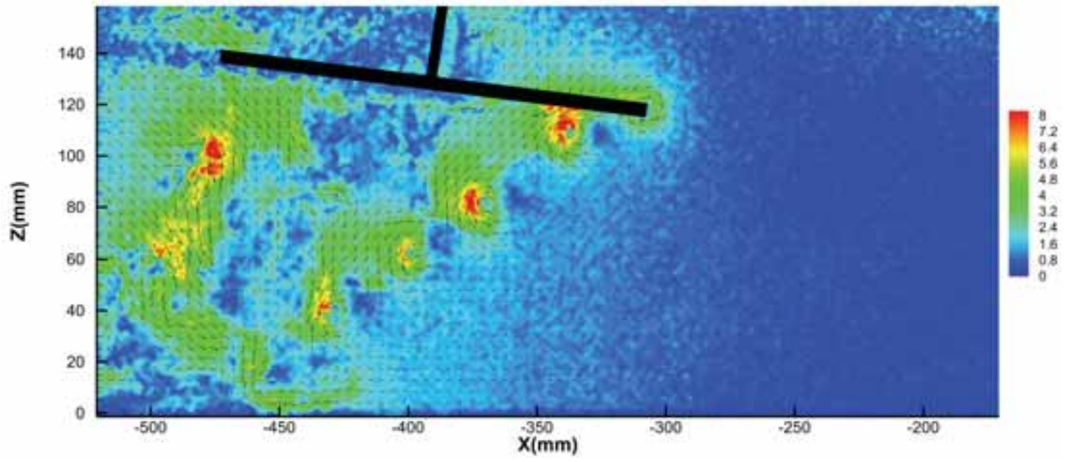

Figure 2.14: Two-bladed rotor in level forward flight at $\mu \approx 0.09$.

Publications

1. Johnson, B., Leishman, J. G., and Sydney, A., "Investigation of Sediment Entrainment in Brownout Using High-Speed Particle Image Velocimetry," American Helicopter Society 65th Annual Forum Proceedings, Grapevine, TX, May 27–29, 2009.

2. Johnson, B., Leishman, J. G., and Sydney, A., "Investigation of Sediment Entrainment Using Dual-Phase, High-Speed Particle Image Velocimetry, *Journal of the American Helicopter Society*, April 2010.

3. Sydney, A., Baharani, A., and Leishman, J. G., "Understanding Brownout Using Near-Wall High-Speed Dual-Phase Flow Measurements," American Helicopter Society 67th Annual Forum Proceedings, Virginia Beach, VA, May 3–5, 2011.

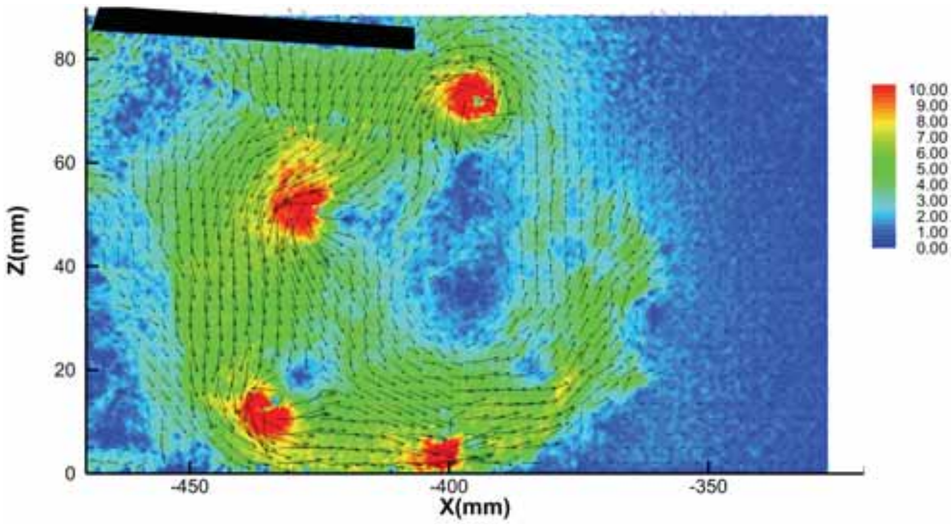

(a) Velocity magnitude

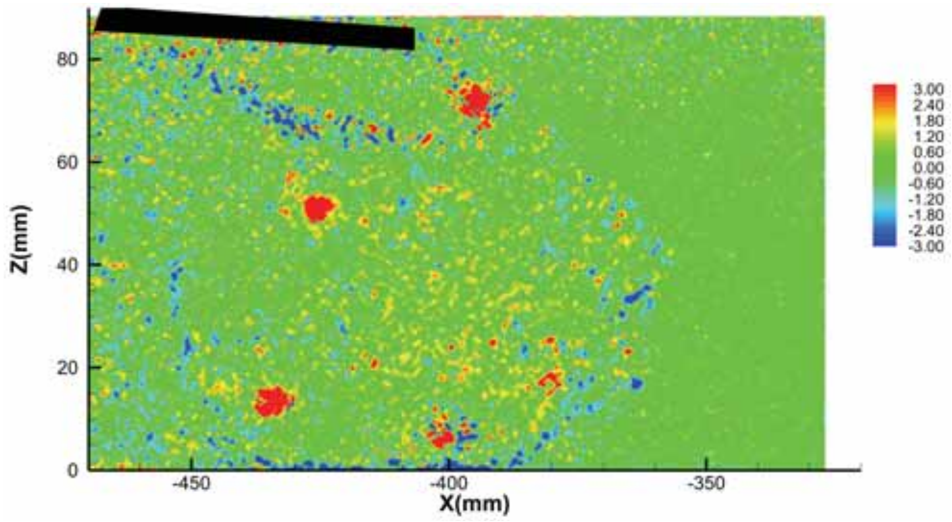

(b) Vorticity

Figure 2.15: Velocity magnitude and vorticity of ground vortex ahead of the rotor.

4. Sydney, A., "Understanding Brownout Using Dual-Phase Particle Image Velocimetry Measurements," M.S. Thesis, Dept. of Aerospace Engineering, University of Maryland, College Park, May 2011.

5. Baharani, A., "Investigation into the Effect of Aeolian Scaling Parameters on Sediment Mobilization Below a Hovering Rotor," M.S. Thesis, Dept. of Aerospace Engineering, University of Maryland, College Park, May 2011.

6. Sydney, A. and Leishman, J. G., "Measurements of Rotor/Airframe Interactions in Ground

Effect Over a Sediment Bed," American Helicopter Society 69th Annual Forum Proceedings, Phoenix, AZ, May 21–23, 2013.

7. Reel, J., "Mechanisms of Vortex-Induced Particle Transport from a Mobile Bed below a Hovering Rotor," M.S. Thesis, Dept. of Aerospace Engineering, University of Maryland, College Park, December 2013.

8. Sydney, A. and Leishman, J. G., "Time-Resolved Measurements of Rotor-Induced Particle Flows by a Hovering Rotor," *Journal of the American Helicopter Society*, Vol. 51, (2), April 2010, pp. 1–16.

9. Sydney, A. and Leishman, J. G., "Measurements of The Plume-Like Three-Dimensionality of Rotor-Induced Dust Fields," American Helicopter Society 70th Annual Forum Proceedings, Montréal, Canada, May 21–23, 2014.

10. Sydney, A., "Contributions Towards the Understanding of Rotor-Induced Dust Particle Mobilization," Ph.D. Dissertation, Dept. of Aerospace Engineering, University of Maryland, College Park, August 2014.

11. Reel, J., and Leishman, J. G., "Mechanisms of Vortex-Induced Particle Transport as it may Affect Rotorcraft Brownout," Presented at the American Helicopter Society 4th International Technical Specialists' Meeting on Vertical Lift Aircraft RDT&E, Patuxent River, Maryland, August 27–28, 2014.

Task 2.3

Fundamental Two-Phase Measurements in Brownout Fluid Mechanics

Investigator(s): Kenneth Kiger

Institution/Department: University of Maryland/Department of Mechanical Engineering

Graduate Student(s):

Rahul Mulinti (GRA, Ph.D., expected graduation: July 2014)

Kyle Corfman (GRA, M.S., expected graduation: July 2014)

Jayson Geiser (M.S., competed 12/2011, employment: NSWC Carderock, David Taylor Model Basin)

Contact email(s): kkiger@umd.edu

Background and Technical Challenges

To make progress in the prediction of particle suspension and sedimentation within coupled particle-laden flows relevant to the problem of rotorcraft brownout, detailed characterization of the micro-scale mechanics is needed within a prototypical flow that captures the essence of the rotorcraft wake/ground interactions. Detailed dynamic characterization of the local particle concentration and velocity statistics are required relative to the large-scale turbulent vortical structures that are inherent characteristics of brownout flow fields. Such measures can be used to obtain local particle flux in response to turbulent fluid stresses, while further details on the coupling can be derived from measures of the particle to fluid velocity cross-correlations. The challenges involved in obtaining this type of information are numerous: 1. Well-controlled particle characteristics are needed to generate repeatability in the experiments, as the suspension characteristics are known to be sensitive to shape, surface roughness, etc.; 2. Making reliable high-resolution simultaneous two-phase measurements requires proper phase discrimination, accurate determination of the effective detection volume and adapt to high concentration and glare near the mobile bed boundary.

Technical Approach

To achieve the goals of this task, several highly detailed experiments have been completed and are being completed in the controlled environment of a dust chamber in the presence of a prototypical flow that captures the essential features of the rotorcraft wake as it interacts with the ground. The prototypical flow consists of a forced jet impinging on a mobile sediment bed. This configuration allows for the generation of coherent vortex rings embedded within a stagnation point flow.

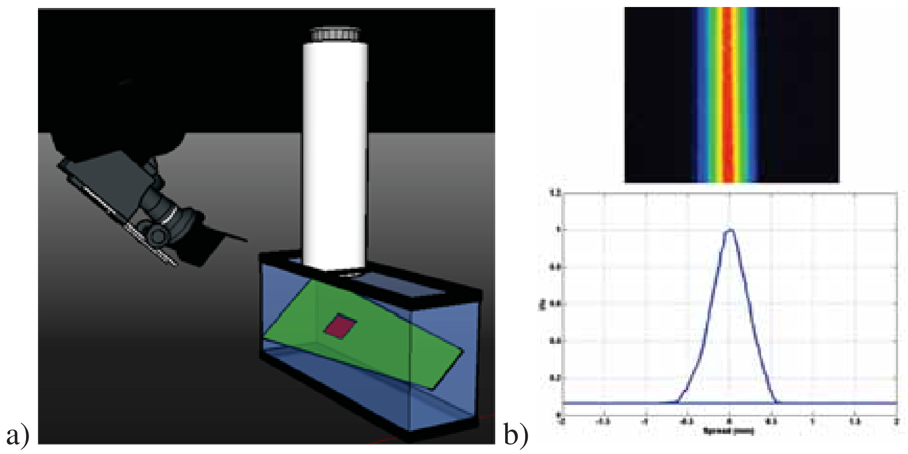

Figure 2.16: a) Schematic of test setup for particle concentration calibration, b) Measured light sheet intensity profile.

Depending on the forcing signal, single or multiple vortex structures of arbitrary strength can be generated and allowed to interact with the stagnating wall flow, providing for the same essential features of radial vortex stretching and vortex/wall interaction seen with a rotor wake. Quantitative measurements of the particle suspension and corresponding fluid velocity are conducted through a combination of high-speed imaging and two-phase PIV.

Results

Particles erosion, suspension and turbulence interaction with impinging forced jet

In-situ concentration calibration

Determination of the effective measurement volume is essential for making quantitative concentration measurements of a dispersed phase when using particle-imaging technique for two-phase flows. Transport equations for both mass and momentum require accurate estimation of particle volume fraction along with particle velocities. The effective measurement volume, while nominally determined by the local light sheet thickness, the actual value depends also on the dispersed phase identification characteristics used to detect the particles (relative brightness, size, etc.), and stray illumination such as scattering by tracer particles and wall reflections, necessitating use of local calibration techniques. A novel method is being investigated where the effective light sheet thickness is estimated using particle image correlation information of free falling dispersed-phase particles settling through a tilted light sheet along with size and brightness criteria of dispersed phase images.

Moving glass particles through air by fixed distances is challenging, so hence a different ap-

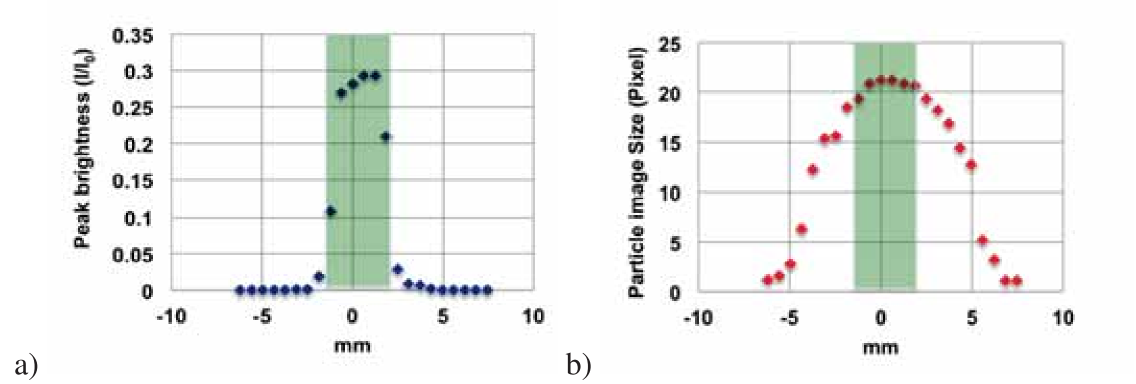

Figure 2.17: a) Particle brightness as a function of position relative to the light sheet, b) Measured particle size as a function of the position relative to the light sheet. The nominal light sheet thickness as identified by the beam profile camera is shown in green.

proach is needed to estimate measurement volume for two-phase PIV measurements in air. Tests have been conducted using a high-speed PIV imaging system working at 3000 Hz. The light sheet is tilted with respect to vertical and the camera is aligned perpendicular to the light sheet as shown in Fig. 2.16a. Glass particles of 50-micron nominal diameter are dropped into the test section from a height of about 1 m, so that they enter the test section moving at terminal velocity. To prevent external air currents influencing the particle motion, a cylindrical PVC pipe is used to shield the falling particles. The terminal velocity of these particles is estimated to be about 1.84 m/s. The estimated depth of focus is 1.2mm (105 mm lens, f#4) and the field of view is 8 cm^2. The light sheet thickness in the field of view is 1 mm, as shown in Fig. 2.16b.

These particles are imaged using a high-speed camera as they fall through the light sheet, as shown in the illustration in Fig. 2.16a. As particles move through the light sheet, their scattering characteristics and hence their size and brightness varies. Shown in Fig. 2.17a is the average peak brightness and size of several particle streaks. When the consecutive images are averaged, the particle paths appear as streaks in the average image. The average peak brightness is estimated from 35 such particle streaks from the ensemble, starting from the first instance when the particle enters the light sheet until the point where it leaves the light sheet. It is evident that the average peak brightness increases dramatically as the particles enter the measurement volume and the average size has a more gradual increase. It can be inferred that a particle image that has its peak brightness value above $0.05I_o$ (where I_o is the saturation limit for the camera) is within the effective measurement volume, which in this case turns out to be 2 mm.

For a phase resolved low-speed PIV system, it is not possible to track size and brightness of individual particles as they pass through the light sheet. In that case, a PTV correlation based

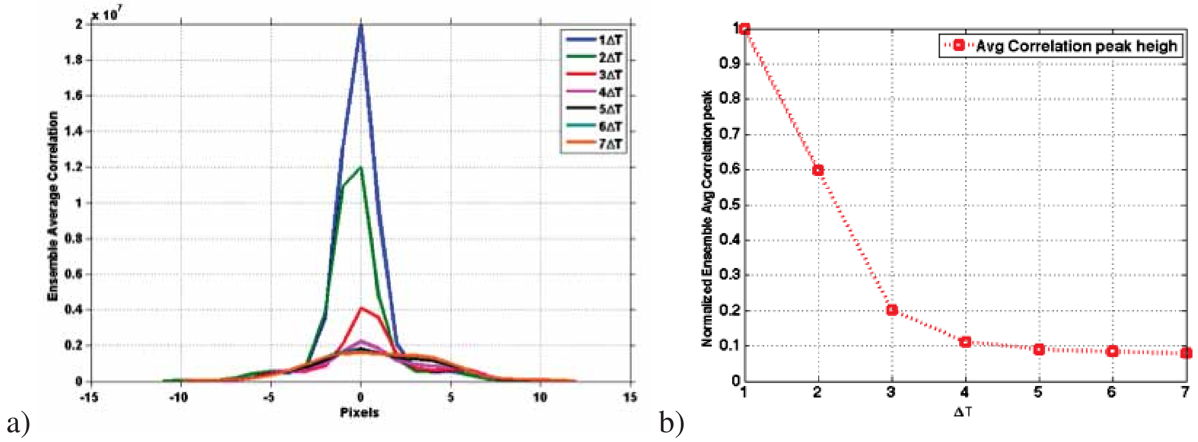

Figure 2.18: a) Average correlation shape as a function of the delay time between images ΔT, b) Decay rate of the correlation peak amplitude as a function of the delay time.

criteria has been implemented that relies on decay of the correlation peak height with increasing delay time to identify the effective measurement volume. Shown in Fig. 4a is the ensemble average correlation peak height of all identified particles from 5000 images as a function of delay time. It is evident that the peak height drops because of out of plane motion of the particles with increasing delay time. When these peaks are normalized with the maximum peak height from the lowest delay time, the decay trend can be established, as shown in Fig. 4b. The peak height drops off dramatically until 3ΔT and remains flat as the delay time is further increased. This indicates that these particles take a time of 3ΔT to traverse through the measurement volume and knowing the terminal velocity of these particles a priori, the effective light sheet thickness can be backed out, which turns out to be 1.85 mm. This is a proof of concept study and needs to be implemented for current work by matching the imaging conditions (lighting, glare from the surface, FOV and f#) from actual two-phase experiments.

Particle suspension mechanisms and particle-turbulence interaction

The strong forcing of this flow produces a coherent (periodic) structure that dominates the flow behavior. These structures rapidly erode the bed, generating specific bed forms that qualitatively alter the strength of the suspended sediment flux. The current work has been aimed at understanding the particle-turbulence coupling and net sediment transport at both the early (denoted as ”flat bed” conditions) as well as the late stages (denoted as ”eroded bed” conditions).

Given the dominance of the forced periodic vortex in these flows, it is useful to use ensemble

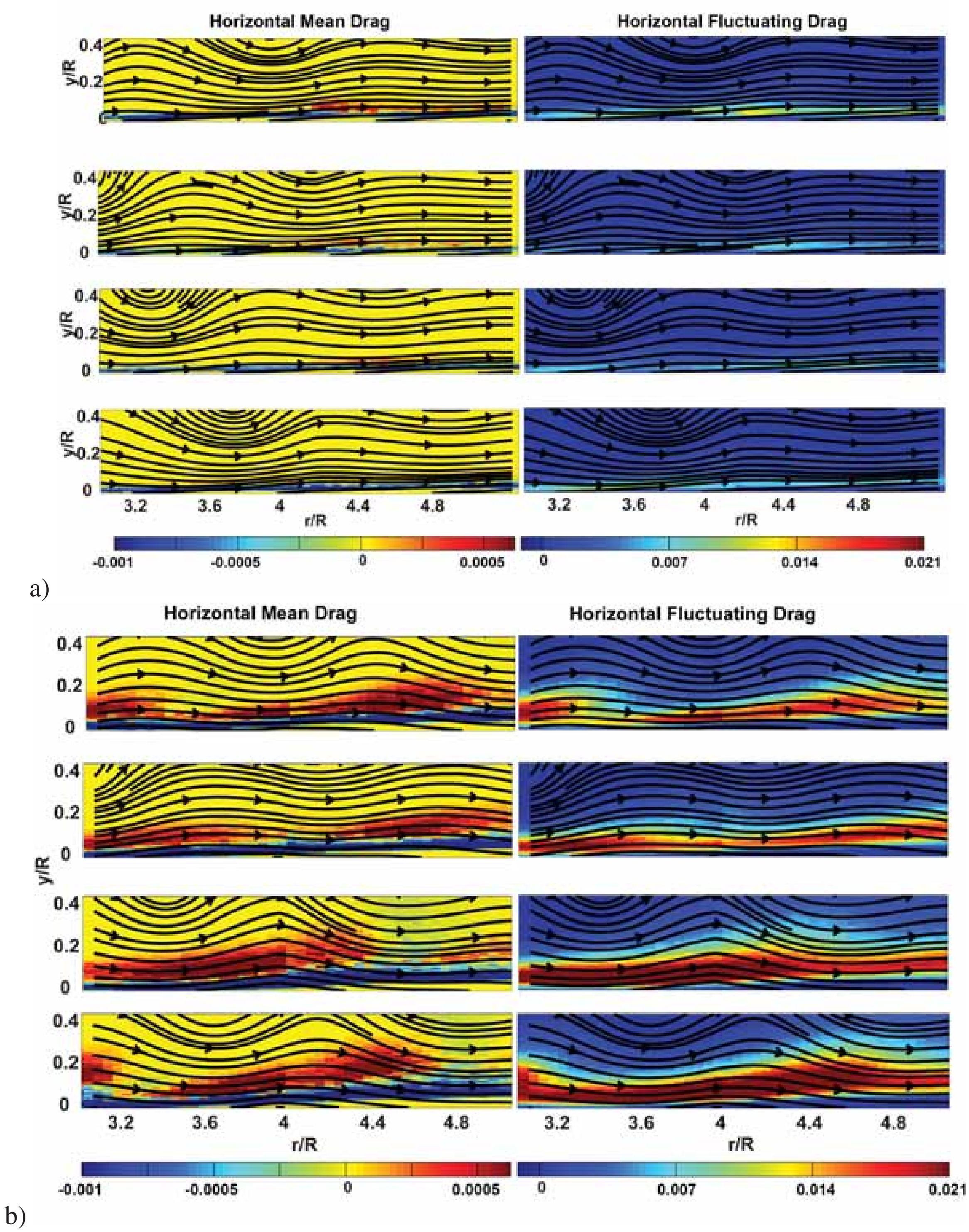

Figure 2.19: Two phase coupling horizontal drag components, $3\pi\mu D\widetilde{C}\widetilde{\Delta\mathbf{u}}$ and $3\pi\mu D\langle C'\Delta u'\rangle$ for the flat bed case (a), and the eroded bed case (b). The magnitude is normalized by the jet reference momentum flux through single measurement cell, $\rho_a U_j^2\Delta y\Delta z$.

averaging and a triple decomposition to describe the flow:

$$\theta = \bar{\theta} + \langle \theta \rangle + \theta' \tag{2.1}$$

where overbar represents the time-average, $\langle\rangle$ represent the coherent periodic fluctuations, and represents the random or stochastic fluctuations. The latter two components by definition have a zero time average. Note that a net ensemble mean value can be defined that combines the effects of the time-average and coherent fluctuation:

$$\theta = \tilde{\theta} + \theta' \qquad \text{where} \qquad \tilde{\theta} = \bar{\theta} + \langle \theta \rangle \tag{2.2}$$

Once the particles are in suspension, their interaction with the fluid can be documented by estimating the forces experienced by them. Using a point-particle drag law for dilute concentrations of particles and assuming a Stokesian drag law, the overall drag on particles in suspension is proportional to the local particle concentration and the square of slip velocity:

$$\widetilde{\mathbf{D}} = \left\langle 3\pi\mu D C \Delta\mathbf{u} \right\rangle \tag{2.3}$$

where

$$\Delta\mathbf{u} = \mathbf{u}_f - \mathbf{u}_p,$$

C is the local particle volume fraction, D is the particle diameter and μ is fluid dynamic viscosity. Expanding the right hand side of the drag equation using Reynolds decomposition into mean and fluctuating components for velocity and volume fraction will result in,

$$\widetilde{\mathbf{D}} = 3\pi u D \left[\widetilde{C}\widetilde{\Delta\mathbf{u}} + \langle C'\Delta\mathbf{u}' \rangle \right] \tag{2.4}$$

The first term in the above equation is the mean particle-fluid drag and the second term is the drag fluctuation due to variation in slip velocity. The two contributions to the horizontal drag force coupling for the flat and eroded bed conditions are highlighted in Figure 2.19, which are related to the turbulent coupling between the particle and fluid momentum.

For the flat bed conditions, the suspended load interaction terms are confined quite close to the bed surface for both the mean and fluctuating contributions to the drag (Fig. 2.19a), which is a signature of primary saltation behavior with little entrainment of particles into the outer flow. There is a small region of positive drag on the particle phase just beneath and slightly downstream of the coherent vortex structure, as particles are entering into a high-speed induced velocities by the vortex. Closer to the bed and extended along the majority of the measurement region, a layer of

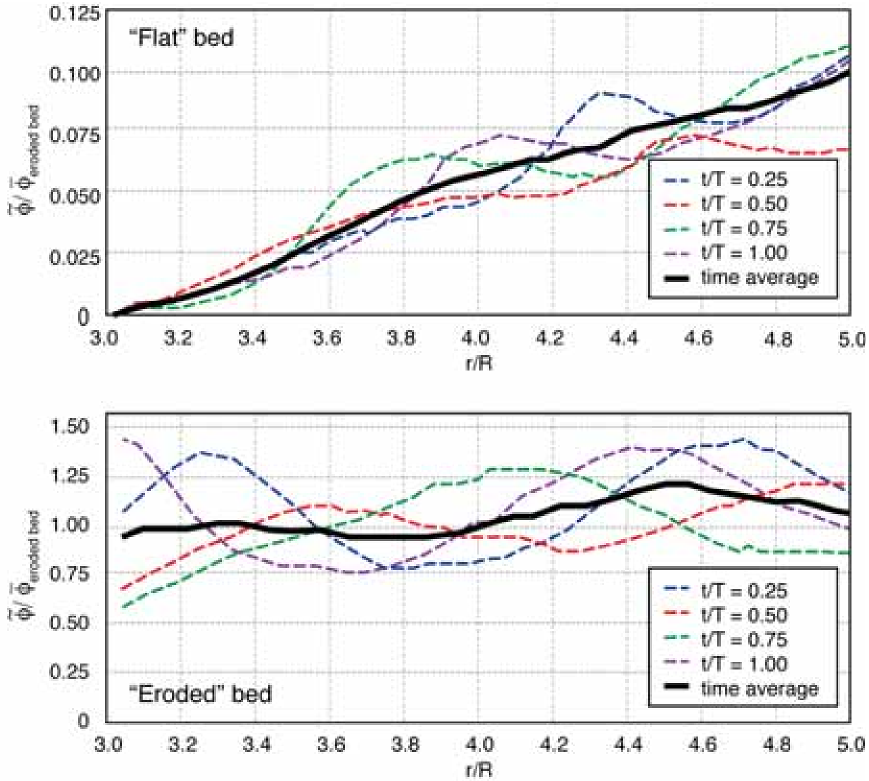

Figure 2.20: Suspended load transport for the nominally "flat" conditions (top) and "eroded bed" conditions (bottom). Plots show the

particles experiencing a negative drag can be observed. The fluctuating component is significantly larger in magnitude (approximately 20x), and also notably skewed towards positive contributions. This is likely due to the high degree of variability in the position of the vortex (jitter) at these far downstream positions caused by the non-linear interactions with the wall.

In the eroded bed case (Fig. 2.19b), the most notable difference is the degree to which the sediment is suspended away from the wall, having significant interactions at distances up to $y/R \approx 0.3$. The general structure of the coupling is similar to that observed for the flat bed (i.e. positive drag accelerating particles far from the wall, and negative drag decelerating particles near the wall), with the exception that the wave of sediment is pushed further downstream relative to the vortex center.

The suspended load flux (i.e. amount of sediment carried by convection in suspension) as a function of radial position is calculated by

$$\langle \phi(r,t) \rangle = \int_0^H \langle C(r,y,t) u_p(r,y,t) \rangle \, \Delta z dy \tag{2.5}$$

and plotted in Figure 2.20 for the nominally flat and eroded bed conditions. Although somewhat arbitrary, here it is presumed that any particle that can be tracked by the PIV code is sufficiently far

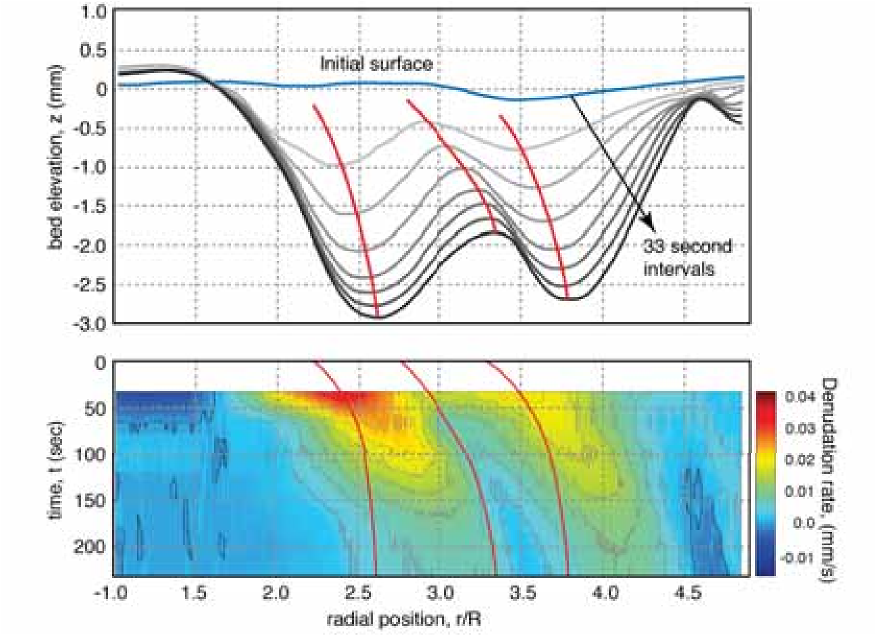

Figure 2.21: Sediment bed profile evolution (top), and map of resulting denudation rate (bottom).

from the bed that they are not undergoing collisional reputations or minor saltation events. As we will see later, there is also a significant bed load transport taking place. From Figure 2.20, it can be seen that in both cases waves of suspended sediment are pushed in advance of the passing vortex. For the flat bed case, the suspended flux is continually increasing as a function of radial distance, whereas for the eroded bed case, there is little spatial variation in the overall time average of the flow.

The erosion of the mobile bed is shown in detail for the small-particle low-speed case in Fig. 2.21. Tests were halted after a maximum scour depth of 10 mm to prevent breakthrough of the 15 mm thick bed. In general, the erosion starts just upstream of the point of closest approach of the primary vortex ($r/R = 2.0$ is the point of closest approach for the low-speed case), with a crest and second shallower trough forming downstream of the first. The wavelength of the bedform is approximately $\lambda/R = 1.2$, and varies little throughout the development of the bed profile. A third trough appears to be forming beyond the second, but with a greatly reduced depth. The reduction in depth with radial distance is to be expected due to both the reduced coherence of the primary vortex as it interacts with the ground surface (becoming highly three-dimensional and rapid dissipation), as well as due to the deceleration of the wall jet due to the axisymmetric expanding flow. Once the initial trough begins to form, scouring occurs progressively, and moves the troughs and crests downstream while keeping the lee slope profile into the first trough approximately constant.

The denudation rate is defined simply as the rate of removal of the bed surface, and is calculated locally by subtracting the difference in elevation of the bed at successive times (see Fig. 2.21). This clearly reveals two maxima in surface erosion rate located about the center of the nascent forming troughs at the earliest times ($r/R \approx 2.3$ and $r/R \approx 3.5$). Although it seems clear that the forcing by the primary vortex is responsible for the initiation of the bed forms, due to the correlation of the periodic Reynolds stress with the initial erosion maxima, it is not yet clear from the evidence we have as to what causes the second erosion maxima. It may possibly that this results from an increase in the stochastic component of the turbulent stresses caused by the breakdown and three-dimensionalization of the primary vortex, which occurs in this region. Soon after formation of the bedforms, the peak erosion rates shift to the stoss slope with similar erosion rates on both dunes, in contrast to the marked asymmetry shown between the two dunes in the initial erosion conditions. Minimal erosion (or even deposition) is evident on the lee slopes.

Finally, the net erosion rate over the measured field of view is determined by total rate of area removed, as plotted in Fig. 2.22. It can be seen that the early times ($t < 30$ seconds, corresponding to the flat bed case), the net erosion rate is comparable to or greater than what was observed under eroded bed conditions ($t \approx 80$ second). This interesting as the suspended flux in the eroded bed conditions shown in Fig. 2.20 carries approximately 10 times the amount of sediment in comparison to the flat bed conditions. This is indicative of the flat bed being dominated by bed load transport, and the role that the bed forms play in ejecting sediment into the upper regions of the flow. The second notable point in Fig. 2.22b is the fact that the sediment transport scales with the number of vortex structures that have occurred. Once scaled, the timing of the events in the erosion curves similar transient behavior, underscoring the fact that the erosion is being dominated by the vortex events.

Publications

1. Knowles, P., and Kiger, K. T., “Quantification of particle concentration in sheet illumination imaging techniques,” 62nd Annual Meeting of the American Physical Society Division of Fluid Dynamics, Minneapolis, Minnesota, November 22-24, 2009.

2. Kiger, K. T., and Knowles, P., “Quantification of dispersed phase concentration using light sheet-based imaging methods,“ The 15th International Symposium on Applications of Laser Techniques to Fluid Mechanics, Lisbon, Portugal, July 5–8, 2010.

3. Mulinti, R., and Kiger, K.T., “Two-phase PIV measurements of particle suspension in a

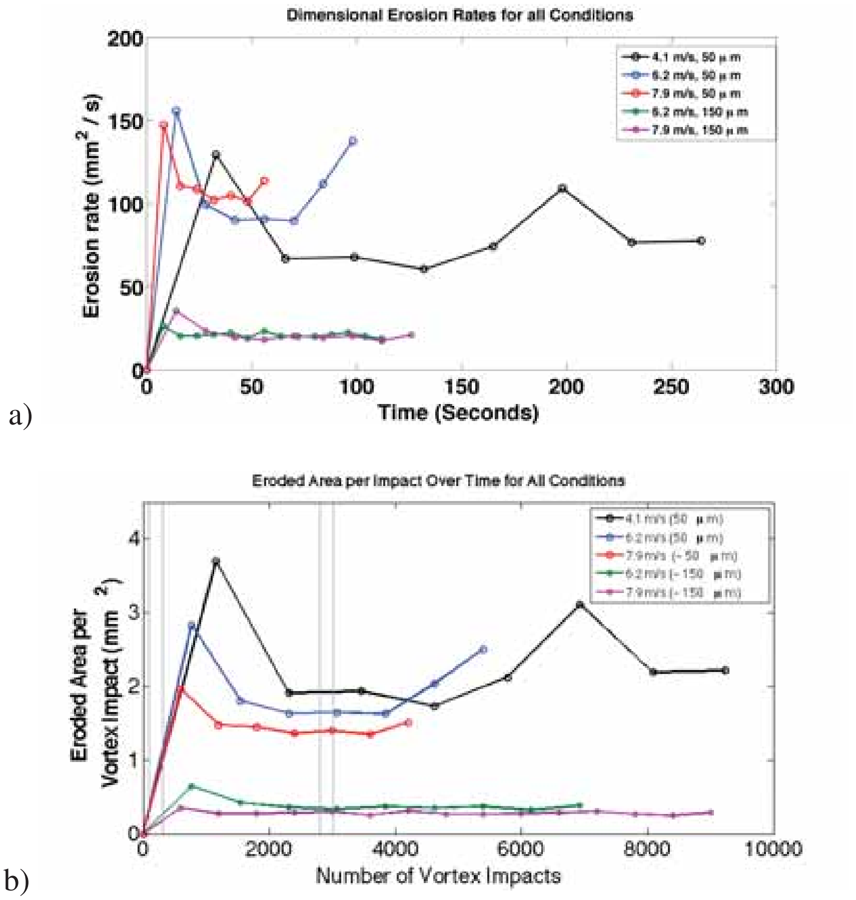

Figure 2.22: a) Dimensional erosion rates, b) Erosion depth per vortex impact.

forced impinging jet," 63rd Annual Meeting of the American Physical Society Division of Fluid Dynamics, Long Beach, California, November 21–23, 2010.

4. Geiser, J., and Kiger, K.T., "A simplified analog for a rotorcraft-in-ground-effect flow using a forced impinging jet," 63rd Annual Meeting of the American Physical Society Division of Fluid Dynamics, Long Beach, California, November 21–23, 2010.

5. Geiser, J., and Kiger, K. T., "Effects of Ground Plane Topology on Vortex-Ground Interactions in a Forced Impinging Jet," 64th Annual Meeting of the American Physical Society Division of Fluid Dynamics, Baltimore, MD, November 20–22, 2011.

6. Mulinti, R. and Kiger, K. T., "PTV Implementation on Two-Phase Flow in a Forced Impinging Jet," 64th Annual Meeting of the American Physical Society Division of Fluid Dynamics, Baltimore, Maryland, November 20–22, 2011.

7. Kiger, K. T., and Geiser, J., "Vortex ring breakdown induced by topographic forcing," 13th

European Turbulence Conference, Warsaw, Poland, September 12–15, 2011 *J. Phys.: Conf. Ser.* 318 062013. DOI:10.1088/1742-6596/318/6/062013

8. Mulinti, R., and Kiger, K. T., “Particle Suspension by a Forced Jet Impinging on a Mobile Sediment Bed,” 16th International Symposium on Applications of Laser Techniques to Fluid Mechanics, Lisbon, Portugal, July 9–12, 2012.

9. Knowles, P. L., and Kiger, K. T., “Quantification of Dispersed Phase Concentration Using Light Sheet Imaging Methods,” *Experiments in Fluids*, 52, (3), pp. 697–708, 2012, DOI: 10.1007/s00348-011-1100-8

10. Mulinti R., Corfman K., and Kiger K. T., “In Situ Calibration of Volume Concentration Measurements using PTV Correlation for Particle-Laden Flows,” 65th Annual Meeting of the American Physical Society Division of Fluid Dynamics, San Diego, California, November 18–20, 2012.

11. Mulinti R., Corfman K., and Kiger K. T., “Particle-Turbulence Interaction of Suspended Load by Forced Impinging Jet on a Mobile Sediment Bed,” 66th Annual Meeting of the American Physical Society Division of Fluid Dynamics, Pittsburgh, Pennsylvania, November 24–26, 2013.

12. Corfman K., Mulinti R., and Kiger K. T, “Erosion and Transport of Particulates by Forced Jet Impinging Jet on a Mobile Sediment Bed,” 66th Annual Meeting of the American Physical Society Division of Fluid Dynamics, Pittsburgh, Pennsylvania, November 24–26, 2013.

13. Kiger K. T., Corfman K., and Mulinti R., “Effect of Bed Form Evolution on Sediment Erosion and Suspended Load Transport in an Impinging Jet,” 17th International Symposium on Applications of Laser Techniques to Fluid Mechanics, Lisbon, Portugal, July 7–10, 2014.

Task 2.4

Large-Eddy Simulation of the Interaction Between Wake Vortices and Ground

Investigator(s): Ugo Piomelli

Institution/Department: Queens University, Dept. of Mechanical and Materials Engineering

Contact email(s): ugo@me.queensu.ca

This task was part of the original MURI proposal, and similar work is currently being performed under separate AFOSR funding by Professor Piomelli at Queens University in Canada. Further information on this work can be obtained directly from Professor Piomelli.

Task 2.5

Two-Phase Large Eddy Simulation Using the Mesoscopic Eulerian Formalism

Investigator(s): Kyle Squires

Institution/Department: Arizona State University, Mechanical and Aerospace Engineering

Graduate Student(s): Dennis Dunn

Contact email(s): squires@asu.edu

Background and Technical Challenges

The brownout problem encompasses multiple scales, from the largest, comparable to the dimensions of the rotorcraft, to the smallest, comparable to the sediment particle size. This extended range leads to complex effects that influence the processes of entrainment, deposition, and resuspension of the dispersed sediment. Once suspended, sediment particle interactions occur with the coherent wake vortices characterizing the rotor flow, and with the finer scale turbulence generated near the ground as it interacts with the sediment bed. Factors that influence transport characteristics of the resulting two-phase flow include particle-turbulence interactions, particle-particle interactions, particle interactions with the bed (e.g., entrainment, suspension, deposition), and a momentum coupling that modifies the carrier flow.

In general, the primary technical challenges can be sub-divided into those residing at the microscale (essentially the scale of a single particle) and the mesoscale (essentially the scale comprised of a large ensemble of particles with dimensions, for example, comparable to the characteristic boundary layer thickness of the two-phase flow). Specific technical challenges include simulation or measurement of the detailed processes of particle lift-off from a sediment bed, the role of turbulence influencing dispersed-phase transport, particle-particle interactions, and the influence of particle momentum exchange on properties of the carrier phase turbulent flow.

Modeling the transport of a second phase of small, dispersed particles within a carrier-gas-phase fluid flow has been successfully simulated in this MURI task by using Eulerian-Lagrangian approaches in which Discrete Particle Simulation (DPS) is used to compute properties of the particle phase. Eulerian-Lagrangian approaches have been, and will remain, an invaluable tool though are often constrained to flows with very small volume fractions and low mass loadings. Additionally, Lagrangian particle tracking approaches become more demanding in terms of inter-processor communication and load balancing for non-uniformly distributed particle concentrations and can be very challenging to model large particle ensembles. Eulerian-based methods overcome these challenges and present a more straightforward implementation on a solution space that is divided among parallel CPU's.

The above considerations provide the main motivation for the development of "two-fluid" Eulerian-Eulerian methods in which the dispersed phase is modeled as a second fluid. These approaches provide a sound framework for modeling flows with large particle concentrations and a range of complex interactions, e.g., particle collisions, breakup, coalescence, etc. Eulerian-based approaches also present computational simplifications in that the same basic framework for solution of the field-based equations can be applied as used to model fluid motion and overcome inter-processor communication and load balancing problems that can arise for non-uniformly distributed particle concentrations. Finally, Eulerian-based approaches provide a pathway to true, two-fluid Large Eddy Simulation of multiphase flows. The approach that has been implemented and tested for Eulerian-based predictions of the rotor-vortex boundary layer is based on Conditional Quadrature-Based Method of Moments (CQMOM). This latter method is being used to model dispersed phase transport and particle interactions and is being assessed against Lagrangian-based modeling strategies that have been successfully implemented in earlier phases of this task.

Technical Approach

The starting point for Eulerian-based approaches is introducing a probability density function (PDF), f, that describes the probability of finding a particle at time t and position x possessing velocity v, diameter d, temperature T, etc. These properties are parameters of the PDF, $f(t,x,v,d,T,...)$, where t and x are independent variables and the remaining variables $\{v,d,T,...\}$ define internal state space coordinates. This approach, in turn, corresponds in practical computations to cell-localized quantities representing the likelihood of a specific coordinate set (e.g., $\{v_0,d_0,T_0,...\}$) existing in that cell. For finite-inertia particles whose resistance to the external flow is characterized by the Stokes number, St, the individual particles in the ensemble may cross paths and exhibit diverse velocities. Consequently, the values of the internal variable set (e.g., velocity, diameter, and temperature) at a given point in space can assume more than one value, again owing to the fact that particles possessing different velocities, diameters, or temperatures can occupy the same cell over which averages are computed. It is thus important for modeling particle-laden flows to account for multi-valued solutions. This goal is accomplished in the context of the PDF by introducing the transport equation for f that for a mono-disperse, isothermal flow (d and T are constant) is a specific version of the Boltzmann Equation, i.e.,

$$\frac{\partial f}{\partial t} + v\frac{\partial f}{\partial x} + \frac{\partial}{\partial v}\cdot(\dot{v}f) = C \tag{2.6}$$

where C is a collision source term and $\dot{v}$ is particle acceleration (dictated by the drag force in work performed to date). The above approach is general in that the Navier–Stokes equations for continuous fluids are also derived from Eq. 2.6. In cases where particle trajectories must be allowed to cross, as occurs in flows with finite-inertia particles that do not follow the fluid streamlines, the assumption that at a given location in space the particle velocity $v(t,x)$ is single-valued is not made.

For practical simulation strategies, it is not feasible to directly solve Eq. 2.6 and instead alternative equations are derived by taking moments of Eq. 2.6, leading to transport equations of the same form as those obtained for continuous fluids governing conservation of mass, momentum, energy, etc. Without loss of generality, the moments of f may be expressed in the following manner

$$M^{\gamma}_{i,j,k}(t,x) = \int v_1^i v_2^j v_3^k f(t,x,v)dv \tag{2.7}$$

where i,j,k are the chosen integer exponents used to skew the PDF integration by the internal particle velocity variables $v \equiv \{v_1, v_2, v_3\}$, and $\gamma \equiv i+j+k$ is the sum of the exponents that simply indicates the order of the moment. This skewed integration of the PDF relies on carefully chosen integer values (≥ 0) for the exponents i,j,k that produce the optimal set of moments. Applying this moment transformation to the PDF transport in Eq. 2.6, produces a general set of integro-differential equations, i.e.,

$$\underset{\text{Unsteady}}{\frac{\partial}{\partial t}M^{\gamma}} + \underset{\text{Convective}}{\nabla_x \cdot M^{\gamma+1}} = \underset{\text{Acceleration}}{i*\dot{v}\cdot M^{\gamma-1}} + \underset{\text{Source}}{\mathbb{C}} \tag{2.8}$$

where the operation $i*\dot{v} \equiv \{i\dot{v}_1, j\dot{v}_2, k\dot{v}_3\}$. For clarity, the equation set described by Eq. 2.8 shows only the order of the moment γ with the subscripts removed. The acceleration term is a source term that arises from drag, gravity, or other body forces and involves moments of order $\gamma-1$, while the convective term always involves moments of order $\gamma+1$. Equations 2.6 through 2.8 are exact representations, but to close the higher order convective moments ($\gamma+1$). A Gaussian quadrature approximation is applied to Eq. 2.7, i.e.,

$$M^{\gamma}_{i,j,k}(t,x) \approx \sum_{\alpha=1}^{\beta} U_{\alpha}^{i} V_{\alpha}^{j} W_{\alpha}^{k} \phi_{\alpha}(x,t) \qquad \gamma = 0,1,2,... \tag{2.9}$$

where β is the total number of discrete nodes allocated to approximate the function f as a sum of Dirac Delta functions. A single “node” describes a complete set of abscissas and associated weight:

$\{U, V, W, \phi\}$. The $D = 3$ variables U, V, W are the three-dimensional particle velocity abscissas and ϕ the associated weight for the α'th quadrature node. In total, this requires $K = \beta^D \cdot (D + 1)$ total moment equations to provide closure for the set of abscissas and weights in CQMOM.

By this method, f is reduced to a β-valued model in which up to β distinct instances of the nodes may be present in any cell. The Gaussian quadrature approximates the area under f such that the moment set retains information for a multi-valued solution. Numerically solving these moment equations is challenging, but can also be extremely effective and useful, even using the approximation of $\beta = 2$ employed in the present model. It should be noted that for Eulerian models that employ a single-valued assumption, such as the Navier–Stokes equations, only one realization of each internal velocity variable ($\beta = 1$) would be stored at every grid point, consistent with the fact that the ability to account for particle trajectory crossing is not required.

Together, the moment set M and nodes $\{U, V, W, \phi\}$ transport the necessary quantities for modeling the flow while offering the ability to impose boundary conditions and/or body forces in a physically feasible manner. This particular version of the CQMOM model was proposed by Yuan and Fox[*] and is employed in the present effort because it offers the ability to represent a three-dimensional multi-valued velocity field for a dispersed Eulerian phase, and it has yielded promising results for monodisperse particle phase distributions in turbulent flows.

Results

The CQMOM model has been incorporated into the DNS fluid solver that has been employed for Lagrangian/DPS studies previously during this MURI task. In total, two phases are being modeled: gas-phase carrier flow, and the dispersed particle phase is being modeled in two different ways. Lagrangian particles are modeled using DPS, and an Eulerian treatment of the particle phase is modeled using CQMOM (referred to as "Eulerian particles" below). For comparative purposes, the two particle phases run concurrently and do not interact with one another, and with one-way coupling to the fluid that in turn ensures each particle treatment experiences the same forcing from the fluid. The Stokes number and inter-collision states (enabled/disabled) are identical between the Eulerian and Lagrangian particle simulations to enable side-by-side comparisons. The following figures may compare all three models as appropriate. Additionally, instantaneous snapshots and time-averaged statistics are available for selected 2-D planes within the computational domain.

---

[*] Fox, R. O. "Higher-order Quadrature-based Moment Methods for Kinetic Equations," *Journal of Computational Physics*, 228, No. 20, 2009, pp. 7771–7791; Yuan, C. and Fox, R. O., "Conditional Quadrature Method of Moments for Kinetic Equations," *Journal of Computational Physics*, Vol. 230, No. 22, 2011, pp. 8216–8246.

(a) Carrier-fluid

(b) Eulerian particles

(c) Lagrangian particles

Figure 2.23: Instantaneous streamwise velocity at half-span, *St*=4, without inter-particle collisions.

The spanwise *z* direction of the computational domain is periodic, while the upper *y* boundary employs a Neumann boundary condition, and the lower *y* boundary acts as a reflective wall. The streamwise inlet *x* direction maintains a fixed weight distribution and the outlet *x* direction also uses Neumann boundary conditions.

Two separate cases are considered. The first uses the turbulent boundary layer (TBL) carrier-flow field (without coherent vortices that impinge into the boundary layer) to drive the lighter particles ($St = 4$) while neglecting inter-particle collisions. Figure 2.23 shows an instantaneous snapshot over about 25% of the extent of the streamwise domain for the fluid flow boundary layer and both models of the particle phases, both at the same instant in time. The shear from the no-slip condition on the wall creates complex vortical structures in the boundary layer even without coherent vortices impinging onto the flow. The results in the figure shows that the lighter particles follow the fluid flow field fairly closely with the largest velocity discrepancies occurring in regions of rapid change (large velocity gradients) or small localized perturbations, owing to the inertia-induced particle lag. Importantly, the figure also shows good, qualitative agreement between the Lagrangian and Eulerian models of the particle motion, in turn providing a key validation of the Eulerian-based approach for predicting the dispersed phase properties.

Unlike the streamwise velocity, both the wall-normal and spanwise velocities (v_2 and v_3, respectively) possess zero (for v_3) or nearly zero (for v_2) long time-averages and deviations from the fluid flow will be more apparent, as shown in Fig. 2.24. Both the Lagrangian and Eulerian particle treatments exhibit large regions of correlated motion that is driven by the interaction of the particles with the motion of the fluid flow. The particle velocity magnitudes shown in Figs. 2.24b and 2.24c are about half as large as those in the fluid shown in Fig. 2.24a, though again exhibit very

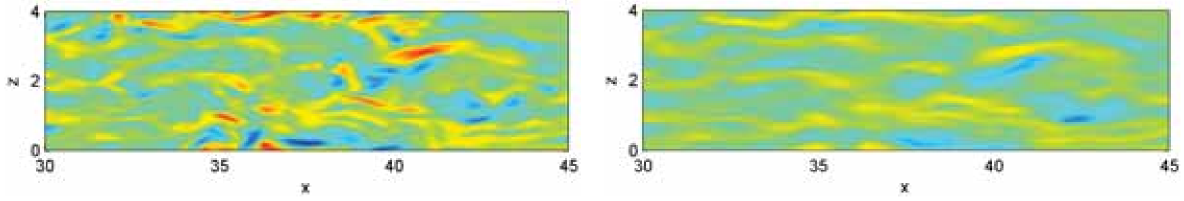

(a) Carrier-fluid

(b) Eulerian particles

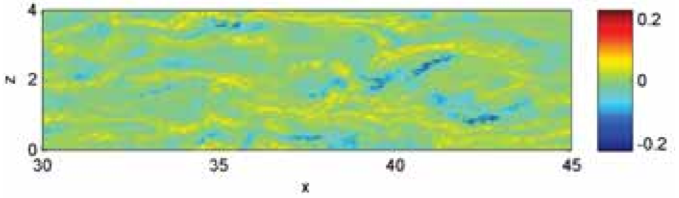

(c) Lagrangian particles

Figure 2.24: Instantaneous wall-normal velocity in a wall-parallel plane at $y \approx 0.31$, $St = 4$, without inter-particle collisions.

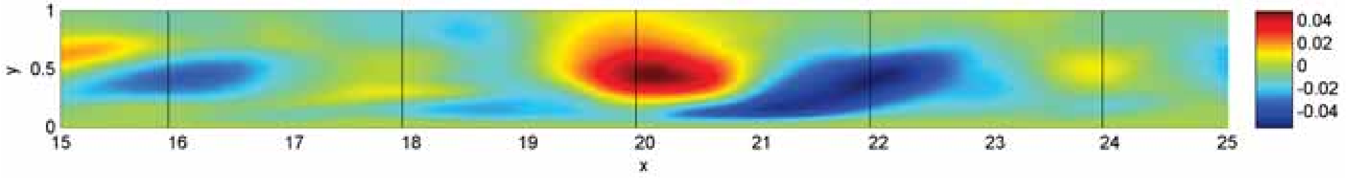

(a) Contours of wall-normal fluid velocity, indicating locations of the velocity profiles.

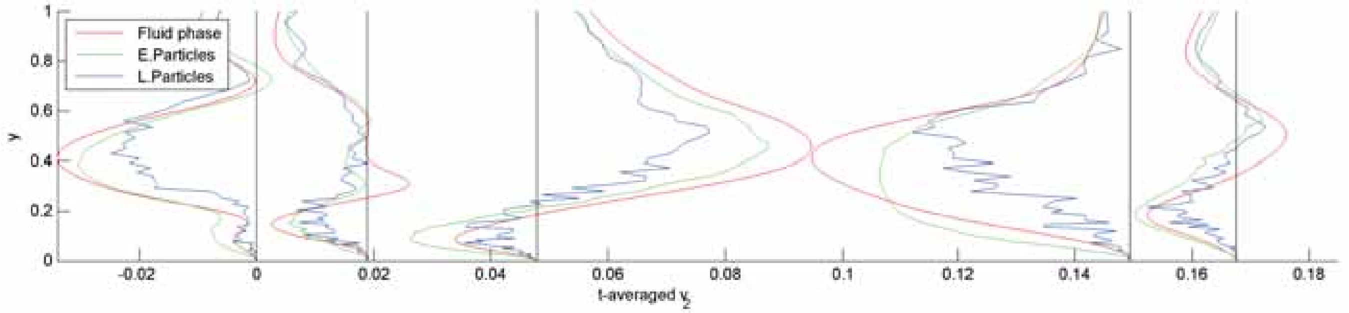

(b) Profiles of the wall-normal v_2 mean velocity.

Figure 2.25: Time-averaged wall-normal velocity at half-span, St=4, without inter-particle collisions.

similar structure. Although the particles, in general, follow the fluid, the important validation of CQMOM is realized because the two particle models are in good qualitative agreement with one another.

The final figure for the TBL case in Fig. 2.25b shows time-averaged wall-normal velocities using line plots for comparison. The plane lies at the half-span and has accumulated statistics that enable some assessment of the two models. The results show that CQMOM generally predicts

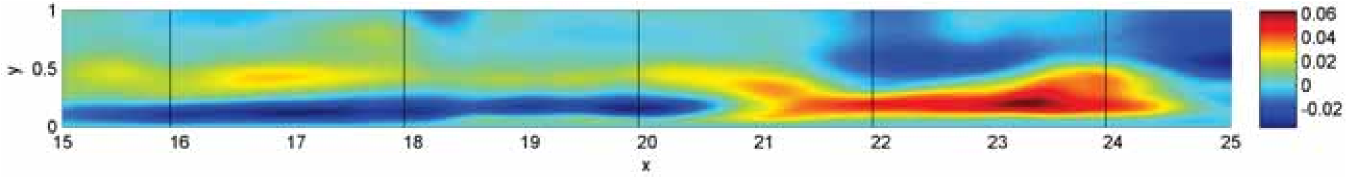

(a) Contours of wall-normal fluid velocity, indicating locations of the velocity profiles.

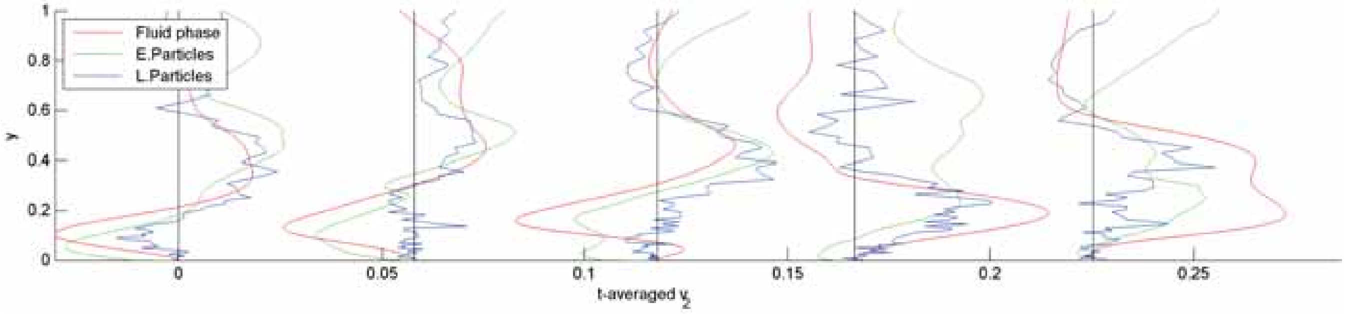

(b) Profiles of the wall-normal v_2 mean velocity.

Figure 2.26: Time-averaged wall-normal velocity at half-span, $St = 16$, with inter-particle collisions.

larger magnitudes than DPS, though this outcome is an artifact of the relatively short statistical sample currently available. In sparsely-populated regions where cells are frequently devoid of Lagrangian particles, the DPS solution will yield lower averages, which also contributes to the much nosier profiles shown in the figure. In denser regions there is better agreement between the CQMOM and DPS models. Additionally, the Eulerian particle velocities are generally different in magnitude than the fluid owing to their inertia.

The second case with larger-inertia particles, $St = 16$, differs from the first in many aspects: a time-periodic vortex impinges into the boundary layer near $x \approx 20$ and with a larger Stokes number that results in greater particle trajectory crossing, and an inter-particle collision model is employed. For these larger inertia particles the fluid and particle velocities can deviate significantly. Similar time-averaged statistical measures are shown in Fig. 2.26b, sampled over 3.85 time units, and show general qualitative agreement between CQMOM and DPS, though with the larger Stokes number the particles do not always conform as closely to the fluid velocities.

The Lagrangian particles are initially randomly seeded throughout the domain, which impacts the current averages sampled over a relatively short period because the cells devoid of particles artificially lower the average. For instantaneous velocities and densities, the DPS model sometimes has difficulty describing the larger-scale structures where an insufficient quantity of particles results in empty cells that are given zero velocity in the initialization. This issue can cause La-

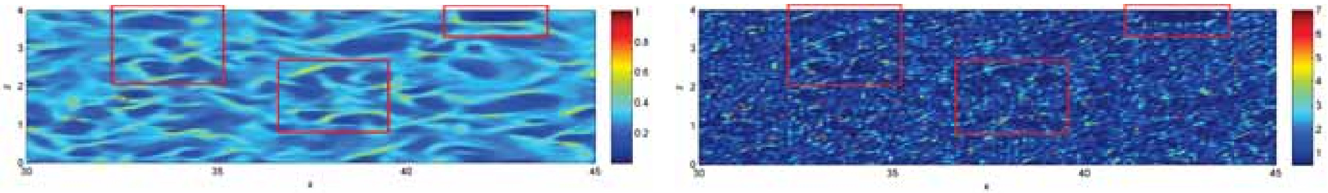

(a) Eulerian density M^0 (b) Lagrangian particles per cell.

Figure 2.27: Instantaneous particle density in a wall-parallel plane ($y \approx 0.31$), *St*=16, including inter-particle collisions.

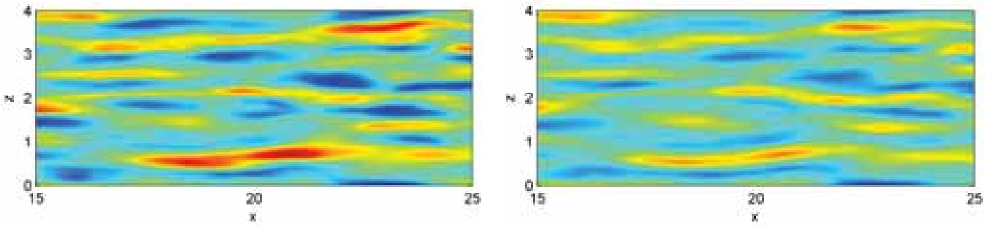

(a) Fluid field (b) Eulerian particle field

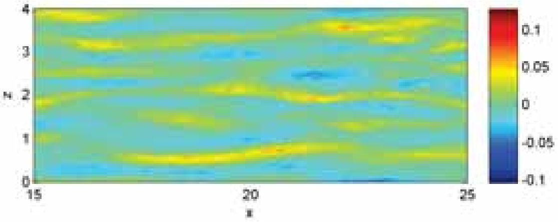

(c) Lagrangian particle field

Figure 2.28: Time-averaged wall-normal velocity v_2 in a wall-parallel plane ($y \approx 0.31$), *St*=16, including inter-particle collisions.

grangian time-averages to require more samples than may be necessary than the Eulerian counterpart. The CQMOM model tracks a density quantity M^0 that was seeded more uniformly no larger than an initial value of 0.3 for ease of implementation and an initial assessment of the model.

The dispersion and accumulation of particles through interaction with the turbulent carrier flow quickly leads to sparse regions with $M^0 \approx 0$ and higher concentration regions where $M^0 \approx 1$ or more, showing that the concentrations may achieve at least three times their initial values. Comparisons can be made between the density fields of the two particle models (the incompressible fluid field is omitted), as shown in Fig. 2.27. The Lagrangian density, on the other hand, is measured in “particles per bin” and yields very similar structures for the particle densities, which are discernible upon careful inspection of Figs. 2.27a and 2.27b. Selected regions are highlighted to showcase the similarity of the structures, which provides an important and powerful validation of the CQMOM model.

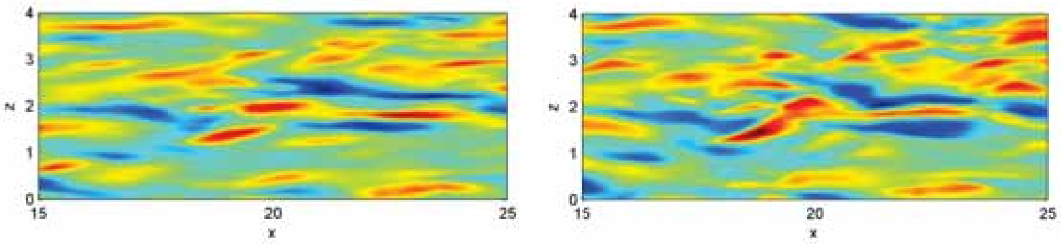

(a) Fluid field (b) Eulerian particle field

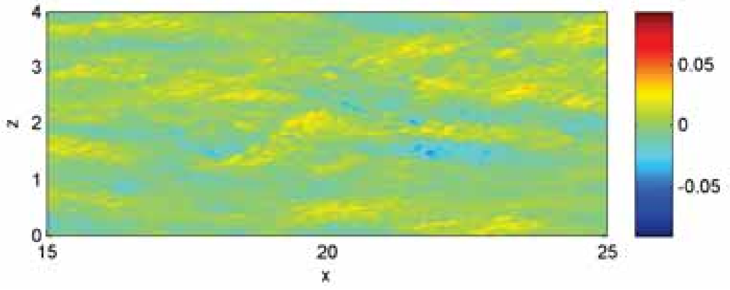

(c) Lagrangian particle field

Figure 2.29: Time-averaged spanwise velocity v_3 in wall-parallel plane ($y \approx 0.0232$), $St = 16$, with inter-particle collisions.

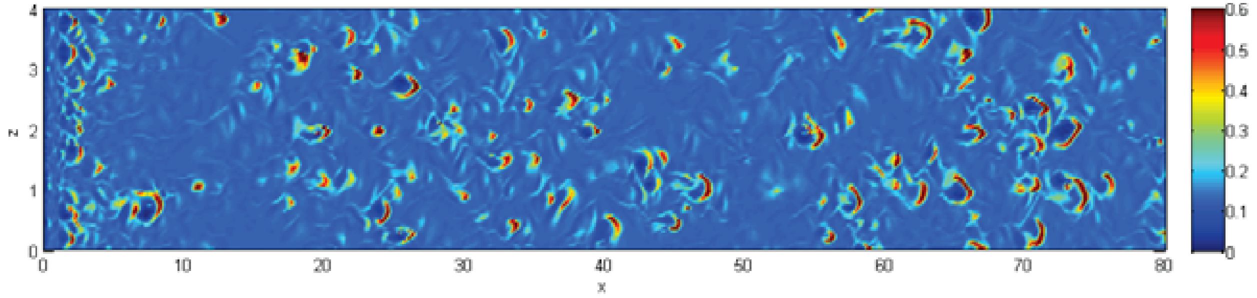

Figure 2.30: Instantaneous particle density in a wall-parallel plane ($y \approx 0.0232$), $St = 16$, with inter-particle collisions.

Good agreement is observed between the two particle models in most cases. Small discrepancies may appear in the results showing instantaneous quantities where the DPS method lacks sufficiently large sample sizes in some bins, giving statistical outliers more weight. CQMOM is essentially showing a statistical representation of an arbitrarily large quantity of pseudo-particles averages as a continuous medium. The wall-normal particle velocities are very similar, showing similar structures in Fig. 2.28b, even with the sparse Lagrangian particle concentrations in Fig. 2.28c, showing smaller values overall.

Figure 2.29 similarly shows the spanwise velocity field near the wall, and shows that CQMOM predicts slightly greater velocity magnitudes than occur in the fluid, though maintains good qualitative agreement with the structural features in the flow between Figs. 2.29b and 2.29c. For both the wall-normal and spanwise velocities of Figs. 2.28 and 2.29, respectively, CQMOM predictions in (b) show larger magnitudes but also show structures more correlated to that of the Lagrangian particles (c) than to that of the fluid flow (a).

Figure 2.30 shows a view of the instantaneous particle density over the entire x-z domain near the wall ($y \approx 0.0232$) where the initial seeding was $M^0 \approx 0.15$. These results were previously not realizable using DPS due to an insufficient number of particles in that region. The near wall plane shown in Fig. 2.30 shows interesting "horseshoe" structure formations in the density field.

Publications

1. F. Morales, I. Iftekhar, K. D. Squires, and U. Piomelli, "Euler-Lagrange Simulations of Particle Interactions with Coherent Vortices in Turbulent Boundary Layers," Bulletin of the American Physical Society, vol. 54 (19), p. 319, 2009.

2. F. Morales, I. Iftekhar, K. D. Squires, and U. Piomelli, "Euler-Lagrange Simulations of Particle Interactions with Coherent Vortices in Turbulent Boundary Layers," Presented at the 62nd Meeting of the American Physical Society, Division of Fluid Dynamics, November, 2009.

3. F. Morales, I. Naqavi, K. D. Squires, and U. Piomelli, "Coherent Vortex Interaction with a Particle-Laden Boundary Layer," Bulletin of the American Physical Society, Vol. 55, (16), p. 197, 2010.

4. F. Morales, I. Naqavi, K. D. Squires, and U. Piomelli, "Coherent Vortex Interaction with a Particle-Laden Boundary Layer," Presented at the 63rd Meeting of the American Physical Society, Division of Fluid Dynamics, November 2010.

5. F. Morales, and K. D. Squires, "Simulation of Rotor Vortex Interactions with a Particle-Laden Turbulent Boundary Layer," AIAA Paper 2011-4041, 2011.

6. K. D. Squires, and F. Morales, "Rotor Vortex Interactions with a Particle-Laden Turbulent Boundary Layer," Presented at the AIAA Honolulu Meeting, 2011.

Task 2.6

Effects of Model Scaling on Sediment Transport

Investigator(s): Anya Jones

Institution/Department: University of Maryland/Department of Aerospace Engineering

Graduate Student(s): Gino Perrotta, Mark Glucksman-Glaser

Contact email(s): arjones@umd.edu

Background and Technical Challenges

Several experiments have been conducted to study rotor aerodynamics in ground effect and the particle phase transport dynamics that underly the problem of rotorcraft brownout (e.g., Tasks 1.1 and 2.3). Because full-scale rotor experiments are impractical, the research has relied on laboratory-scale experiments in a controlled environment to investigate the various phenomena. However, although the bulk of the ongoing work currently relies on small scale experiments, the effects of scaling on the aerodynamics (carrier phase) and particle transport (dispersed phase) in a complex and tightly-coupled dual-phase flow such as brownout are not yet understood.

The brownout problem requires that both the aerodynamics and the sediment transport be scaled together, and so the many dimensionless similarity parameters associated with both the aerodynamics and the sediment must be matched simultaneously to obtain a truly scaled dual-phase flow. Because this requirement is nearly impossible to meet, a sensitivity study can be used to gain confidence that laboratory-scale experimental results are applicable to the full-scale rotorcraft brownout problem. The focus of this task is to identify aerodynamic and sediment transport similarity parameters that can be used to relate laboratory-scale studies of rotor-induced sediment mobilization and uplift to full scale brownout events. The classical aerodynamic and sediment transport similarity parameters have been evaluated, and the sensitivity of the dual-phase flow observed in the laboratory to these parameters has been assessed. The current experiments are being performed in water rather than air to allow for a broad parameter space for sensitivity studies by increasing the viscosity of the fluid and so changing the the time and length scales of the flow.

The primary objectives of this task are: 1. To determine which, if any, of the classical aerodynamic and sediment transport similarity parameters best characterize the scaling of brownout; 2. To identify new scaling parameters; 3. To evaluate the sensitivity of brownout (severity, sediment uplift/transport mechanisms, sediment dispersion/suspension, etc.) to scaling over a wide range of model scales.

Technical Approach

Experiments have been performed on a single-bladed rotor (thrust-matched to previous experiments in air performed under Task 2.2) operating in ground effect above a sediment bed in a water tank of dimensions $1.2 \times 1.2 \times 1.2\,\mathrm{m}$. Several types of sediment particles were used to provide a wide range of scaling parameter values. The experiments have made use of particle image velocimetry (PIV) to quantify the carrier flow as well as the quantity, location and trajectory of the sediment particles. The specific goals were: 1. Quantify the behavior the carrier phase using time-resolved PIV measurements of the rotor wake to evaluate the relationship between unsteady flow phenomena (e.g., a vortex passing over the sediment bed) and sediment uplift and/or transport. 2. Assess the relationship between sediment uplift in a scaled brownout flow environment to classical aerodynamic and sediment transport scaling parameters. 3. Investigate and evaluate new potential scaling parameters for the dual-phase flow produced by a rotor that is operating in ground effect over a mobile sediment bed.

Results

The wake generated by a rotor in ground effect is highly unsteady and cannot be adequately characterized near the ground by a time-averaged flow field. Figure 31(a) shows a time-averaged velocity field in the region where the rotor wake impinges on the ground. Figure 31(b) shows an instantaneous velocity field of the same region in which cross-sectional elements of the helical tip vortex can be seen impinging on the ground plane and producing large velocity transients. Previous experiments in air (Task 2.2) have suggested that the unsteady local disturbances caused by the passage of these vortices initiates the sediment uplift cycle. This latter finding has been supported by flow visualization experiments in water that have been conducted under the current task. Sediment uplift has been observed primarily just below and ahead of a vortex.

One research challenge is that of characterizing the unsteady features of the rotor wake. To enable comparisons between different cases and different studies, the wake characteristics were summarized in a concise set of scalar quantities, the primary flow feature of which is the rotor tip vortex, which can be described by three quantities: the total circulation contained in the rotating flow, Γ_v, the maximum tangential flow velocity around the vortex center, $V_{\theta\,\mathrm{max}}$, and the vortex core radius, r_c. Given a model for the variation in tangential velocity along the vortex radius, any one of the three parameters can be found in terms of the other two.

A vortex tracking program was developed and used to identify the locations of the vortices in

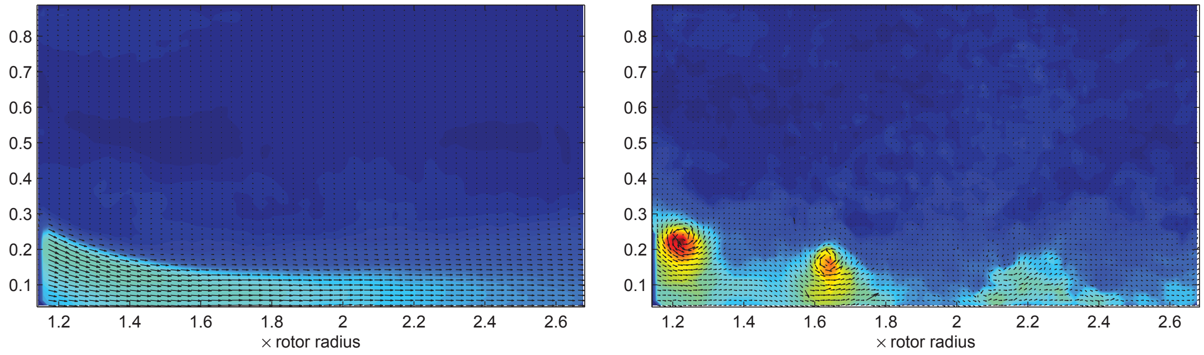

(a) Time-averaged flow field (20 revolutions)

(b) Instantaneous flow field

Figure 2.31: Contours of magnitude of total velocity and velocity vectors for a rotor wake impinging on a ground plane. 85 mm radius rotor hovering at 300 rpm. Rotor is one radius above ground and the field of view is approximately 1–2 radii from axis of rotation and approximately 1 radius from the ground plane.

each flow field. Each of the identified vortices in each image was then measured in terms of $V_{\theta max}$, Γ_v, and r_c. This was accomplished by fitting the Lamb–Oseen vortex profile to a scatter plot of the local tangential velocities compared to radial distance from the vortex center. The best fit of this model to the data provided a repeatable quantification of the size and strength of each vortex flow, which in turn allows for quantification of the flow field in terms of unsteady characteristics.

When compared to the rotor speed, two of the mean vortex parameters, $V_{\theta \max}$ and Γ_v, form nearly linear trends (see Figure 2.32). This observation agrees with intuition because the energy in the flow increases with the rotor speed, and the increased energy would create higher rotational speed and higher circulation in the vortices. The highly non-linear trend for r_c warrants more discussion. The core radius was found to decrease as the rotor speed is increased from the lowest speed cases to the middle of the range. After that, the radius increased with the rotor speed out to the highest speed.

Two primary phenomenon are in conflict here. As the rotor speed increases, the lift of the blade is also increased. High lift creates a stronger tip vortex, which more closely resembles an irrotational vortex. At the extreme limit of this, the peak velocity would occur at the vortex center. Approaching this limit means that the peak swirl velocity occurs closer to the center, and so the stronger vortices have a smaller core radius. At the same time, higher speed flow experiences increased shear stress. This stress can promote turbulence that will increase the rate of diffusion, spreading the vorticity to the surrounding flow and increasing the measured core radius. The trend

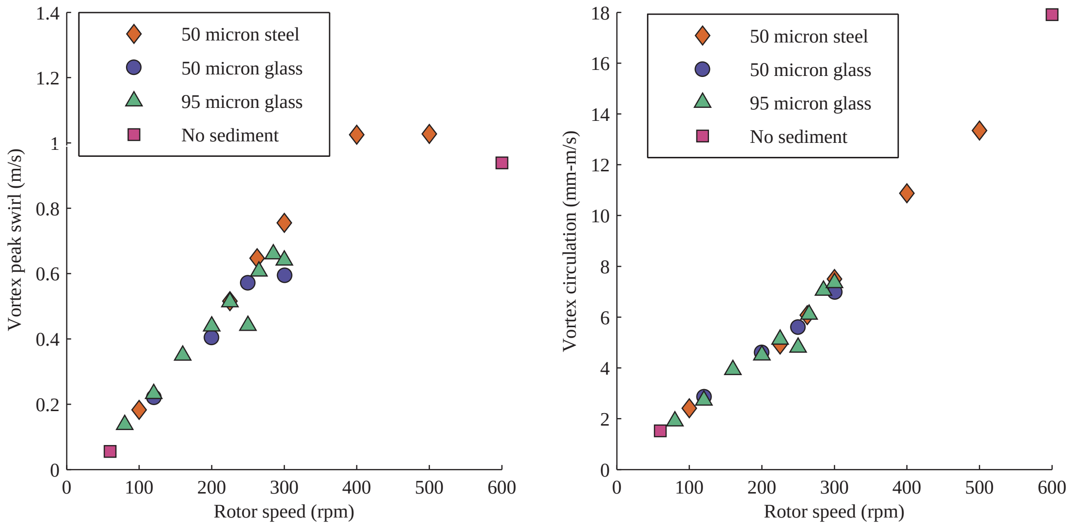

(a) Mean peak swirl velocity (b) Mean circulation

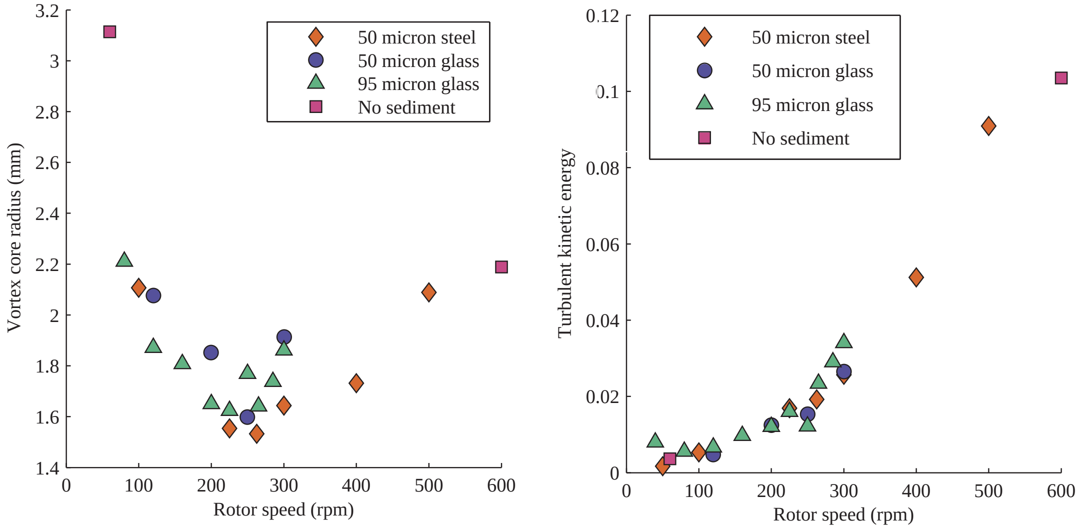

(c) Mean core radius (d) Turbulent kinetic energy

Figure 2.32: Wake characteristics plotted with respect to rotor speed

observed for r_c suggests that the core-reducing effect is dominant at low rotor speeds and the core-expanding effect is dominant at high rotor speeds.

Given time-resolved images of the two phase flow, the “severity” of the particle field in the dispersed phase was quantified by counting the total number of sediment particles suspended in the field of view. This quantity provides a simple measure of the intensity of the brownout, but could be further modified to also include the height and/or velocity of the particles above the bed. A minimum threshold and median filter were used to remove most of the nylon tracer particles from the images. Using Khalitov’s search function, Gaussian-like peaks in image intensity were identified as individual particles, and another minimum threshold was then used to eliminate any data that were not part of the Gaussian peaks. A sediment particle was defined to have a certain minimum size and minimum mean brightness in the image; data below threshold values were eliminated. A maximum particle size was implemented to eliminate groups of sediment particles that were not uplifted but were identified by the Gaussian search. The final sediment search function was controlled by the following five parameters: median filter width, minimum threshold, minimum and maximum sediment size, and minimum sediment brightness. For two images, each visible sediment particle was manually identified. Values for each search parameter were tested using a Monte Carlo method, where results were scored for accuracy compared to the manually identified particle locations. This process was run separately for the steel and glass sediment. Given a time series of PIV images, a record of sediment uplift as a function of time was obtained for each test condition.

To evaluate how well similarity parameters characterize the amount of suspended sediment, experiments were repeated over a range of rotor speeds, representing different wake velocities, blade passing frequencies, and vortex strengths. Figure 2.33 shows the average number of uplifted sediment particles for each recorded rotor revolution as a function of rotor rpm. Each data point represents the average number of particles uplifted over one rotor revolution. It is clear that the intensity of the particle field during each revolution varies significantly, even for a given rotor rpm. For the steel and glass sediment particles (Fig. 33(a) and Fig. 33(b)), the particle field intensity increased with rotor speed.

The Buckingham-Π method of dimensional analysis was employed to extract the relevant scaling parameters, i.e., non-dimensional groupings of parameters. As expected, the classical similarity parameters arose through this analysis, but so did new parameters. Based on previous findings, the vortices are known to affect sediment transport, an effect not captured in the classical analysis. To characterize this critical component of the flow, tip vortex characteristics were included in the

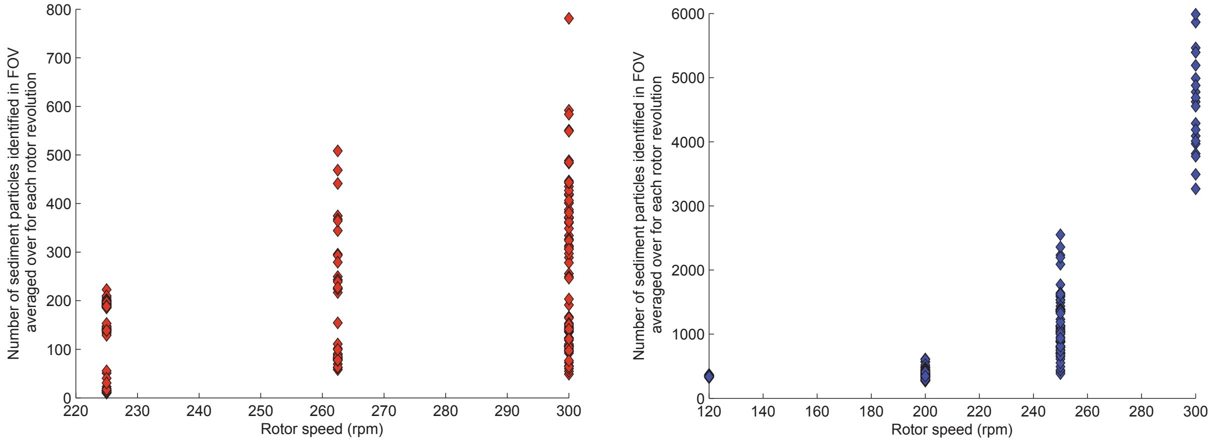

(a) Steel sediment

(b) Glass sediment

Figure 2.33: Relative brownout intensity at different rotor speeds.

dimensional analysis along with the more traditional characterizations of the rotor, particles and the working fluid. Specifically, the rotor was characterized by its radius, chord, tip speed, and its rotational frequency; the sediment was characterized by particle diameter, density, terminal velocity and threshold friction velocity; the carrier fluid was characterized by density, a characteristic velocity, kinematic viscosity, and boundary layer thickness at the ground. To introduce the unsteady aspects of the flow to the analysis, the tip vortices were described by their strength, core size, maximum swirl velocity, and area.

The resulting parameters were paired down to fewer groupings. Because the intention was that these groupings would also characterize the unsteady features of the flow, it was required that the parameters have at least one of the four parameters that can be used to describe the vortices. This requirement eliminates 5 of the 16 groupings. Likewise, two groupings were eliminated because they did not include sediment properties. Several of the remaining groupings are related to each other by one of the six classical similarity parameters; for example, $\frac{RU_F}{\Gamma_v}$ is related to $\frac{D_pU_F}{\Gamma_v}$ by $\frac{D_p}{R}$. Finally, four groupings were selected and one additional grouping was formed by the product of two of these. The final candidates were:

1. $\dfrac{\Gamma_v}{D_pU_t^*}$, called the stationary inertia ratio.
2. $\dfrac{\Gamma_v}{D_pU_F}$, called the mobile inertia ratio.
3. $\dfrac{V_{\theta_{\max}}}{U_F}$, called the terminal-swirl velocity ratio.

4. $\frac{V_{\theta_{\max}}}{U_t^*}$, called the threshold-swirl velocity ratio.

5. $\frac{V_{\theta_{\max}}^2}{U_F U_t^*}$, called the terminal/threshold-swirl velocity ratio.

To study the relationships between these similarity parameters and the intensity of the particle mobilization and uplift, data were collected across a range of rotor operating conditions and particle species. The terminal velocity and threshold friction velocity of the particles was varied by the selection of appropriate particles. The vortex strength and maximum swirl velocity were varied by changing rotor speed.

Figure 2.34 shows results for the quantity of particle uplift in terms of each of the five candidate similarity parameters. Cases with multiple data points are experiments that were repeated. In Fig. 34(a), the quantity of particles uplifted is plotted with respect to the stationary inertia ratio and shows a general increasing trend for each sediment type. However, this similarity parameter does not seem to properly account for the characteristics of the sediment. Figure 34(b) shows the same results in terms of the mobile inertia ratio. Again, each sediment type shows the same trend as seen in Fig. 2.33 but they are not consistent. The same outcome was obtained for remaining three parameters. The threshold-swirl velocity ratio results shown in Fig. 34(d) is notable as it is the only parameter of these five for which the steel and glass particle results overlap.

Publications

1. Glucksman-Glaser, M., and Jones, A., “Effects of Model Scaling on Sediment Transport in Brownout,” AIAA Paper 2012-2915, 30th AIAA Applied Aerodynamics Conference, New Orleans, LA, June 2012.

2. Perrotta, G., and Jones, A., “Characterization of Rotor Wake in Ground Effect,” AIAA Region I-MA Student Paper Conference, Ithaca, NY, April 2014. (Awarded 1st place in the Graduate category.)

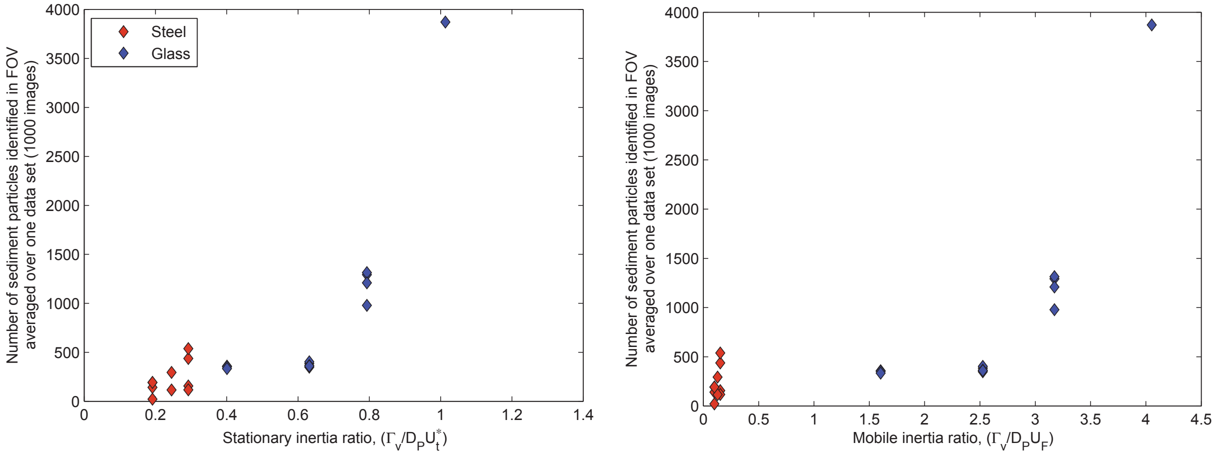

(a) Stationary inertia ratio (b) Mobile inertia ratio

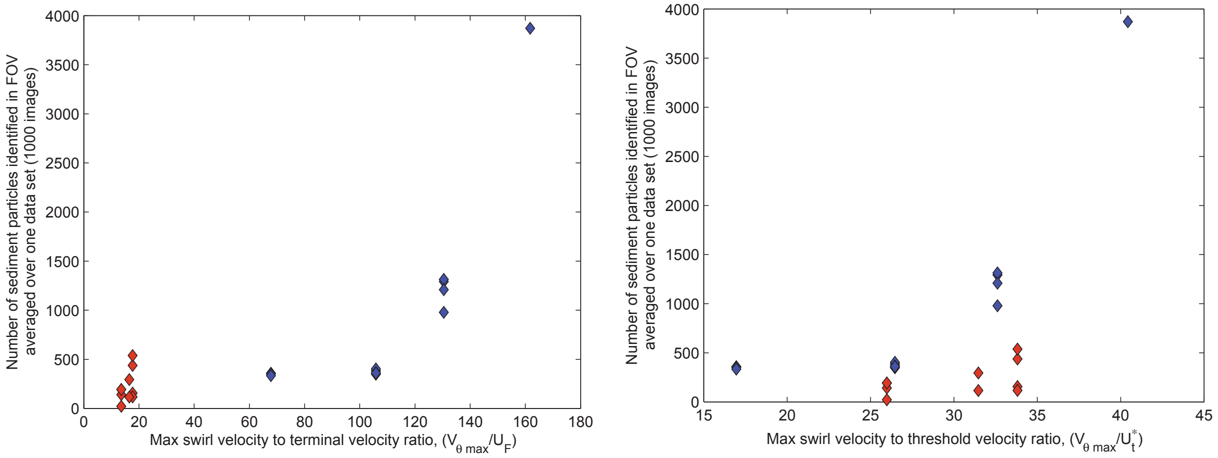

(c) Terminal-swirl velocity ratio (d) Threshold-swirl velocity ratio

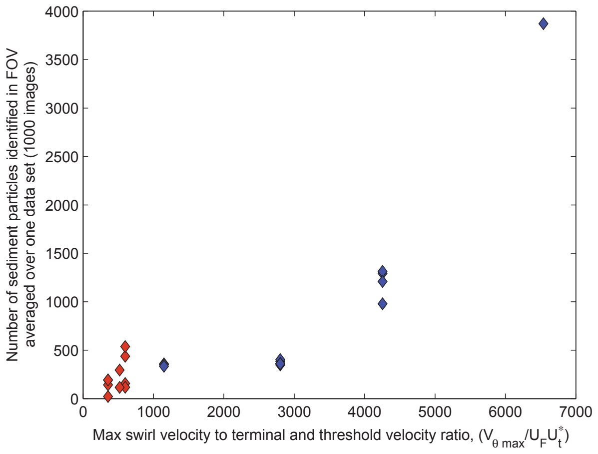

(e) Terminal-threshold-swirl velocity ratio

Figure 2.34: Quantity of particles uplifted in terms of the similarity parameters.

Task 2.7

Turbulent Near-Bed Flows Under Impinging Vorticity

Investigator(s): J. Gordon Leishman

Institution/Department: University of Maryland/Department of Aerospace Engineering

Graduate Student(s): Jürgen Rauleder

Contact email(s): leishman@umd.edu

Background and Objectives

There is still a relatively poor understanding as to how discrete turbulence events and secondary flow structures affect the mobilization, transport, and entrainment of particles in vortically dominated flows, which are characteristic of those found in brownout conditions. Also, turbulence effects have not yet been modeled satisfactorily for such flows. Specifically, for the vortically dominated flows found in the wake below a rotor, time-resolved measurements of the detailed turbulence characteristics are not available, even for the single-phase flow environment (i.e., without dust particles). However, detailed measurements for such a flow problem are needed to validate computational models, both for the single-phase and also for the dual-phase dusty flow. Furthermore, the sediment entrainment models used in brownout simulations are semi-empirical in nature and have been derived for more canonical flows other than rotor flows (i.e., steady, uniform boundary layer flows for the most part). Therefore, these entrainment models do not explicitly account for unsteadiness and turbulence in the flow, and they have not been validated for the rotor-induced vortical dual-phase flow involved in the brownout problem.

The pickup and suspension of particles from the sediment bed is at least partly caused by sufficiently high surface shear stresses. However, the actual process is also affected by fluctuations in the flow velocities and the turbulent Reynolds stresses, discrete turbulence events, and the unsteady upward flow velocities induced by the vortices. Most prior particle-laden two-phase flow studies have been performed on channel flows with relatively “clean” boundary layers. However, turbulence effects (including the effects of discrete turbulent motions) and the potential effects of secondary vortical structures on particle uplift and entrainment have not been studied in detail in regard to the underlying flow-physical mechanisms in non-uniform flows.

In previous work under this task, it was shown that it was the rotor-generated vortices that were primarily responsible for sediment uplift from an underlying sediment bed. It was observed that particle pickup and suspension occurred mostly in phase with the periodic passage of the tip vortices over the bed, but the role of turbulence in this process was less clear. In this latest research effort, a more detailed investigation on the instantaneous dual-phase flow field at the ground below the rotor has been carried out. Time-resolved dual-phase measurements of the detailed vortex flow–particle interactions were analyzed to further the understanding of the fluid dynamic mechanisms involved in such rotor-induced particle flows.

Particular attention has been given to the effects of organized turbulent motions (or turbulence events) and secondary vortical structures at the ground, the goal being to better understand the fluid–particle interactions and the mechanisms behind particle uplift. The quadrant analysis method was also used to expose any correlations between the fluid motion and the particle motion near the sediment bed. The longer-term objectives were to help with the development of more appropriate dual-phase flow models that are based on justifiable physical assumptions that could be used to improve brownout simulations.

Technical Approach

A two-bladed rotor system with a rotor radius of 0.085 m (0.279 ft) was used for the experiments. The rotor blades used thin airfoils (with camber and a sharpened leading edge) of rectangular planform with a chord of 0.018 m (0.059 ft). For the present measurements, the rotational plane of the rotor was located at a height of one rotor radius above a ground plane on which a mobile sediment bed was placed; see Fig. 2.35. The rotor was operated at a rotational frequency of 60 Hz (3,600 rpm), which corresponded to a blade tip speed of 32.04 m s^{-1} (105.12 ft s^{-1}) and a chord Reynolds number, Re_c, at the blade tip of approximately 35,000.

The blade pitch was set to 12° to produce a blade loading coefficient, C_T/σ, of 0.156, which yielded a theoretical hover induced velocity, v_h, of 3.3 m s^{-1} (10.8 ft s^{-1}). From the measured velocity field, the circulation of the tip vortices was determined to be Γ_v = 0.0172 m^2s^{-1} (± 8.6 x 10^{-4} m^2s^{-1}) giving a vortex Reynolds number of Re_v = 1,100. These rotor operating conditions were chosen to generate a representative rotor wake with enough intensity to mobilize and uplift particles of sufficient size, to allow for good discrimination of the flow phases in the resulting dual-phase flow, as well as to avoid significant depletion of the sediment bed during the measurement period.

A mobile sediment bed consisting of well-characterized glass microspheres with a diameter of 45–63 μm was used. The particles were loosely deposited on the ground plane to an approximate thickness of 1 cm and the surface made smooth with a scraper. The Stokes number was estimated to be 60 and the particle Reynolds number was less than 30. The simultaneous time-resolved flow

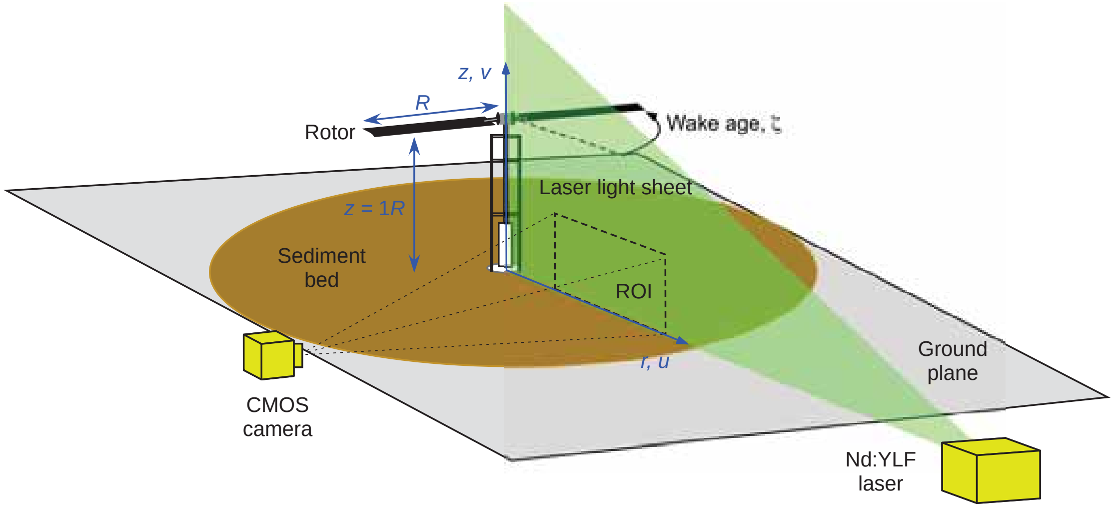

Figure 2.35: Schematic of the experimental setup used to conduct the dual-phase PIV/PTV flow measurements, also showing the coordinate system used in the analysis.

measurements were performed using two-dimensional, two-component PIV for the carrier phase, while PTV was used to measure the motion of the sediment particles.

A high-repetition rate Nd:YLF laser and a 4 Mp CMOS camera (2,560 x 1,600 pixels at 725 frames per second) were used to interrogate the flow, the high frame rate capability allowing for a contiguous time-history of the flow to be recorded. This time-history enabled detailed assessments as to how the fluid flow, its primary and secondary vortical flow structures, and turbulence events near the sediment bed affected the particle motion, most importantly, how they affected the processes of particle uplift and entrainment. The selective results shown in this report are planar, simultaneous PIV/PTV measurements performed in the regions of interest (ROI) as shown in Figs. 2.35 and 2.36. An exemplar instantaneous dual-phase flow measurement below the rotor inside the larger ROI 1 is shown in Fig. 2.37.

Results

Although the younger tip vortices at radial positions of $r/R \approx 1.2$–1.3 convected at the same height above the sediment bed and they were of the same strength or stronger than the older vortices (because of vortex distortion and diffusion becoming more prevalent further downstream), they were mostly unable to lift up particles from the bed at these upstream locations; see Fig. 2.38. Therefore, in this reporting period, attention of the present task was given to secondary flow structures and organized turbulent motions as they may contribute to the complex flow environment near the bed and to the processes of sediment mobilization and uplift. To visualize the turbulent motions,

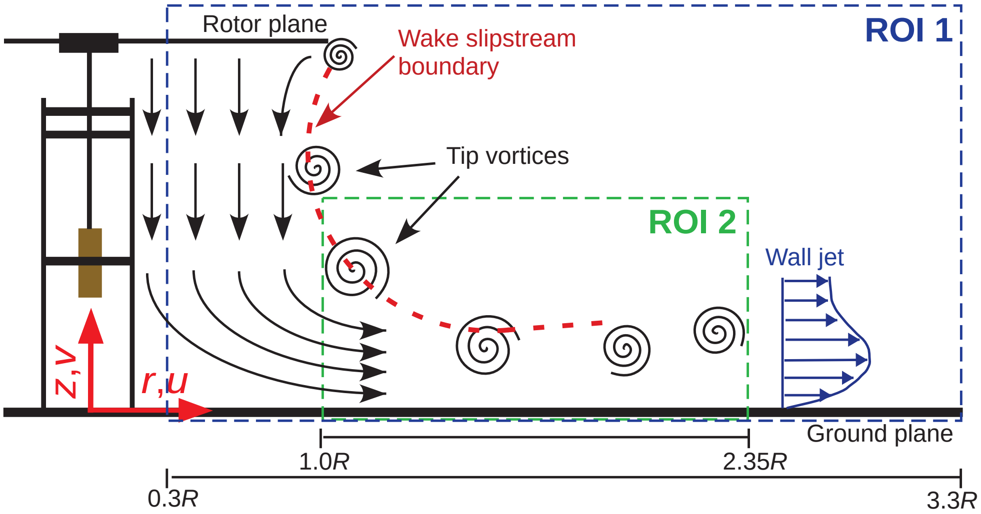

Figure 2.36: Schematic showing the regions of interest (ROI) that were investigated.

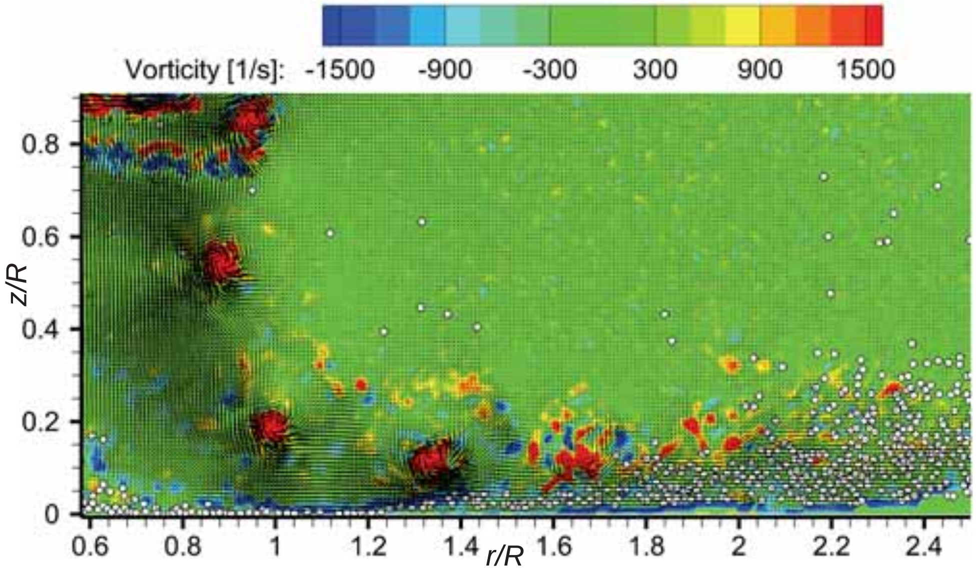

Figure 2.37: Instantaneous dual-phase flow realization below the rotor. Background contour based on instantaneous vorticity.

it is necessary to observe the flow in a moving reference frame. Therefore, the mean convection velocity at each spatial point was subtracted a posteriori from the instantaneous fluid velocity components measured by the PIV. This process leaves the turbulent fluctuations about the mean at each location in the flow (i.e., a Reynolds type of decomposition), as shown in Fig. 2.38.

For the instance shown in Fig. 2.38, the tip vortices are still coherent and they constitute by far the strongest vortical structure in this flow, their local induced velocities being much greater than the local mean flow velocities; see also Fig. 2.37. Therefore, the tip vortices are apparent in both vector maps, i.e., both when the flow vectors are shown on basis of the instantaneous velocity

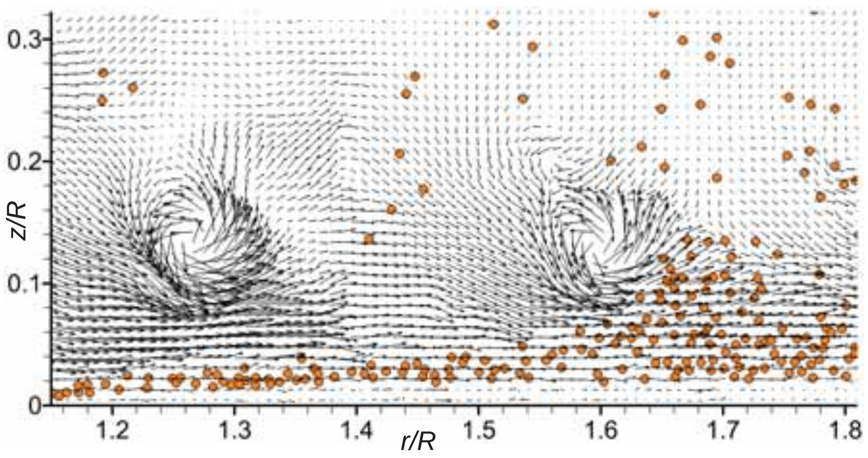

(a) Instantaneous velocity vectors

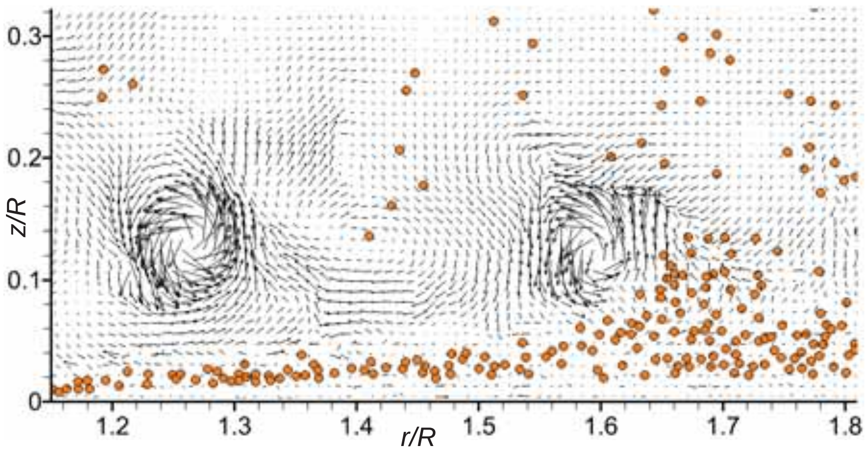

(b) Instantaneous fluctuation velocity vectors (Reynolds decomposed)

Figure 2.38: Velocity vector maps superimposed by detected particle locations for the same instance in ROI 2. Only every other measured vector shown and particle sizes exaggerated for clarity.

components (Fig. 2.38(a)) and when shown on basis of the Reynolds-decomposed velocity fluctuations, u' and v'; see Fig. 2.38(b). However, most of the other vortical structures and organized turbulent motions in the flow are omitted in the former representation of the flow, as shown in Fig. 2.38(a). The Reynolds-decomposed fluctuation (or perturbation) velocity gives further insight into the turbulent flow near the ground, and a secondary vortical structure becomes visible that is counter-rotating with respect to the tip vortices (vortical center at $r/R = 1.4$ and $z/R = 0.12$ in this case).

Notice that the vortex that is located further away from the rotor (viscous core at $r/R = 1.6$ in this case) lifts up a relatively large quantity of particles, whereas the younger tip vortex further upstream does not. In general, the younger vortices carried more concentrated vorticity than the vortices further downstream because they were more coherent and less diffused than the vortices that had aged more in the flow and that have undergone significant interactions with the sediment particles. This observation indicated that the tip vortex alone was not always able to lift up particles from the sediment bed, but that there were other physical mechanisms that can also contribute to the process. From Fig. 2.38(b), notice the turbulent motion just downstream of the older vortex ($r/R = 1.6$–1.8) in the region where most particles are uplifted by the vortex. This decelerated flow region (in the streamwise direction) appears to convect particles onto the powerful tip vortex that is then able to pick up the particles and elevate them to greater heights above the bed and even into the main flow closer to the rotor.

Figure 2.39 shows consecutive instantaneous, Reynolds-decomposed flow realizations near the ground (within ROI 2) for every 30° of wake age. The coherent blade tip vortices exposed a distinct quadrupole structure when the $u'v'$ correlation was plotted; see Fig. 2.39. Most tip vortices trailed a decelerated flow region (so-called "inward interaction" motion, for $r/R = 1.6$–1.8 in this case), that seemed to convect particles back towards the succeeding vortex, where they were subsequently picked up and elevated to greater heights off the bed. This interesting observation rises the question if this turbulent fluid motion was a precursor to particle uplift, and if it was a necessary but insufficient condition.

Figures 2.38(b) and 2.39 suggested that positive values of v' (i.e., excess velocities in the upward direction away from the bed) prevailed in the regions where most of the sediment particles were picked up and suspended by the tip vortices (statistical distributions of these fluctuation velocities are shown later). Furthermore, an ejection motion was observed downstream of most tip vortices and it contributed to the process of particle uplift. This ejection motion was mostly caused by a clockwise-rotating secondary vortical structure that was downstream of the tip vortex.

The quadrant analysis method can further characterize the turbulence based on organized turbulence structures that are present in turbulent flows as it shows the correlative structure of the fluctuation (or perturbation) velocities, u' and v'. The four types of turbulence events (sweeps, ejections, outward and inward interactions) are classified by the signs of the fluctuation velocities. The measurements are then plotted on a quadrant map that shows the probability with which a certain turbulence event occurs at one spatial location in the flow. This quadrant map essentially shows the main directions of the turbulent momentum transfer relative to the bulk movement of the fluid.

Relatively high wall-normal velocity fluctuations, v', were observed throughout all downstream measurement locations at a height of $z/R = 0.1$ above the sediment bed; see Fig 2.40. These

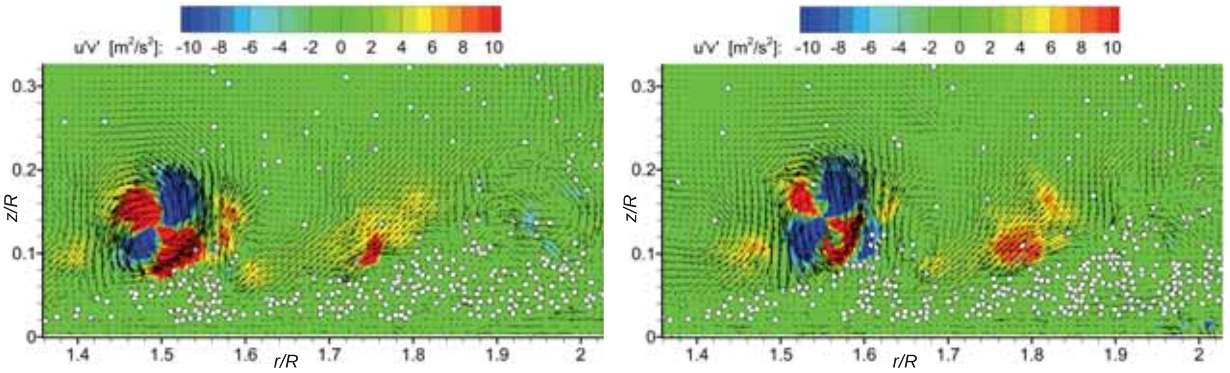

(a) $\zeta \approx 660^\circ$ (b) $\zeta \approx 690^\circ$

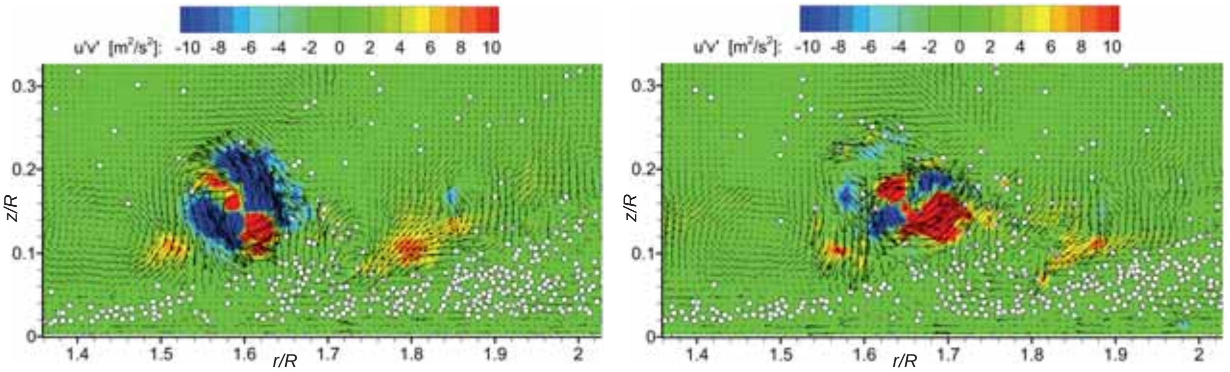

(c) $\zeta \approx 720^\circ$ (d) $\zeta \approx 750^\circ$

Figure 2.39: Consecutive carrier velocity vector fields (Reynolds decomposed) superimposed by the particle distribution on a background contour showing the instantaneous $u'v'$ correlation in ROI 2. Only every other measured velocity vector is shown.

wall-normal velocity fluctuations were largely produced by the blade tip vortices. Following the development of the flow in downstream direction for this constant height above the bed shows a shift from the prevailing streamwise decelerated fluid ($r/R < 1.4$) to ejection motions (r/R = 1.5–1.65), and to more and more turbulence events with greater positive wall-normal fluctuations ($v' > 0$; upward, away from the ground) at r/R = 1.65–1.8. These positive (upwards) excess velocities are important for particle uplift and suspension and they were measured to be more prominent further downstream from the rotor (r/R = 1.65–1.8), which correlated well with the region where much sediment was uplifted to sufficient heights above the ground to be entrained into the main vortex flow; see Fig. 2.39.

The outward interaction events gained increasingly more weight (i.e., their occurrence was more probable) downstream of $r/R = 1.6$; see Fig. 2.40. The instantaneous flow vectors based on the (Reynolds-decomposed) velocity fluctuations shown in Figs. 2.39(c) and (d) further confirmed that these turbulence events were induced by the blade tip vortices when they passed by and lifted

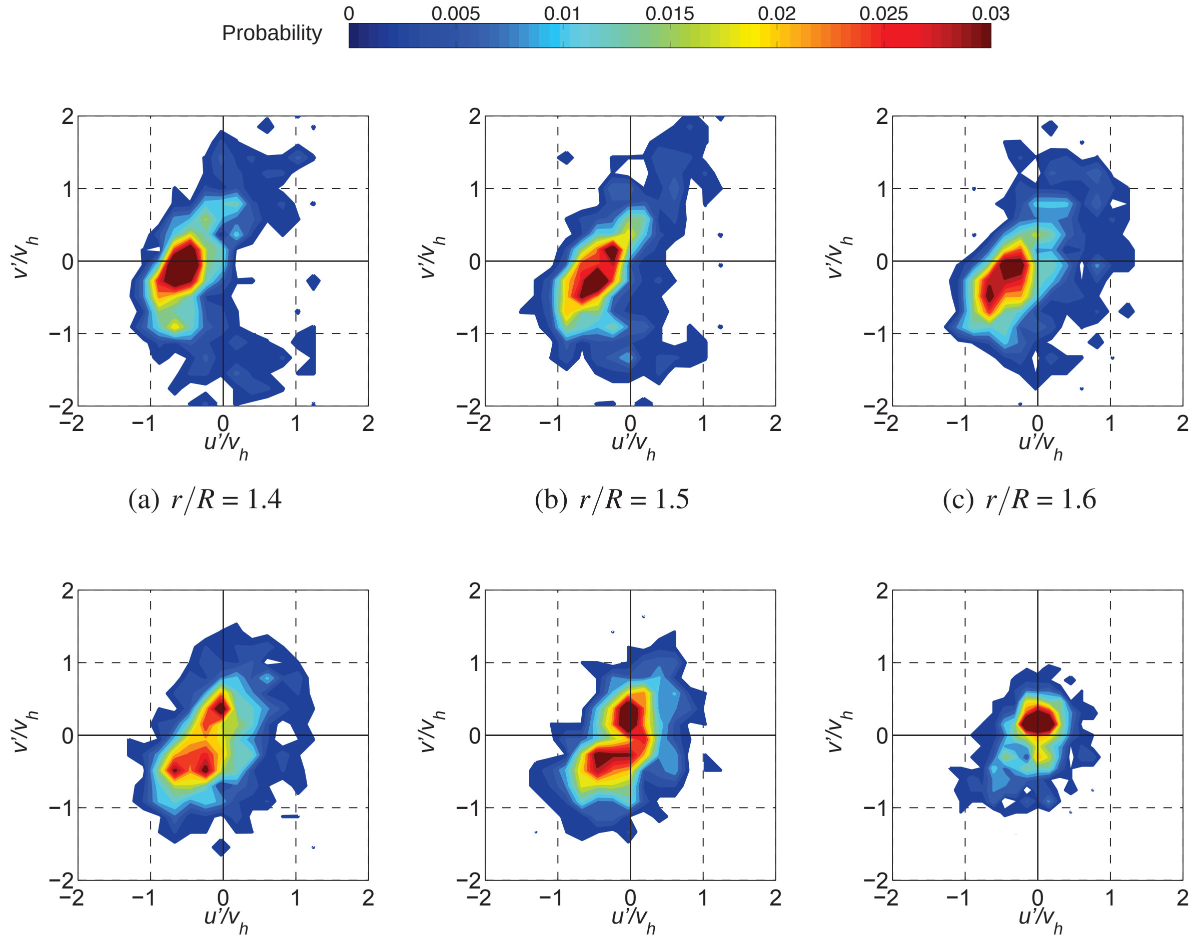

(a) $r/R = 1.4$ (b) $r/R = 1.5$ (c) $r/R = 1.6$

(d) $r/R = 1.65$ (e) $r/R = 1.7$ (f) $r/R = 1.8$

Figure 2.40: Joint frequency distributions of turbulence events for the carrier at $z/R = 0.1$ above the sediment bed.

up particles from the sediment bed in this region ($r/R \approx 1.6$–1.8).

Figure 40(d) shows the statistically prevailing ejections and inward interactions around $r/R \approx 1.65$ that were shown to facilitate initial particle uplift; see e.g., Figs. 2.38 and 2.39. These decelerated ($u' < 0$) turbulence events needed to be followed by a tip vortex convecting downstream. In most cases, only with this interplay between the decelerated turbulent motion downstream of the vortex and the positive excess velocities induced by this tip vortex itself, may the particles then be uplifted and entrained into the main rotor flow above the sediment bed, as also previously discussed in Fig. 2.39.

The local probability density distributions for the turbulence fluctuation velocities will be useful for modeling and simulation, in that existing numerical models can be validated. Furthermore, future computational models for the flow near the ground below rotors may be developed by including the statistical distributions of the turbulence fluctuations given by this task. For example, in computational models that are unable to predict turbulent fluctuations (i.e., models that are merely descriptions of the mean flow), these perturbations could be prescribed by statistical probability distributions to better simulate the flow near the sediment bed, which then will have effects on particle mobilization and uplift.

Publications

1. Rauleder, J., and Leishman, J. G., "Interactions of a Vortical Flow with Dispersed Particles Below a Rotor," *AIAA Journal*, submitted on August 5, 2014.
2. Rauleder, J., and Leishman, J. G., "Fluid–Particle Interaction in Vortex-Induced Dual-Phase Flows Above a Sediment Bed," Proceedings of the 44th AIAA Fluid Dynamics Conference, Atlanta, GA, June 16–20, 2014.
3. Rauleder, J., and Leishman, J. G., "Particle–Fluid Interactions in Rotor-Generated Vortex Flows," *Experiments in Fluids*, Vol. 55, (3), 2014, pp. 1–15.
4. Rauleder, J., and Leishman, J. G., "Flow Environment and Organized Turbulence Structures near a Plane below a Rotor," *AIAA Journal*, Vol. 52, (1), 2014, pp. 146–161.
5. Rauleder, J., and Leishman, J. G., "Turbulence Modifications and Phase Couplings in Ground Effect under Simulated Brownout Conditions," American Helicopter Society 69th Annual Forum Proceedings, Phoenix, AZ, May 21–23, 2013.
6. Rauleder, J., and Leishman, J. G., "Measurements of Organized Turbulence in the Dual-Phase Flow below a Rotor," 38th European Rotorcraft Forum Proceedings, Amsterdam, The Netherlands, September 4–7, 2012.
7. Rauleder, J., and Leishman, J. G., "Flow Environment and Organized Turbulence Structures at the Ground Below a Rotor," American Helicopter Society 68th Annual Forum Proceedings, Fort Worth, TX, May 1–3, 2012.
8. Rauleder, J., and Leishman, J. G., "Measurements of the Turbulent Flow Environment on the Ground Below a Hovering Rotor," 37th European Rotorcraft Forum Proceedings, Gallarate, Italy, September 13–15, 2011.

Part 3: Brownout Synthesis, Mitigation and Validation

- Task 3.1 – Pilot-in-the-Loop Brownout Simulation and Mitigation Strategies
- Task 3.2 – Development of Efficient Airborne Sediment Tracking Algorithms
- Task 3.3 – Understanding Brownout and Developing Mitigation and Control Strategies
- Task 3.4 – ABATE Simulation Framework and Validation
- Task 3.5 – Computational Considerations in the Prediction of Brownout Dust Clouds

Task 3.1

Pilot-in-the-Loop Brownout Simulation and Mitigation Strategies

Investigator(s): Monica Syal, Chengjian He, Jin-Young Hong, and Jinggen Zhao

Institution/Department: Advanced Rotorcraft Technology, Inc.

Graduate Student(s): None

Contact email(s): syal@flightlab.com, he@flightlab.com

Background and Technical Challenges

Modeling brownout and the associated optical degradations in a flight simulation is very challenging. This goal requires modeling several complex physical phenomena in real-time, which include: (a) a high-resolution flow field produced by a rotor operating in ground effect, (b) the mobilization and convection of a very large number of dust particles over relatively long time scales, (c) the optical attenuation caused by the presence of dust particles, and (d) the rendering of the dust clouds in a flight simulator environment. Conducting brownout simulations in real-time in flight simulators requires that the calculations be performed in less than 20 ms at each simulation time step. This computational goal can only be achieved by using advanced parallel computing techniques developed from scientific computing, and by tapping the computing power available from General Purpose Graphics Processing Units (GPGPUs).

GPU-accelerated brownout simulation methodology was developed by coupling ART's flight dynamic simulation method FLIGHTLAB, Viscous Vortex Particle Method (VPM) and Particle Transfer Method (PTM, developed in MURI Task 3.2). Recently, the focus was on the development of physics-based methodologies to "visualize" brownout dust clouds in a flight simulator, which includes modeling of optical obscuration and scattering effects of dust clouds to visualize them on graphic processors. Existing image generation software with brownout visualization capabilities have limited applicability because they simply produce brownout dust clouds as "rough and ready" special effects instead of representing the true physical aspects of the problem, i.e., the correct optical attenuation of light based on spatial frequency and the correct motion of the dust. To produce realistic and physics-based brownout conditions from an image generator, the brownout simulation methodology needs to be extended to render the optical obscuration and scattering effects of the dust using graphical libraries like Open Graphics Library (OpenGL).

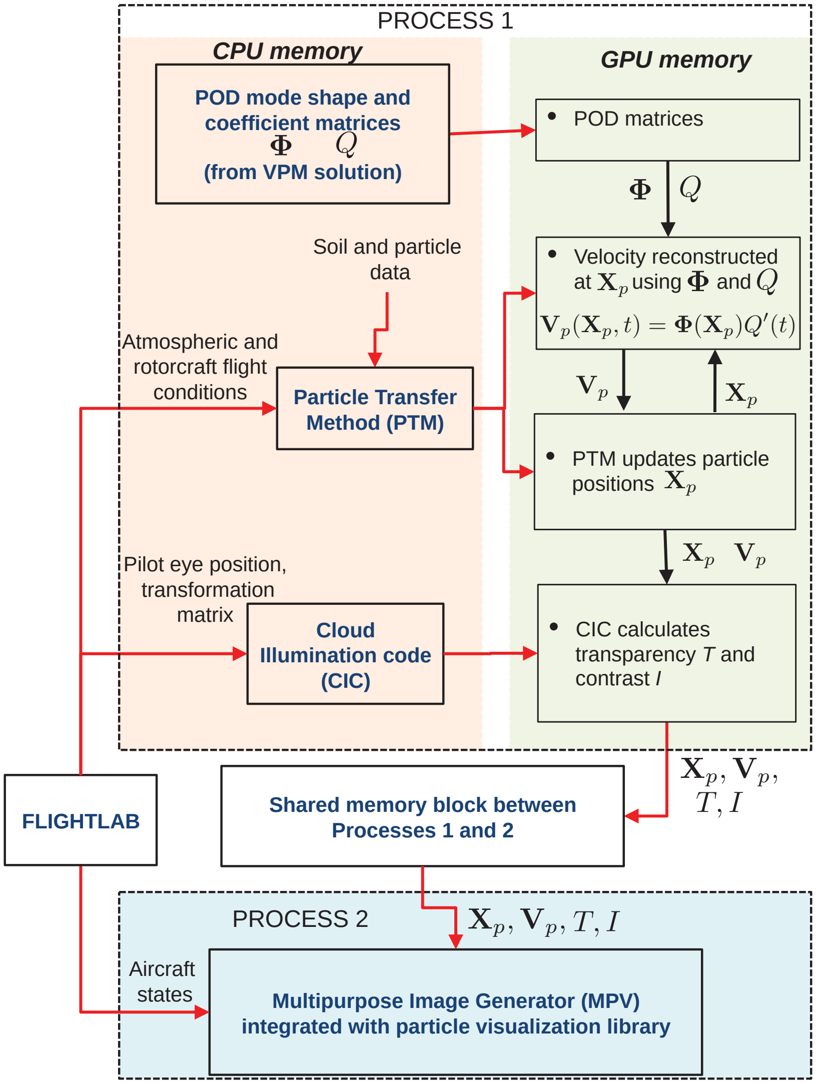

Figure 3.1: A flow chart showing integration of different methodologies to develop a brownout simulation tool for flight simulators.

Development of Methodologies

Several physics-based methodologies were developed to calculate: (a) the attenuation of light caused by brownout dust clouds, (b) the rendering of dust clouds on computer graphics, and (c) the integration of all the methodologies to simulate and render dust clouds with flight simulator developed at Advanced Rotorcraft Technology (ART) Inc. A flowchart showing an integration of all of the relevant methodologies is shown in Fig. 3.1. A brief discussion of the new methodologies developed and their integration is given below.

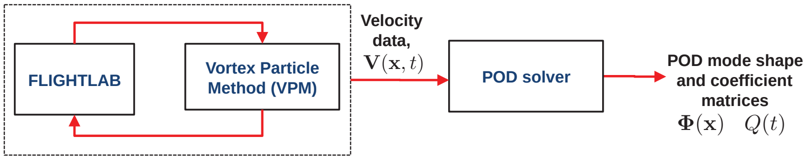

Figure 3.2: A flow chart showing extraction of POD mode shape Φ and coefficient Q matrices from a VPM calculated velocity field V.

Rotor Flow Field Using Proper Orthogonal Decomposition (POD)

One of the major challenges being encountered in the development of brownout simulation methodology for flight simulator applications is the real-time modeling of rotor wake solution using VPM. The cost of conducting VPM simulations is $O(N_v^2)$, where N_v is the number of vortex particles and for a good fidelity solution $N_v \approx O(10^5)$. While efforts are underway to make the VPM computationally faster to achieve real-time speedups, an interim approach has been followed in the present work to achieve real-time performance. In this approach, a pre-computed VPM solution of rotor wake is used to calculate induced velocities at dust particles in real-time. A Proper Orthogonal Decomposition (POD) [1] based algorithm was used to capture the dominant features of the VPM calculated flow field using only a very small number of "modes." This technique decomposes the initial velocity data set into separate space and time dependent modes, also called as mode shape functions $\Phi(\mathbf{x})$ and coefficients $Q(t)$, respectively; see Fig. 3.2. In the present work, the methodology to reconstruct induced velocity $\mathbf{V}_p$ on the dust particle positions $\mathbf{X}_p$ at each simulation time step using POD modes was implemented in parallel on GPUs using Compute Unified Device Architecture (CUDA) to achieve real-time performance; see Fig. 3.1.

Development of Dust Cloud Illumination (DCI) Methodology

The appearance of a dust cloud from pilot's perspective depends upon the interaction of light with the dust particles, which determines the "transparency or transmittance" and overall "brightness" of the dust cloud. The transmittance T of a medium is the ratio of light leaving a particular point along the light direction and reaching another point. Brightness (or radiance) I of the dust cloud determines its color contrast with respect to the surroundings. The computational modeling of these effects is a complex problem. In the present work, the radiative characteristics of light and its interactions with particles were modeled using the Radiative Transfer Theory (RTT) [2].

When a ray of light interacts with matter (e.g., particles), it's electromagnetic power changes because of: (a) absorption (that converts the light energy into other forms of energy, e.g., heat

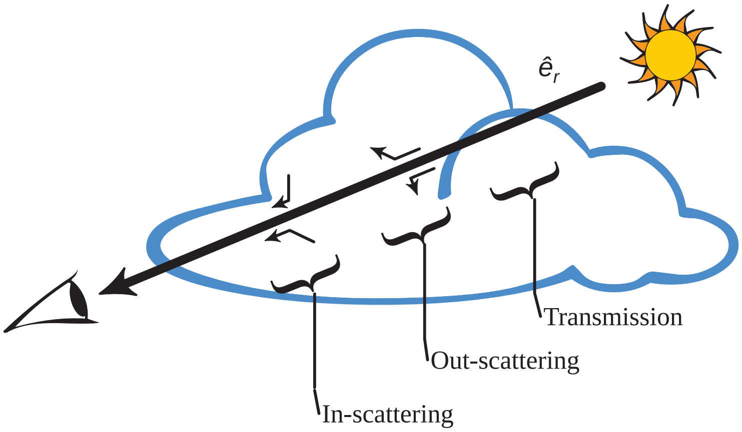

Figure 3.3: A schematic showing the processes of scattering and transmission of the incident light along direction $\hat{e}_r$ as it passes through a cloud. Source: Harris [2].

energy), and (b) scattering (that changes the direction of light after it interacts with the matter). The changes in the power of electromagnetic radiation as it travels through the dust cloud can be calculated using RTT, which solves for the changes in radiance of light as it travels through the dust cloud because of the effects of scattering and absorption.

The calculation of the RTT equation can be explained using Fig. 3.3, which shows a ray of light incident from the sun along a direction $\hat{e}_r$ on the dust cloud as perceived by an observer. The RTT equation evaluates how radiance I of the incident light changes along a direction $\hat{e}_r$ (see Fig. 3.3) as it travels through the dust cloud.

RTT accounts for two types of effects: (a) single-scattering effects that account for the amount of incident radiance that gets transmitted through the dust cloud as a result of scattering and absorption, and (b) multiple-scattering effects that account for the changes in radiance along the incident light direction because of scattering from multiple particles present in the dust cloud. The modeling of the multiple-scattering term is complex because it involves an integration of the scattered light from all the scattered directions from all the particles to the direction of the incident light and is, therefore, usually ignored in the existing models to predict optical attenuation by brownout dust clouds [3, 4]. However, by not modeling this term it can lead to artificially darker dust clouds. In the present work, the multiple-scattering term is modeled using the "multiple forward scattering" approximation, in which multiple-scattering of light is only considered in the direction of the eye. This assumption is based on work by Harris & Lastra [5].

The RTT equation has been solved in the spherical reference frame. The particle positions are first transformed from the inertial Cartesian system to the pilot-fixed spherical coordinate system using the methodology developed earlier in MURI Task 3.1. The pilot's FOV is divided into different "bins," each bin being characterized by its solid angle and its radial distance from the pilot's eye. The RTT equation is solved along each solid angle using a line integral method (see details in Ref. [2]) starting from outside of the dust cloud and moving along each bin in the solid angle toward the pilot's eye. The solution of the RTT equation is transmittance T and contrast I at each bin. These parameters T and I are used to determine opacity and color blending for rendering of dust clouds in flight simulators. In the present work, the solution of the RTT equation and the calculation of T and I have also been fully implemented on the GPUs.

Development of Dust Cloud Rendering Methodology

The transmittance and brightness of dust clouds calculated using DCI are used to "render" dust clouds in flight simulators. Rendering means creating 2D images from 3D objects using computer graphics. This process involves a camera view of the scene based on a light source. The scene comprises of objects (e.g., particles, helicopter) and terrain, which are converted into 3D triangles. Based on the light source, these triangles defining the scene are then converted into an image on the computer screen.

The dust clouds are rendered on computer graphics using an OpenGL based open-source software visualization toolkit OpenSceneGraph (OSG). This toolkit is written in standard C++ and OpenGL, and can run on most of the operating systems. In the present work, a particle rendering software was developed based on in-built OSG data structures by defining the physical and graphical properties of particles. The physical parameters include number N_p, positions $\mathbf{X}_p$ and velocities $\mathbf{V}_p$ of particles provided by PTM and VPM. The graphical or optical parameters include size, contrast I and transparency T (calculated using DCI).

Integration with Flight Simulator

The OSG-based rendering methodology developed in this work was integrated as a plugin with an open-source, cross platform image generator called Multi Purpose Viewer (MPV). Figure 3.1 shows that all of the methodologies used in this work have been coupled into two separate processes, which are launched in parallel in the FLIGHTLAB simulation environment using two CPU threads in the same computer. In the first process, FLIGHTLAB, VPM solution (using POD matrices), PTM and DCI methodologies are linked together to calculate particle velocity $\mathbf{V}_p$, position $\mathbf{X}_p$, transparency T, and contrast I. All of these methodologies are integrated by passing data pointers on the GPU memory, i.e., all methods are integrated within the GPU memory using CUDA. At the beginning of the simulation, all of these methodologies are initialized and the data is transferred to the GPU memory. There after, all of these methodologies interchange data with each other with in the GPU memory. This approach was followed to reduce expensive CPU–GPU memory transfers. The outcomes of the first process, i.e., $\mathbf{V}_p$, $\mathbf{X}_p$, T, and I are integrated to a second process, which is running MPV with the brownout rendering software developed in this work as a plugin. This integration is performed using a shared memory block on the computer's main memory.

Results

1. Rendering of Dust Clouds:

   Dust clouds are rendered (in OSG) with graphical properties, i.e., transparency and contrast, calculated using the Dust Cloud Illumination (DCI) methodology. The results showing rendered dust clouds were obtained for a representative single-rotor helicopter in an approach maneuver developed from Moen et al. [6]. The approach simulation was conducted for about 11 seconds. A total of 8.0×10^5 monodisperse particles with a diameter of 20 μm were used in this study.

   The pilot's FOV was divided into 300,000 bins. The transparency and radiance of light that reaches pilot's eye depend on particle concentration η in each bin, which is the number of particles per unit volume of each bin. Typically, the value of η varies between $O(10^{10})$ and $O(10^1)$ for particles of sizes d_p varying between $O(1)$ μm and $O(1000)$ μm, respectively [7, 8]. Representing such high concentration of particles in dust cloud simulations is impractical because of the limitations of computer memory and the required simulation time. Therefore, in the present work particle concentrations were scaled to represent high concentration for the calculations of transparency and brightness (or radiance).

   Figures 4(a), 4(b) and 4(c) show the instantaneous realizations of three rendered dust clouds (using OSG) in the pilot's FOV with particle concentrations $O(10^6)$, $O(10^8)$ and $O(10^9)$, respectively. These figures show that as η increases, a dust cloud becomes less transparent because of the presence of more particles in the optical path. The dust clouds are rendered in the present work by rendering individual particles. There is a paradox in this approach because the transparency and brightness are scaled to achieve $\eta \approx O(10^8)$ to $O(10^9)$. However, rendering such a large number of particles in real-time becomes impractical. One way

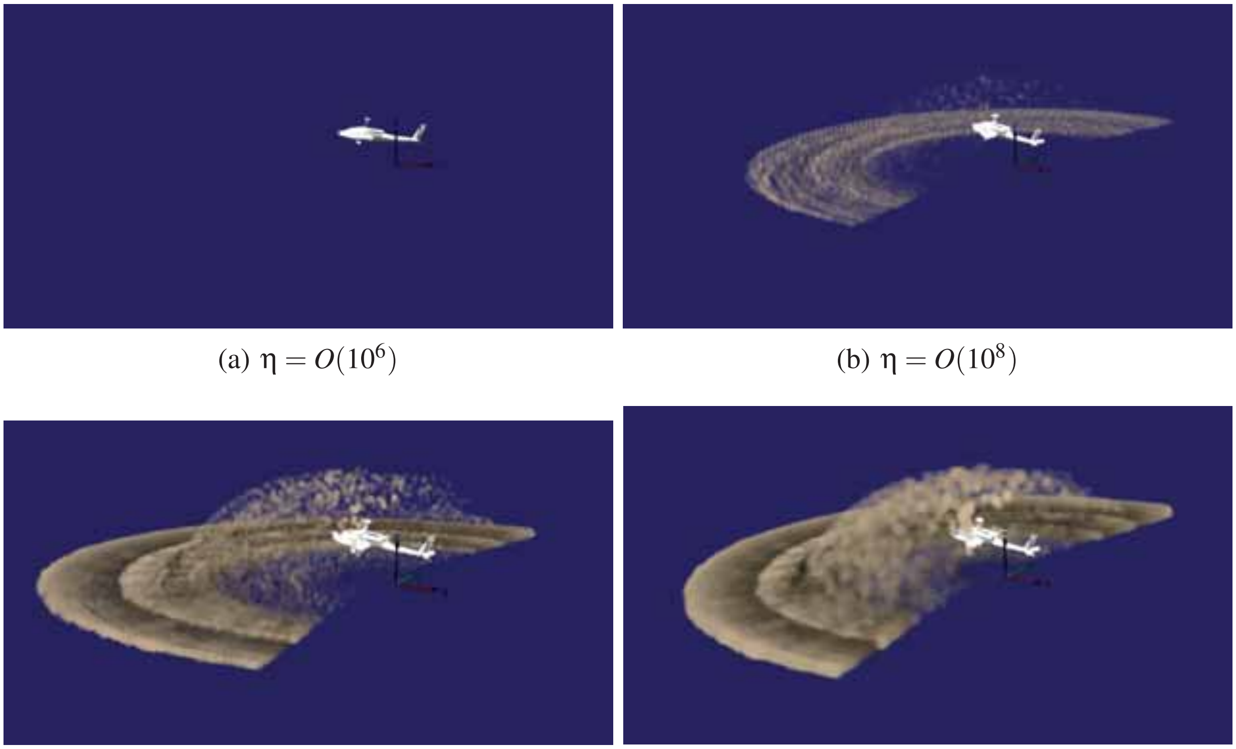

(a) $\eta = O(10^6)$

(b) $\eta = O(10^8)$

(c) $\eta = O(10^9)$

(d) $\eta = O(10^9)$, bigger sized particles

Figure 3.4: Instantaneous realizations of dust clouds at $t = 11$ s obtained using particle concentrations: (a) $\eta = O(10^6)$, (b) $O(10^8)$, (c) $O(10^9)$, and (d) $O(10^9)$ with bigger size particles to represent high particle concentrations.

to achieve the effect of such large number of particles is by representing each particle by a bigger texture that can cover more number of pixels, see Fig. 4(d).

Figures 5(a) and 5(b) show instantaneous realizations of dust clouds in the OpenSceneGraph (OSG) by using only the single-scattering term, and including the multiple-scattering term to calculate brightness of dust clouds, respectively. It is apparent from the two figures that the dust cloud visualized using the multiple-scattering model is significantly brighter when compared to the single-scattering models because multiple-scattering produces higher contrast in the forward direction because of scattering from all of the particles in the dust cloud. Therefore, it is important to model multiple-scattering in calculating light attenuation.

2. Integration of All Methodologies with ART's Flight Simulator:

   NVIDIA's Kepler K10 GPU was used in the present work. Figure 3.6 shows a variation of the taken taken by the K10 GPU to calculate: (a) the induced velocity using the pre-calculated POD matrices, (b) the particle positions using PTM, and (c) the transparency and contrast

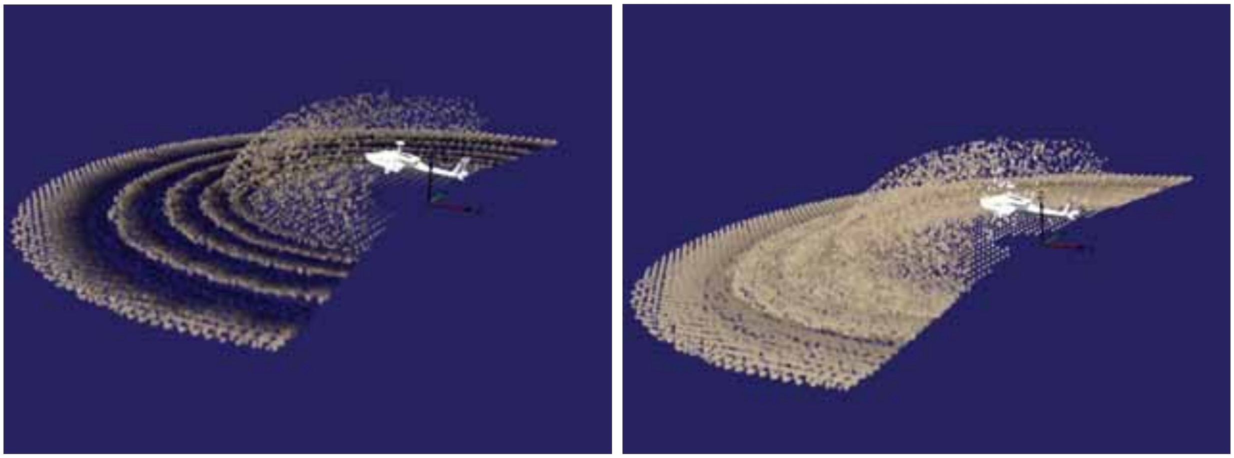

(a) Radiance calculated using single-scattering model (b) Radiance calculated using multiple-scattering model

Figure 3.5: Instantaneous realizations of a dust cloud with rendering calculated using: (a) only single-scattering model, and (b) both single and multiple scattering models.

using DCI. The number of bins used in DCI to bin pilot's FOV are 300,000. Notice that for $N_p < 10^6$, all of these simulations collectively require less than 10 ms to be calculated on one GPU. For the current goal of $N_p \approx 10^5$, these simulations require < 3 ms, i.e., they can be calculated in real-time.

Figure 3.7 shows set-up of the flight simulator in ART with the brownout simulation plugin. Instantaneous realizations of brownout dust clouds obtained during an approach maneuver in the flight simulator are shown in Fig. 3.8. These figures show that the brownout simulation methodology has been successfully integrated with the flight simulator.

References

1. Rajmohan, N., Zhao, J., He C., Kim, J., Sankar, L. N., and Prasad, J. V. R., "An Efficient POD based Technique to Model Rotor/Ship Airwake Interaction," American Helicopter Society 68th Annual Forum Proceedings, Fort Worth, Texas, May 1–3, 2012.

2. Harris, M., J., *Real-Time Cloud Simulation and Rendering*, Ph.D. Dissertation, Department of Computer Science, University of North Carolina, Chapel Hill, 2003.

3. Keller, J. D., Whitehouse, G. R., Wachspress, D. A., Teske, M. E., and Quackenbush, T. R., "A Physics-Based Model of Rotorcraft Brownout for Flight Simulation Applications," American Helicopter Society 62nd Annual Forum, Phoenix, AZ, May 9–11, 2006.

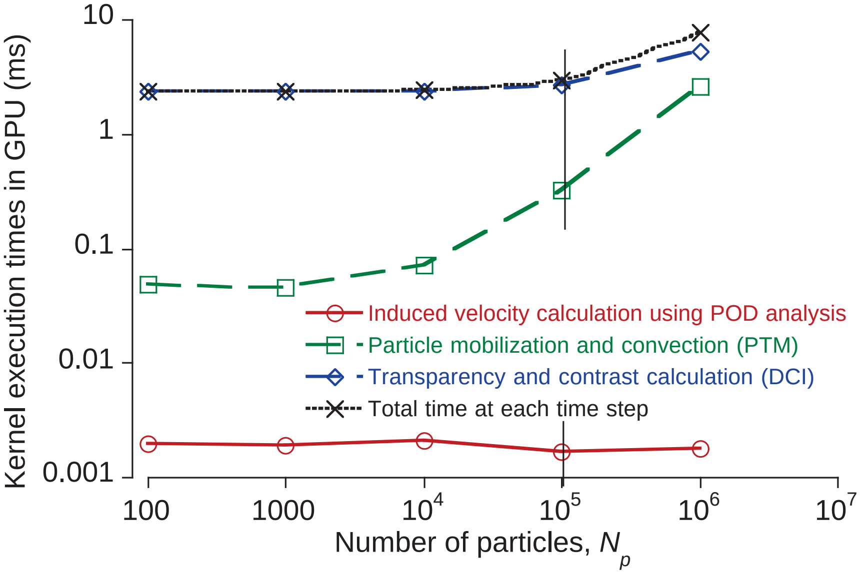

Figure 3.6: Variation of average time taken by GPU to execute different methodologies, i.e., reconstruction of velocity field using POD modes, PTM and DCI.

Figure 3.7: Set-up of ART's flight simulator integrated with brownout plugin.

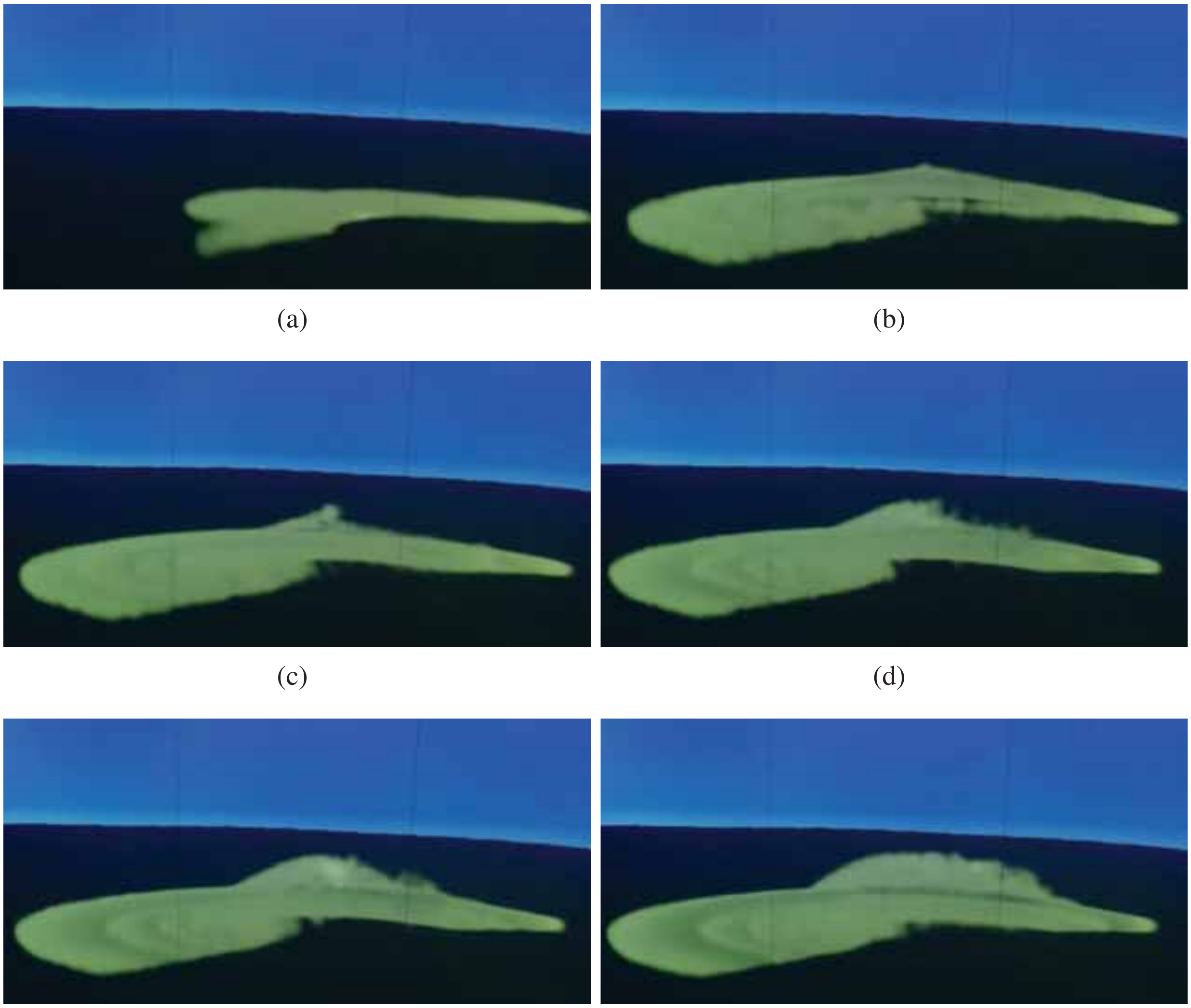

(a) (b)

(c) (d)

(e) (f)

Figure 3.8: Dust cloud images of a brownout simulation captured from ART's flight simulator.

4. Wachspress, D. A., Whitehouse, G. R., Keller, J. D., Yu, K., Gilmore, P., Dorsett, M., and McClure, K., "A High Fidelity Brownout Model for Real-time Flight Simulations and Trainers,"American Helicopter Society 65th Annual Forum, Grapevine, TX, May 27–29, 2009.

5. Harris, M. J., and Lastra, A., "Real-Time Cloud Rendering," Computer Graphics Forum, Eurographics 2001 Proceedings, Vol. 20, (3), 2001, pp.: 76–84.

6. Moen, C. G., DiCarlo, D. J., and Yenni, K. R., "A Parametric Analysis of Visual Approaches for Helicopters," NASA TN D-8275, Dec. 27, 1976.

7. "Sandblaster 2 Support of See-Through Technologies for Particulate Brownout," Task 1 Tech-

nical Report, Sponsored by Defense Advanced Research Projects Agency (DOD) Strategic Technology Office, Issued by U.S. Army Aviation and Missile Command Under Contract No. W31P4Q-07-C-0215, MRI Project No. 110565, October 31, 2007.

8. "Sandblaster 2 Support of See-Through Technologies for Particulate Brownout," Task 5 Final Technical Report, Sponsored by Defense Advanced Research Projects Agency (DOD) Strategic Technology Office, Issued by U.S. Army Aviation and Missile Command Under Contract No. W31P4Q-07-C-0215, MRI Project No. 110565, October 31, 2007.

Task 3.2

Development of Numerically Efficient Airborne Sediment Tracking Algorithms

Investigator(s): J. Gordon Leishman, Nail Gumerov
Institution/Department: University of Maryland/Department of Aerospace Engineering
Graduate Student(s): Monica Syal, Bharath Govindarajan
Contact email: leishman@umd.edu

Background and Technical Challenges

A significant issue in realistic dust cloud simulations is the very large number of particles that are needed to obtain dust clouds of acceptable fidelity. Computing the motion of each and every individual sediment particle in a dust cloud is a computationally very expensive problem, and so novel solution approaches must be used. Additional technical challenges include the modeling of the detailed processes of particle mobilization and lift-off from a sediment bed, the convection of the particles in a complex vortical flow, the potential for particle-particle interactions if the dust clouds become sufficiently dense, and the effects of previously suspended particles colliding with the sediment bed, i.e., more particles that are liberated by bombardment mechanisms.

Technical Approach

This task involves the development of computationally efficient algorithms that can be applied to the simulation of dilute gas-particle suspensions at low Reynolds numbers of the relative particle motion. Computationally expeditious algorithms have been developed to solve for the particle dynamics in a Lagrangian framework, including both the uplift from the sediment bed and the subsequent convection through the flow. Surface shear stresses and unsteady pressure forces mostly determine the threshold for the mobilization of particles from the bed.

After the particles are lofted into the flow from the bed, their trajectories are computed using particle equations of motion (EOMs) in the Lagrangian frame of reference. These three-dimensional equations are a coupled set of ordinary differential equations (ODEs), involving inertial terms (gravity, centrifugal, Coriolis), and aerodynamic terms (drag and lift). Efficient, stable and time-accurate multi-step predictor-corrector based numerical integration schemes have been explored to solve the particle EOMs. Of course, the fidelity of the approach depends upon the number of dust particles that can be simulated in reasonable time frames. Because it may require $O(10^{13})$–$O(10^{16})$ individual particles to produce a realistic brownout cloud, the resulting approaches have been parallelized to run on multiple processors as well as Graphical Processing Units (GPUs) (see Task 3.5), and also takes advantage of particle clustering schemes.

Particle Mobility Modeling

Stationary particles on a bed below the rotor can experience several types of forces such as shear, pressure, inter-particle, and gravitational. Shear forces on the stationary particles arise because of the velocity gradients produced by the boundary layer on the sediment bed. Significant unsteady pressures may also be produced in the vorticity-laden flow field below the rotor. Besides these forces, a particle on the bed also experiences gravitational forces and inter-particle forces. A new model has been developed in this task to represent the process of particle mobilization by considering the effects of both shear and pressure forces. The expression of the threshold friction velocity, $u_{\star t}$, which is the minimum friction velocity required to mobilize particles, is

$$u_{\star t} = A\sqrt{\frac{3}{2}\frac{\Delta P}{\rho} + \frac{\rho_p - \rho}{\rho} g d_p + \frac{\gamma}{\rho d_p}} \tag{3.1}$$

where ΔP is the unsteady pressure difference acting on the particle, ρ_p is particle density, d_p is particle diameter, ρ is flow density, g is the acceleration under gravity, A is a threshold friction velocity parameter that depends upon particle Reynolds number, and γ is a parameter that depends upon the inter-particle forces acting on the particle.

Sediment Tracking

Once the particles are uplifted into the main flow, the primary forces acting on the particles are aerodynamic drag and gravitational forces. The resulting particle motion is governed by the Basset–Boussinesq–Oseen (BBO) equations, which under the assumptions of dilute gas-particle suspensions of low Reynolds number Stokes' flow, can be decoupled in the three spatial dimensions. The resulting equations becomes two sets of three first-order ODEs, i.e.,

$$\frac{dV_{p_i}(X_{p_i},t)}{dt} = -\frac{V_{p_i}(X_{p_i},t) - f_i(X_{p_i},t)}{\tau_{p_s}} \tag{3.2}$$

$$\frac{dX_{p_i}(t)}{dt} = V_{p_i}(X_{p_i},t) \tag{3.3}$$

where $i = x$, y, z, and $\mathbf{f}$ is the forcing function containing the contributions from the flow velocity,

V, and the gravitational force, and can be written as

$$\begin{aligned} f_x &= V_x \\ f_y &= V_y \\ f_z &= V_z - g\tau_{p_s} \end{aligned} \qquad (3.4)$$

where τ_{p_s} is the particle response time given by $\tau_{p_s} = \rho_p d_p^2/18\mu$.

Several time-marching integration schemes have been developed in this task to solve the particle equations of motion (EOMs), as given by Eqs. 3.2 and 3.3. These schemes were developed by considering their stability, accuracy and convergence characteristics for the practical time step sizes that would be needed in a brownout simulation. Most of the explicit numerical integration schemes are unstable for solving such stiff equations unless a very small time step size is used. The stability of implicit schemes, such as Euler implicit, two-point and three-point backward difference formulae, were examined. Several predictor-corrector based time-marching algorithms using the BDF2 and BDF3 schemes were also developed, with better results, but they incur a higher cost because two induced velocity field calculations are needed. The accuracy of these schemes have been analyzed for several prototypical problems, and the the schemes based on the BDF2 and BDF3 methods were second- and third-order accurate, respectively. A time-marching method based on the BDF2 scheme was ultimately used for the dust cloud simulations because its accuracy is consistent with the accuracy of the free-vortex wake solution.

Bombardment Ejections

A suspended particle can also impact the ground and so lose part of its kinetic energy. Depending upon its momentum before the impact, as well as the inelasticity and frictional forces produced by the sediment bed, the particle will rebound. Some of this energy goes into ejecting more particles from the bed, which is called bombardment ejections; see Fig. 3.9. The bombardment mechanism was modeled by assuming that the particle impacting the bed excavates void-shaped craters, the volume of particles emitted being equal to the volume of the crater formed by the impacting particle. The initial locations of the ejected particles is based on a probabilistic approach using energy conservation. Both calculations and experiments have shown that bombardment ejection is one of the primary modes of sediment uplift during the development of brownout conditions.

Use of GPU Programming

One of the primary challenges in the modeling of brownout dust clouds is the tracking of the

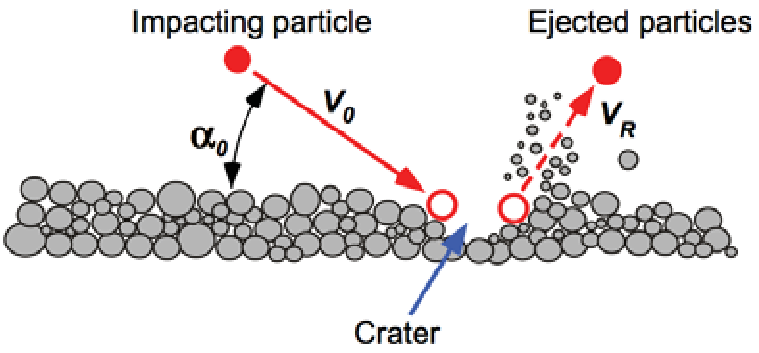

Figure 3.9: Schematic of a sediment particle impacting the ground, forming a crater, and ejecting new particles.

typically very large number of particles over the time scales characteristic of the flight maneuvers, i.e., when a rotorcraft is performing a landing or takeoff. To contain this cost, both the aerodynamic and dust cloud simulations were structured so that they could be executed on multiple processors. The particle simulation algorithm was also implemented on graphic processor units (GPUs) by dividing and assigning particle data to each GPU thread and spawning a large number of similar threads. Further details of this approach are given in Task 3.5.

Clustering Methods

Particle clustering methods have been examined in detail for their potential application to the problem of predicting rotorcraft brownout. Computationally efficient algorithms were developed that can be applied to the simulation of dilute gas-particle suspensions. In particular, the Gaussian distribution, k-means and Osiptsov's clustering methods were examined for a prototypical flow field that mimics the highly unsteady, two-phase vortical particle flow found during brownout conditions.

The Gaussian method was generally the most successful approach to clustering. In this method, the individual particles in the brownout simulation are treated as clusters, each representing a specific number of particles. The clusters are convected at each time using the EOMs. The positions of the individual particles associated with a cluster are calculated by using a multi-variate Gaussian distribution. The position of the particles within a specific cluster are recomputed at every time, and therefore, can be implemented as a post-processing step in the simulation framework.

Figure 3.10 shows an example of the application of the Gaussian clustering technique to a three dimensional brownout cloud. A comparison of the solution was obtained with 10^6 cluster centers (denoted by the black dots in Fig. 3.10(a)) and using the distributed particle clusters (Fig. 3.10(b)) with a total of 100 particles per cluster, giving a total of 10^8 particles. Notice that the clustered

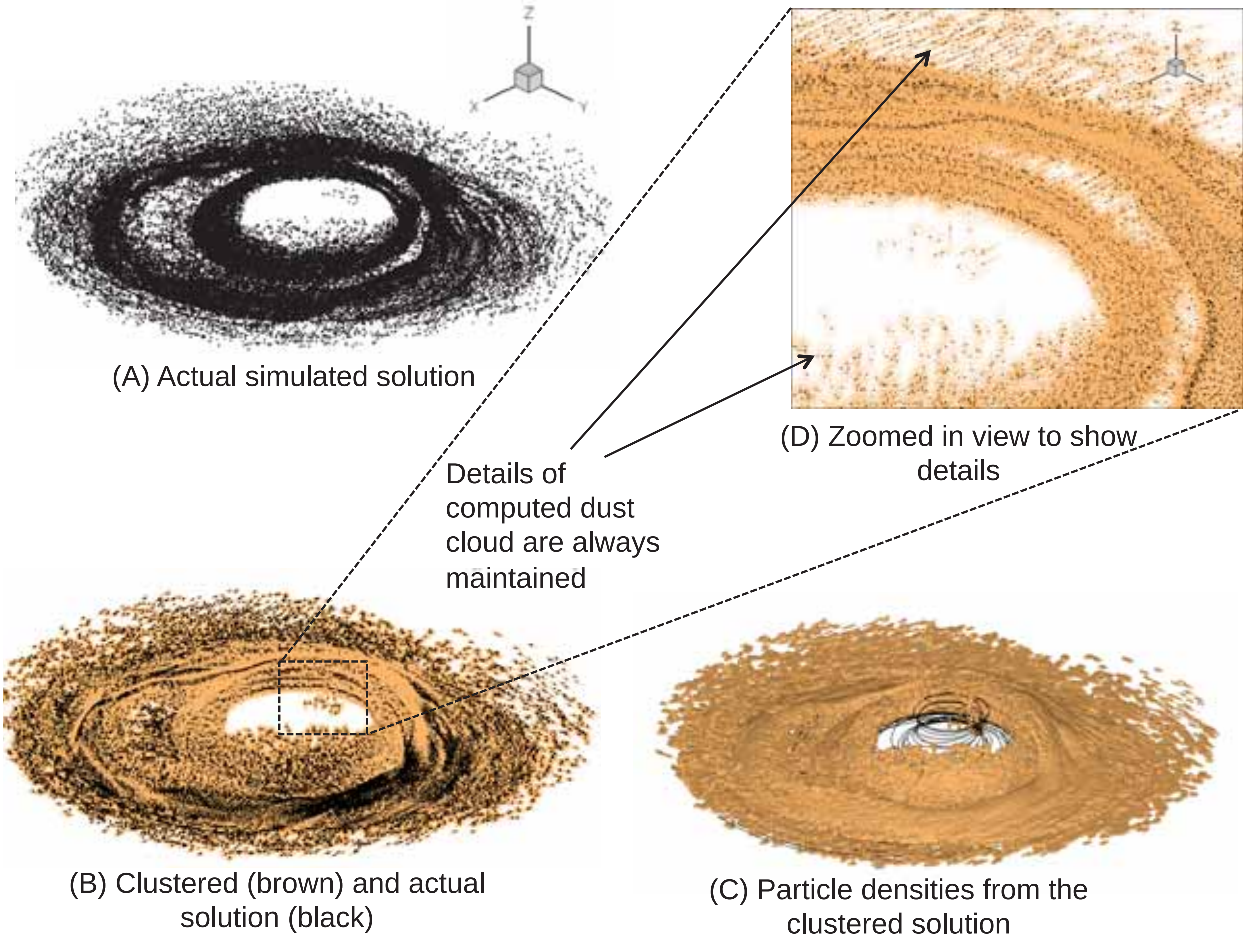

(A) Actual simulated solution

(D) Zoomed in view to show details

Details of computed dust cloud are always maintained

(B) Clustered (brown) and actual solution (black)

(C) Particle densities from the clustered solution

Figure 3.10: A solution obtained from brownout dust field computations when using the Gaussian clustering method.

solution, as shown by Fig. 3.10(b), identifies the actually computed cluster centers as black dots, and the particles obtained through the Gaussian clustering technique as brown dots. The results clearly show that the clustered solution brings out the finer, structured details of the dust cloud. Figure 3.10(c) shows the density of the dust cloud that is derived from the clustered solution, and Fig. 3.10(d) shows some details of the dust cloud near the ground, the concentrations of which can be correlated to the positions of the tip vortices in the flow.

Two other clustering methods have also been explored. The k-means clustering method is based on the principle that certain sets of individual particles can be decomposed into smaller groups of clusters, and that the resulting EOMs are solved only for the clusters. There are two aspects to this method: 1. Selecting the candidate particle groups to form a cluster; 2. The effects produced by clustering, declustering, and reclustering of the particle groups. The third method, Osiptsov's method, has its roots in full Lagrangian theory and involves integrating the equations for particle density along individual pathlines. The particle densities are obtained from the Lagrangian form of the conservation of mass by computing the change in volume of an element of "particle fluid" along its pathline.

Papers Published

1. Syal, M., Govindarajan, B., and Leishman, J. G., "Mesoscale Sediment Tracking Methodology to Analyze Brownout Cloud Developments," American Helicopter Society 66th Annual Forum Proceedings, Phoenix, AZ, May 10–13, 2010.

2. Hu, Q., Syal, M., Gumerov, N., Duraiswami, R., and Leishman, J. G., "Toward Improved Aeromechanics Simulations Using Recent Advancements in Scientic Computing," American Helicopter Society 67th Annual Forum Proceedings, Virginia Beach, VA, May 3–5, 2011.

3. Govindarajan, B., and Leishman, J. G., " Evaluation of Particle Clustering Algorithms in the Prediction of Brownout Dust Clouds," American Helicopter Society 67th Annual Forum Proceedings, Virginia Beach, VA, May 3–5, 2011.

4. Govindarajan, M. B., Leishman, J. G., and Gumerov. ,N. A., "Particle Clustering Algorithms for the Prediction of "Brownout" Dust Clouds," Published in the *AIAA Journal*, 2012.

5. Syal, M., Govindarajan, B., and Leishman, J. G., "Mesoscale Sediment Tracking Methodology to Analyze Brownout Cloud Developments," AHS 66th Annual Forum Proceedings, Phoenix, AZ, May 10–13, 2010.

6. Syal, M., and Leishman, J. G., "Modeling of Bombardment Ejection in the Rotorcraft Brownout Problem," *AIAA Journal*, 2012.

7. Syal, M., and Leishman, J. G., "Comparisons of Predicted Brownout Dust Clouds with Photogrammetric Measurements," AHS 67th Annual Forum, Virginia Beach, VA, May 3–5, 2011. Also published in the *Journal of the American Helicopter Society*.

Task 3.3

Understanding Brownout and Developing Mitigation and Control Strategies

Investigator(s): Roberto Celi, J. Gordon Leishman, and J. Baeder
Institution/Department: University of Maryland, Department of Aerospace Engineering
Graduate Student(s): John Tritschler, Jillian Alfred
Contact email(s): celi@umd.edu, leishman@umd.edu, baeder@umd.edu, chopra@umd.edu

Background and Technical Challenges

The development of a brownout dust cloud is a complex phenomenon that is affected by many parameters that define the characteristics of the rotorcraft as well as by the flight profile and landing trajectory that is followed by the pilot. The sediment bed itself also introduces complexities into the brownout problem in that it has properties and characteristics that vary from location to location.

The mitigation and control of brownout is a correspondingly complex problem: (i) "Mitigation" must be defined through some quantitative metric or metrics, (ii) the design methodology must capture the fundamental physics of all potential mitigation solutions, (iii) numerical optimization is an ideal tool to quantify and achieve mitigation, but it is difficult to apply because of the large computational requirements associated with brownout modeling as well as the potential complexities of the design space (e.g., its nonconvexity, time dependency, disjointness). Finally, brownout mitigation cannot be the sole design objective, and additional requirements (e.g., vehicle performance, vibration levels, handling qualities, etc.) need to be considered.

Technical Approach

In this task, the problem of brownout has been better understood by running simulations that expose the underlying mechanisms of dust cloud formation around a helicopter rotor that is in dynamic motion, i.e., one that is moving relative to the ground plane. The brownout analysis used is that described under Task 3.2. Dust particles that are originally stationary on the ground are mobilized by the action of the rotor wake, mainly by the shear stresses induced on the sediment bed by the tip vortices, which also cause the particles to be convected upwards and then into suspension. As the concentration of particles increases in front of the rotor, the pilot's visibility of the ground and the landing zone will diminish, which in practice leads to a loss of situational awareness.

This research has examined the problem of brownout mitigation from several perspectives: 1.

Mitigation through flight path management; 2. Mitigation by means of changes to the rotor design; 3. Mitigation by means of direct changes to the characteristics of the blade tip vortices, i.e., by diffusing the vortices. In each case, the mitigation activities have been formulated as a formal numerical optimization problem. The objective function $B(\mathbf{X})$ that has been used in the present research is based on the space and time distributions of the particle concentrations, weighing more heavily areas of good visibility that allow the pilot to close attitude and position loops, i.e., the areas immediately in front and to the side of the pilots. While this metric is only a surrogate for the actual optical attenuation of the light as it passes through the brownout cloud, this objective function has proved successful in the present work in the sense that its minimization has led to the prediction of dust clouds around the rotor that are less concentrated in the pilot's field of view, i.e., that there are fewer particles uplifted there.

Results

To mitigate the severity of brownout, previous work performed under this task has examined how several aspects of the rotor design (including the effects of rotor radius, blade chord, blade twist rate, and the number of blades) can affect brownout severity. Results were obtained for a 4-bladed rotor that is representative of a medium size utility helicopter of a prescribed weight that is executing and approach to landing over a sediment bed. It has been shown that for a given number of blades the reducing the disk loading resulted in reduced brownout severity. At the same time, the range of different results that are obtained from the same (or similar) disk loading values indicates that brownout severity cannot be attributed to the effects of disk loading alone. The research has also shown that the severity of brownout is closely associated with the blade tip vortex strengths. For example, the combined effects of simultaneously increasing number of blades and reducing the individual tip vortex strengths leads to greater brownout severity, which arises from the complicated effects that these parameters have on the interactions of the tip vortices with the ground and with each other.

The recent activities performed under this task have been related to brownout mitigation by means of flight path management. The previous brownout mitigation study, which consisted of the determination of optimum landing trajectories, was repeated with a more sophisticated simulation model. Whereas the previous model was limited to an isolated rotor with rigid blades and prescribed blade control angles, the new model consisted of a full flight dynamic simulation, including a detailed representation of rotor blade dynamics. The brownout analysis (see Task 3.2) was coupled with a comprehensive flight dynamic model, which included first principles descriptions of aircraft and rotor dynamics. In last year's mitigation study, the thrust on the isolated rotor and the corresponding controls along the trajectory, were determined through a procedure resembling trim at every time step. The values of the rotor thrust were plausible but not exact. In the latest model, both the controls and the rotor forces and moments were those required to follow the desired trajectories. Aircraft body motions and blade flapping responses were also those appropriate to the flight trajectories.

The basic trajectory optimization methodology was the same as that used previously. The objective function to be minimized was a measure of the particle concentration of the cloud (i.e., particle density in the flow in terms of numbers of particles per unit volume) at each instant of the terminal phase of landing. Behavior constraints were used to protect the rotor from entering the vortex ring state conditions (an undesirable and potentially unsafe flight condition), and from entrance into dangerous areas of the height-velocity diagram where a safe engine-out autorotational landing would not be feasible. The solution methodology was iterative. At each optimization step, first, a genetic algorithm was used to find all the minima (the optimization problem is not convex) of a response surface-type approximation of the objective function. Next, the optimum was analyzed precisely, i.e., a more thorough brownout simulation was carried out. Finally, the precise objective function was used to update the response surface approximation.

The design variables used in the optimization were the same as that used in the previous optimization study, i.e., three parameters describing the flight path and landing trajectory. It was assumed that the helicopter was equipped with a flight control system (FCS) that, for each design vector selected by the optimizer, i.e., for each trajectory, the FCS would adjust the aircraft controls so as to follow that trajectory. The control laws were obtained using a simple LQG/LTR methodology. This is a "pseudo-FCS" actually meant to represent a human pilot, albeit an especially well trained one, and one that is not affected by the potential loss of visual cues. This optimization formulation had the same general convergence characteristics and computational requirements as that solved previously, but the recent results are considered to be more realistic.

The original plans for current study called for the formulation of the optimization as an inverse simulation problem, where the design variables would have been the time histories of the pilot controls. This situation is the most realistic formulation but it is computationally much more intensive (in this case it would have required at least 12–16 design variables). The procedure described above, with the "pseudo-FCS" was intended to be a preliminary step to the inverse simulation, to provide good initial guesses of the controls and identify the regions of the design space with local minima. Instead, it proved to be a very effective optimization procedure on its

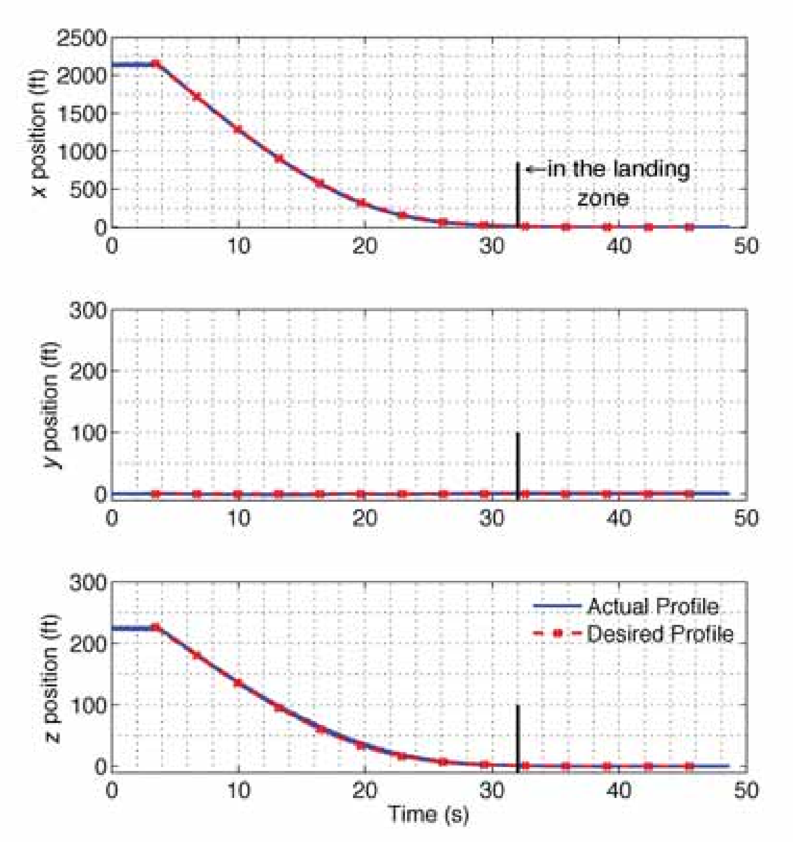

Figure 3.11: Time history of body positions of the actual flight trajectory compared to the desired approach profile for $\mathbf{X} = [6^\circ \;\; 110\,\textbf{kts} \;\; 300\,\textbf{ft}]^T$.

own. The resulting trajectories for one of the cases are shown in Fig. 3.11. The simulated pilot controls were also very realistic. Some spurious high frequency content was present in some phases of the maneuver, but these had negligible effects on the brownout simulation.

The key conclusions of the recent study are:

1. It is possible to define a controller that will generate the time histories of the controls required to track a specified approach profile, in place of a more rigorous but more computationally intensive inverse simulation procedure. A sufficiently accurate trajectory resulted from customizing the controller for the flight condition at each time step. The pilot stick inputs remained within a range that was realistic relative to their hard limits.

2. The results of the study with a full, free-flight model of the helicopter, largely confirmed those obtained with the simpler, isolated rotor only model, in particular, that the roll up of the blade tip vortices in the rotor wake and the formation of a ground vortex ahead of the rotor plays a key role in the formation of a brownout dust cloud.

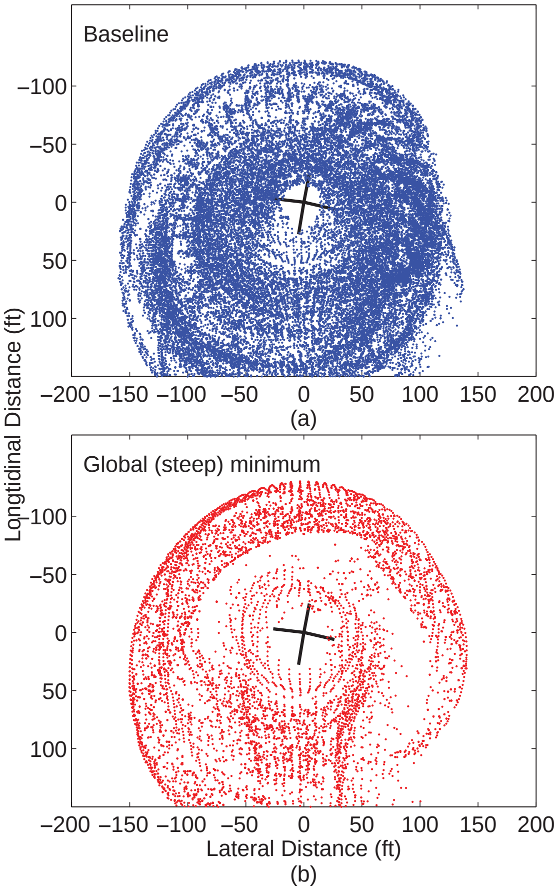

Figure 3.12: Dust cloud geometries top view for (a) the baseline approach profile and (b) the shallow optimum approach.

3. The design space for the approach profile optimization was non-convex and contained at least two optima: a local optimum corresponding to a shallow angle approach in which the pilot “outruns” the cloud that is forming behind the helicopter until the actual landing, and a global optimum corresponding to a steep trajectory in which the pilot effectively keeps the rotor wake further above the ground for as long as possible until landing. These results are known to be consistent with current operational practice, but there are also other possible variations. Dust cloud geometries for the baseline and the optimum steep approach profiles are shown in Fig. 3.12.

4. While the optimum approach trajectories were found to be very similar to that of the previous study, which was based on a simplified rotor-only model, the characteristics of the resulting brownout cloud were different. The addition of aircraft dynamics to the simulation changed the position of the center of gravity of the aircraft, and hence changed the rotor tip-path-plane

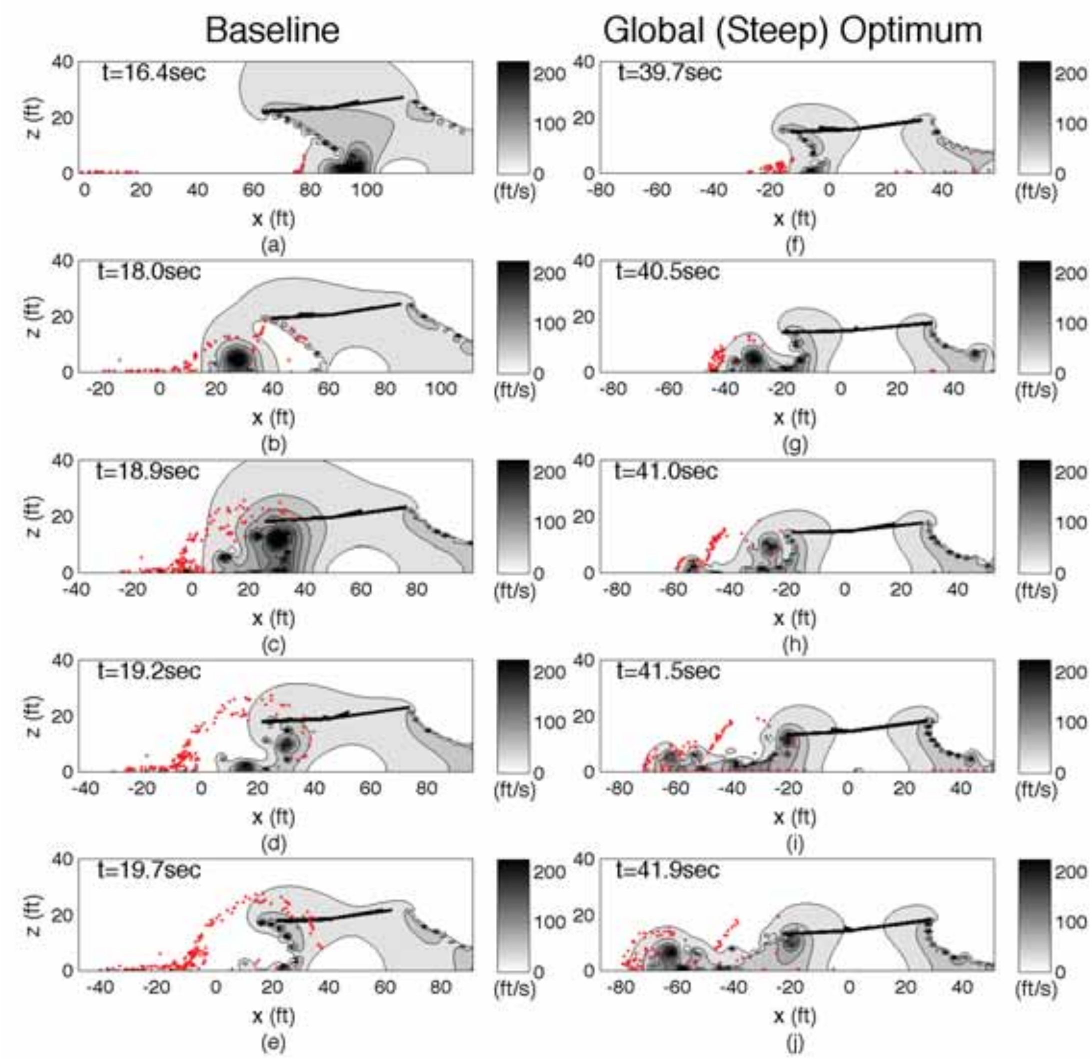

Figure 3.13: Realizations of the velocity magnitudes and developing cloud in a longitudinal plane through the flow field for (a)–(e) the baseline, X_1, and (f)–(j) the global (steep) optimum, X_{20}, approach profiles. The motion of the rotor over the ground is from right to left. Particles are enlarged for illustrative purposes.

angle of attack. The difference in blade flapping response caused the blade tip vortices to impinge on the ground further inboard of the blade tips, resulting in the dust particles being mobilized and uplifted closer to the rotor. The forward pitching of the rotor also resulted in greater fuselage pitch up angles seen during the maneuver. Furthermore, changing the center of gravity of the helicopter changed the characteristics of the resulting brownout cloud. An example of the velocity magnitudes and developing cloud in a longitudinal plane through the flow field for the global optimum, corresponding to a steep descent approach, is shown in Fig. 3.13.

Publications

1. Tritschler, J. K., Syal, M., Celi, R., and Leishman, J. G., "A Methodology for Rotorcraft Brownout Mitigation using Rotor Design Optimization," Proceedings of the American Helicopter Society 66th Annual Forum, Phoenix, AZ, May 2010. To be published in the *Journal of the American Helicopter Society*.
2. Tritschler, J. K., Celi, R., and Leishman, J. G., "The Effect of Number of Blades on Optimum Rotor Design for Brownout Mitigation," Future Vertical Lift Aircraft Design Conference Proceedings, San Francisco, CA, January 18–20, 2012.
3. Tritschler, J. K., Celi, R., and Leishman, J. G., "A Methodology for Rotorcraft Brownout Mitigation Through Flight Path Optimization," American Helicopter Society International 68th Annual Forum Proceedings, Fort Worth, TX, May 1–3, 2012. (Awarded Best Paper in the Modeling and Simulation Session)
4. Tritschler, J. K., "Contributions to the Characterization and Mitigation of Rotorcraft Brownout," Ph.D. Dissertation, Department of Aerospace Engineering, University of Maryland, College Park, June 2012.
5. Syal, M., Rauleder, J., Tritschler, J., and Leishman, J. G., "On the Possibilities of Brownout Mitigation Using a Slotted-Tip Rotor Blade," AIAA Applied Aerodynamics Conference, Honolulu, HI, June 2011.
6. Tritschler, J. K., Celi, R., and Leishman, J. G., "A Methodology for the Numerical Optimization of Approach Profiles for Rotorcraft Brownout Mitigation," AHS 3rd International Technical Specialists' Meeting on Vertical Lift Research, Development, Test, and Evaluation, Pax River, MD, August 2011.
7. Alfred, J., Celi, R., and Leishman, J.G., "Rotorcraft Brownout Mitigation through Flight Path Optimization using a High-Fidelity Rotorcraft Simulation Model," American Helicopter Society International 69th Annual Forum, Phoenix, AZ, May 2013. To be published in the *Journal of the American Helicopter Society*.
8. Alfred, J., "Rotorcraft Brownout Mitigation through Flight Path Optimization using a High-Fidelity Rotorcraft Simulation Model," M.S. Thesis, Department of Aerospace Engineering, University of Maryland, College Park, MD, November 2012.

Task 3.4

ABATE Simulation Framework and Validation

Investigator(s): James Baeder

Institution/Department: University of Maryland, Department of Aerospace Engineering

Graduate Student(s): Sebastian Thomas

Contact email(s): baeder@umd.edu, sthomas2@umd.edu

Background and Technical Challenges

Rotorcraft brownout problem is a complex, multi-physics phenomenon, the modeling of which, requires the capability to reliably predict the rotor loads and the vortex wake generation from the rotor in ground effect, the interaction of the wake with the fuselage, and the dual-phase flow field near the ground involving the rotor wake and sediment particles entrained into the flow field. A first-principles based continuum dynamics treatment of the brownout problem is impractical. However, a modular approach using domain decomposition principles, for e.g., domain decomposition at the fluid-structure interface, is a more practical option. Such an approach allows the individual solvers to use the most efficient, domain-specific solution technique to solve the governing equations. This type of approach also allows greater flexibility in the development, testing and validation of the individual solvers, thereby providing greater confidence in the final coupled simulation framework as a predictive tool.

The design of a robust, scalable and numerically accurate modular framework poses many technical challenges. In addition to the numerical accuracy of the participating solvers, care must be taken to ensure that the coupling processes preserve the desired order of accuracy and do not introduce additional errors during information transfer across domain boundaries. The modular framework must have a well-defined interface, over which the participating solvers can exchange data with other solvers without having extensive knowledge of the implementation details of the participating solvers. Such capability is extremely valuable in the development and testing of newer solvers by permitting easier coupling with previously validated solvers. Because the simulation of the brownout problem will inevitably involve the use of high-fidelity CFD solvers, the capability to support execution in a parallel environments (using domain decomposition strategies or shared memory approaches) in a transparent manner is of utmost importance. The framework must be capable of managing the execution of participating solvers across multiple processors or on modern platforms like Graphics Processing Units (GPUs), and must ensure seamless informa-

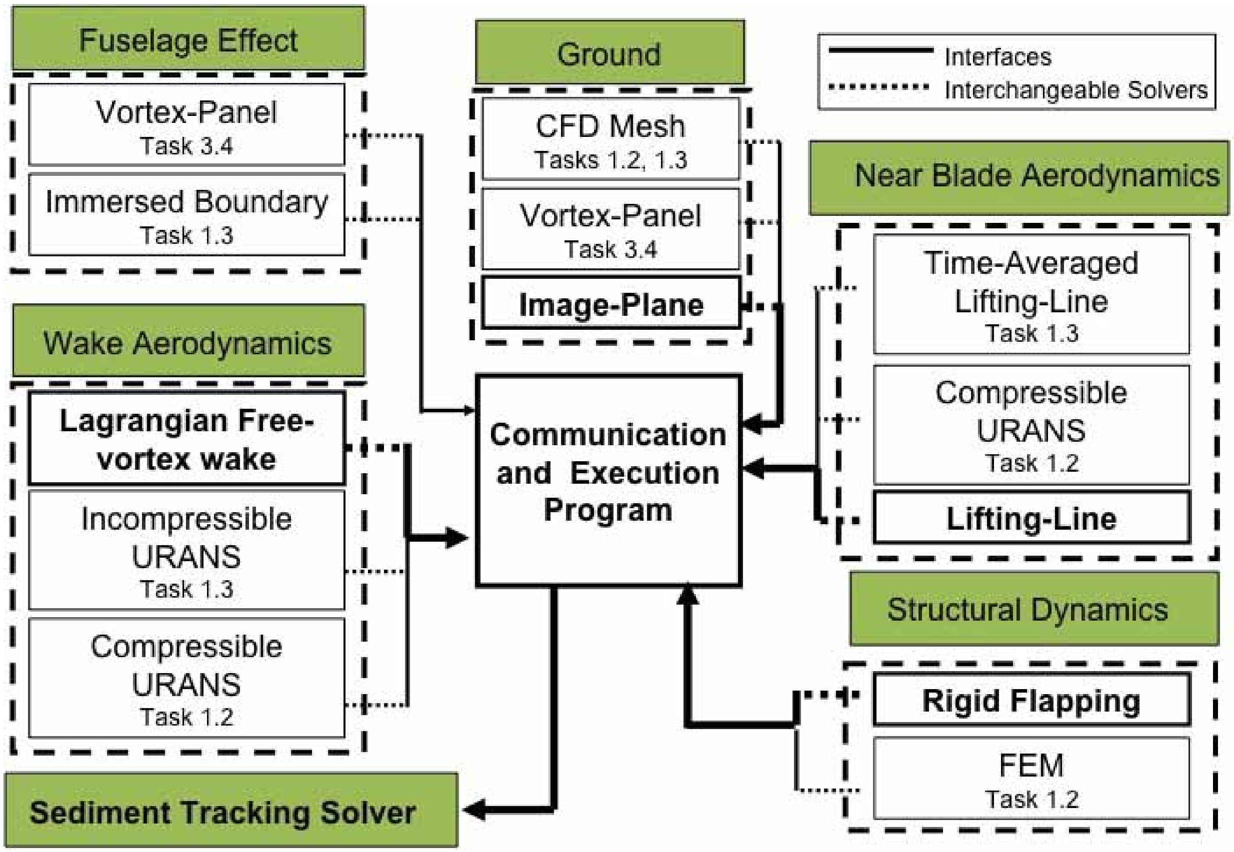

Figure 3.14: Schematic illustrating the interaction of the various MURI tasks.

tion transfer not only between different solvers, but also across different processors without the intervention from participating solvers or the end user.

Technical Approach

The primary objective of this task is to synthesize a highly efficient, Advanced Brownout Aeromechanic Technology Environment (ABATE) simulation. The approach builds upon expertise in comprehensive rotorcraft aeromechanics analyses while incorporating strategies and computational models that are developed and used in the other MURI tasks - RANS solvers, Lagrangian vortex methods, sediment uplift and suspension models, as well as optical transmissibility through the resulting dust clouds (Task 3.1). Figure 3.14 summarizes the various interactions between the different MURI tasks.

The primary purpose of Task 3.4 is the integration of the computational models that are developed and validated under the other MURI tasks. For the simulation of each individual domain, the framework allows the user to choose from multiple models varying in sophistication and computational expense. In the present approach, the fluid phase is modeled using a hybrid methodology

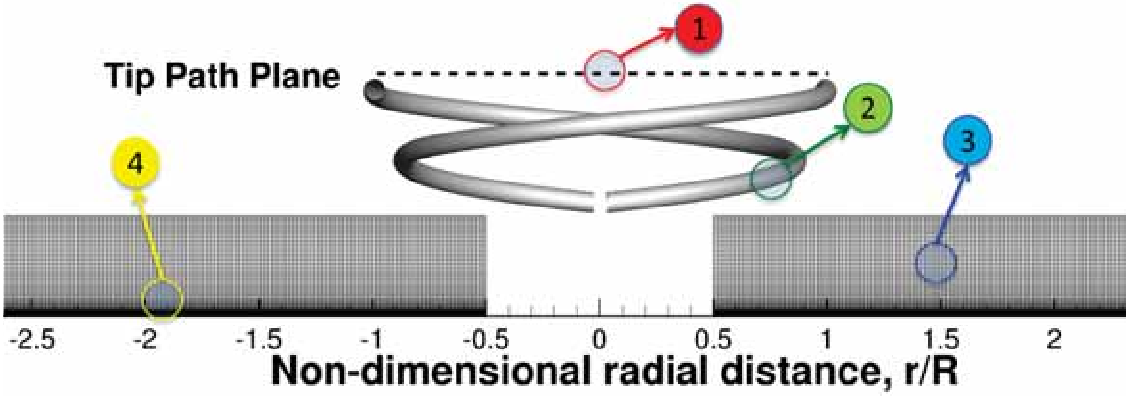

Figure 3.15: Schematic describing the structure of the Hybrid FVM-RANS Solver. (1) For the airloads distribution, a linearized aerodynamics module is used. (2) Computations in the far-wake region between the rotor tip path plane are performed using a free-vortex method. (3) A high-fidelity RANS solver is used for computations near the ground plane. (4) For dual-phase flows, the RANS solution is coupled to a particle transport solver.

combining the capabilities of a RANS solver with a free-vortex wake method. The central idea involves the usage of the grid based solver near the ground plane where complex phenomena like vortex-ground interactions and boundary layer formation/separation occur. The precise location and clustering of this ground mesh is chosen based on a careful analysis of the full-RANS results from Task 1.2. For regions that are well separated from the ground, a filament based free-vortex method (FVM), similar to the model used in Task 3.2, is employed.

Figure 3.15 illustrates the combination of RANS and free-vortex wake that is used to model the fluid-phase. At the RANS-FVM interface, a non-reflecting boundary condition is employed to admit vortical structures into the Eulerian mesh. Figure 3.16 shows a representative ground mesh system used in the hybrid methodology.

For the dual-phase calculations, the sediment phase is currently being modeled using a Lagrangian particle tracking algorithm (see Task 3.2), which is one way coupled. In the current work, all simulations are performed in a time-accurate fashion.

This hybrid approach leads to a large reduction in computational expense when compared to full RANS simulations that employ Eulerian grids to simulate the entire domain. While this strategy is superior to the full-RANS simulations in terms of numerical efficiency, for peak performance

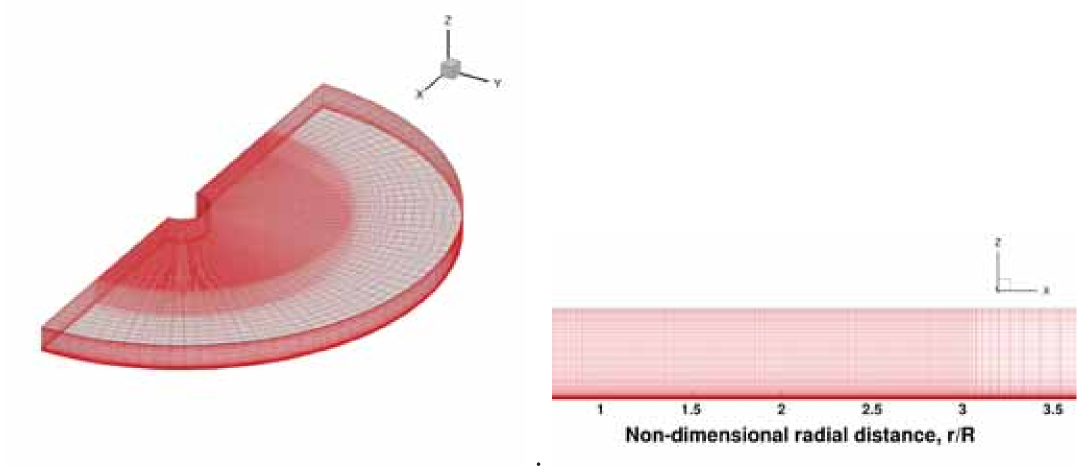

(a) Isometric view of the ground mesh used for RANS calculations. The dimensions of this mesh are 60x180x120

(b) Side view of the ground mesh showing refinement to resolve both tip vortices and the boundary layer

Figure 3.16: Mesh system used in the hybrid simulation of the micro-rotor.

it is still required to run the hybrid method on dozens of processors using a domain decomposition strategy. For a given problem size, domain decomposition is not scalable to an arbitrarily large number of processors – in this limit, the time taken for information transfer between sub-domains becomes comparable to the time taken for computations. To circumvent this difficulty, a new approach was sought.

In Task 3.2, one of the strategies employed for algorithmic speedup involved the use of GPU technology to accelerate the highly data-parallel Biot-Savart computations in the free-vortex wake model. The resulting solver demonstrated considerable speedup over equivalent serial versions. Using this performance gain as a benchmark, all components of the hybrid method were rewritten and optimized in CUDA-C. Each component was then validated using canonical test cases and benchmarked on various gaming and general-purpose GPU platforms. On combining these different GPU-based solvers, the resulting desktop simulations using the hybrid method were shown to be significantly faster than previous calculations involving domain decomposition strategies. Previously, a single revolution of an MAV-scale rotor required close to 6 hours on 32 Intel Xeon cores. Now, using the GPU-based hybrid method on a gaming platform like the GTX Titan, a single revolution is completed in just 1.25 hours.

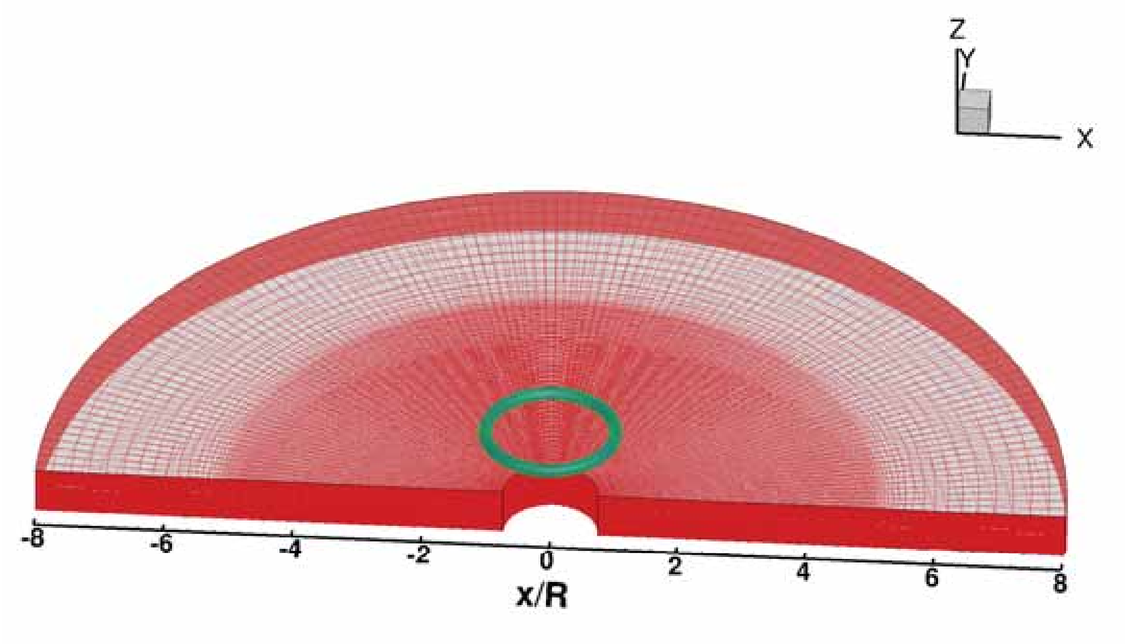

(a) Mesh system used for RANS calculations in the impinging vortex ring simulations

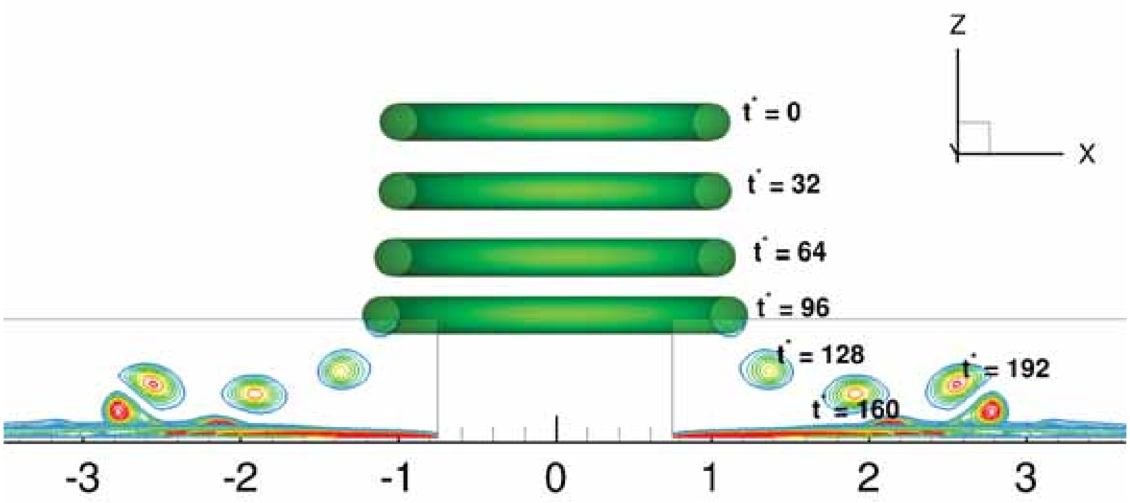

(b) Hybrid methodology prediction of vortex ring trajectory

Figure 3.17: CFD validation using hybrid methodology of experiments performed under Task 2.3.

Results

The GPU-based hybrid methodology was first validated with experiments performed under task 2.3. The experiments consisted of an impinging wall jet formation by modulating the flow at the exit plane of a nozzle to produce a coherent vortex ring that proceeded to interact with the ground plane. Figure 3.15(a) shows the CFD mesh system that consisted of a cylindrical background mesh for RANS calculations. The free-vortex wake filaments in the Lagrangian wake were initialized in

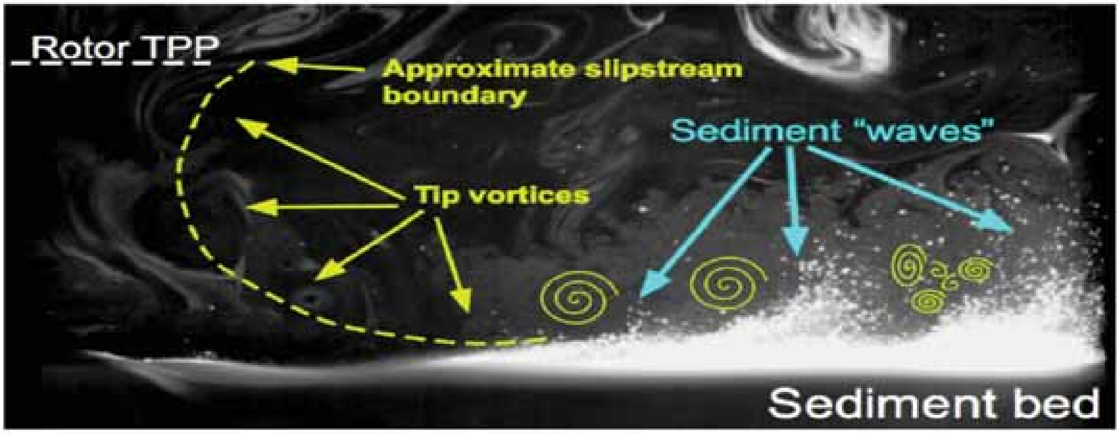

(a) Formation of sediment waves seen in the experiments

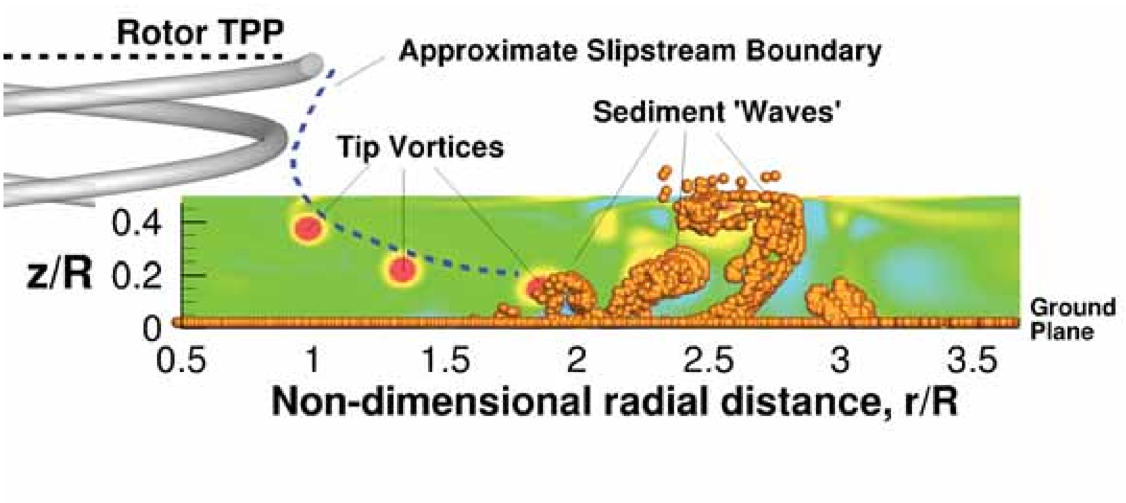

(b) Formation of sediment waves seen in the simulations

Figure 3.18: The formation of sediment waves outboard of the rotor. Note: The particles are not drawn to scale.

a ring topology with the end of the last filament with the beginning of the first. The impinging vortex ring was modeled using an analytical expression. Figure 3.15(b) shows the tip vortex trajectory predicted by the hybrid methodology by superimposing seven representative time instances in the simulation. The formation of a secondary vortical structure was observed at the ground plane similar to a phenomena reported in experiments. The approximate position, size and strength of this secondary vortex, relative to the primary vortex were also found to be in good agreement with experimental observations. The computations were quantitatively validated by comparing predicted time-averaged, velocity profiles at the ground plane with experimental measurements.

The hybrid methodology was then used to model the single-phase and dual-phase flow environment beneath a hovering micro-scale rotor. The simulations were performed in a time-accurate

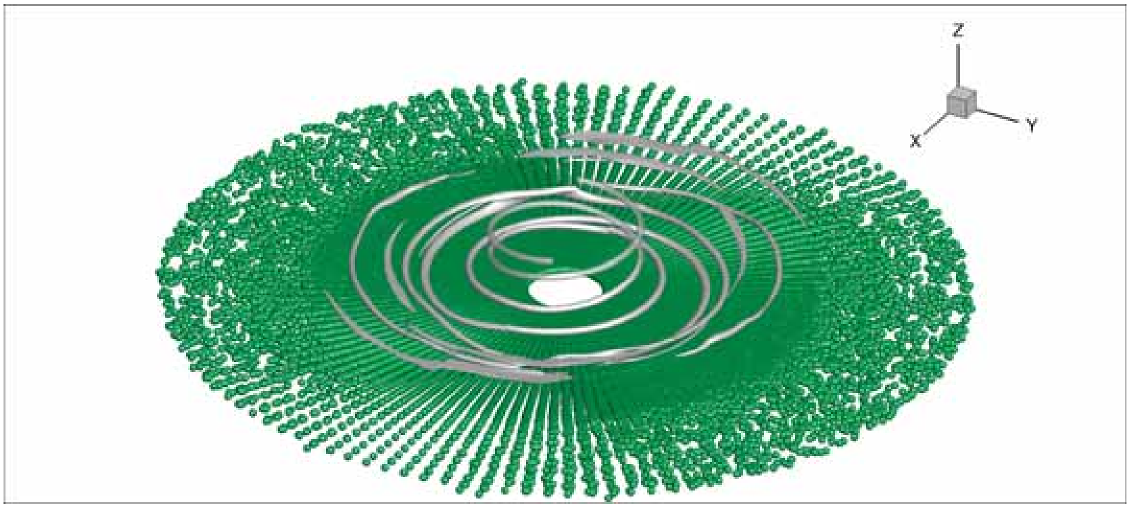

(a) Isometric view of the dual-phase flow field at the start of the computations. Both the free-vortex wake away from the ground and iso-surfaces of vorticity inside the RANS mesh are plotted to show the tip vortex trajectory. Most particles are lying immobile on the ground plane.

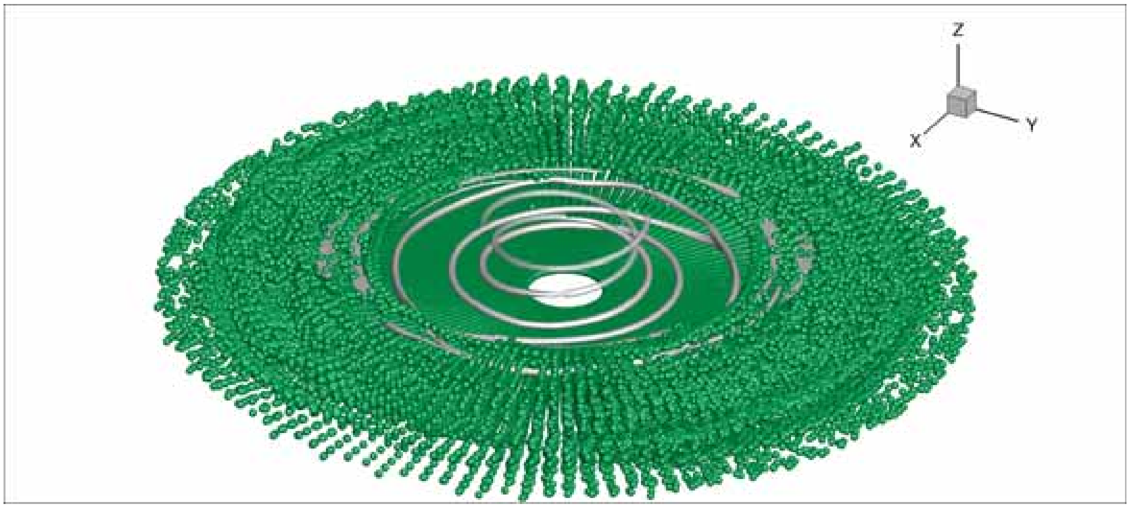

(b) Isometric view of the dual-phase flow field after 16.25 revolutions. The dispersed phase is highly active with particles being entrained around close-proximity vortices to form well defined three-dimensional waves.

Figure 3.19: Predicted 3D structure of the dual-phase flow field with 50 micron particles beneath a hovering MAV-rotor. Note: The particles are not drawn to scale.

fashion. The single-phase results were validated with experiments performed under Task 1.1. The work under Task 2.2 with a micro-scale rotor operating in ground effect over a sediment bed had identified six primary transport mechanisms that dominated the dispersed phase in vortical flows. These experimental results were used to validate computational approaches that simulate the two-phase flow field. In the present approach, sediment particles were mobilized and entrained into the flow using threshold friction velocity condition based on Bagnolds model. Unsteady pressure effects and particle collisions were neglected, though the modular structure of the ABATE environment means that other sediment mobility models can be used. Figure 3.18(a) compares a snapshot of the dual-phase simulation with an image visualizing the particle distribution seen in the laboratory experiments (Fig. 3.18(b)) conducted under Task 2.2. The creation of sediment waves was observed outboard of the rotor similar to those seen in experiments, if multiple layers of particles existed in the sediment bed. Figure 3.19 shows an isometric snapshot of a dual-phase simulation showing the 3D structure of a typical brownout cloud. Clearly defined and sustained three-dimensional sediment waves are seen to form in simulations involving particles of 50 microns. This size of particles were also observed to exhibit the mechanisms of creep and vortex trapping with the latter mechanism being the dominant mode of transport at this scale. Furthermore, the regions of sediment mobility were seen to coincide with the radial zones where the predicted friction velocity was observed to be the largest.

Papers Published

1. Thomas, S., Laksminarayan, V., Kalra, T and Baeder, J.D., “Eulerian-Lagrangian Analysis of Cloud Evolution using CFD coupled with a Sediment Tracking Algorithm,” American Helicopter Society 67th Annual Forum, Virginia-Beach, VA May 2011.

2. Kalra, T., Laksminarayan, V., Baeder, J.D. and Thomas, S., “Methodological Improvements for Computational Study of a Hovering Micro-Rotor in Ground Effect,” AIAA Summer Conference, Honolulu, HI June 2011.

3. Thomas, S., Kalra, T and Baeder, J.D., ‘A Hybrid CFD Methodology to Model the Two-phase Flowfield beneath a Hovering Laboratory Scale Rotor,” AIAA Summer Conference, New Orleans, LA June 2012.

4. Thomas, S., Amiraux, M and Baeder, J.D., ‘GPU-accelerated FVM-RANS Hybrid Solver for Simulating Two-phase Flow beneath a Hovering Rotor,” American Helicopter Society 69th Annual Forum, Phoenix, AZ May 2013.

5. Thomas, S., Amiraux, M and Baeder, J.D., ‘Modeling the Two-phase Flowfield Beneath a Hovering Rotor on Graphics Processing Units using a FVM-RANS Hybrid Methodology,” AIAA Summer Conference, San Diego, CA June 2013.

Task 3.5

Computational Considerations in the Prediction of Brownout Dust Clouds

Investigator(s): Ramani Duraiswami, Nail A. Gumerov, J. Gordon Leishman

Institution/Department: University of Maryland, University of Maryland, Department of Aerospace Engineering & Department of Computer Science

Graduate Student(s): Qi Hu, Monica Syal

Contact email(s): leishman@umd.edu

Background and Technical Challenges

The primary goal of this task was to develop and test high performance computing (HPC) methods capable of efficiently handling the large-scale numerical problems that occur in the computation of rotorcraft brownout. There are several approaches that can be used to compute such flows, including Eulerian methods based on finite difference discretization and Lagrangian methods. The latter are among the most advanced of contemporary computational fluid dynamics methods. The present work makes use of Lagrangian methods, although the modeling and computational approaches being developed in this research task are not restricted to only these. Lagrangian methods are mesh free (or may require only surface meshing as opposed to volumetric meshes), but require the tracking and interaction of large numbers of flow singularities and particles, or particle clusters.

The technical challenges faced included: 1. The effective utilization of advanced hardware, including single and multiple graphics processors (GPUs) as well as clusters consisting of many heterogeneous nodes, each of which consists of multicore CPUs and several GPUs; 2. The development and use of advanced scalable algorithms that reduce computational cost of the problem from $O\left(N^2+NM\right)$ to $O\left(N+M\right)$, thus providing orders of magnitude improvements in computational speed. Such algorithms are also memory compact, which is very important; 3. Integrating the cumulative effects of hardware and algorithmic accelerations, i.e., the implementation of the advanced algorithms on advanced heterogeneous architectures, which requires solution of many technical tasks such as heterogeneous programming and the modification of the algorithms for the most efficient use of workstations and clusters, etc.; 4. Challenges related to mathematical modeling to reduce the computational complexity of the problems, which includes brownout particle clustering algorithms, developing a combination of methods of continuum mechanics of multiphase flows with direct simulations, development of efficient interpolation techniques, stabilization of numerical schemes (e.g., the use of high-order symplectic time marching schemes, error control, and the use of heterogeneous precision computations), and frameworks for comparisons with other numerical techniques.

Technical Approach

Modeling the brownout problem is complex and requires expensive computations of two-phase, unsteady, three-dimensional vortical flows. The memory and speed limits of conventional computational resources, such as personal computers and small or mid-size CPU clusters present a barrier in the use of computations to conduct parametric studies, solve optimization and design problems, and investigate the brownout phenomenon based on first principles modeling. The research conducted in this task has focused on several directions to help solve these problems:

1. **Hardware acceleration.** The use of graphics processors (GPUs) for acceleration of already developed and tested methods for brownout simulations;
2. **Algorithmic acceleration.** Performing fundamental research on the development of a scalable fast multipole method (FMM) on heterogeneous computing architectures, which can substantially accelerate simulations by the realization of scalable algorithms;
3. **Combined hardware/algorithmic acceleration.** The design of efficient data structures and homogeneous/heterogeneous algorithms for single PCs, multicore PCs, multicore PCs with graphics processors and heterogeneous clusters, which have computing nodes that consist of multicore CPUs and several GPUs.

While initial work in items 2 and 3 was focused on the algorithms themselves, the technology was transferred to other members of the MURI team. Also, with a view to extending the algorithms to situations involving tail rotors and fuselages, research was conducted on fast-multipole accelerated vortex-lattice methods and versions for these new algorithms have been developed and tested. Special attention was paid to the development of a user-friendly Matlab front end environment for CPU/GPU heterogeneous programming. Research and development of basic algorithms has also continued, so that they can be accelerated and applied to large scale problems. The latter includes extension of the algorithms to problems with periodic boundary conditions.

Results

The research has proceeded toward: 1. Validation and testing of the methods, and 2. Finding solutions to bottleneck problems that affect the performance and scalability of the algorithms.

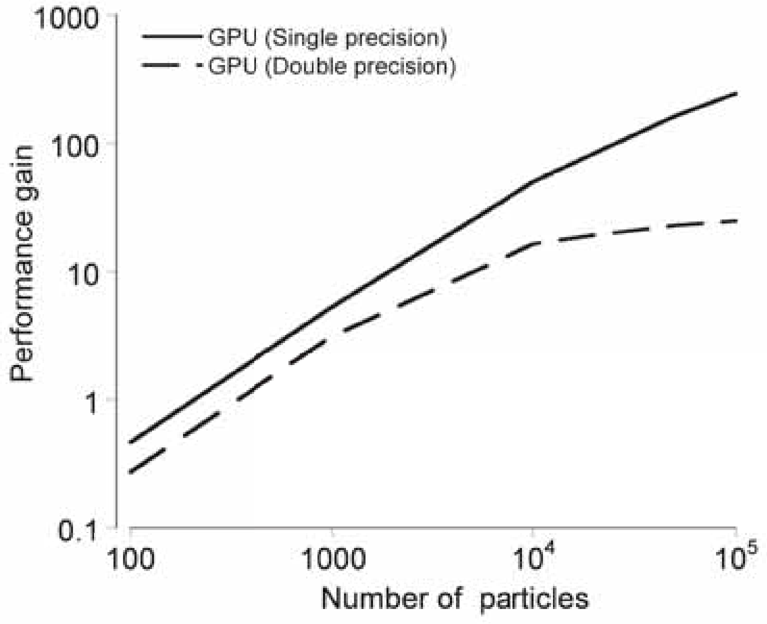

Figure 3.20: Brute force acceleration of brownout simulations using the GPU.

Graphics Processors and Brute Force Acceleration

This activity is related to the efficient utilization of graphics processors to accelerate existing algorithms and methods. The parts of the FORTRAN algorithm related to computation of the velocity field at the particle location and translation of particles were mapped on the GPU using FLAGON middleware library [1]. The dust clouds during a landing maneuver were computed for a representative single rotor helicopter with a 4-bladed rotor. A total of 1 million particles were used in this case to obtain the dust cloud. To obtain 35 seconds of actual simulation time (approximately 150 rotor revolutions) of the dust cloud development computed in a CPU only environment takes about 23 days of wall-clock time. If implemented on the GPUs, the same solution can be obtained in 23 hours, and without compromising on accuracy [2]. However, the actual performance gains obtained from the GPU depend upon the problem parameters and the desired numerical precision.

Figure 3.20 shows the computational performance gains obtained for such brownout simulations, implemented on both single precision and double-precision GPU architectures for different particle counts. The performance gain is defined as a ratio of wall-clock times required to run a case on the GPU architecture and the full CPU simulation. The results obtained are clearly very good: 250 times speed-up for single-precision and 25 times speed-up for double-precision. Notice that the latter numbers are obtained using NVIDIA C1060 cards, for which there is almost an order of magnitude difference in single and double precision simulations. Newer cards, such as the NVIDIA C2050 have reduced this gap substantially (only two times difference in the performance).

Important things learned during this task were related to the stability of the time marching schemes with single and double precision, multi-language programming, and interfacing of the conventional FORTRAN and C/C++ codes with graphics processors, which basic programming was performed using the CUDA environment and the middleware library mentioned previously.

Algorithmic Accelerations

Methods to compute high Reynolds number vortical flows include the Eulerian, Eulerian-Lagrangian, and fully Lagrangian methods. Each approach has its relative advantages. The present work has focused on Lagrangian methods, which are better suited to handle enormous amount of spatially non-uniform unstructured data because they avoid large volumetric meshes. The computation of single-phase flows can be undertaken using vortex element methods (VEM), while the computation of the two-phase flow can be realized by means of the tracking of individual representative particles in a given carrier fluid flow or in a flow affected by the dust particles by using one- and two-way interaction schemes, respectively; see Task 3.2.

The major challenge in the efficient use of Lagrangian methods in the simulation of brownout is the modeling of the large number of singularities (e.g., markers in the rotor wake) that are required to represent the flow with the necessary level of detail and accuracy. Each Lagrangian marker also may interact with another Lagrangian marker (vortex element or other fluid particle), so the number of such interactions at each time step becomes N^2, where N is the number of markers. In the case when a second phase (particle or dust) is present and is represented by M particles, there are an additional NM interactions. Therefore, the overall computational complexity of the problem becomes extremely large, i.e., $O\left(N^2+NM\right)$. In terms of algorithm developments two major improvements can be envisioned. First, reduction of M via some intelligent scheme. Second, the use of scalable algorithms of complexity $O(N+M)$ or with some additional logarithmic factors with respect to N and M.

The first problem can be attacked by using clustering algorithms, continuum descriptions of the multiphase flow, and fully Lagrangian approaches for the particle number density. Several algorithms of these type have been tried and showed some improvement [3], but technical challenges still remain, especially in algorithms related to particle number density tracking because they require advanced interpolation techniques for unstructured data sets. Several algorithms have been developed for this purpose, however they still require more study for high performance implementations and so far comprehensive tests have been conducted only in two dimensions.

One of the major algorithmic developments of the present research is related to the fast-multipole accelerated vortex-element methods. A new translation theory has been developed for such methods based on the Lamb–Helmholtz decomposition of the vortical fields [10]. Such a formulation and theory enables reduction of computations of velocity and velocity gradient fields to the evaluation of just two coupled scalar harmonic potentials (solutions of the Laplace equation). In some reported high performance computing of vortical flows using the fast multipole methods, the computation of the vortex stretching terms was found to be very computationally expensive. The algorithms developed in this research task were shown to reduce the computational cost by several times.

Another algorithmic improvement was the efficient computation of vortex core functions. Several versions of the VEM were developed, including vortex particle method and vortex filament method, which were carefully tested on a number of well-known problems, such as the interaction of vortex rings and filaments. The method was also tested for some experimental cases conducted in Task 1.1. One such comparison is presented in Fig. 3.21. Here, measurements of the velocity field generated by a single rotating blade that were obtained using particle image velocimetry (Task 1.1) were compared to results using the vortex method. It can be seen that the measured and simulated fields are in good general agreement.

Fast Multipole Methods

The vortex methods are accelerated in the present work via the fast multipole methods (FMM). Solution of practical problems using a Lagrangian approach with scaling $O(N^2)$ makes it impossible to simulate problems larger than $N \gtrapprox 10^5$. The FMM is the break-through algorithm, which increases this limit by several orders of magnitude. One of the major contributions of this project was the development of a much faster distributed parallel version of the FMM.

In the beginning of this task, a basic commercial FMM code was available for the scalar Laplace equation in three dimensions. This code was used as a kernel and routines were built to accommodate the new translation theory mentioned above. In addition, new methods were developed to create an FMM on distributed parallel computing architectures. In the developed algorithm each component had fine grain parallelization for multicore machines, while the work was distributed by a novel strategy across many machines. The whole algorithm was revised, profiled,

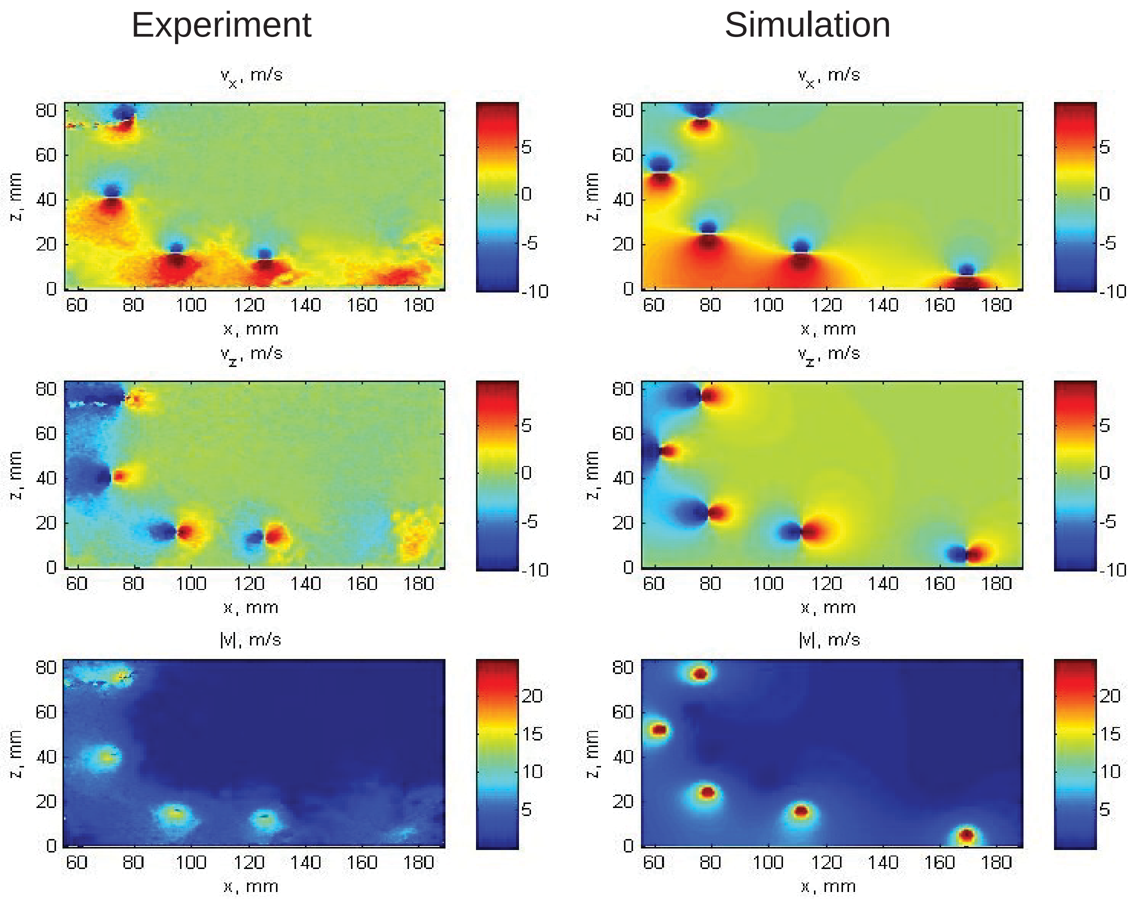

Figure 3.21: Comparison of the measured and simulated velocity field components, v_x, v_z, and $\left|v_{||}\right| = \left(v_x^2 + v_z^2\right)^{1/2}$ for a single blade of length R =77 mm, rotating in the plane parallel to the ground z = 0 at height $z_0 = R$ at frequency 85 Hz. The distance, x, is measured from the axis of rotation. The circulation of the tip vortex in simulations was $\Gamma = 0.25$m^2/s.

and the functionality of each module was carefully tested.

One of the major developments was related to FMM data structures. The research led to the development of a novel and different approach to the computation of data structures that avoids conventional sorting algorithms, which are relatively costly. Instead, algorithms were developed based on partial sorting, fixed-grid sorting, and other improvements (see list of publications). Such improvements enabled accelerations that were several times more than that of the conventional algorithm on a PC, and up to two orders of magnitude acceleration on the GPU. The reason why so much attention was placed on the data structures and this part of the FMM algorithm is related to the fact that in the present project the FMM was applied to dynamic problems where particles

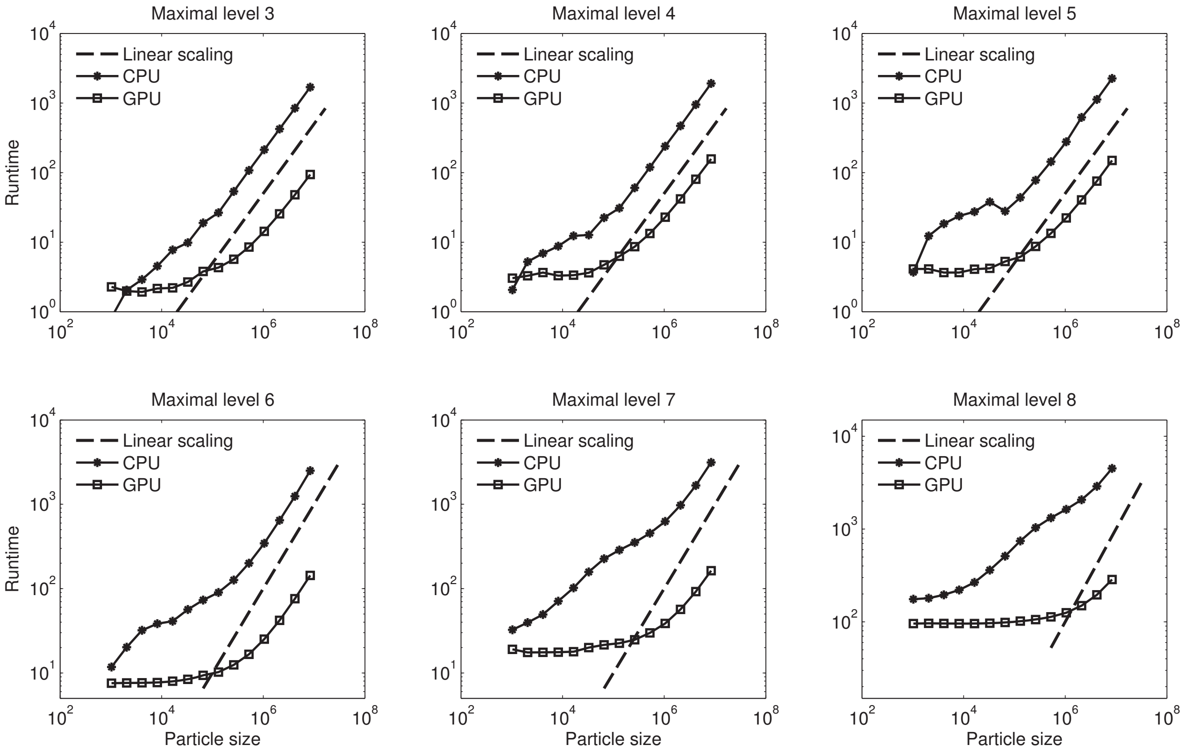

Figure 3.22: Data structure construction time vs number of particles for a non-uniform (spherical-surface) distribution of particles. Computations on a single node using one GPU. Each sub-figure corresponds to a maximal level setting for the octree.

change their location every time step, and efficient construction of the FMM data structures becomes a bottleneck, especially in the GPU versions. Figure 3.22 show the speedups that were obtained for the construction of data structures, which includes both hardware and algorithmic accelerations.

One of the achievements of the present research is a full FMM on a single GPU suitable for simulation of *dynamics problems*. The very first implementation of the FMM on the GPU did not utilize the GPU for construction of data structures, as it was found to be relatively inefficient [7, 8]. This algorithm may have an important impact on a number of fields where dynamic FMM-based computations are important.

Comparison of the results obtained by the FMM with other high-performance techniques, such as the FFT-based algorithms (pseudospectral, DNS simulations) requires solution of problems with periodic boundary conditions, which within the known approaches requires substantial modification of the core FMM code and data structures. Within the present project a novel method to obtain periodic solutions using an available FMM for free-space problems is developed [13]. This was also implemented on the GPU. Tests demonstrate a good performance. The algorithm should find applications in many problems in CFD, molecular dynamics and crystallography.

Heterogeneous Algorithms and Architectures

Despite the achievement of an efficient FMM realization on a single GPU, to solve larger problems one must use heterogeneous architectures. These could be a single workstation (with several multicore CPU chips and a few GPUs), or a distributed network of such inter-connected workstations.

Careful analysis of the FMM showed that some parts of the algorithm cannot be efficiently mapped on GPUs and that these parts have comparable or better performance on the multicore CPU. This is because of limited local memory of graphics processors (cache), and some parts of the FMM are memory bound. However, for other parts the GPU can be very efficient, and accelerate them by a factor of a hundred or so. Hence, the use of heterogeneous CPU/GPU architectures provides a natural mapping/advantage for algorithms with different parts such as the FMM. We developed this concept theoretically, which includes parallel execution of different parts of the algorithm on the CPU and GPU, compacting of information for CPU/GPU exchange, data structures, designing for different levels of parallelism (fine and coarse grained), and developing basic concepts for the implementation of the FMM on heterogeneous architectures.

A paper on this research was presented at the Supercomputing'11 conference [4], and the algorithm has since been subsequently further developed and extended to handle vortex elements [6, 12]. The algorithm showed very good performance and scalability and enabled computations of test problems of size up to 1 billion particles on a midsize heterogeneous cluster (32 heterogeneous nodes with 64 GPUs on the Chimera Cluster at the University of Maryland Institute for Advanced Computer Studies). While different performance depending on the problem can be achieved, estimates show that the peak performance was of the order of 20 Teraflops, but if the same size problem should be computed without algorithmic acceleration (FMM), a 2 Exaflop performance is needed to achieve the observed timing. Figure 3.23 illustrates timing for one time step achieved by this algorithm for different problem sizes. It is important to note that heterogeneous computing is a trend in contemporary high performance computing because it utilizes resources (multicore PCs) neglected in pure GPU computing, provides better energy efficiency, substantial acceleration, and overall economical benefit.

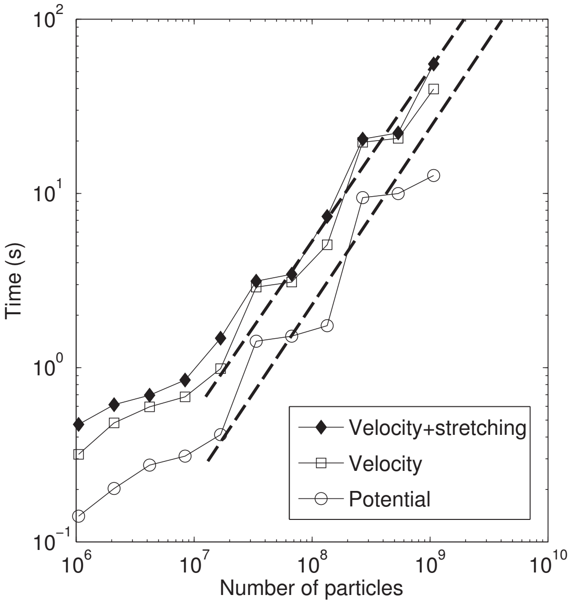

Figure 3.23: The wall clock time for one time step of the VEM (vortex blob version) accelerated by the FMM running on 32 heterogeneous nodes of the UMIACS Chimera cluster. The curves correspond to the case of a scalar potential computation, velocity only, and velocity plus stretching term.

Recent Results

During this past year, besides continuation tasks as development of user friendly interfaces for the developed code and test runs, work was started on the pilot development of another vortex element method, which is known as the vortex-lattice method (VLM). The method is designed for simulation of high Reynolds number unsteady flows generated by lifting surfaces, and has been successfully applied to solution of a number of aerodynamics problems. A feature of this method is that it computes the development of vortex sheets, as opposed to vortex filaments and blobs. In principle, such an approach can be combined with other vortex methods, such as Task 3.2. Accurate description of the flows generated by rotorcraft and observed in experiments requires modeling and computations of such sheets; see Task 1.1 for experimental measurements.

The standard implementation of the VLM is even more limited in terms of the size of the problem than the vortex particle or vortex filament methods because at every time step the lifting surface generates additional elements of the sheet, which propagate in space and interact with solid objects. After several time steps the vorticity distribution becomes very complex, the number of lattice elements very large, and as all pairwise interactions need be taken into account, making the problem computationally very challenging. The use of the FMM is one component of an approach

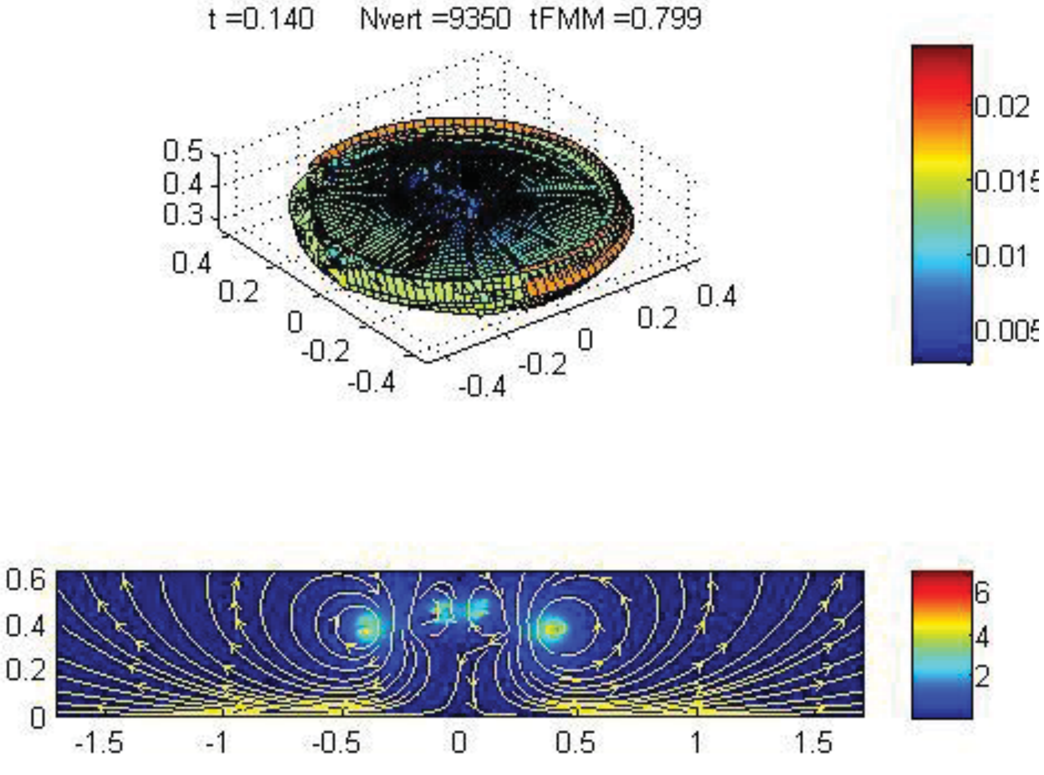

Figure 3.24: An example of the VLM computations accelerated by the FMM. Here a rectangular wing rotates and creates a vortex sheet (ground effect is taken into account, which doubles the number of vertices shown on the upper chart). The chart on the bottom shows a slice of the velocity field (*xz* plane, *z* is the vertical coordinate).

to reduce the problem complexity. Estimates show that even for simple surfaces the savings attributed to the FMM can be several orders of magnitude. A VLM code has been developed and tested, and then extended to use the FMM. The first results show a good performance and potential for its use in the future. Figure 3.24 illustrates a preliminary test simulating the vortex sheet generated by a single rotating blade.

The VLM code then was used as an example to create user friendly Matlab interface for heterogeneous computing using the Parallel computing toolbox (PCT). Extensive tests of the VLM using only hardware (GPU) acceleration and both algorithmic and hardware acceleration (heterogeneous FMM) were conducted. While successful the tests also showed some bottlenecks, particularly, related to schemes of splitting of the heterogeneous algorithm, which should be addressed in the future.

References

1. N. Gumerov, Y. Luo, R. Duraiswami, K. DeSpain, W. Dorland, and Q. Hu, FLAGON: Fortran-9X library for GPU numerics. GPU Technology Conference NVIDIA Research Summit, San Jose, CA, USA; September 30-October 2, 2009.
2. Q. Hu, M. Syal, N.A. Gumerov, R. Duraiswami and J.G. Leishman, "Toward Improved Aeromechanics Simulations Using Recent Advancements in Scientific Computing," Proceedings 67th Annual Forum of the American Helicopter Society, Virginia Beach, May 3-5, 2011.
3. B. Govindarajan, J.G. Leishman, and N.A. Gumerov, "Evaluation of Particle Clustering Algorithms in the Prediction of Brownout Dust Clouds," Proceedings 67th Annual Forum of the American Helicopter Society, Virginia Beach, May 3-5, 2011.
4. Q. Hu, N. A. Gumerov, and R. Duraiswami, "Scalable Fast Multipole Methods on Distributed Heterogeneous Architectures, Proceedings of International Conference for High Performance Computing, Networking, Storage, and Analysis, ser. SC'11. New York, NY: ACM, 2011, pp. 36:1–36:12.
5. Q. Hu, N. A. Gumerov, and R. Duraiswami, "Scalable Distributed Fast Multipole Methods," Proceedings of the 14th International Conference on High Performance Computing and Communications, Liverpool, UK, June 25-27, 2012.
6. Q. Hu, N. A. Gumerov, R. Yokota, L. Barba, and R. Duraiswami, "Scalable Fast Multipole Methods for Vortex Element Methods," International Conference for SC'12Proceedings of the 2012 SC Companion: High Performance Computing, Networking, Storage, and Analysis, 1408-1409, IEEE Computer Society, Washington, DC, 2012.
7. Q. Hu, N. A. Gumerov, and R. Duraiswami, "GPU Accelerated Fast Multipole Methods for Dynamic N-Body Simulation," Parallel CFD 2012, Atlanta, GA, May, 2012.
8. Q. Hu, N. A. Gumerov, and R. Duraiswami, "GPU Accelerated Fast Multipole Methods for Vortex Particle Simulation," Computers and Fluids, 88, 857-865, 2013.
9. Q. Hu, N. A. Gumerov, R. Yokota, L. Barba, and R. Duraiswami, "Scalable Fast Multipole Methods for Vortex Element Methods," International Conference for SC'12Proceedings of the 2012 SC Companion: High Performance Computing, Networking, Storage, and Analysis, 1408-1409, IEEE Computer Society, Washington, DC, 2012.

10. N. A. Gumerov, and R. Duraiswami, "Efficient FMM Accelerated Vortex Methods in Three Dimensions via the Lamb-Helmholtz Decomposition," Journal of Computational Physics, 240, 310-328, 2013.
11. B. Govindarajan, J.G. Leishman and N.A. Gumerov. "Particle-Clustering Algorithms for the Prediction of Brownout Dust Clouds," AIAA Journal, 10.2514/1.J051907, 1-15, 2013.
12. Q. Hu, N. A. Gumerov, and R. Duraiswami, "Parallel Data Structures for Fast Multipole Methods, *Journal of Parallel Computing* (under revision). Also published on arXiv `http://arxiv.org/abs/1301.1704`.
13. N.A. Gumerov and R. Duraiswami, "A method to compute periodic sums," Journal of Computational Physics, 272, 307-326, 2014.
14. Q. Hu, N. A. Gumerov, and R. Duraiswami, "A Scalable Fast Multipole Method for Heterogeneous Architectures," *Journal of Computational Physics* (under preparation).

Task 3.6

Blade Tip Actuation for Tip Vortex Modifications for Brownout Mitigation

Investigator(s): D. Stefan Dancila, Joe Milluzzo, J. Gordon Leishman

Institution/Department: University of Texas at Arlington, Department of Mechanical and Aerospace Engineering, the University of Maryland, and The U.S. Naval Academy

Graduate Student(s): Julia Elaine Cline and Reza Azizi Ghasrehelal

Contact email(s): dancila@uta.edu

Background and Technical Challenges

Brownout is a major rotorcraft operational concern in military rotorcraft operations. Brownout results in massive particle uplift into the rotor flow and can lead to the loss of visual references and situational awareness for the pilot who is flying the aircraft. Brownout conditions can also result in excessive erosion of rotor blade, engine components and other mechanisms.

One approach to mitigating brownout relies upon specific flight paths/maneuvers in ground proximity, which is aimed at minimizing the quantity of particles entrained in the rotor flow and/or in redirecting those already entrained away from the field of view; see Task 3.3 for details. This type of mitigation approach, however, may restrict the flight envelope of the helicopter and cause operational issues. A second approach relies upon electronic ground sensing means that are not impaired by brownout, and with the use of an associated cockpit display can provide the crew with sufficient information to operate the aircraft safely. Both of these approaches, however, do not solve the excessive abrasion and wear caused by the suspended dust, and also do not preserve an unconstrained operational flight envelope.

Another approach to brownout mitigation, and the approach followed in this task, seeks to significantly reduce particle entrainment into the rotor flow. This approach fundamentally relies upon the recognition that while brownout is a complex, two-phase flow phenomenon, it may have a flow control solution. The key to this approach is an understanding of the fundamental physical aspects of this complex flow. To this end, a focused, concerted research effort in this direction is being undertaken at the University of Maryland; see Tasks 1.1, 2.2 and 3.3. The complexity of the underlying flow physics suggests that, ultimately, a combined experimental aerodynamics and CFD approach is the most profitable avenue of research.

Technical Approach

Experimental results focused on brownout studies on scaled rotors in ground effect have provided a better understanding of the phenomenon of particle entrainment into the complex, tip vortex dominated hovering rotor flow in ground proximity; see Tasks 1.1 and 2.2. The results show that blade tip vortices play a dominant role in the entrainment of particles from the ground, as well as in their subsequent convection into the rotor flow. The entrainment is amplified by the vortex strength and structure, and by the distance between the vortex and the ground. This observation provides insight into possible avenues for entrainment mitigation, i.e., increase in miss distance and/or a reduction in vortex strength and/or the radial diffusion of vorticity. The peak-to-peak velocity of the vortex, the dominant characteristic for particle mobilization and entrainment, is not determined by vortex strength (circulation) alone, but by the combination of vortex strength (circulation) and the vortex core structure and size (vorticity and velocity distribution). Therefore, a strong circulation vortex with a larger core size may show lower particle mobilization and entrainment compared to a weaker circulation vortex with a smaller core size. This behavior suggests that it should be possible to reduce the entrainment by a given blade tip vortex, with a given circulation level (determined by the lift developed by the blade), by radially diffusing its vorticity and increasing its core size.

The objectives of this research are to investigate the validity of the following two working hypotheses: 1. Modulated blade tip blowing—active (piezoelectric) or passive (resonant)—provides sufficient flow control authority to modify the structure, strength, size, and/or trajectory of the blade tip vortex such that with proper selection of input the particle entrainment capability of the blade tip vortex, and implicitly that of the rotor flow as a whole, are significantly reduced, resulting in the mitigation of brownout. 2. Modulated blade tip blowing—active (piezoelectric) or passive (resonant)—provides sufficient flow control authority to excite instabilities of the tip vortex resulting in vortex burst and consequently spreading vorticity and reducing the particle entrainment capability of the blade tip vortex, and implicitly that of the rotor flow as a whole, resulting in the mitigation of brownout.

Results

The focus of the work was initially upon the development of a set of four ducted blade configurations representing a progression from the baseline slotted blade configurations and obtained by migrating the blowing orifices to the upper edge and by progressively varying their dihedral orientation in increments. These blade configurations will allow a comparative investigation of steady

Figure 3.25: A modification made by relocating the blowing orifices at the upper edge and oriented at 45 degrees dihedral. Blade tip detail.

Figure 3.26: A modification made by increasing the dihedral angle to 60 degrees. Blade tip detail.

Figure 3.27: A modification made by reducing the dihedral angle to 30 degrees. Blade tip detail.

blowing effectiveness. Four blade model configurations have been manufactured that implement steady blowing driven by centrifugal pumping and with blowing nozzles progressively migrating from the baseline configuration (demonstrated effective previously at the University of Maryland) towards locations and orientations that may provide increased effectiveness; see Figs. 3.25 to 3.27.

Recent work on this task has been performed by Milluzzo and Kuerbitz at the U.S. Naval Academy under the Office of Naval Research (ONR), award number N0001614WX30023, examining the fluid dynamics of the wake produced by a rotor these rotor blades as it interacted with a ground plane. Two-component PIV and FV was used to evaluate the flow field generated by a rotor operating at one rotor radius above the ground. The goal of this study was to quantify the effect centrifugal pumping blade designs had on the flow field generated by the rotor. Five different blades were tested; a rectangular (non-slotted) blade was used as a baseline case. The other four blade designs had an inlet slot near the root of the blade and a internal channel that connected the inlet slot to exit slots on the side edge of the blade. The exit slots were designed such that they exited along the blade chord line (i.e., 0° from the horizontal) or facing the upper surface of the blade at 30°, 45°, and 60° from the horizontal.

Performance measurements were also taken to quantify the changes in performance associated with the pumping blade designs. Preliminary results have indicated that at lower blade collective pitch angles (i.e., lower thrust) the rotor with the baseline blades had the lowest power required. However, as the rotor thrust was increased the power required for each of the pumping blade designs began to approach the power required for the rotor with the baseline blades. Furthermore, at the higher values of thrust the blade with the 0° exit slots required less power than for the baseline blades.